technische universität
dortmund

Investigations on the Manipulation of Excited State Properties in Luminescent Copper(I)-Carbene Complexes

A thesis presented for the degree of

Doctor rerum naturalium (Dr. rer. nat.)

at the Department of Chemistry and Chemical Biology
of the TU Dortmund University

submitted by
Justin Krieger, né Wieland
born September 22, 1996 in Hagen

Dortmund 2025

Submitted at the Department of Chemistry and Chemical Biology on: 29. 10. 2025

Referees of the written work:
First referee: Prof. Dr. Andreas Steffen
Second referee: Prof. Dr. Carsten Strohmann

Examiners at the public colloquium:
First examiner: Prof. Dr. Andreas Steffen
Second examiner: Prof. Dr. Carsten Strohmann
Chair of the examination commitee: Prof. Dr. Max Hansmann

Date of the public colloquium: 16. 01. 2026

This

PhD thesis

was prepared at the Department of Chemistry and Chemical Biology
of the TU Dortmund University under the supervision of

Prof. Dr. Andreas Steffen

between November 2020 and October 2025.

Complete List of Puplications

Parts of the present work were published in peer-reviewed journals or were presented on scientific conferences.

Paper Articles

A. M. T. Muthig, M. Krumrein, J. Wieland, M. Gernert, F. Kerner, J. Pflaum, A. Steffen, *Inorg. Chem.* **2022**, *61*, 14058.

A. M. T. Muthig, J. Wieland, S. Koop, C. Lenczyk, F. Kerner, B. Hupp, A. Steffen, *Inorg. Chem.* **2022**, *61*, 17427.

A. M. T. Muthig, J. Wieland, C. Lenczyk, S. Koop, J. Tessarolo, G. H. Clever, B. Hupp, A. Steffen, *Chem. Eur. J.* **2023**, *29*, e202300946.

A. M. T. Muthig, S. Maity, J. Krieger, A. Belyaev, B. Hupp, B. Ewald, J. Pflaum, A. Steffen, *Angew. Chem.* 2024, manuscript submitted.

J. Krieger, M. Gernert, A. Steffen, *Inorg. Chem.* **2025**, manuscript in preparation.

J. Krieger, A. Radojcic , A. Steffen, *Chem. Commun.* **2025**, manuscript in preparation.

Conference Contributions

J. Wieland, A. Radojcic, A. Steffen *N-heteroarylic Carbenes (NHArCs) as Chromophore Ligands for NIR emissive Cu(I) complexes* **2022**, 17. Koordinationschemie-Treffen, Jena.

J. Wieland, H. Busen, A. Belyaev, A. Steffen, *Merging Mechanochromic and Circularly Polarized Luminescence with Copper(I) Complexes* **2023**, SPP 2102 LCRMC, Rostock.

For Michael

"If I knew everything, Matrim, I would not need to ask questions."

—Robert Jordan, *The Shadow Rising*

Kurzzusammenfassung

Während phosphoreszente Komplexe des Ir(III) und Pt(II) den Markt der übergangsmetall-basierten OLED-Luminophore im sichtbaren Spektralbereich dominieren, ist es in der Regel schwer besondere Eigenschaften zu modulieren. Als vielversprechende Alternative haben sich die Komplexe der Münzmetalle Cu und Au in Oxidationsstufe +I herausgestellt.

Insbesondere Cu(I), trotz vergleichsweise niedrigem SOC, besitzt neben der hohen strukturellen Fülle über eine einzigartig vielfältige Landschaft energetisch naher angeregter Zustände, wodurch sich Lumineszenzeigenschaften besser modulieren lassen als in den homologen Gold-Komplexen. Im ersten Teil dieser Arbeit werden diverse Kupfer(I)-carbenkomplexe auf ihre Eignung als (Nah-)Infrarot Emitter untersucht. Zunächst wird über die Synthese und photophysikalische Charakterisierung einer Reihe von Kupfer(I)-Halogenidkomplexen berichtet, die *N*-substituierte Phthalazinylidenliganden als Chromophore enthalten.

Unter Verwendung dieser stark π-sauren Carbene in Kombination mit Halogeniden unterschiedlicher Größe wurden monometallische und halogenidverbrückte bimetallische Koordinationsverbindungen synthetisiert. Die bimetallischen Komplexe zeigen im festen Zustand eine schwache orangefarbene Emission mit (XM)LCT-Charakter. Die monometallische Verbindung zeigt hingegen eine sehr schwache Lumineszenz bei 710 nm ($\Phi_{em} < 1\%$), die aus einem niedrig liegenden MLCT-Zustand hervorgeht. In begleitenden TD-DFT Studien für andere Promotionsvorhaben wird der Einfluss von Koordinationsgeometrie und Donorstärke auf den Emissionsmechanismus und den Ursprung der beobachtete bathochromen Verschiebung untersucht. Aus unseren (TD-)DFT-Studien folgt, dass die strukturelle Flexibilität von [Cu(CAAC)(acac)] und strukturell verwandten Verbindungen der Hauptmechanismus für die bathochrome Verschiebung der Emission ist, während in pseudolinearen [Cu(CAAC)(^{R}cp)]-Halbsandwich-Komplexen erhöhte Elektronendichte am

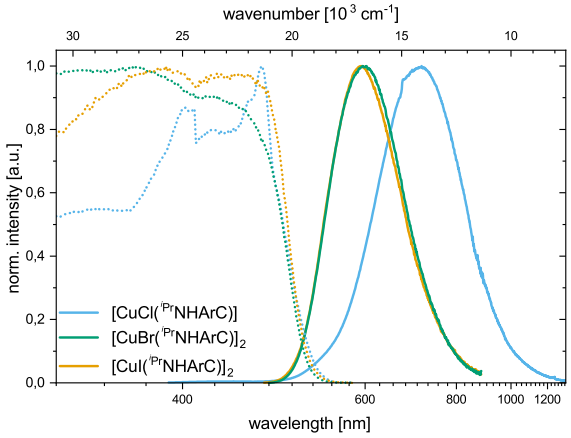

Figure 1: Emissionsspektren (durchgezogene Linie) und Anregungsspektren (gepunktete Linie) von $[Cu(NHArC)(X)]_n$ im festen Zustand bei Raumtemperatur.

Kupfer-Zentrum für die rotverschiebung verantwortlich ist. Sowohl durch Verzerrung als auch erhöhte Donorstärke wird der Grundzustand destabilisiert und die Emissionsenergie reduziert. Während die auftretende Verzerrung in den trigonalen Komplexen zu starker vibronischer Kopplung mit dem Grundzustand führt und so nichtstrahlende Prozesse beschleunigt werden, können sterische Effekte elektronenreicher cp-Derivate (z.B. cp*) solche Prozesse unterdrücken. Die Untersuchung Kupfer(I)-Komplexe für mechanoresponsive und zirkular polarisierte Lumineszenz wird im zweiten Teil dieser Arbeit beleuchtet.

Aufbauend auf mechanoluminochromen Komplexen des Typs [Cu(NHC)(^{R}py)]BF_4 wurde der Austausch des BF_4-Anions gegen chirale Anionen untersucht. Ziel war es durch mechanisch stimulierte Cu-Anionen-Wechselwirkung CPL zu realisieren.

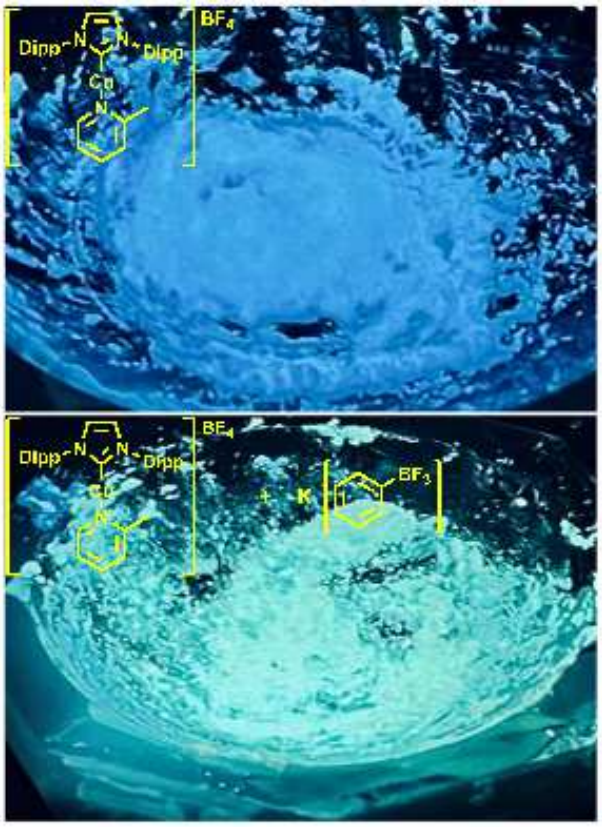

Figure 2: Verriebenes [Cu(IDipp)(^{Me}py)]BF_4 (oben) und verriebenes [Cu(IDipp)(^{Me}py)]BF_4 mit KF_3BPh (unten) unter UV-Bestrahlung.

Im Rahmen dieser Arbeit konnten einige Anionen aufgrund chemischer Inkompatibilität ausgeschlossen werden, die Synthese stabiler Komplexe durch Metathese gelang jedoch nicht. In qualitativen Experimenten konnte jedoch Hinweis gefunden werden, dass Cu – F Wechselwirkungen wichtig für die Mechanoresponsivität sind.

In Cu(CAAC)(NR_2) Komplexen basiert die Mechanoluminochromie hingegen nicht auf der Assoziation eines Anions in die innere Koordinationssphäre, sondern auf der Auflösung von Dipol-Dipol-Wechselwirkungen. Jedoch zeigten unsere theoretischen Untersuchungen, dass für NR_2 = pnz (Phenoxazinat), eine thermisch zugängliche lokale Minimumstruktur mit erhöhter Rotationsstärke existiert. Diese, in PMMA-Matrix durch Wasserstoff-Brücken stabilisierte, geknickte Geometrie liefert eine Begründung, warum trotz kleiner Absortions-Dissymmetrie von etwa $-1 \cdot 10^{-4}$, ein für Übergangsmetalkomplexe hoher g_{lum} von $-3.4 \cdot 10^{-3}$ gemessen werden konnte.

Abstract

While phosphorescent complexes of Ir(III) and Pt(II) dominate the market for transition metal-based OLED phosphors in the visible spectral range, it is generally difficult to modulate specific properties. Complexes of the coin metals Cu and Au in oxidation state +I have proven to be a promising alternative.

In particular, Cu(I) despite its comparatively low SOC, possesses high structural richness and a uniquely diverse landscape of energetically close excited states, which allows luminescence properties to be modulated more effectively than in the homologous gold complexes. In the first part of this work, various copper(I) carbene complexes are investigated for their suitability as (near) infrared emitters. First, the synthesis and photophysical characterisation of a series of copper(I) halide complexes containing *N*-substituted phthalazinylidene ligands as

Using these strongly π-acidic carbenes in combination with halides of different sizes, monometallic and halide-bridged bimetallic coordination compounds were synthesised. In the solid state, the bimetallic complexes exhibit a weak orange emission with (XM)LCT character, while the monometallic compound exhibits a very weak luminescence ($\Phi_{em} < 1\%$) at 710 nm, which originates from a low-lying MLCT state. In accompanying TD-DFT studies for other doctoral projects, the influence of coordination geometry and donor strength on the emission mechanism and the origin of the observed bathochromic shift is being investigated. Our (TD-)DFT studies show that the structural flexibility of [Cu (CAAC)(acac)] and structurally related compounds is the main mechanism for the bathochromic shift of the emission, while in pseudolinear [Cu(CAAC)(^{R}cp)] half-sandwich complexes, increased electron density at the copper centre is responsible for the red shift. Both distortion and increased donor strength destabilise the ground state and reduce the emission energy. While the distortion occurring in trigonal complexes leads to strong vibronic coupling with the ground state and thus accelerates non-radiative processes, steric effects of electron-rich cp derivatives (e.g. cp*) can suppress such processes. The investigation of copper(I)

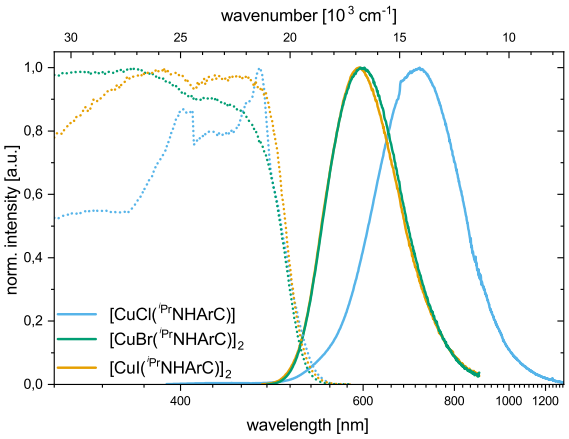

Figure 1: Emission (solid line) and excitation spectra (dotted line) of [Cu[NHArC)(X)]$_n$ in solid state at room temperature.

complexes for mechanoresponsive and circularly polarised luminescence is discussed in the second part of this work.

Building on mechanoluminochromic complexes of the type [Cu(NHC)(^{R}py)]BF_4, the exchange of the BF_4 anion for chiral anions was investigated. The aim was to realise CPL through mechanically stimulated Cu-anion interaction.

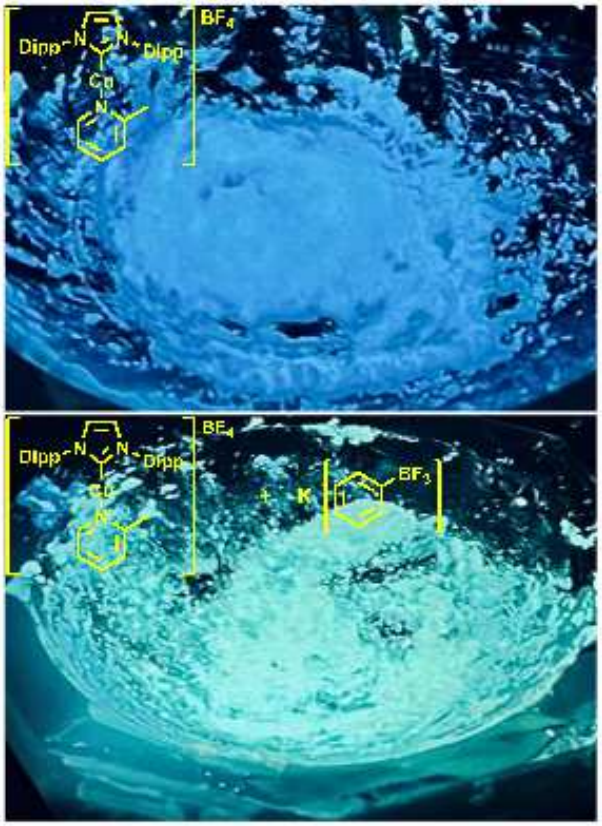

Figure 2: Ground [Cu(IDipp)(^{Me}py)]BF_4 (upper) and ground [Cu(IDipp)(^{Me}py)]BF_4 with KF_3BPh (lower) under UV irradiation.

In the course of this work, some anions could be excluded due to chemical incompatibility, but the synthesis of stable complexes by metathesis was not successful. However, qualitative experiments provided evidence that Cu – F interactions are important for mechanoresponsivity. In Cu(CAAC)(NR_2) complexes, however, mechanoluminescence is not based on the association of an anion in the inner coordination sphere, but on the dissolution of dipole-dipole interactions. However, our theoretical investigations showed that for NR_2 = pnz (phenoxazinate), a local minimum structure with increased rotational strength is thermally accessible. This bent geometry, stabilised in a PMMA matrix by hydrogen bonds, provides an explanation as to why, despite a small absorption dissymmetry of about $-1 \cdot 10^{-4}$, a high g_{lum} of $-3.4 \cdot 10^{-3}$ could be measured for transition metal complexes.

Contents

1 Theoretical Background **1**
1.1 Application of Luminescent Materials 1
1.2 Photophysics of the Photoluminescent Triplet Manifold 4
1.3 Relevance of TM-based emitters 9
1.4 Copper(I)-complexes as a highly modifiable emitter class 13
1.5 Relevance of Low-Energy Luminescence in the (N)IR 18
1.6 Stimulus Responsive Behavior 22
1.7 Molecular Description of Circularly Polarized Luminescence 26
1.8 Objective 29

2 NIR Emission using Cu(I)-Carbene Complexes **31**
2.1 Phthalazin-2-ylidenes as Accessible N-heteroarylic Carbene π-Chromophor Ligands for Deep-Red Luminescent Copper(I)-Halide Complexes 31
2.2 "Trigonal Copper(I) Complexes with Cyclic (Alkyl)(amino)carbene Ligands for Single-Photon Near-IR Triplet Emission" 44
2.3 "Synthesis and Photophysical Studies of Copper(I) CAAC Half- Sandwich Complexes as a Highly Modifiable Class of Emitters" 56
2.4 New Insights into the Design of NIR Emitters 68

3 Merging CPL with Mechanoluminochromism **70**
3.1 Mechanically Induced CPL by Chiral Anion Interaction 70
3.2 "Towards Fast Circularly Polarized Luminescence in 2-Coordinate Chiral Mechanochromic Copper(I) Carbene Complexes" 78
3.3 New Insights into CPL-active Emitters 88

4 Appendix **89**
4.1 General Remarks 89
4.2 Experimental Details to Section 2.1 92
4.2.1 Synthesis and Characterization 92
4.2.2 NMR Spectra 97
4.2.3 Single-crystal X-ray diffraction studies 115
4.2.4 Photophysical measurements 118
4.2.5 Computational Studies 120
4.3 Experimental Details to Section 3.1 135

4.3.1 Synthesis and Characterization 135
4.3.2 NMR Spectra 138
4.4 Supporting Information of Paper Contributions 144

5 Bibliography **173**

List of Abbreviations

A	generic monoanion
A*	generic chiral monoanion
AC	avoided crossing
acac	acetyl acetonate
AER	anion exchange resin
AIM	atoms in molecules
BINOL	binaphthol
bpy	2,2'-bipyridine
Bz	benzoyl
CAAC	cyclic alkyl amino carbene
CAArC	cyclic amino aryl carbene
CI	conic intersection
COD	cyclooctadiene
cp	cyclopentadienyl
cp*	pentamethyl cyclopentadienyl
CPL	circularly polarized luminescence
d	doublet (in NMR-analysis)
DCM	dichloromethane
DET	Dexter energy transfer
Dipp	2,6-Di(isoprpyl)phenyl
EGL	energy gap law
EQE	external quantum efficiency

HOMO	highest occupied molecular orbital
IC	internal conversion
IDipp	1,3-Bis(2,6-diisopropylphenyl)imidazol-2-ylidene
IPh	1,3-Diphenylimidazol-2-ylidene
IRI	interaction region indicator
ISC	intersystem crossing
J	NMR couling constant in Hz
LC	ligand centered
LED	light emitting diode
LLCT	ligand-to-ligand-charge-transfer
LMCT	ligand-to-metal-charge-transfer
LUMO	lowest unoccupied molecular orbital
m	multiplet (in NMR-analysis)
m/z	mass-to-charge-ration
MC	metal centered
ment	menthyl
MLCT	metal-to-ligand-charge-transfer
MO	molecular orbital
NHArC	*N*-hetero arylic carbene
NHC	*N*-heterocyclic carbene
NIR	near infra-red
NMR	nuclear magnetic resonance
OLED	organic light emitting diode
PDT	photodynamic therapy
PMMA	polymethylmethacrylate

pnz	phenoxoazinate
ppm	parts-per-million
ppy	2-phenylpyridine
py	pyridine
q	quartet (in NMR-analysis)
QY	quantum yield
rISC	reversed intersystem crossing
ROS	reactive oxygen species
s	singlet (in NMR-analysis)
sept	septet (in NMR-analysis)
SOC	spin-orbit-coupling
SOCC	spin-orbit-coupling constant
SOM	small organic molecule
SVC	spin-vibronic-coupling
t	triplet (in NMR-analysis)
TADF	thermally activated delayed fluorescence
tart	tartrate
(TD-)DFT	(time-dependent) density functional theory
Tf	trifluoromethylsulfonyl
THF	tetrahydrofuran
TMC	transition metal complex
tpy	terpyridine
TTA	triplet-triplet-annihilation
vdW	van der Waals
VR	vibronic relaxation

XLCT	halid-to-ligand-charge-transfer
(XM)LCT	halide+metal-to-ligand-charge-transfer
δ	chemical shift in ppm
λ	wavelength in nm
$\bar{\nu}$	wavenumber in cm^{-1}
$\Phi_{\mathbf{em}}$	emission quantum yield
τ	life-time
ζ	spin-orbit-coupling constant in cm^{-1}

1 Theoretical Background

1.1 Application of Luminescent Materials

The development of artificial lighting marks a significant turning point in the history of mankind and laid the foundations for a large number of technological innovations that were previously unthinkable. After the incandescent lamp dominated the global lighting market for a long time, the last few decades have seen a shift towards more energy-efficient alternatives. Sodium vapour lamps, mercury vapour lamps and light-emitting diodes (LEDs) have made a substantial contribution to modern lighting technology. These light sources are characterised not only by improved energy efficiency, but also by an increased service life and greater tolerance to various environmental influences.

To fully understand the benefits of LED technology, it is essential to take a look at the underlying mechanism. The functionality of an LED is based on electroluminescence in a semiconductor material. This material consists of layers of different doping: a p-doped (positively doped) layer with defect electrons (holes) and an n-doped (negatively doped) layer with excess electrons. At the interface of these two layers, the p-n junction, electrons and holes recombine when a voltage is applied.[2]

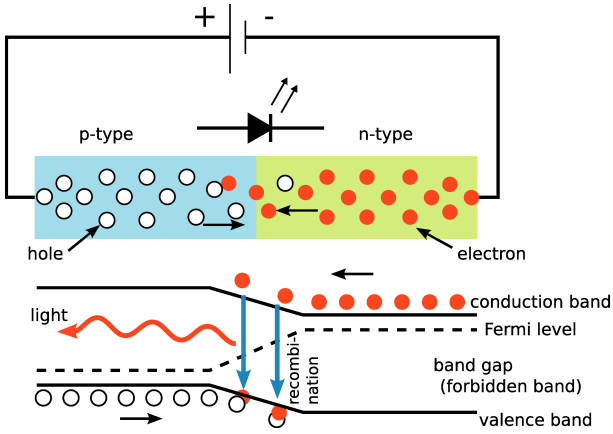

Scheme 1.1: "The inner workings of an LED, showing circuit (top) and band diagram (bottom)" by user *S-kei*. Reprinted from Ref. [1]. Licenced under CC BY-SA 2.5 (https://creativecommons.org/licenses/by-sa/2.5/).

Photons are emitted whose energy corresponds to the band gap of the semiconductor material (Scheme 1.1). The manufacturing of LEDs requires high-purity and low-defect semiconductor materials. In practice, a number of materials have been established spanning the visible spectrum (Table 1.1). In particular the direct band-gap of many gallium pnictogenides, such as gallium arsenide oder gallium nitride, are paramount for efficient charge-to-photon conversion and minimizing thermal losses. Parallel to the further development of general illumination, the use of light sources in display technology has become increasingly important. The quest for brighter, longer-lasting and more colour-true displays has significantly driven research into new

emitter materials in recent years[3,4]. A common example are Liquid Crystal Displays (LCD) in which liquid crystal pixels are photonically excited by LED back-lighting and thus generate the image.

Table 1.1: Typical LED materials and their wavelength range.

LED material	emission wavelength [nm]
GaAs	850–940
GaAsP	605–660
GaAsP:N	585–595
AlGaP	550–570
GaN	450–490

Blue or UV LEDs are used as excitation sources, resulting in a generally high energy consumption. Additionally, such screens cannot display "true black" as a small amount of the back-lighting penetrates through the LC layer. While LED-based liquid crystal displays (LCDs) with LED back-lighting are currently the industry standard, organic light-emitting diodes (OLEDs) are increasingly emerging as competitors.[Chen2017a] In contrast to LEDs, OLEDs are based on organic materials. They utilise electron-hole recombination to electrically excite molecular emitters. The schematic structure of an OLED is shown in Fig. 1.1. Electrons are injected at the cathode and holes are injected at the transparent anode.

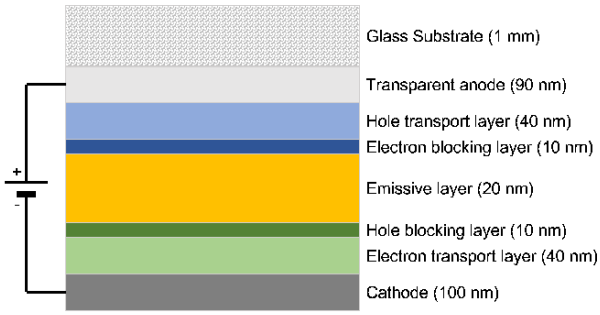

Figure 1.1: Schematic structure of an OLED (not to scale), based on reference [5].

After charge transport, recombination occurs in the emissive layer.[5] Charge-neutral quasi-particles with integer spin, called excitons, are formed. Due to the underlying spin statistics, singlet excitons (S = 0) and triplet excitons (S = 1) are formed in a ratio of 1:3.[6] When an exciton reaches an emitter molecule, an energy transfer occurs, whereby the emitter molecule is converted into an electronically excited state. Depending on the emission mechanism (*vide infra*), up to 100% internal efficiency can be achieved. A large number of commercial dopants are available for this purpose. The possibility of applying the OLED layer structure (Fig. 1.1) to flexible plastic substrates and thus realising flexible displays is another advantage to LCDs. For example, vapour deposition or solution processing are available.[7,8] Unfortunately, OLEDs also have a range of weaknesses. Fluorescent OLEDs are prone to photo-bleaching and can only utilise 25% of the excitons formed. In addition to a rapid drop in efficiency, this also leads to increased energy requirements. Phosphorescent emitters, on the other hand, tend to accumulate highly reactive triplet species due to their long excited state lifetimes, which lead to the decomposition of matrix molecules and other emitter molecules, es-

pecially at high brightness.[9] Emitters that can utilise the triplet excitons via a singlet pathway would therefore be ideal. One of the most prominent processes, based on this principle, is known as thermally activated delayed fluorescence (TADF) and enables up to 100% internal efficiency whithout the disadvantages of phosphorescent emitters. As the pixels in an OLED display are self-illuminating, "true black" can be displayed. These displays are also significantly more energy-efficient than classic LC displays. In some OLEDs, an internal efficiency of up to 100% can be achieved, whereby the luminosity is only limited by the decoupling of the photons.[10–12] The thermal stability of an OLED architecture is limited by the low glass transition temperature of the individual layers, in particular the hole transport layer, so that they are not yet competitive with metal halide or LED light sources for lighting applications.[13–15] Due to their molecular properties, small organic molecules (SOM) and transition metal complexes (TMC) not only offer application potential in electrical devices, but also open up a wide range of possibilities in light-driven catalysis, medical diagnostics and therapy (*vide infra*). The key to these diverse applications lies in the photophysical properties of SOM and TMC, in particular in the control of the triplet state. Due to comparably long excited state lifetimes, the triplet manifold plays a crucial role in energy transfer and photochemical reactions (*vide infra*).

1.2 Photophysics of the Photoluminescent Triplet Manifold

After considering applications of electroluminescence in OLEDs, the photophysics of the triplet manifold, which are necessary for understanding the aforementioned photoluminescent applications, will now be explained. While in electroluminescent devices triplet states can be formed directly by electron-hole recombination, the triplet states are usually not directly accessible by photoexcitation, since S_0–T_n absorption is spin-forbidden and therefore provided with low oscillator strengths.[16]

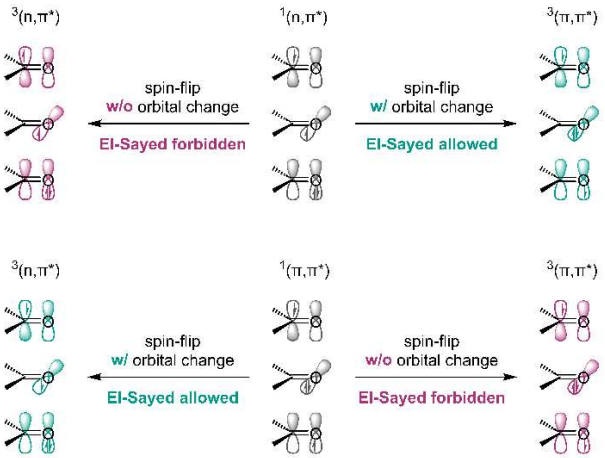

Scheme 1.2: El-Sayed's rule visualized with selected transitions of acetone.

This chapter deals with the mechanisms for the population of triplet states (e.g. intersystem crossing), as well as the phenomena of their radiative deactivation (i.e. phosphorescence and TADF). Intersystem crossing (ISC) is the isoenergetic and spin-forbidden, multiplicity changing transition of a singlet state into a vibrationally excited triplet state. From this state, both a second ISC into the singlet manifold or phosphorescence are possible.[17,18] The change of the total spin however is forbidden according to the selection rules, since the total momentum is not conserved[19]. As a result, the ISC is usually relativly slow.

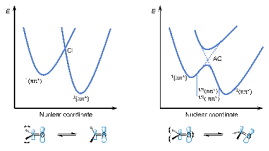

Figure 1.2: In-plane vibrational mode with neglegible spin-vibronic coupling resulting in a conical intersection (left) and out-of-plane mode with strong SVC leading to an avoided crossing (right). Adapted from reference [16].

However, the following options allow a sufficiently fast multiplicity transition. In 1963, El-Sayed reported that the ISC becomes particularly fast when the transition results not only in a spin flip, but also in a simultaneous orbital change, as a result of which the change in the spin angular momentum is compensated for by a change in the orbital angular momentum.[20] El-Sayed's rule can be illustrated using the electronic transitions of an acetone molecule (Scheme 1.2). The first excited singlet state (i.e. S_1) corresponds to a $^1(n,\pi^*)$ state. Due to the lack of orbital change, ISC into the $^3(n,\pi^*)$

triplet state is prohibited. Intersystem crossing into a state of $^3(\pi,\pi^*)$ nature is permitted due to the additional p_x–p_y orbital change and is therefore comparatively fast. However even El-Sayed-forbidden transitions can occour quickly if a molecular vibration with similar timerange is accesible. A breaking down of the Born-Oppenheimer-approximation leads to the coupling of molecular motion and electronic transitions. This spin-vibronic coupling (SVC) can greatly enhance ISC-rate with transitions on the ps timescale.[16] Again acetone, namely its $^1(\pi,\pi^*)$–$^3(\pi,\pi^*)$ transition can be used as an example. In-plane vibration does not change the orbital nature, so that this vibration mode cannot mediate spin-vibronic coupling. A conical intersection (CI) occurs (Fig. 1.2, left). However, as a result of an out-off-plane vibration, a partial sp^3 hybridisation on the carbonyl carbon atom can be temporarily formulated, whereby an allowed $^1(n,\pi^*)$–$^3(\pi,\pi^*)$ transition is "mixed in" with the otherwise forbidden transition, creating an avoided crossing (AC) and thus accelerating the ISC (Fig. 1.2, right). In addition to carbonyl compounds, SVC is also an important mechanism for populating triplet states for arenes and other organic molecules with a π-system. While the previous phenomena can be observed in any molecule, the magnetic coupling of the electron spin with its orbital angular momentum is reserved to heavy atoms, namely higher homologues and transition metals. This coupling known as spin-orbit-coupling (SOC) can be quantified using the spin-orbit-coupling Hamiltonian[18]:

$$\mathbf{H}_{\mathrm{SOC}} = \frac{1}{2m_e^2c^2}\sum_i\sum_j \frac{z_i^{\mathrm{eff}}}{r_{ij}^3}\mathbf{l}_j\mathbf{s}_j = \sum_j \zeta\mathbf{l}_j\mathbf{s}_j \tag{1.1}$$

Table 1.2: Selected elements and their spin-orbit-coupling constant.[Montalti2006a]

Element	ζ [cm^{-1}]	Element	ζ [cm^{-1}]	Element	ζ [cm^{-1}]
H	0.24	Br	2460	P	230
C	32	I	5069	As	1202
N	78	Ir	3909	Sb	2593
O	154	Pt	4481	S	365
Cu	857	Au	5104	Se	1695

According to Table 1.2, the presence of halogens, higher pnictogens or heavy metal atoms in the emitter molecule impacts the spin-orbit and thus the ISC process. The rate constant of ISC can be quantified by the equation:

$$k_{\mathrm{ISC}}^{\mathrm{i}\to\mathrm{f}} = \frac{2\pi}{\hbar}\langle\Psi_{\mathrm{i}}|\mathbf{H}_{\mathrm{SOC}}|\Psi_{\mathrm{f}}\rangle\sum_n\langle\theta_{\mathrm{i},0}|\theta_{\mathrm{f},n}\rangle^2 \tag{1.2}$$

Based on Eq. (1.2), three conditions for fast ISC can be derived: A high orbital overlap between the intial and final state, a high spin-orbit coupling, and a large density of states. The SOC can be mediated both by spatial proximity (external heavy-atom effect) and by the involvement of heavy-metal orbitals (internal heavy-atom effect). After a molecule has been excited to the triplet state through ISC, two possible paths of radiative deactivation open: On the one hand, reversed ISC (rISC) can occur back into a singlet manifold followed by fluorescence (*vide infra*). On the other hand, there is the possibility of phosphorescence, in which the molecule returns directly to the singlet ground state under light emission.

$$\tilde{S}_0 = S_0 + \sum_m \delta_m T_m \tag{1.3a}$$

$$\tilde{T}_1 = T_1 + \sum_n \delta_n S_n \tag{1.3b}$$

$$\delta_m = \frac{\langle T_m | \mathbf{H}_{SOC} | S_0 \rangle}{\Delta E_{T_m, S_0}} \tag{1.3c}$$

$$\delta_n = \frac{\langle S_n | \mathbf{H}_{SOC} | T_1 \rangle}{\Delta E_{S_n, T_1}} \tag{1.3d}$$

As this is also a spin-forbidden transition, phosphorescence is significantly slower than the spin-allowed fluorescence. Like ISC, phosphorescence is mediated by the coupling of the electron spin with the orbital angular momentum. Spin-orbit coupling allows higher excited states to be "mixed in" and lend oscillator strength to the otherwise forbidden transition. In terms of perturbation theory, this can be understood as a perturbation of the pure excited states (Eq. (1.3a), Eq. (1.3b)).

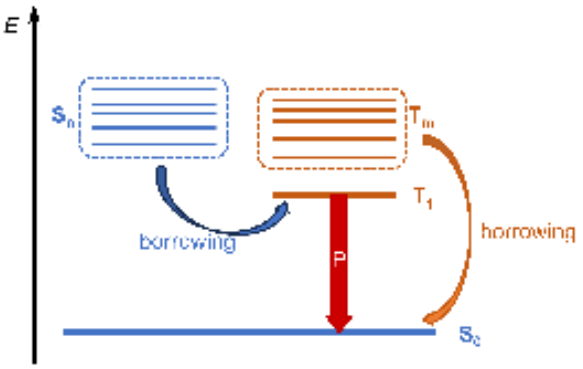

Scheme 1.3: Illustration of the admixture of higher excited states into the "pure" states involved in the emission pathway. Adapted from reference [21].

The degree of mixing in the pertubated states $\tilde{S}_0$ and $\tilde{T}_1$ can be quantified by the mixing coefficient δ_i and is proportional to the overlap integral and inversly proportional to the energy difference of the mixing states (Eq. (1.3c), Eq. (1.3d)).[21] In addition to sufficiently strong spin-orbit coupling, energetic proximity is also necessary for efficient state mixing. However, the energetic distance between higher triplet states and the electronic ground state is generally much greater than between high singlet states and the T_1. Due to the inverse proportionality to the energy difference, triplet admixture into the ground state is usually only of secondary importance (Scheme 1.3).

The radiative rate constant of phosphorescence can be quantified in terms of the energy gap between the emitting triplet state and the ground state (orange term of Eq. (1.4)), as well as triplet- (blue term) and singlet-admixture (green term). The direct dependance to the energy difference is also known as energy gap law (EGL).

$$k_{\mathrm{P}} = \frac{4e^2}{3c^2\hbar^4}(\Delta E_{\mathrm{T}_1,\mathrm{S}_0})^3 \left| \sum_{m=0}^{\infty} \delta_m \left\langle \mathrm{S}_0 \middle| \Sigma_j e\mathbf{r}_j \middle| \mathrm{S}_m \right\rangle + \sum_{n=1}^{\infty} \delta_n \left\langle \mathrm{T}_n \middle| \Sigma_j e\mathbf{r}_j \middle| \mathrm{T}_1 \right\rangle \right|^2 \tag{1.4}$$

The spin-orbit-coupling that would lead to efficient state mixing in organic luminophores is not large enough and non-radiative processes become competitive, so that they usually show fluorescence at room temperature and can only show phosphorescence in polymer matrices or at very low temperatures. In transition metal complexes, however, phosphorescence is often a dominant process, not least due to the large heavy atom effect (Table 1.2).[16] Because metal-d orbitals are directly involved in phosphorescent decay, for example in metal-to-ligand charge transfer states, and additionally mediate a strong SOC, many phosphorescent emitters, mostly based on It(III) and Pt(II) with microsecond lifetimes, are known (*vide infra*). The ISC into a vibrationally excited state of the electronic ground state represents a non-radiative deactivation path and will be addressed later. For now, only the ISC into the S_1, rISC and subsequent fluorescence will be considered. The main condition for rISC to occur is that a vibrationally excited T_1 state is thermally accessible, from which an isoenergetic transition to the S_1 state can occur. As this process follows the Boltzmann distribution, the rate of rISC is given as:

$$k_{\mathrm{rISC}} \propto \exp\left(-\frac{\Delta E_{\mathrm{ST}}}{k_{\mathrm{B}}T}\right) \tag{1.5}$$

The larger the ΔE_{ST}, the slower and at the same time less likely the rISC becomes. It is not yet possible to specify an exact limit up to which efficient rISC can take place. While singlet-triplet gaps of up to 100 meV (approx. $4\,k_{\mathrm{B}}T$) are regarded as the optimum for rISC[22], a threshold of approx. 186 meV ($7\,k_{\mathrm{B}}T$) is specified elsewhere.[16] Fluorescence that results from this ISC/rISC pathway is delayed relative to the prompt, direct fluorescent decay of S_1 states and thermally activated. This so-called TADF (thermally activated delayed fluorescence) mechanism utilises the generally high oscillator strengths of a S_1–S_0 transition and is known as "singlet harvesting" particularly in the context of OLEDs, for its ability to convert triplet excitons into emissive singlet states. The magnitude of the singlet-triplet-gap is given by the exchange integral J between the donor and acceptor orbital wavefunctions ϕ_i:.[23,24]

$$\Delta E_{\mathrm{ST}} = 2J = 2 \iint \phi_{\mathrm{H}}(r_1)\phi_{\mathrm{L}}(r_2)\frac{1}{|r_2 - r_1|}\phi_{\mathrm{H}}(r_2)\phi_{\mathrm{L}}(r_1)\,\mathrm{d}r_1\,\mathrm{d}r_2 \tag{1.6}$$

A sufficiently small singlet-triplet gap can thus be realised by spatially separating the donor (HOMO) and acceptor (LUMO) orbitals(Eq. (1.6)).[23,24] This orbital separation can be achieved in luminophores with pronounced charge transfer transitions, such as donor-acceptor- and multi-resonance-systems. Although excessive orbital separation results in almost degenerate singlet and triplet states, this also leads to reduced rate constants due to a very low density of states. Some residual coupling between donor and acceptor orbitals is therefore necessary and can be achieved for example by extended *pi*-systems or transition metal complexes.

1.3 Relevance of TM-based emitters

While organic donor-acceptor systems and multi-resonance luminophores offer promising approaches, transition metals allow precise control of orbital interactions due to their diverse electronic structures and ligand environments.

The presence of d-orbitals and the possibility of forming diverse ligand fields open up new ways to modulate excited states. In addition, transition metal complexes can significantly influence the mixing of singlet and triplet states due to their versatile SOC (*vide supra*), which can be used to selectively tune triplet lifetimes.[19,25] While only $\pi - \pi*$ transitions are available to an organic luminophore, transition metal complexes have a large number of possible transitions in a small energetic window (Scheme 1.4). In addition to ligand-centred (LC) states, states involving the metal-d orbitals also occur, including ligand-to-metal, metal-to-ligand charge transfer (LMCT and MLCT respectively), as well as metal-centred (MC) transitions. Due to the enormous spin-orbit coupling constants of iridium and platinum, their complexes have radiative lifetimes in the lower microsecond range, which makes them particularly suitable for OLED applications.

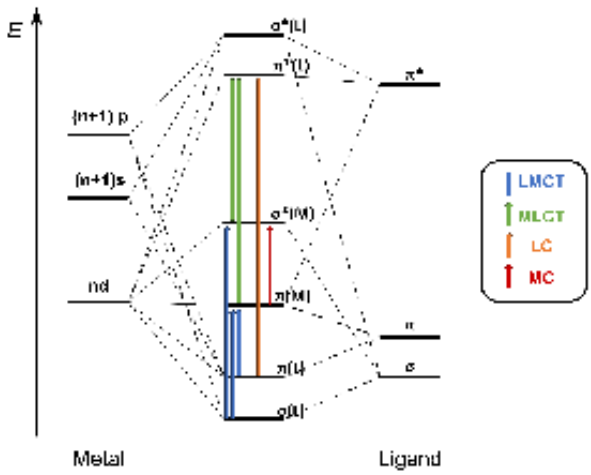

Scheme 1.4: Simplified MO-scheme of a (pseudo-)octahedral transition metal complex with selected electronic transitions.

In an effort to substitute these rare and expensive heavy metals, attention was turned to more earth-abundant, cheaper and lighter transition metals, e.g. copper and zinc. From that arises the challenge of having to compensate for considerably smaller SOC. While long-lived triplet states are undesirable in an OLED (*vide supra*), there are applications in photocatalysis and photodynamic therapy, which will be discussed below. Photoredox catalysis is essentially independent of ecited state lifetimes as long as they can compete with diffusion ($\tau > 1$ ns).[31] The characteristic feature is

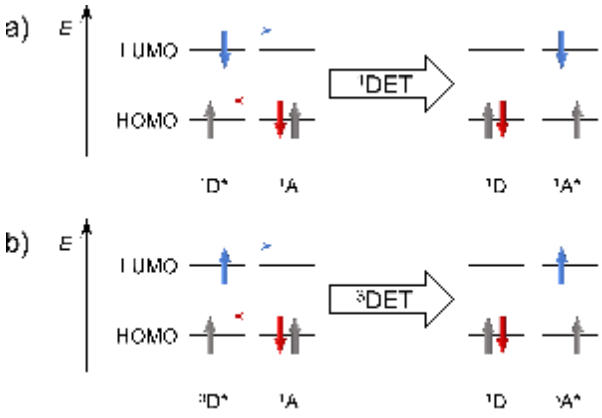

Scheme 1.5: Simplified frontier orbital representation of singlet DET (a) and triplet DET (b).

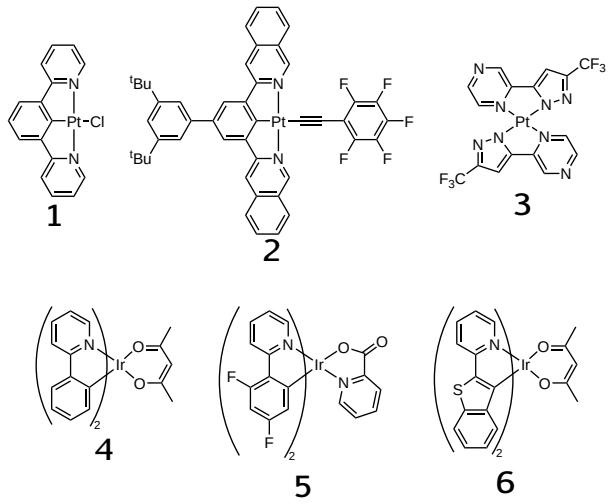

Compound	λ_{EL} [nm]	EQE [%]
1	491	4–10
2	520	22.8
3	740	24.0
4	525	12.3
5	475	5.7
6	616	7.0

Figure 1.3: Selection of electroluminescent Pt(II)- and Ir(III)-complexes and their emissive properties.[**Lamansky2001b**, 26–30]

only the redox potential of the excited state. However, a different picture emerges in energy transfer catalysis. For successful energy transfer catalysis, it is necessary that sufficiently long-lived triplet states are accessible.

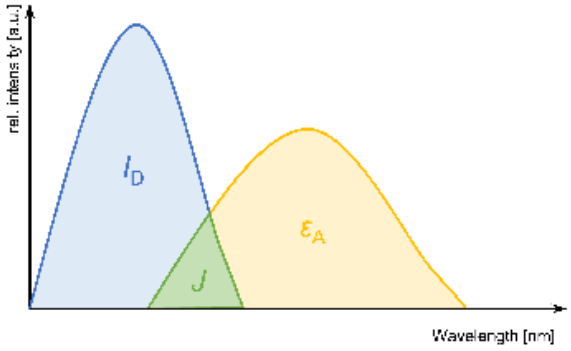

Figure 1.4: Schematic spectra of the triplet emission of a donor (blue), the S_0–T_1 absorption of an acceptor (yellow) and the spectral overlap (green) in DET.

Dexter energy transfer (DET) in particular will be considered below. This energy tranfer involves a bilateral exchange of electrons. Depending on the excited state multiplicity of the donor (i.e. the photocatlyst), singlet or triplet states can be "transferred", but only triplet energy transfer is catalytically active, as singlet energy transfer converts between different chemically inert singlet states.[32] Triplet transfer leads to the formation of reactive triplet states in the acceptor (i.e. the substrate) that would not be accessible by direct photoexcitation. Two parameters play a cru-

cial role here: energy gap and spectral overlap. The energy transfer is exothermic if the excited state of the acceptor is lower in energy than the excited state of the donor. At the same time, the energy transfer is effective if the spectral overlap between the emission of the photocatalyst and the triplet absorption of the substrate is large (Fig. 1.4). The choice of the appropriate photosensitiser is therefore always dependant on the substrate.[32,33] The fact that energy transfer photocatalysis is not only useful for simple low-molecular transformations, but can also provide access to complex bioactive molecules, is demonstrated by the following literature examples.

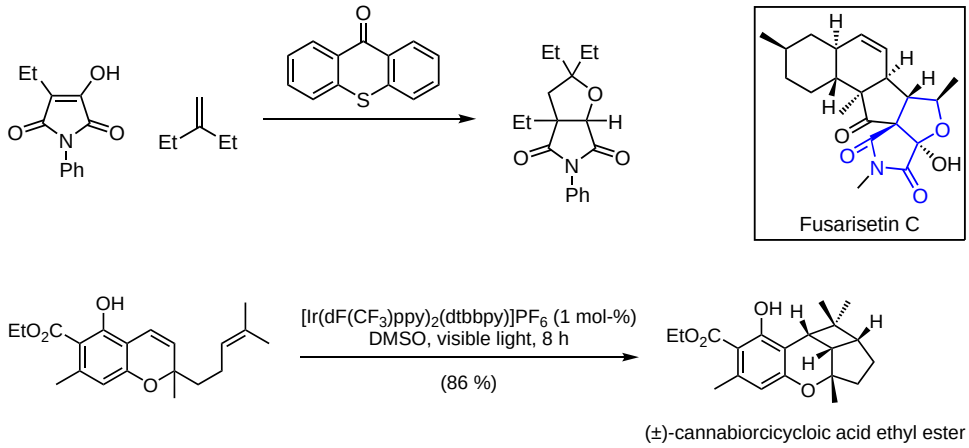

Scheme 1.6: Upper: Light-driven [3+2]-cycloaddition of a 3-hydroxy-maleimide with an alkene and comparison to fusaresitine C.[34] Lower: Iridium-photocatalyzed intramolecular [2+2]-cycloaddition yielding cannabiorcicycloic acid ethyl ester.[35]

Energy transfer catalysis using thioxanthone as a photosensitiser enables the construction of a bicyclic system that is very similar to parts of fusarisetin C. This polycyclic compound, found in the marine fungus *Fusarium equiseti D39*, is of particular interest in research into novel chemotherapeutics due to its cytotoxic properties.[34,36] Similarly, the cannabinoid cannabiorcicycloic acid is accessible by [Ir]-photosensitised energy transfer catalysis, which was originally isolated from *Rhododendron anthopogonoides* and is responsible for the antiphlogistic and antitussive effects of this phytopharmaceutical used in parts of Tibet.[35,37]

So far, only the energy transfer with an acceptor in a singlet state has been considered, but it is also possible for the sensitiser to transfer energy to a triplet state (Scheme 1.7).[38] In this case, the sensitiser switches to the ground state and the acceptor is excited to a higher singlet state. In photocatalysis, this is generally an undesirable pathway, as reactive triplet substrates are quenched unpro-

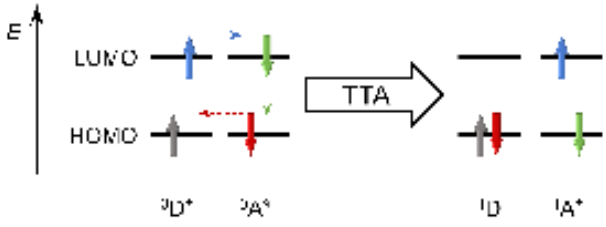

Scheme 1.7: Simplified frontier orbital representation of triplet-triplet-annihilation (TTA).

ductively. However, there are applications in which this process, known as triplet-triplet annihilation (TTA), is the key mechnism utilized. Probably the most relevant application of TTA can be found in medicine in the form of photodynamic therapy (PDT).[39] By using suitable physiologically compatible, locally or systemically administered sensitising agents, molecular dioxygen with a triplet ground state can be converted into highly reactive singlet oxygen. This reactive oxygen species (ROS) enables the otherwise spin-forbidden reaction of oxygen and reacts readily with a variety of biomolecules, such as amino acid side chains, enzymes, unsaturated lipids of the cell membrane or nucleobases in DNA and RNA. The damage, which is usually irreversible, can prevent important metabolic processes or induce cell death.[39,40] PDT is currently indicated for the treatment of carcinomas of the urinary bladder, oral cavity and pharynx, as well as some pathological neovascularisation of the eye. It is also effective in the treatment of some non-cancerous skin diseases. Currently, approved drugs are generally based on chlorin or porphyrine bodies (Fig. 1.5).

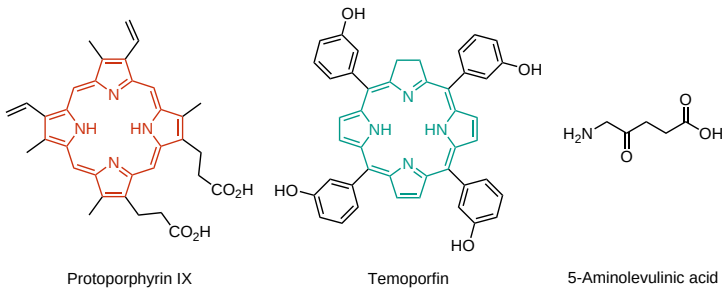

Figure 1.5: PDT-active photopharmaceuticals (porphyrine core in red, chlorine scaffold in green).

Metabolic precursors of the body's own protoporphyrin IX, like 5-aminolevulinic acid, are also suitable, as transport mechanisms are lacking in tumour tissue, resulting in an accumulation of the drug in affected regions. In addition, azadipyrromethenes (ADPMs), methylene blue and 4d/5d metal complexes are also currently undergoing in vitro studies(Fig. 1.6).[41–44] The control over the lifetimes of excited states is closely linked to the coordination geometry and the variety of ligands in transition metal complexes. While d^6-Ir(III) complexes almost exclusively have an octahedral geometry and work with bi- or tridentate ligands such as bpy or ppy, d^8-Pt(II) complexes favour a square-planar structure with similar chromophore ligands. This structural rigidity limits the modulation of photophysical properties, especially of emission wavelengths and quantum yields. Due to their great structural and electronic diversity, d^{10}-coinage metal complexes present a promising alternative. In the following, we will investigate in which systems and through which structural modifications lifetimes, emission wavelengths and other quantum properties can be specifically influenced.

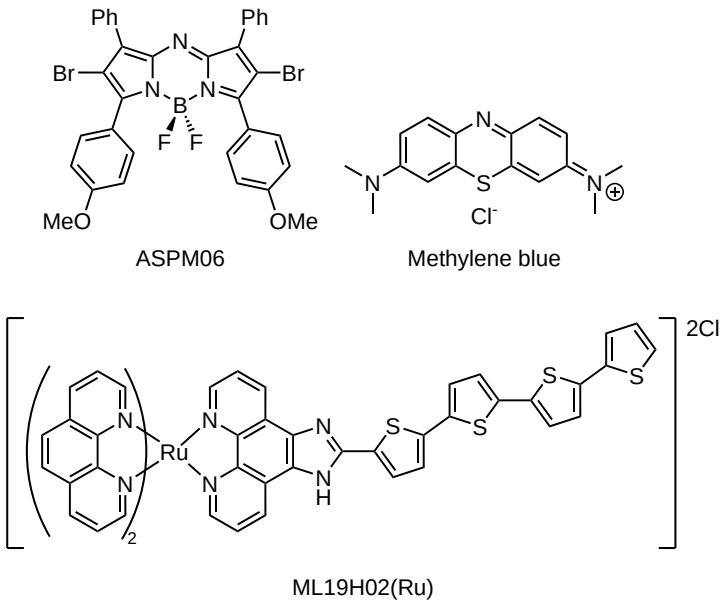

Figure 1.6: Photopharmaceuticals currently under investigation.[41–44]

1.4 Copper(I)-complexes as a highly modifiable emitter class

In the previously illuminated metal complexes with incomplete d-subshells, transitions to unoccupied d-orbitals can occur (i.e. LMCT and MC). While such d–d transitions can provide interesting photophysical properties (*vide infra*), they also limit the efficiency of the luminophores.

These transitions in centrosymmetric complexes are parity-forbidden acoording to the Laporte-rule. They become weakly allowed due to molecular distortion and compete with non-radiative processes. In addition, MC states are usually dissociative due to electrons being promoted into anti-bonding d-orbitals (Scheme 1.8), which necessitates strong and chelating ligands. In complexes with d^{10} configuration, these transitions are not accessible, so that only transitions within or between two ligands (LC and LLCT), as well as from the metal to a ligand (MLCT) can occur. The MLCT formally corresponds to a one-electron oxidation of the metal atom, so that the redox potential of the central ion provides information about the relative energy. The standard redox potential of the pairs (M^+ /M^{2+}) are

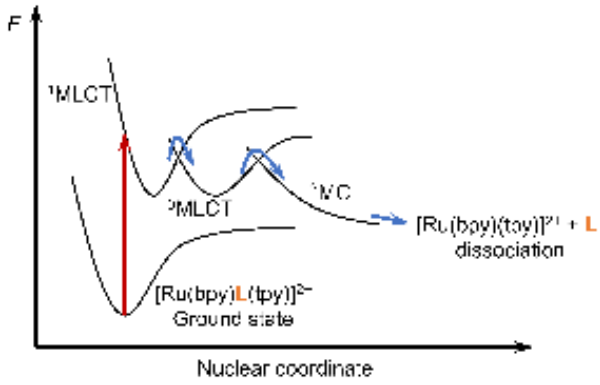

Scheme 1.8: Illustration of the dissociative character of the ^{3}MC state of photoexcited $[Ru(tpy)L(bpy)]^{2+}$. Adapted from reference [45].

sorted: Ag (1.98 V) > Au (1.8 V) >> Cu (0.153 V). The MLCT states of silver and gold are very high in energy, while copper has low-energy MLCT states due to its low redox potential. Transitions in silver and gold complexes are therefore generally of LC/LLCT in nature. The sequence of Ag > Au > Cu is also found for the radiative rate constants of homologous carbene-M-amide systems and is related to the distance between the carbene acceptor and the amide donor moities.[46] Silver(I) has both the highest redox potential and the longest bonds, since gold is smaller than average due to lanthanide contraction and relativistic effects. The increased distance reduces the exchange integral (see Eq. (1.6)) and thus also the singlet-triplet gap, which increases the speed of rISC and can lead to fast TADF.[47] Despite the high radiative rate constants, silver(I) compounds suffer from enormous photosensitivity and quickly precipitate elemental silver, so that only gold and copper will be considered to in the following. Due to the low proportion of MLCT states in the emission of gold complexes, gold mediates spin-orbit coupling only through spatial proximity, so in these complexes it serves exclusively to fix chromophore ligands in spatial proximity and to accelerate the ISC.

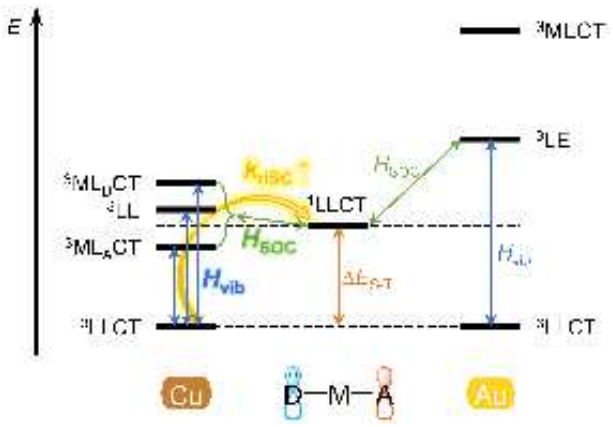

Scheme 1.9: Qualitative comparison of the operative spin-orbit coupling in D-M-A complexes of copper and gold, and its influence on the efficiency of the TADF process.

However, as the d-orbitals are also involved in the transition in copper complexes (MLCT), this results in a much higher operational SOC than the spin-orbit coupling constant would suggest, so that very efficient phosphorescence and TADF are also possible here. At the same time, the large number of low-energy MLCT states enables a modularity that neither silver nor gold complexes possess (Scheme 1.9). Copper is suitable not only because of its photophysical advantages, but also because it is around 15,000 times more common on earth than gold, while at the same time several orders of magnitude less water is used and CO_2 is released during the production of pure copper.[48,49] Copper(I) complexes are therefore superior to gold complexes not only from a photophysical point of view, but also from a sustainability perspective, despite their lower chemical stability. Copper(I) ions have a diverse coordination chemistry, the coordination numbers two, three and four are known and the nature of the ligands is almost unlimited. This high modularity in coordination number and ligand sphere enables a high modifiability of the luminescence properties (Fig. 1.7). The examples in Fig. 1.7 are selected from current literature to represent the variety of phosphorescent copper(I) complexes.[50–52] Compound **9** in particular is representative of a special subgroup of luminescent copper(I)

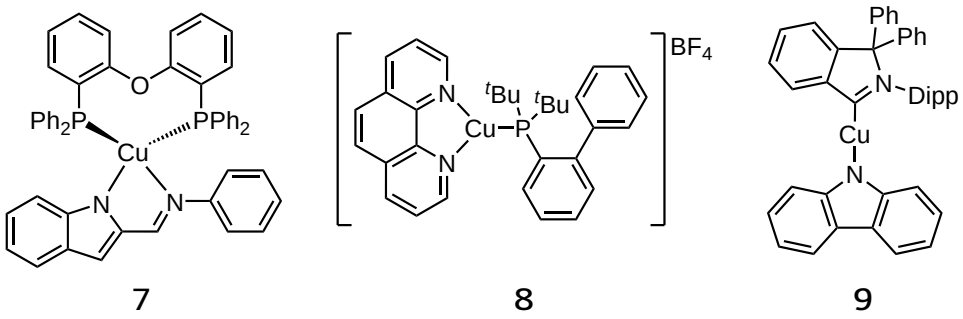

Figure 1.7: Selected Cu(I) coordination compounds with variable coordination number.[50–52]

complexes. Linearly coordinated Cu(I) has only 14 valence electrons and is therefore strongly coordinatively unsaturated. In general, these complexes are comparatively unstable and tend to associate other ligands quickly, as the bending vibration along L-Cu-L is freely accessible.[53] For the complexes of *N*-heterocyclic carbenes (NHC), however, the linear geometry is not only stable, but is the main geometry found in most Cu(I) carbene complexes.

Due to the pronounced σ-donor strength of the carbene ligands, the electron density at the copper centre in carbene complexes is significantly higher than in comparable phosphine complexes. The increased electron density leads to increased repulsion within the d-orbitals, whereby the $3d_{z^2}$-orbital in particular is energetically raised. This destabilisation contributes significantly to the preference for a linear geometry, as in this arrangement an interaction between the metals 4s and $3d_{z^2}$ orbitals with the carbene ligands can be described. The resulting combination of these interactions leads to the formation of a new molecular orbital that is lower in energy than the original $3d_{z^2}$ atomic orbital, which stabilises the linear geometry against bending distortions (Scheme 1.10). The linear geometry paired with the low redox potential allows efficient MLCT. At the same time, formal oxidation in MLCT states usually leads to a distortion of the molecular geometry in the excited state, which opens up non-radiative paths to the ground state.[54–58] Therefore, phosphorescent copper(I) complexes are usually not competitive with conventional Ir(III) or Pt(II) emitters for use in devices. The stable, but at the same time structurally flexible nature of linear carbene complexes with comparatively long-lived triplet states can be utilised in

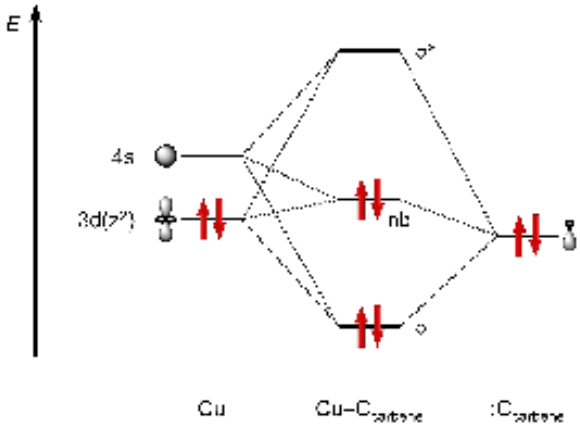

Scheme 1.10: Simplified MO scheme of a linear copper(I) carbene complex.

(photo-)catalysis. By changing the geometry, coordination sites can be created for substrate molecules, which can then react further either by energy transfer or in the sense of "classical" metal-organic catalysis. The lifetime of the triplet states can be estimated on the basis of the relative ligand composition. Homoleptic complexes generally have longer lifetimes than heteroleptic complexes. In homoleptic systems, the MLCT state can be equally delocalised to both chromophore ligands, which reduces the density of local states due to the chemical identity of the ligands. Heteroleptic complexes, on the other hand, have a higher density of oscillator strength-lending LC states, which can lead to an increased transition probability and thus to accelerated phosphorescence. In most NHC complexes, the carbene ligand forms the acceptor chromophore of the MLCT state, where the empty p-orbital at the carbene carbon atom is of central importance, so that the energetic position of the T_1 state can be estimated in a first approximation by the LUMO of the carbene. The classic Arduengo carbene with an imidazole backbone has two nitrogen atoms in the immediate vicinity of the carbene carbon atom.

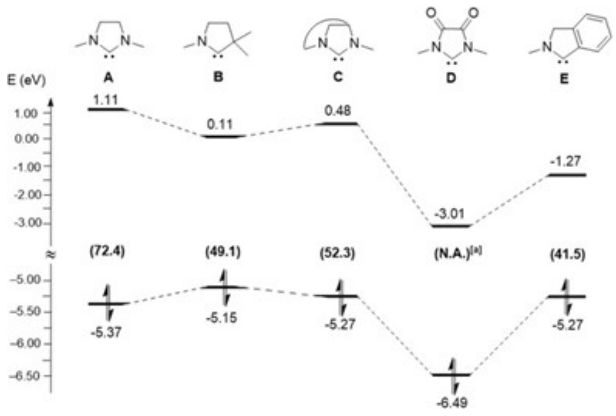

Scheme 1.11: "Energy (eV) of the HOMO and LUMO of carbenes A–E, and singlet–triple gap in parentheses (kcal mol⁻1) of carbenes A–C and E calculated at the B3LYP/TZVP level of theory. [a] The triplet state of D is a biradical involving the carbonyl groups, and thus the singlet–triplet gap cannot be compared with those of the other carbenes." Printed with permission from reference [59]. Copyright 2015 Wiley-VCH Verlag.

On the one hand, their high electronegativity ensures reduced electron density at the carbene carbon atom and thus reduced donor strength. On the other hand, they donate electron density to the unoccupied p-orbital at the carbene carbon atom (the carbene LUMO) *via* their free electron pairs. As a result of this partial filling, the LUMO is destabilised and the acceptor strength is reduced. Substituents with a strong –M effect (e.g. nitro, nitrile or carbonyl functionalities) can weaken this electronic interaction by reducing the electron density of the nitrogen atoms. Alternatively, the acceptor strength can also be influenced by the targeted modification of the ligand structure, for example by using carbenes that only have one nitrogen donor on the carbene carbon atom. In both cases, the reduced electronic interaction leads to an energetic lowering of the LUMO.[59] Another way to modify the electronic properties is to extend the conjugated π-system of the carbene ligand. In analogy to the frontier orbitals of polyenes, this results in an additional energetic stabilisation of the LUMO and an increased density of

$\pi\pi^*$ LC states, which can lend oscillator strength to the phosphorescence. However, an excessively extended π-system can lead to long-lived LC states lying energetically below the ^{3}MLCT state. As the LUMO energy decreases, the energy of the MLCT also

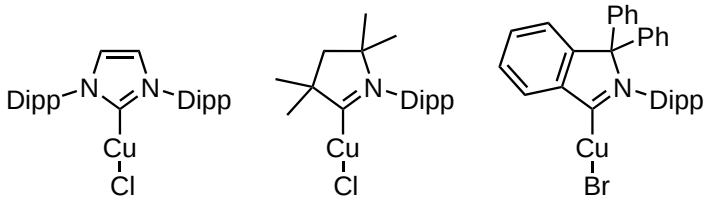

10 **11** **12**

Figure 1.8: Selection of luminescent [Cu(carbene)(halide)] compounds with emissive ^{3}MLCT states.[52,60,61]

decreases and the emission shifts bathochromically, i.e. to longer wavelengths. This can be seen as an example in a series of copper halide complexes of different carbenes. There is a clear red shift of the emission maximum (λ_{max}) from 347 nm for complex **10** with the weakest acceptor, to 511 nm (**11**), up to 662 nm for the complex with the strongest acceptor (**13**). The stabilisation of the carbene LUMO opens up a promising possibility to systematically shift the emission wavelength bathochromically and thus make the near infrared accessible.

1.5 Relevance of Low-Energy Luminescence in the (N)IR

Near-infrared (NIR) emitters with emission maxima beyond 750 nm are employed across a broad spectrum of applications, particularly in optical communication technologies. In this context, silicon dioxide-based optical fibres are of central importance due to their high transparency in the NIR range. This results in significantly reduced signal attenuation, enabling long-distance communication without the need for intermediate optical amplification. Beyond telecommunications, NIR emitters are integral to various sensing and imaging technologies, including optical iris and fingerprint recognition, night vision systems, and counterfeit detection. In biomedical contexts, physiologically compatible luminophores emitting in the so-called biological windows, NIR-I (650–950 nm), NIR-II (1050–1350 nm), and NIR-III (1550–1870 nm), are of particular interest. Within these ranges, absorption by water and haemoglobin is minimized, allowing for deeper tissue penetration. This feature is crucial in optical imaging techniques such as optical coherence tomography (OCT) and near-infrared spectroscopy (NIRS).[62] A large class of NIR emitters in this domain are small organic molecules (SOMs) with extended π-conjugated systems. These molecules offer remarkable structural modularity, allowing precise tuning of their emission properties. For instance, polymethine dyes exhibit bathochromic shifts in emission wavelength as the conjugated chain is extended, which enables coverage of broad areas within the NIR-I and NIR-II windows.[63–66] Numerous examples, such as **1PhSQ** (λ_{max} = 740 nm)[64],

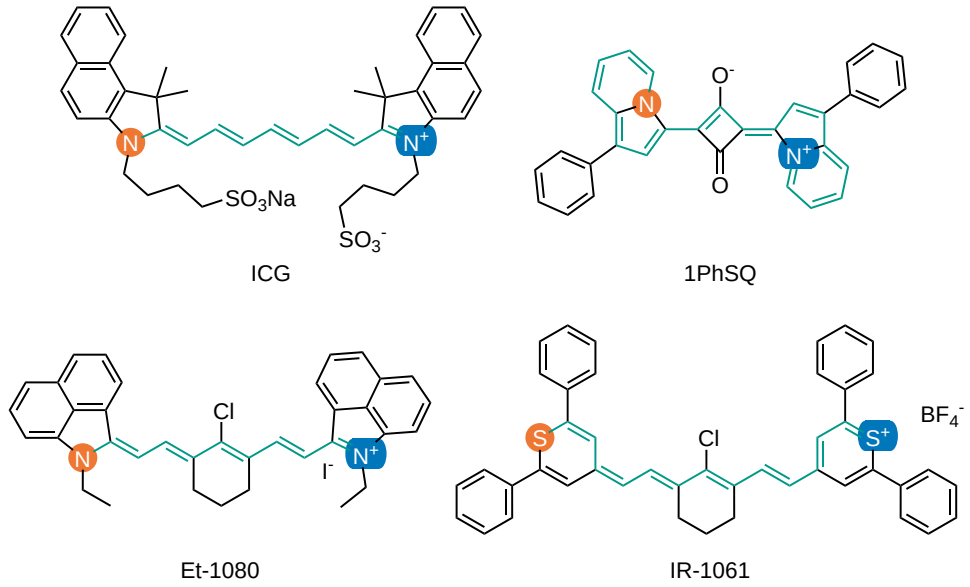

Figure 1.9: NIR-active SOM with emission maxima in the biological windows NIR-I/II.

Et-1080 (λ_{max} = 1080 nm)[65] and **IR-1061** (λ_{max} = 1061 nm)[66], are currently confined to preclinical or academic use. However, indocyanine green (**ICG**), with an emission maximum of around 835 nm is clinically approved and widely used in fluores-

cence angiography (ICGA, Fig. 1.10) and intraoperative imaging.[63,67,68]

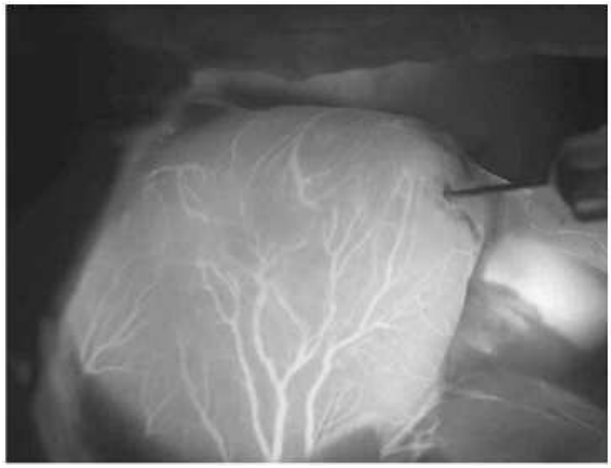

Figure 1.10: An ICGA image of a rat's heart with coronary arteries clearly visible. Liver shining on the right. Reproduced from Ref. [63] used under CC BY 3.0 (https://creativecommons.org/licenses/by/3.0/).

The deep tissue penetration of NIR photons allows even deeply situated blood vessels to be visualised with high spatial resolution. However, the Stokes shift of organic luminophores is typically small due to limited structural reorganisation in the excited state. The resulting spectral overlap between absorption and emission leads to self-absorption, reducing signal contrast in imaging applications. Furthermore, organic luminophores often exhibit limited efficiency in electroluminescent devices due to non-radiative decay and photoinstability under electrical excitation (*vide supra*). A compelling bridge between biological and electronic applications is formed by lanthanide complexes. These systems are widely studied for bioimaging due to their sharp-line emissions stemming from f–f transitions, which extend into the NIR-III region (Fig. 1.11, (c)).

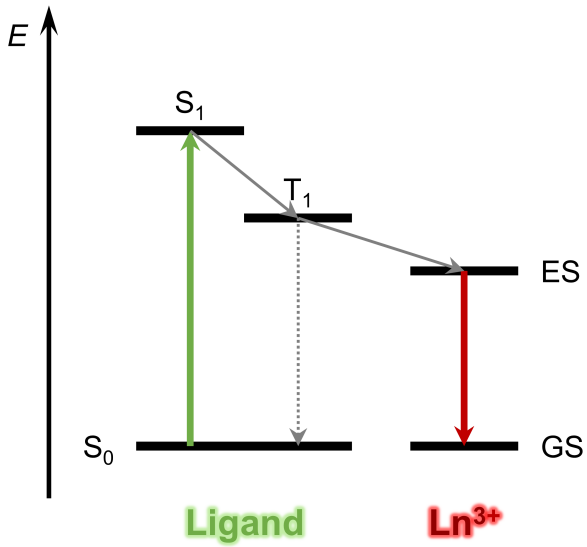

Scheme 1.12: Antenna-effect for harvesting metal-centred excited states through LMCT using highly absorbing ligands of appropriate excited state energy.

However, these same f–f transitions are formally Laporte-forbidden, resulting in inherently low extinction coefficients and long excited-state lifetimes. This makes direct excitation inefficient and limits their performance in electroluminescent contexts. The absorption bands of the lanthanide ions, which occur due to direct f–f absorption, are generally rather sharp and have a characteristic fine structure (Fig. 1.11, (a)-(b)). To overcome this, antenna ligands are used to harvest energy via highly absorbing singlet or triplet excited states and subsequently transfer it to the lanthanide ion through a ligand-to-metal charge transfer (LMCT) process (Scheme 1.12). This so-called antenna effect improves excitation efficiency but does not

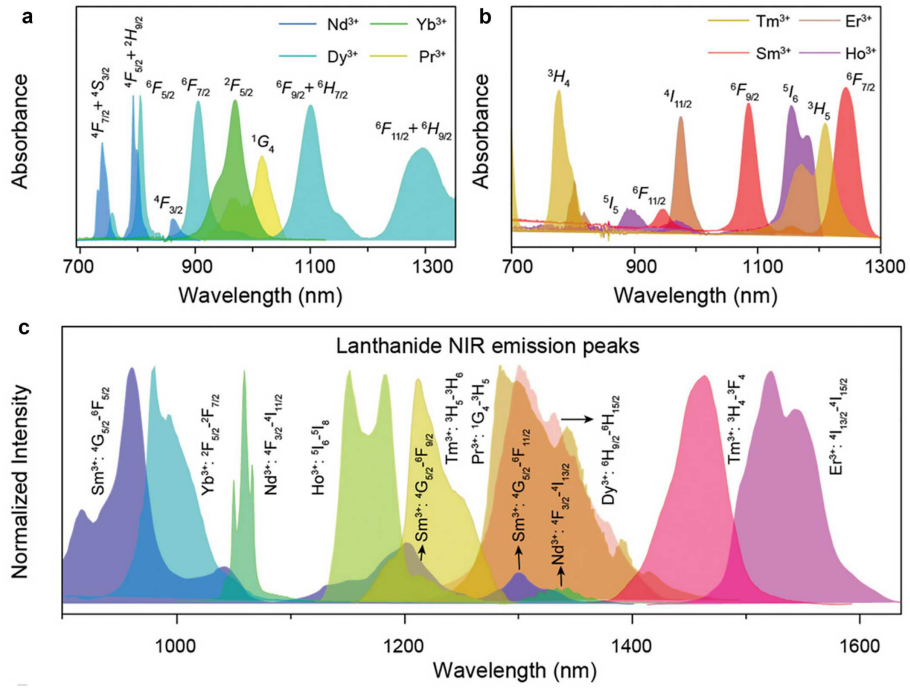

Figure 1.11: Absorptionspectra of lanthanide ions in aqueous solutions (a)-(b). NIR-II luminescence spectra of these lanthanide ions (c). Reprinted from Ref. [69] under CC BY 3.0 (https://creativecommons.org/licenses/by/3.0/). Cropped by the original authors from Ref. [**Zhao2023a**]. Copyright *2022 Wiley-VCH GmbH*.

fully resolve the issue of inefficient emission under electrical current. The long excited-state lifetimes associated with f–f transitions lead to quenching *via* non-radiative decay and significant energy roll-off in OLED architectures. This limitation sets the stage for transition metal complexes, particularly those based on iridium(III) and platinum(II). As discussed before, strong spin–orbit coupling induced by the heavy metal center facilitates rapid intersystem crossing (ISC), populating the triplet excited state.

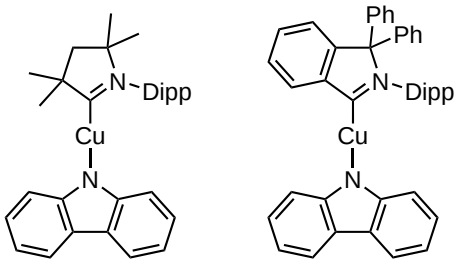

14 **15**

510 nm
^{1}LLCT (TADF)

621 nm
^{1}(LM)LCT (TADF)

Figure 1.12: Linear copper(I) complexes with donor-acceptor motif, featuring TADF.[47,52]

However, as the emission shifts to longer wavelengths, the decreasing energy gap leads to increased non-radiative decay, requiring rigid and sterically protected ligand scaffolds to maintain emission efficiency. An alternative strategy is to accelerate radiative decay processes to remain competitive with non-radiative pathways. One such approach involves thermally activated delayed fluorescence (TADF; *vide supra*), where fast reverse intersystem crossing (rISC) is enabled by a small singlet–triplet energy gap. Linear copper complexes have proven

particularly promising in this regard. Complexes featuring donor–acceptor motifs often exhibit efficient TADF due to spatial separation of the frontier orbitals, which leads to a small exchange integral. The presence of the copper atom facilitates both electronic coupling and enhanced spin–orbit interaction via admixture of MLCT-like states. The combination of the advantageous photophysical properties of linear copper complexes with the structural tunability of π-acceptor carbene ligands and strong π-donor ligands, such as carbazolates, has yielded a diverse set of emitters with tunable emission wavelengths and lifetimes (Fig. 1.12). Complex **15** even rivals commercial Ir(III) complexes in performance and shows potential for use in energy-transfer catalysis, making it a highly promising candidate for the development of next-generation "designer luminophores".

1.6 Stimulus Responsive Behavior

Even if the linear geometry of copper(I) carbene complexes is of particular importance due to its stability, these systems offer sufficient flexibility, which is not only interesting for catalytic properties (*vide supra*), but also enables stimulus responsivity and thus opens up access to "smart materials". The change in luminescence properties induced through mechanical stress is usually only referred to as mechanochromism in literature. However, since chromic phenomena describe the change in absorption properties, the term *mechanoluminochromism* will be used in this work to emphasize the distinction more clearly.[70] The most common mechanical stimuli include grinding and breakage (triboluminochromism), anisotropic compression (piezoluminochromism), isotropic compression or hydrostatic pressure (baroluminochromism) and shear forces (rheoluminochromism).[**Bamfield2018**] However, a clear distinction between the stimuli is not always possible and they can merge into one another, e.g. anisotropic compression can also lead to breakage. In crystalline and amorphous solids, stimulus responsiveness usually manifests itself in a partially reversible manner. This means that a different stimulus is required to regenerate the original luminescence, for example heat (thermoluminochromism) or solvent vapours (vapoluminochromism).[70] Areas of application for stimulus-responsive materials are diverse and range from molecular sensing to security inks and anti-counterfeit features.[71–73] The conceivable applications of mechanoresponsive materials are particularly concentrated in the area of pressure or stress detection, e.g. in components that are exposed to high loads during use, such as in the automotive and aviation industries.[74,75]

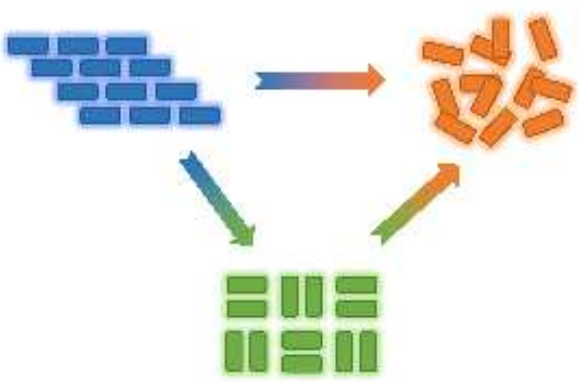

Scheme 1.13: Schematic representation of stimulus-induced intermolecular rearrangements leading to mechanoluminochromism.

Although the applications are diverse and there is great interest in such materials, there is as yet no generally valid structure-property relationship that can be used to predict mechanoluminochromism. However, various mechanisms are known that lead to responsivity, some of which will be discussed below. Mechanoresponsivity can occur when the crystal packing changes between two crystalline polymorphs or when a crystalline phase transitions into an amorphous phase (Scheme 1.13). This type of mechanoluminochromism often occurs in organic emitters with an extended π-system. In modified pyrenes[76]or perylenediimides[77] changes in the interaction between neighbouring π-systems occur due to mechanic stimulus (Fig. 1.13). The

formation or dissolution of π-stacking influences the electron density of the luminophores in such a way that changes in the emission occur. These are therefore mechanically induced (de)aggregation effects. In addition to changes in crystal packing,

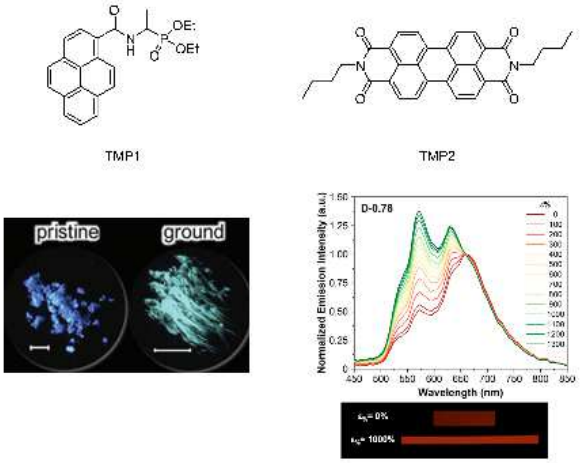

Figure 1.13: Mechanoluminochromism of two organic emitters, as a result of pertubated π-interactions. Adapted with permission from references [76, 77] Copyright 2020 The Royal Society of Chemistry. Licenced under CC BY 4.0 (https://creativecommons.org/licenses/by/4.0/)

inter- and intramolecular non-covalent interactions can also develop or break down (**??**) These include hydrogen bonds, metallophilic interactions and other weak interactions. In some transition metal complexes, this mechanism leads to mechanoresponsiveness. For example, in the cyclometallated Ir(III)-carbene complex **18**, the rotation around a σ-bond with a relatively high energy barrier in the carbene ligand leads to the development of intra-ligand $\pi\pi$-interactions, which shifts the emission maximum from 546 nm to 571 nm (Fig. 1.14).[78] In the case of **19**, π-stacking occurs between the fluorinated aromatic compounds of the cyclometallated ligands and intermolecular hydrogen bonds are formed, mediated by the carboxylic acid function in the salicylaldimine ligand. In both cases, the change in emission energy is below 1,000 cm^{-1}, as the changes in the electronic situation are restricted to the ligand sphere due to the limited structural flexibility. In contrast, it is assumed that the mechanoluminochromism of **20** results from a change in the emission mechanism. In the crystalline phase, emission takes place from a mixed ^{3}(LC/MLCT) state. Intermolecular C–H···Cl, C–H···Pt and π-interactions between the N–C–N ligands are broken up by grinding. The LC is destabilised in such a way that the emission changes to a pure ^{3}MLCT state, so that a shift of over 3,500 cm^{-1} can occur.

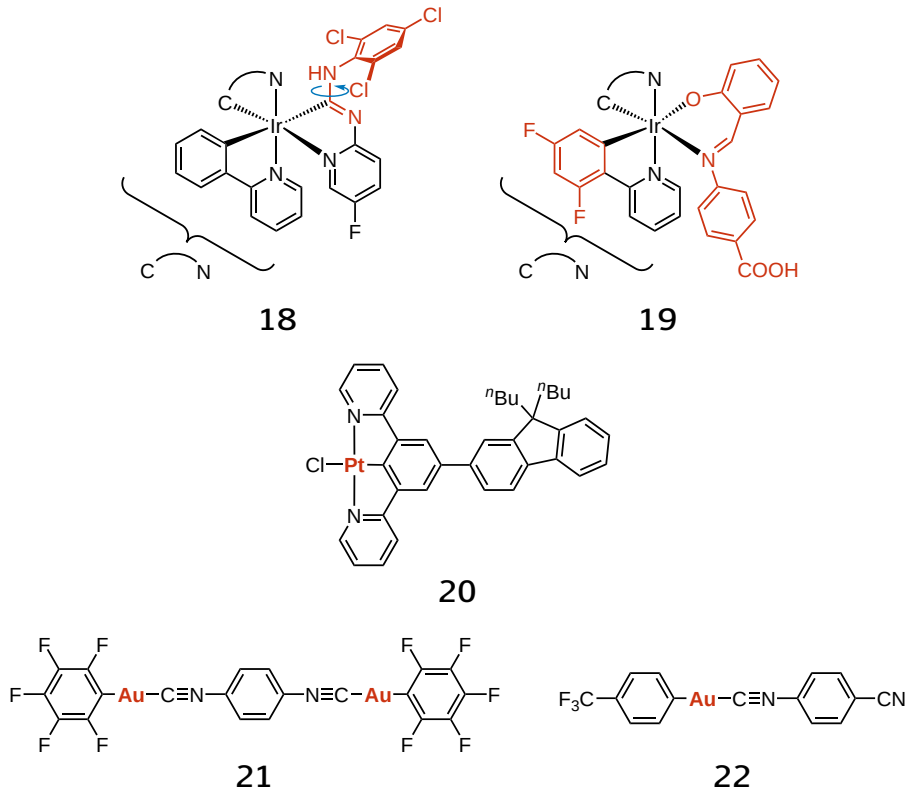

Figure 1.14: Structure of selected mechanoluminochromic transition metal complexes. Structural elements that lead to stimulus responsivity are labelled in red.[78–82]

Table 1.4: Photophysical Properties of pristine and ground complexes in Fig. 1.14.[78–82]

	Pristine		Ground		
Compound	λ_{max} [nm]	Φ_{em} [%]	λ_{max} [nm]	Φ_{em} [%]	ΔE [cm^{-1}]
18	546	30	571	9	802
19	566	–	596	–	889
20	538	12	671	8	3,684
21	415	9	533	19	5,335
22	522	8	582	23	1,975

While metal-metal interactions are hardly pronounced in the examples **18**, **19** and **20**, the responsiveness of the linear gold(I) isonitrile complexes **21** results from these weak metallophilic interactions. Due to the pronounced relativistic expansion of the fully occupied d-orbitals, aurophilic interactions reach the strength of typical hydrogen bonds and act in a range of around 3 Å. In both complexes, a crystalline-to-crystalline transition occurs. Increased proximity of neighbouring luminophores enable Au···Au interactions to develop. The distance between neighbouring gold atoms decreases from

around 3.7 to 3.1 Å. Increased involvement of the d-orbitals results in pronounced mechanoluminochromism with changes of up to 5,300 cm^{-1}. Furthermore, mechanical stimuli can induce spatial proximity in the molecular network, which favours eximers or exiplexes or leads to a (partially) irreversible chemical reaction (*vide infra*).

1.7 Molecular Description of Circularly Polarized Luminescence

The possibilities of "switching" luminescence by mechanical stimulus is paramount for a plathora of potential applications. It is of particular interest to link responsivity with other quantum properties of light. Circular polarisation is one such properties and will be discussed in the following. Polarisation is the spatial orientation of an electromagnetic wave. In classical electrodynamics, the polarisation of an ensemble of photons can be described with the direction of propagation parallel to the wave vector **k**. The electric field vector **E** is always perpendicular to this wave vector.[83] By convention, the cartesian coordinate system is chosen such that **k** is parallel to the z-axis. The choice of coordinate system implies that the electric field vector is always parallel to the x-y plane. The electric field $\mathbf{E}(z,t)$ can thus be decomposed into x and y components:

$$\mathbf{E}(z,t) = \begin{pmatrix} E_x \cos(kz - \omega t) \\ E_y \cos(kz - \omega t + \Delta\phi) \end{pmatrix} \tag{1.7}$$

Here, E_i represents the amplitude in the x or y direction, ω the angular frequency and $\Delta\phi$ the phase shift between the x- and y-components. The polarisation results from the phase shift. For an integer multiple of π, the maxima of both components always coincide and the resulting **E**-field oscillates in one plane, linear polarisation occurs. For phases that are shifted against each other by $\pi/2$, the extrema of one component falls on the zero crossings of the other. Superposition here creates an electric field that follows a circular path, which is why this polarisation is referred to as circular polarisation. All other values of $\Delta\phi$ result in elliptical polarisation.[**Wolschin2022a**, 83]

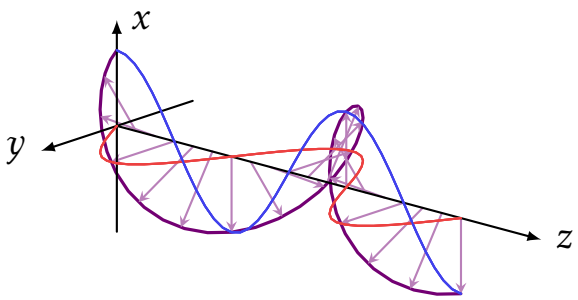

Scheme 1.14: Total electric field vector **E** (purple) taking a circular path around the z-axis, as a result of superpostion of $\mathbf{E_x}$ (blue) and $\mathbf{E_y}$ (red) with a phase shift of $\pi/2$.

While this classical description only covers ensembles, the circular polarisation of a single photon can be derived quantum mechanically. All bosons have integer spin, with the photon's spin being +1. This results in three values that the spin angular momentum (SAM) can assume, namely $J_S \in 0, \pm\hbar$, whereby $J_S = 0$ is forbidden for

massless particles and would correspond to a longitudinal polarisation, with the **E**-field oscillating along the direction of propagation.[84] The remaining two values of the angular momentum correspond to a left-hand and a right-hand circular polarisation. If the emission process does not discriminate between these two directions of rotation, superposition always results in unpolarised luminescence.[83] A necessary but not sufficient condition for this discrimination is the chirality of the luminophore, but there is no general structure-property relationship beyond this. Organic CPL-active emitters usually have a helical structure or a non-planar π-system. Due to this structure, these emitters "force" the electrons to take a helical path during the electronic transition. Examples of such molecules are given in Fig. 1.15.

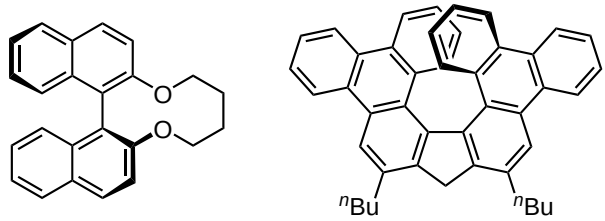

23 **24**

Figure 1.15: CPL-active small organic molecules featuring helical π-systems.[Sawada2012a, 85]

For phenomena such as NIR-emission or stimulus responsivity an electronical description is sufficient. However, CPL is also dependent on magnetic transitions. That means for quantification of this process, both the electronic transition dipole moment $\boldsymbol{\mu}$ and the magnetic dipole moment **m** must be taken into account. The emission dissymmetry g_{lum} is a frequently used parameter for describing the excess of one helicity over the other and assumes values between –2 (100% right-handed rotation) and +2 (100% left-handed rotation):[86]

$$g_{\mathrm{lum}} = 2\frac{I_{\mathrm{L}} - I_{\mathrm{R}}}{I_{\mathrm{L}} + I_{\mathrm{R}}} = 4\frac{|\boldsymbol{\mu}|\,|\mathbf{m}|}{|\boldsymbol{\mu}|^{\,2} + |\mathbf{m}|^{\,2}}\cos\theta \tag{1.8}$$

The magnetic transition in organic molecules is usually very weak and thus g_{lum} arbitrarily small. **23** shows an emission of 368 nm with a dissymmetry of only $1.4 \cdot 10^{-3}$ in chloroform solution and **24** with a maximum of 428 nm and a g_{lum} of 0.032 (Fig. 1.15).[Sawada2012a, 85] In particular, transition metal complexes of Cr(III)[Jimenez2019a, Dee2019a] and the rare earths[Schnable2024a, 87] utilise these magnetic transitions much more strongly and can thus achieve very high dissymmetries (Fig. 1.16). These complexes emit from metal-centred d–d or f–f states. The electronical transition between orbitals of the same parity is forbidden, but allowed for magnetic transitions. This means that **m** is particularly high, while $\boldsymbol{\mu}$ is small, giving rise to a beneficial $|\mathbf{m}|/|\boldsymbol{\mu}|$ ratio. Electronically forbidden transitions are accompanied by a very small radiating rate constant, so that such emitters are hardly suitable for use in devices. Due to the proportionality of the radiative rate constant and the inverse proportionality of the dissymmetry to the size of the electrical transition dipole moment, a

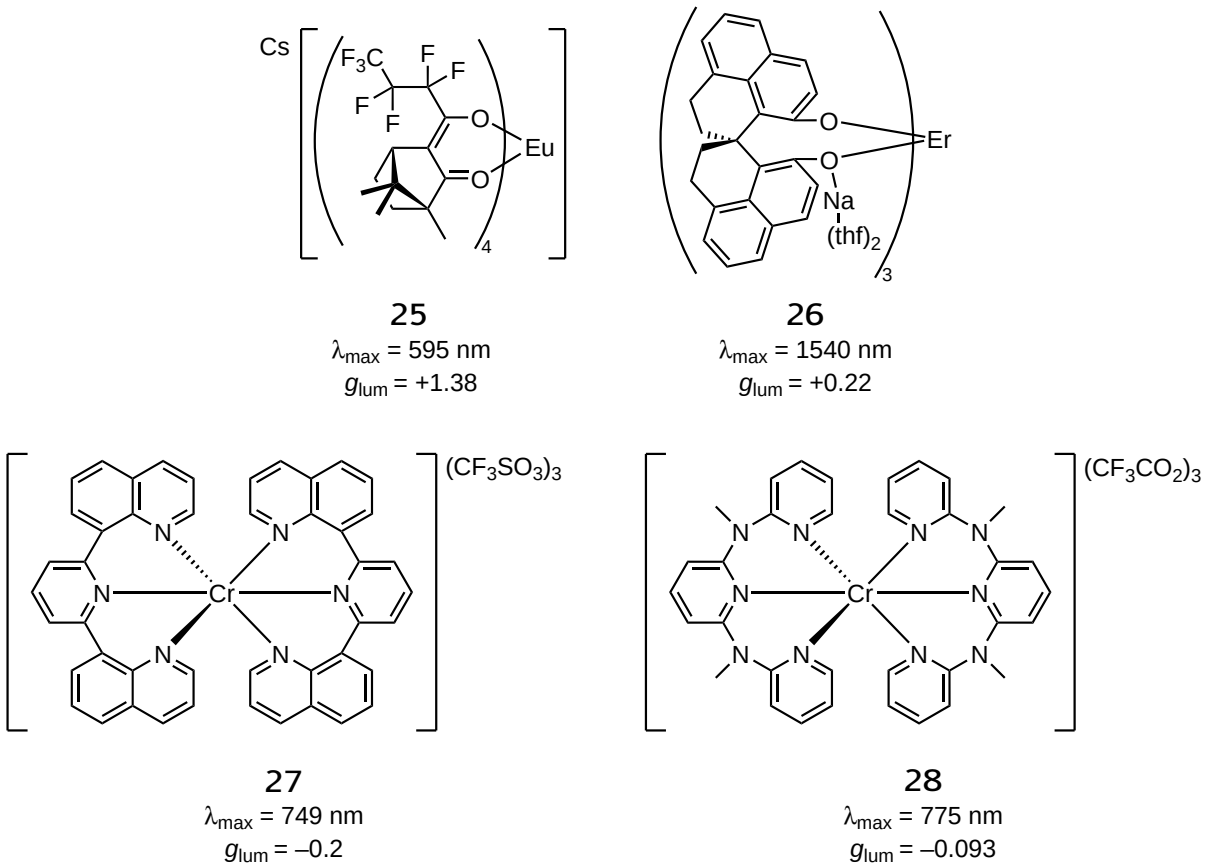

Figure 1.16: Selected lanthanide- and chromium-complexes featuring high emission disymmetries.[**Schnable2024a**, **Jimenez2019a**, **Dee2019a**, 87]

mutually exclusive relationship results. This means that a particularly efficient emitter only ever exhibits a low dissymmetry and vice versa. The aim is therefore to increase the g_{lum} value of a new emitter as much as possible without sacrificing too much radiative rate constant. Linear carbene copper complexes with donor-acceptor motifs are standout examples, successfully reconciling these contradictory requirements. Their simultaneous achievement of high radiative rate constants, often through TADF, and significant g_{lum} values places them as promiing templates for next-generation CPL-active materials. Currently values in the order of 10^{-3} to 10^{-2} are not uncommon.[88,89] Although both CPL and stimulus-responsiveness are common phenomena, mechanically responsive organic CPL emitters are sparsely known and transition metal complexes are even rarer (*vide infra*).[90–92]

1.8 Objective

Photoactive copper(I) complexes have been the focus of research for several years. In particular, emission in the (near) infrared range is indispensable for a variety of cutting-edge technologies (e.g. optical telecommunications, quantum cryptography, photodynamic therapy, imaging techniques). However, efficient luminophores in the low-energy spectral range remain rare. Although organic NIR emitters are accessible through targeted molecular design and are particularly relevant for biological applications, they are hardly suitable for optoelectronic applications. Platinum(II) and iridium(III) complexes, which dominate the OLED market in the visible range, are also not very suitable for the near-infrared spectral range.

In particular, the limited ligand diversity and geometric rigidity limit the modularity in terms of emission wavelength. Copper(I) complexes have significant advantages over other metal organic compounds. In the first chapter of this thesis, various linear copper carbene complexes will be investigated for their suitability as NIR emitters. A class of phthalazine-based carbenes, first described by Magriz *et al.*, but largely ignored to date, is of particular interest due to their synthetic accessibility. In addition initial quantum chemical calculations suggested high π acidity, which, depending on the substituents chosen on the α-nitrogen atom, even exceeds that of the extensively studied CAArC (Scheme 1.15).

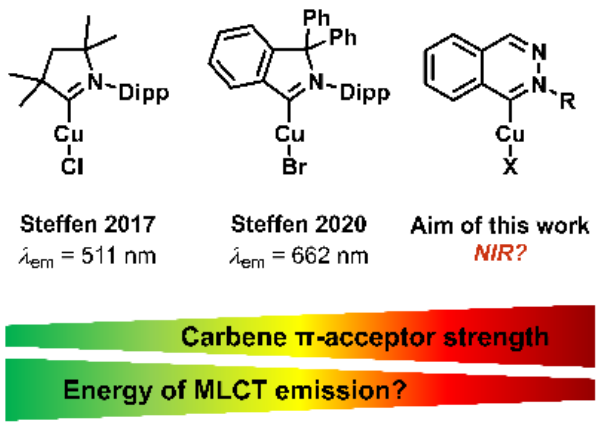

Scheme 1.15: Carbene acceptor strength as guiding principle of this work's investigation of NIR emitters.

Since such linear complexes of copper often exhibit rapid TADF, especially in combination with electron-rich donors (e.g. carbazole), NIR emission could be achieved with electron-poor carbenes and the intrinsic limitations could be minimised. Additionally, to gain deeper insight into the emission mechanisms governing a multitude of copper(I) coordination compounds, a series of [Cu(CAAC)(X_{donor})] complexes from other PhD projects will be analyzed theoretically.

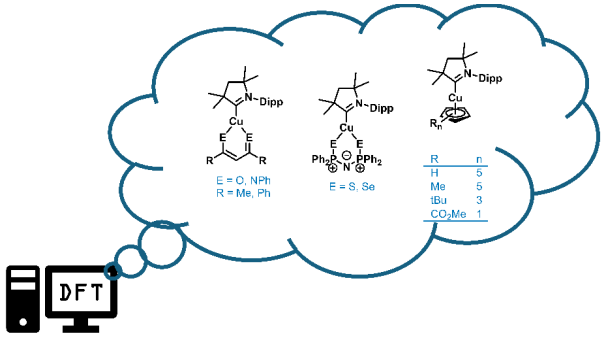

Figure 1.17: DFT-Studies on CAAC complexes.

Building on structural and spectroscopic results from Dr. André Muthig's doctoral thesis, both trigonal and half-sandwich complexes are investigated. The emission of these compounds is shifted bathochromically relative to their parent [Cu(CAAC)Cl] (see Scheme 1.15) and feature diverse structural flexibilities. From those theoretical findings, new and robust design criteria for efficient NIR emitters are to be gathered. Besides NIR emission, CPL and mechanoluminochromism are also of particular importance for a multitude of optoelectronic applications (*vide supra*). Despite the diverse areas of application, reliable structure-property relationships are still lacking and progress is slow, as these phenomena are poorly understood at the molecular level. According to current understanding, CPL can only occur if a chiral environment inparts helicity to the photon during radiative decay. It is therefore essential that chiral structural elements are not only present in close proximity to the orbitals involved in the transition, but can also interact electronically with them. Both Hupp

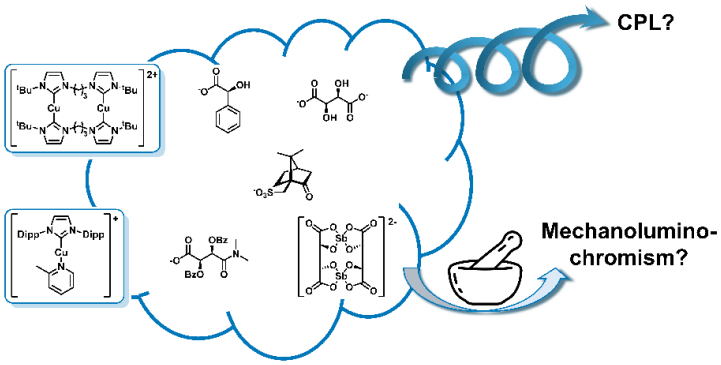

Figure 1.18: Extending known stimulus responsive copper complexes with chiral anions for mechanostimulated CPL.

et al. and Liske *et al.* were able to produce linear cationic copper(I)-NHC complexes which show pronounced mechanoluminescence. Since the mechanoluminochromism in both cases results from Cu-anion interactions, derivatives with chiral counterions will be discussed in the second part of this work. The forced spatial proximity and electronic coupling of the anions to the photoactive copper centre represents a promising starting point for mechanically stimulated CPL.

Carbene metal amides (CMAs) are generally characterised by high radiative rate constants, as their linear geometry and suitable orbital alignment enable rapid charge transfer processes. Dr. André Muthig showed that in the carbazolate complexes investigated with an ex-chiral pool carbene (^{Ment}CAAC), the emission has no measurable asymmetry. However, when phenoxazine is used as the donor ligand, the CPL signal increases dramatically. This phenomenon will be investigated and rationalised using quantum chemical calculations in this work.

2 NIR Emission using Cu(I)-Carbene Complexes

2.1 Phthalazin-2-ylidenes as Accessible *N*-heteroarylic Carbene π-Chromophor Ligands for Deep-Red Luminescent Copper(I)-Halide Complexes

Introduction

Due to the growing demands on displays and optical communication channels, considerable research has been focused on developing increasingly stable and efficient molecular emitter materials.[93,94] One notable class of these emitters is transition metal complexes, which generally exhibit high phosphorescence rate constants because of their strong spin-orbit coupling compared to purely organic luminophores.[95,96] While significant progress has been made on transition metal complexes with emission wavelengths in the visible spectrum (380–700 nm), less advancement has been achieved in efficient emission in the (near) infrared range.[97]

Many IT applications, including fibre optics and quantum cryptography, rely heavily on deep red and infrared emission.[98,99] This reliance is due to the high transparency of silicate glass to low-energy light. Thus, developing more efficient and stable NIR luminophores is essential for enhancing the usability of light-based communication. However, the lack of progress is not due to a lack of effort but to intrinsic problems associated with low-energy luminescence. As the energy gap between the ground state and the emitting excited state decreases, multiple non-radiative processes become dominant, limiting the overall efficiency of a luminophore.[100–102] These non-radiative processes are explained by the energy-gap law (EGL).[101,102] According to the strict version of the EGL, applicable to very rigid luminophores with similar potential hypersurface topologies in both ground and excited states (known as nested states), the high density of ground state vibronic states near the continuum allows for fast internal conversion (for singlet excited states) or intersystem crossing (for triplet excited states) from the vibronic ground state of the electronic excited state into a vibronic excited state of the electronic ground state, followed by vibronic relaxation, as predicted by Fermi's golden rule.[19,103] For less rigid systems, a similar argument can be made. Due to their flexibility, significant distortion occurs during electronic ex-

citation, resulting in very different potential hypersurface topologies. In these cases, there is significant overlap of the vibrational wave functions. It is generally accepted that to design luminophores with sufficiently high quantum yields and adequate radiative rates in the IR, vibronic processes must be suppressed either by rigidification or (partial) deuteration, or radiative rates must be increased to outcompete non-radiative pathways.[104] The latter is usually achieved by using rare and expensive 4d or 5d transition metal complexes, such as those of rhodium or iridium, which utilize their high spin-orbit coupling abilities to facilitate fast phosphorescence.[25] Start-

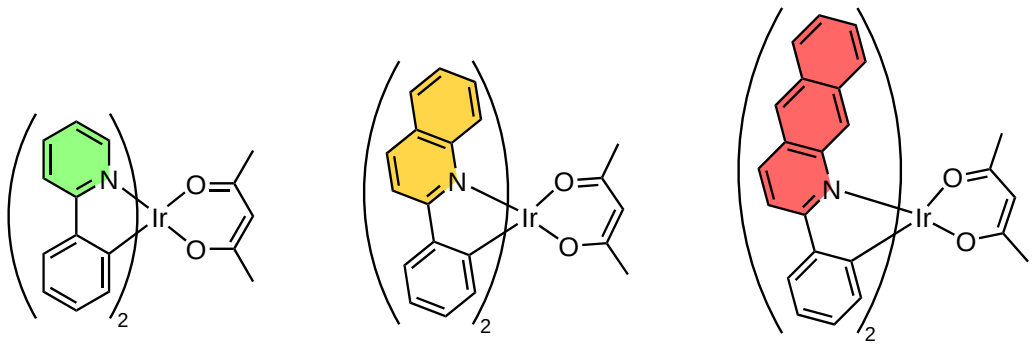

29
λ_{max} = 516 nm
τ = 1.6 µs
Φ_{em} = 34%

30
λ_{max} = 597 nm
τ = 2.0 µs
Φ_{em} = 10%

31
λ_{max} = 708 nm
τ = 0.6 µs
Φ_{em} = 2.5%

Figure 2.1: Structures and photophysical properties of cyclometalated Ir-complexes **29**, **30** and **31**.[105,106]

ing from the green emissive complex [Ir(ppy)$_2$(acac)] **29**, the groups of Thompson[105] and Qui[106] successfully shifted the emission maxima of related complexes **30** and **31** bathochromically by extending the ligands' π-system, thereby decreasing the gap between the ground state and the lowest excited state (Fig. 2.1). While achieving a pronounced red-shift of about 80 to 100 nm per additional annulated phenyl body, the quantum yields decrease by a factor of about three. This highlights how non-radiative processes dominate even in iridium-based luminophores, which are usually known for their high efficiencies. Furthermore, the long lifetimes typically associated with phosphorescent emitters result in the accumulation of highly reactive diradical species, which ultimately shortens the lifespan of electrically driven light sources.[9,107] To render radiative processes competitive with non-radiative decay, even in the low-energy regime, and limit energy roll-off in electroluminescent devices, current research focuses on singlet harvesting through thermally activated delayed fluorescence (TADF).[24,108,109] Due to their versatile coordination chemistry and relatively high redox stability, copper(I)[89,92,110–113] and zinc(II)[114,115] complexes have emerged as promising candidates for visible light emission. In particular, copper(I) complexes with strongly π-accepting carbenes exhibit unique properties.[52,89,92,110,111,116] These

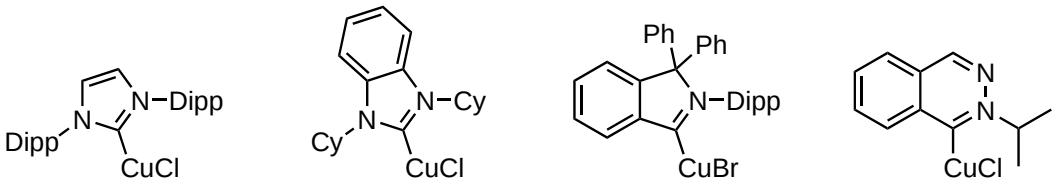

10
λ_{em} = 347 nm

32
λ_{em} = 495 nm
$\langle\tau\rangle_{amp}$ = 7.92 µs
Φ_P = 0.38

12
λ_{em} = 651 nm
τ = 9.5 µs
Φ_P = 0.20

33a
λ_{em} = 710 nm
$\langle\tau\rangle_{amp}$ = 360 ns
Φ_P < 0.01

Figure 2.2: Emissive copper carbene halides and their luminescence properties.[52,60,61]

complexes often adopt a linear geometry, leading to excited states with pronounced metal-to-ligand charge transfer (MLCT) and/or ligand-to-ligand charge transfer (LLCT) character, facilitating efficient (reversed) intersystem crossing. To shift the emission of these complexes, represented by the general formula [Cu(carbene)X] where X is an arbitrary anionic ligand, towards longer wavelengths, researchers have explored strategies to increase the π-donor strength of the anionic ligand. As demonstrated by Romanov *et al.* in their series of carbene copper amides, this approach can effectively tune the emission properties of these complexes.[113]

Based on this rationale, a valuable tool for ligand screening is calculating the frontier orbital energies of different free carbenes (Scheme 2.1). Alternatively, increasing the π-acceptor strength of the carbene, for example by extending the ligand's π-system and thereby stabilizing the ligand's LUMO, similarly shifts the emission to lower energies due to the significant carbene LUMO participation in the lowest excited state (generally a donor-to-acceptor charge-transfer state).[52,60,61] With its high-lying LUMO, the classic imidazolium NHC is a weak acceptor, resulting in the emission of [Cu(NHC)Cl] complexes in the UV-A region.[60] Extending the π-system and removing π-donating neighboring heteronuclei lowers the LUMO energy and shifts the emission to longer wavelengths, as observed in complexes of benzimidazolium-based NHCs[61] and cyclic amino(aryl)carbenes (CAArCs).[52] By introducing strong –M-substituents, such as

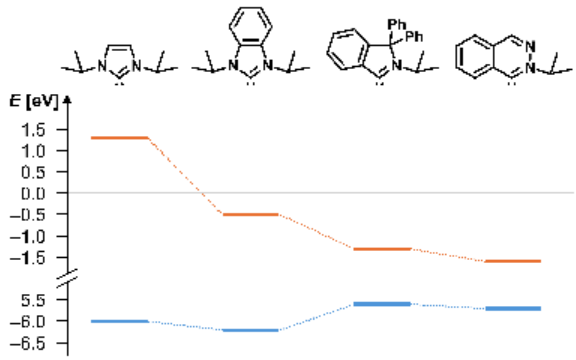

Scheme 2.1: Frontier orbital energy diagram of selected carbenes from DFT caclulations (PBE0/def2-TZVP).

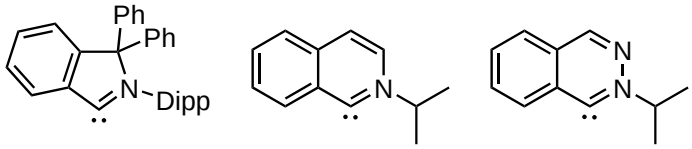

34 35 36

Figure 2.3: Structures of strongly π-acidic carbenes.[59,117–119]

imine moieties, into the backbone, we predicted and experimentally confirmed an even more pronounced red-shifted emission in our copper(I)-halide complexes (*vide infra*) of phthalazine-based *N*-heteroarylic carbenes. (Fig. 2.2) Despite the Bertrand group's early introduction of strongly π-accepting CAArCs in 2007, their electronic properties were not extensively explored until 2015.[59,117] Notably, the Lassaletta group independently investigated and published N-heteroarylic carbenes (NHArCs) based on isoquinoline scaffolds, demonstrating comparable π-acceptor strength just months earlier.[118] Phthalazine-based NHArCs, reported by Magriz *et al.* in 2010, were subsequently shown to exhibit even stronger π-acceptor properties (Fig. 2.3).[119] While CAArCs have gained widespread recognition and application in catalysis and photophysics, with over 50 publications citing the 2015 paper, both classes of NHArCs remain relatively unstudied. In the present study we sought out to investigate the phthalazine-ylidenes as potential chromophore ligands for NIR emissive copper(I) complexes.

Results and Discussion

Synthesis and Structural Characterization

The air- and moisture-stable phthalazinium salts, namely **37**, **38** and **39**, were synthesized following modified procedures outlined by Magriz *et al.* (Scheme 2.2).[119] Compounds **37** and **39** were obtained by reacting phthalazine (**40**) with excess 2-iodopropane and bromodiphenylmethane, respectively, under elevated temperatures without additional solvent, resulting in yellow solids (method A). To prepare **38**, phthaldialdehyde (**41**) was first reacted with tert-Butylhydrazine in refluxing THF. Subsequently, a Tf_2O-mediated dehydration of the intermediate dihydrophthalazinol was conducted in dry diethyl ether, yielding the product as an off-white solid (method B). It is noteworthy that this reaction exhibits unusual sensitivity to the precise procedural conditions; our successful synthesis was achieved only once. Subsequent attempts to replicate the synthesis led to the formation of an undefined black to dark brown tar-like substance upon addition of Tf_2O in the second reaction step. Unfortunately, all well-established protocols for the synthesis of copper(I)halide carbene complexes failed. Magriz *et al.* already discussed their inability to isolate neither the free carbene,

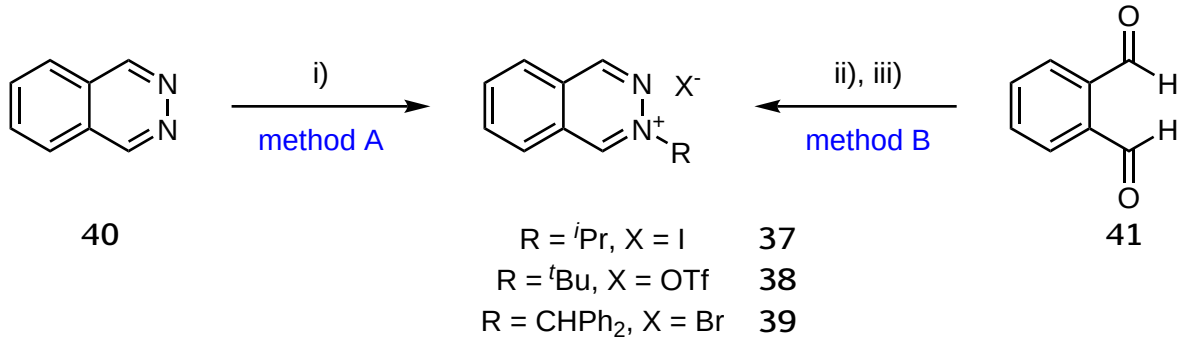

40 41

Scheme 2.2: Synthesis of carbene precursors **37**, **38** and **39**. i) R-X (1.5 equiv.), neat, 2 h, 90 °C; ii) $RNHNH_2$ (1.1 equiv.), THF, 24 h, reflux; iii) Tf_2O (1.05 equiv.), Et_2O, 30 min, 0 °C.

nor a rhodium-carbonyl complex by transmetalation.[119] We also added the weak-base

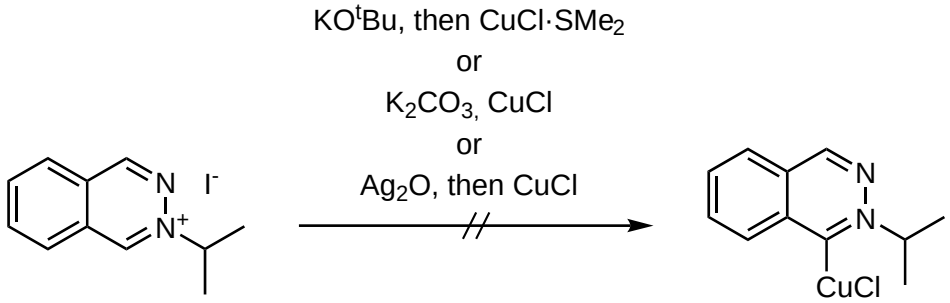

37 **33a**

Scheme 2.3: Failed attempts of preparation of **33a**.

method of Nolan[120] and Gimeno[121] to the list of procedures not suitable for preparing the desired copper(I) complexes (Scheme 2.3). Building upon Magriz's initial observation that $[Rh(OtBu)(COD)]_2$, formed in-situ from KOtBu and $[RhCl(COD)]_2$, generates the corresponding carbene complex upon reaction with **37** in low yields, we adapted this approach. Initially, we obtained small amounts of highly contaminated samples of **42** using KOtBu and CuI. Dissatisfied with this method, we then synthesized pure copper(I)-tert-butoxide[122,123], enabling us to finally produce the desired copper(I)iodide complex **42** in moderate yields and high purity (Scheme 2.4). Lacking any additional external anions, it is evident that the anion of the carbene precursor now plays a crucial role in product composition. To avoid mixed halide complexes, carbenium salts of weakly coordinating anions were prepared either by metathesis from the iodides or by direct synthesis in the case of **38**. In the presence of excess sodium halide, reaction of these precursors with copper(I)-tert-butoxide resulted in the slow formation of the desired complexes. However, contamination of the final product with sodium salts and other by-products was unavoidable. Upon crystallisation of crude **33a**, synthesized from PF_6 analogue of **37**, mostly yellow crystals mixed with a

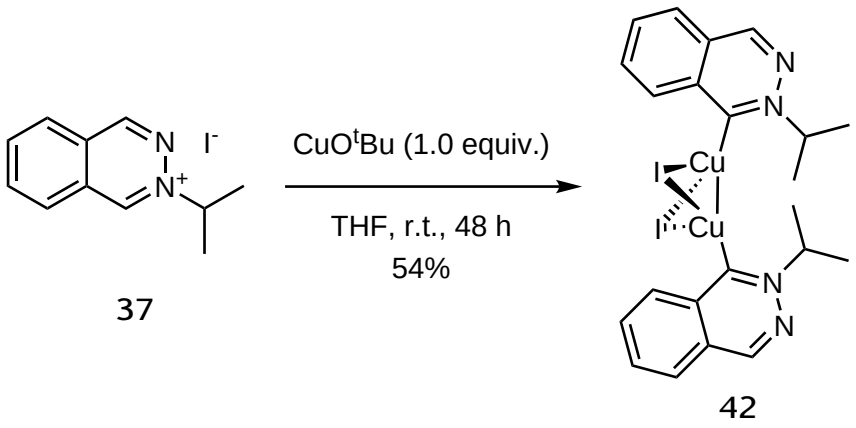

Scheme 2.4: Succesful synthesis of **42** from **37**.

small number of red-orange ones formed. From SC-Xray diffraction, the yellow specimen was confirmed to be the expected monomeric **33a**, while the red crystal contained a tetrametalic species **33b**. Attempts of targeted synthesis of this structurally interesting compound failed and **33a** was obtained instead. We assume an equilibrium to be present in solution between these two compounds. Alternatively, using the different carbenium halides directly would circumvent the issues with sodium salts. Carbenium chloride and bromide analogues were prepared by anion exchange, utilizing efficient and reusable anion-exchange resins (AER) according to modified literature-known procedures for imidazolium-based ionic liquids[124], avoiding volatile and less reactive alkyl chlorides and bromides. From these halides, the copper(I) complexes were prepared in a similar fashion to their iodide analogous (Scheme 2.5).

SC-X-ray and non-covalent interaction studies

Comparison of the structural information of the compounds **33a**, **42** and **47**, from single-crystal X-ray diffraction analysis reveals a strong dependence of the structure on the halide anion. A summary of selected bond-lengths and angles is given in the appendix (Table 4.1).

Nearly linear coordination geometries and monomeric structures are favoured for the copper chloride complexes regardless of steric shielding of to the carbene ligand (Fig. 2.4). While compound **33a** features a C-Cu-N angle of 173.126° the corresponding angle in **46** is nearly 10° smaller, this however is hypothesised to not arise from steric effects, since the chlorides distance to the carbene substituents is too large, but rather a result of additional Cu-H-interactions (*vide infra*). Interestingly the monomers also stack via π-interactions of the phthalazine backbone, resulting in short Cu-Cu-distances (i.e. 3.2403 Å) of significantly less than the sum of van der Waals radii, $2 \cdot r_{cov} = 4.76$ Å,[125] and is close to the covalent distance, that is 2.64 Å.[126] Due to poor quality of **33b** crystals, only the connectivity of **33b** could be determined and

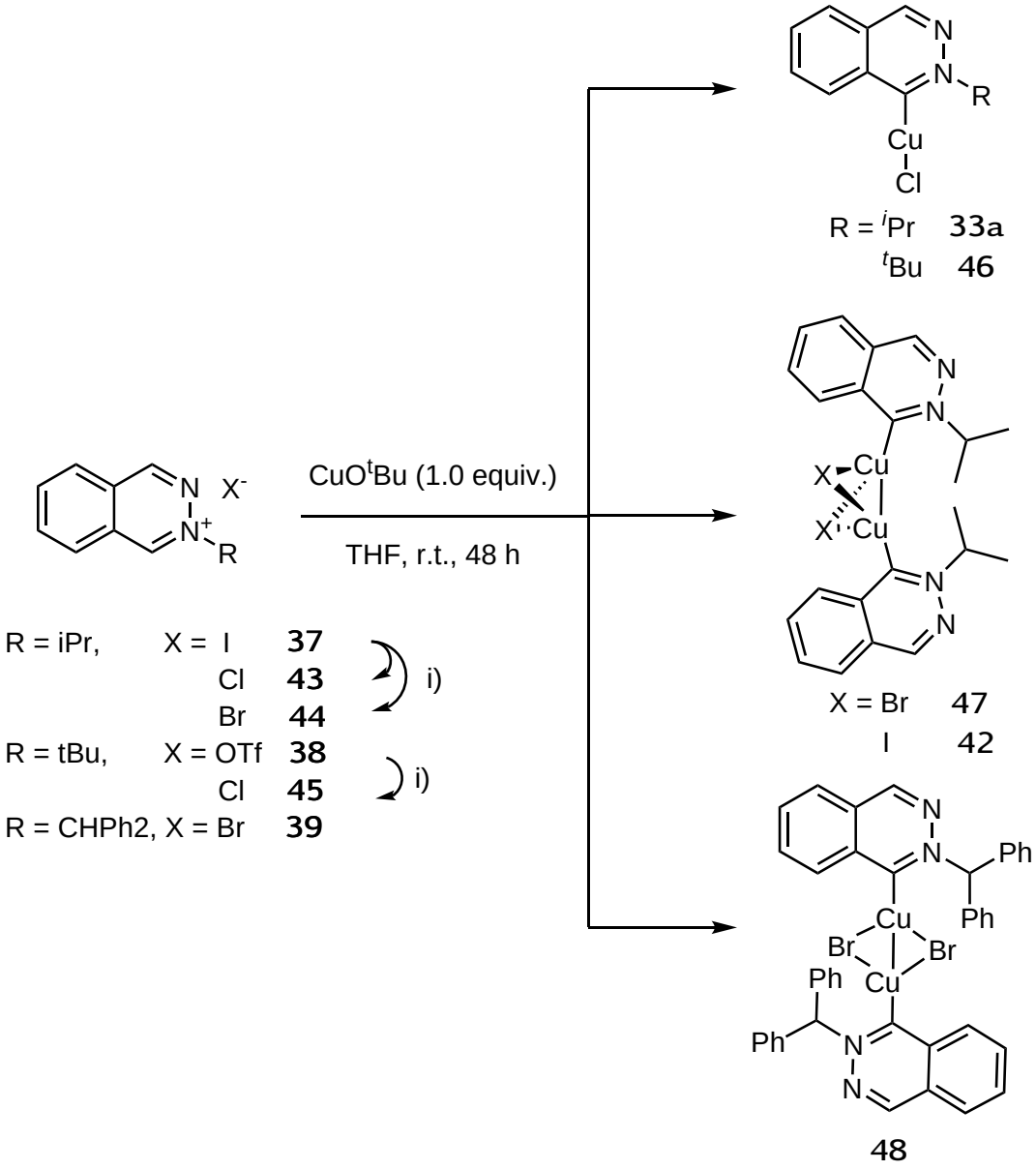

Scheme 2.5: Synthesis of novel precursors **43**, **44** and **45** by anion exchange resin and copper complexes **33a**, **42**, **46**, **47** and **48**. i) AER(X^--form), MeOH, 15 min, r.t.

therefore bonding situations will not be discussed in detail. A fast scan revealed a helical compound formed by incomplete PF_6-to-Cl anion exchange. **33b** features a tetrametalic helical $[Cu_4(NHArC)_4Cl_3]$ cation, where two of these helices with opposing chirality stack on top of each other (Fig. 2.5, c), most like due to intermolecular π-stacking of the carbenes (Fig. 2.5, b). In the cases of the copper bromide and iodide complexes, halide bridged dimers are found with trigonal coordination geometry. For the isopropyl decorated carbene, the carbene ligands adopt a *syn*-like relative conformation, as indicated by the small N1-C1-C1'-N1' torsion angles of only around 30°. The Cu_2X_2 fragments of both **47** and **42** exhibit a butterfly-like shape with short Cu–Cu-distances of about 2.8 Å, indicating significant cuprophilic interactions which are most

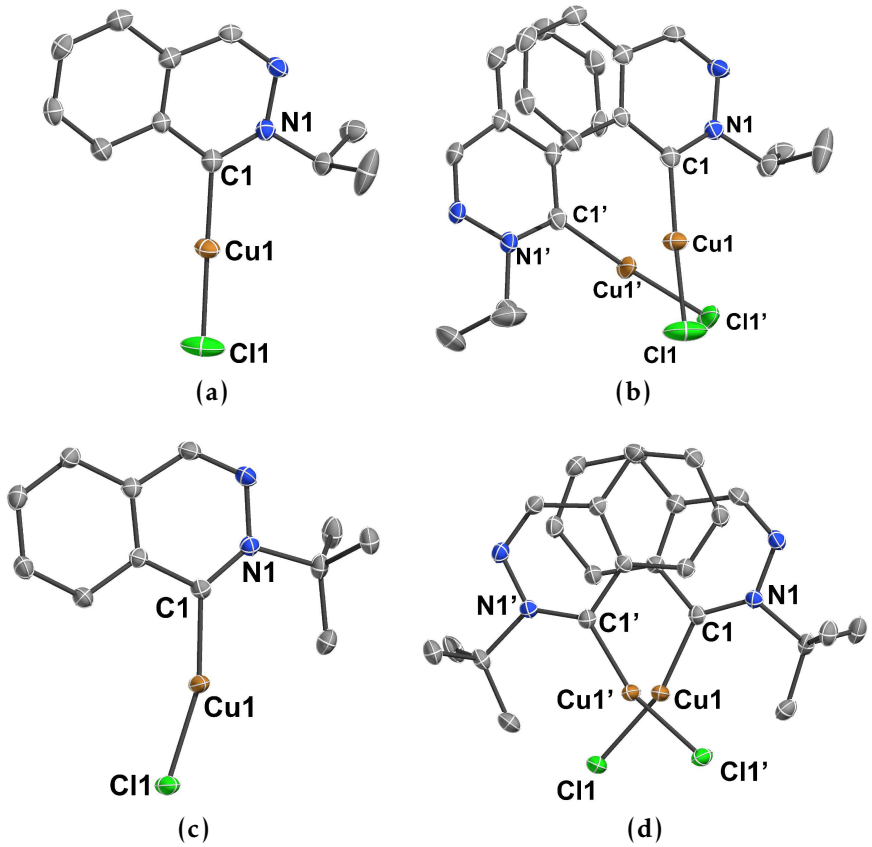

Figure 2.4: SC-XRD structures of **33a** (a-b) and **46** (c-d). Thermal ellipsoids are drawn at the 50% level, hydrogen atoms are omitted for clarity.

pronounced in the iodide complex **42** (Table 4.1, Fig. 2.6). In contrast **48** bears a nearly coplanar Cu_2Br_2 fragment despite the benzhydryl-substituted carbene being sterically and electronically very similar to the isopropyl-bearing carbene. In addition, the carbene ligands now, unlike *syn*-like oriented **42** and **47**, adopt an *anti*-like configuration with a torsion angle close to 170°. We assume, that more favourable intermolecular hydrogen-π-system interactions between neighbouring benzhydryl fragments can occur in this non-tilted, *anti*-like configuration. To gain deeper insight into the inferred structure-determining weak interactions, we carried out an interaction region indicator (IRI) analysis according to Chen *et al.*[127] employing the electron densities from the H-only DFT-optimised structures (ωB97X-D3BJ/def2-TZVP) of the complexes. For the monomers **33a** and **46**, agostic interactions between the methylene- and methyl-protons of the isopropyl groups are found, respectively, which are most pronounced for **46** and thus explain the larger distortion from linear coordination geometry (Fig. 2.7, a-b). IRI analysis of the π-stacked dimers (Fig. 2.7, c-d) in the crystal structures shows van der Waals interactions around several atoms of the carbene backbone. Surprisingly, weak interactions are also found between the copper atoms of adjacent molecules, implying that the close proximity is indeed due to attractive electronic effects and not purely because of packing effects, even though the inter-

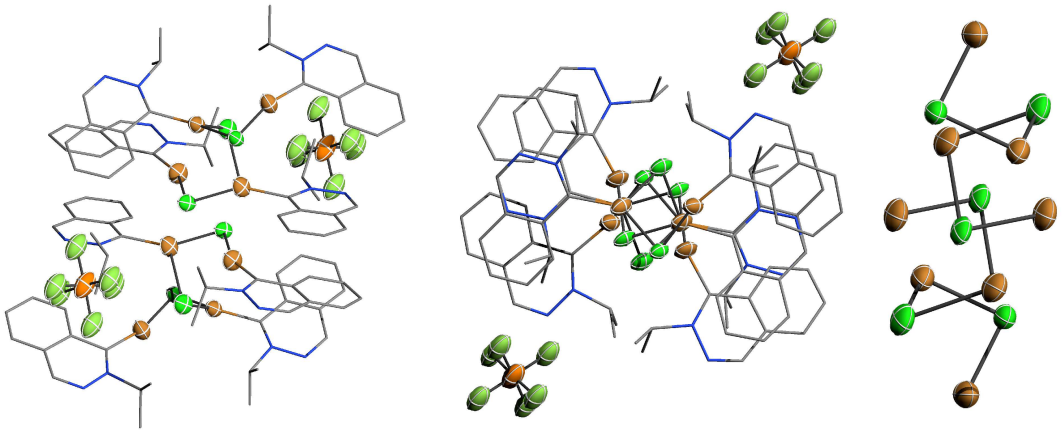

(a) (b) (c)

Figure 2.5: Different views of the SC-XRD structure of **33b**. Thermal ellipsoids are drawn at the 50% level, carbene backbones are reduced to a stick-representation or omitted (c) and hydrogen atoms are omitted for clarity.

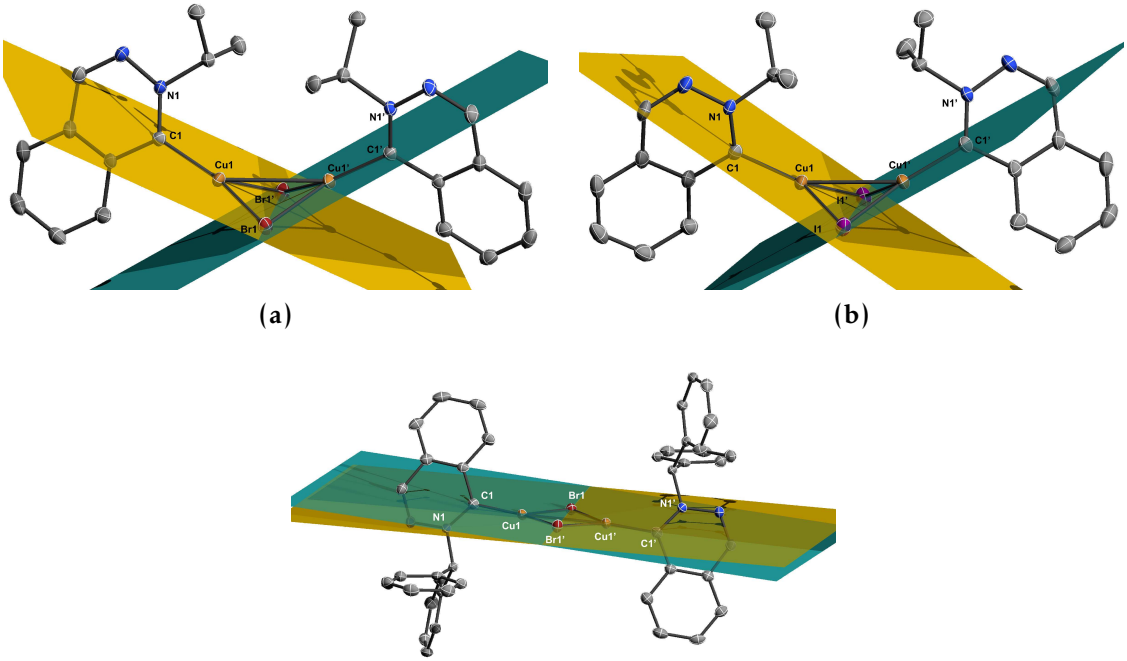

Figure 2.6: SC-XRD structures of **47** (a), **42** (b) and **48** (c). Thermal ellipsoids are drawn at the 50% level, hydrogen atoms are omitted for clarity.

metal distances are slightly larger than in the dimeric bromide and iodide complexes (Table 4.1) or in other literature known luminescent copper(I) complexes featuring cuprophilic interactions with distances of 2.4–2.8 Å.[128,129] The dimeric bromide and iodide complexes **42** and **47**, are very similar with respect to their weak intermolecular interactions, but we note that the copper-copper interaction is stronger in the iodide complex, which is also seen in the shorter Cu-Cu distance (2.8703 Å vs 2.7495 Å).

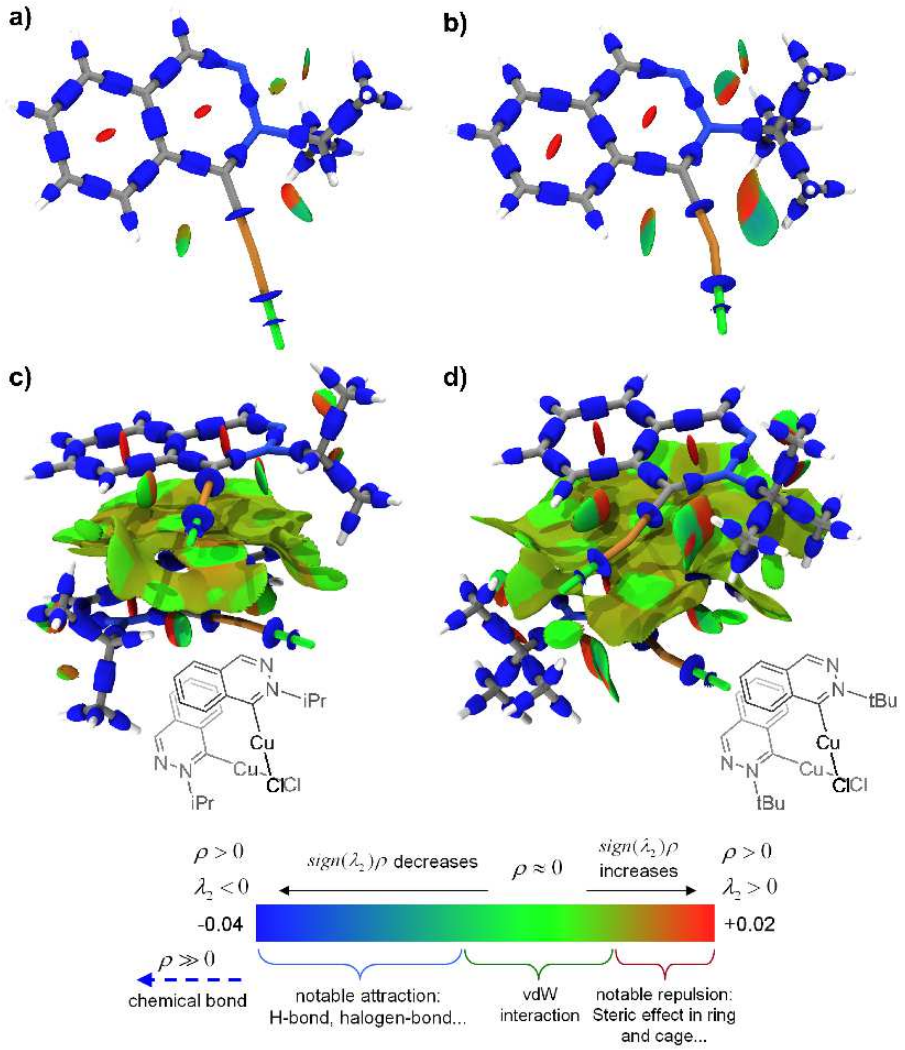

Figure 2.7: 3D IRI analysis of **33a** (a, c) and **46** (b, d).

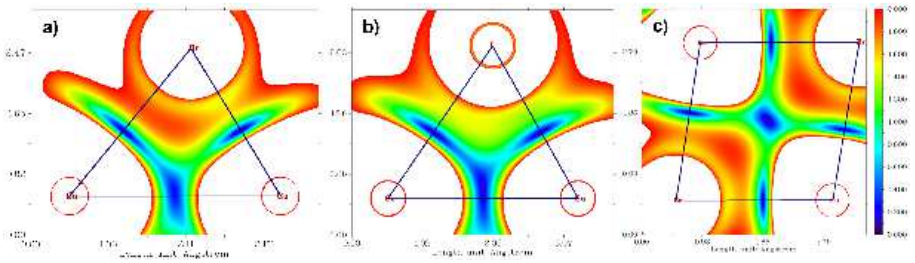

Figure 2.8: 2D IRI analysis in copper-halide-plane of **47** (a), **42** (b) and **48** (c).

Because the regions around the Cu-Cu path is quite crowded due to repulsive contributions common to cyclic systems, we analysed the IRI properties of the region of interest in the plane spanned by the two copper atoms and one of the halides. From this perspective the increased cuprophilic interaction is clearly visible. Although Cu-Cu distance in **48** (3.1514 Å) is significantly increased, attractive interaction is still found in the Cu_2Br_2 plane (Fig. 2.8).

UV-Vis Absorption and PL Studies

The isolated copper(I) halide complexes **33a**, **42** and **47** each show two broad and featureless absorption bands between 290 and 330 nm with molar absorptivity of around $7–9{\cdot}10^3\ \mathrm{cm^2mol^{-1}}$ (**33a**) , $20–22{\cdot}10^3\ \mathrm{cm^2mol^{-1}}$ (**47**) and $16–17{\cdot}10^3\ \mathrm{cm^2\,mol^{-1}}$ (**42**) in THF solution typical for fairly allowed ^{1}MLCT and ^{1}LLCT/^{1}XLCT transitions (Fig. 2.9). The overall similarities in the shape of these absorption bands suggest all three compounds to assume a similar structure in solution. Dissociation of the dimeric **42** and **47**

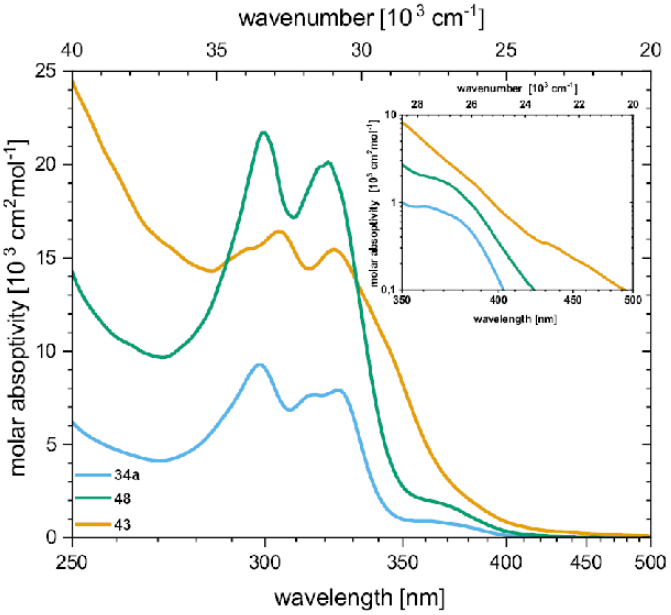

Figure 2.9: Absorption-spectra of **33a**, **42** and **47** in THF solution. Insert: Zoom-in of the low-energy region in logarithmic scale.

(*vide supra*) into monomeric chromophores explains the generally high absorptivity of both compounds, by introducing an additional factor of two in the Beer-Lambert law. Our TD-DFT calculations confirm these transitions to be predominantly of (X+MLCT) type ($(d_{Cu} + p_{halide}) \rightarrow \pi^*_{carbene}$), with XLCT contributions being least pronounced in **33a** (Fig. 2.9). Interestingly, the calculations also identified the $S_0 \rightarrow S_1$ transitions to be of ^{1}(X+MLCT) type ($(d_{Cu} + p_{halide}) \rightarrow \pi^*_{carbene}$), but with far smaller oscillator strength due to the symmetry forbidden nature (Table 4.9). Thus, the lowest energy singlet absorption is observed as a weakly allowed shoulder ($\epsilon = 1–10{\cdot}10^3\ \mathrm{cm^2mol^{-1}}$) between 370–430 nm, shifting bathochromically with increasing polarizability of the halide ligand. An additional very weakly allowed absorption ($\epsilon = 0.5{\cdot}10^3\ \mathrm{cm^2mol^{-1}}$) is observed at around 460 nm for **42** arising from triplet excitation facilitated by iodines strong heavy atom effect (Fig. 2.9, insert). In solid (amorphous) state all three complexes show faint visible photoluminescence (Fig. 2.10,(a)). Steady state spectra reveal broad and featureless emission bands typical for CT processes. **33a** exhibits very weak near-infrared emission centred at $\lambda_{max} = 710$ nm and even weaker residual

fluorescence centred at $\lambda_{max} = 425$ nm (Fig. 2.10,(b)). Non-radiative decay is efficient, giving a low quantum yield of <0.01 with an associated average lifetime of 360 ns. A large Stokes-Shift of around 13,400 cm^{-1} implies strong deformation upon excitation, likely by means of a Renner-Teller-type bending mode around the copper atom. In contrast for dimeric **49** and **47** nearly identical emission bands with maxima at

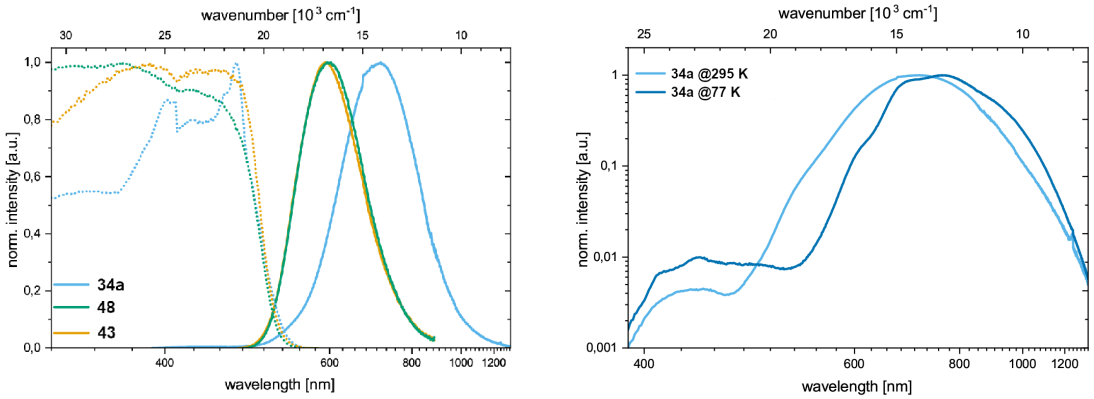

Figure 2.10: Emission- (solid line) and excitation-spectra (dotted line) of **33a**, **42** and **47** in solid state at room temperature (a). Logarithmic solid state emission spectra of **33a** at 295 and 77 K (b).

595–600 nm and associated average lifetimes of 6.6 and 7.6 ms are observed, respectively. Increased rigidity and steric hindrances, reflected in the smaller Stokes-shifts of only around 10,000 cm^{-1}, greatly increases luminescent quantum yield to 0.06 (**42**) and 0.12 (**47**) and explains the hypsochromically shifted emission relative to **33a**. We note that multi-exponential decays are observed in all three compounds, for which the origin may be related to rotational freedom of the carbene ligand. Upon cooling to 77 K emission of **33a** is shifted to lower energy at 760 nm and now features multiple shoulders, inferring LC states to participate in the emission process. Similar behaviour is observed for the afore mentioned residual fluorescence (Fig. 2.10). Deep-red/NIR emission of **33a** by introduction of highly π-acidic phthalzine-based carbene was successful, achieving a bathochromic shift of almost 1 300 cm^{-1} compared to well-studied [Cu(CAArC)Br] (**12**).[52] However, luminescence quantum yield was reduced greatly according to the energy gap law. Unhindered Renner-Teller-distortion leads to efficient non-radiative decay, making the current structural motif unsuitable for any possible applications in NIR-OLEDs. As a proof-of-principle, further work is directed towards improving luminescent performance by introducing stronger donor-ligands and rigidification to supress afore mentioned Renner-Teler-type modes.

Conclusion

We have reported on the synthesis, structure and photophysical properties of the first luminescent copper(I) halide complexes bearing widely overlooked phthalazine-based NHArC ligands as π-accepting chromophore unit. The synthesis of the carbene precursors is in part much simpler than for the typical CAArC precursors, however modification at the nitrogen atom is limited by the reactivity of alkylating reagents. Furthermore, constructing the pyridazine ring by consecutive condensation/ dehydratization proofed to be unreliable and further optimization is needed. The big advantage would be the ability to introduce sterically demanding aryl substituents as found in a plethora of currently used carbenes. All complexes **33a**, **42** and **47** featured detectable triplet emission with wavelengths lower than 600 nm in solid state and even reaching as low as 710 nm for **33a**. Ongoing efforts are taken to supress aggregation and flexibility by steric and electronic modification of the carbene backbone. Our goal is to further decrease emission energy and simultaneously hinder deactivating Renner-Teller distortion.

2.2 "Trigonal Copper(I) Complexes with Cyclic (Alkyl)(amino)carbene Ligands for Single-Photon Near-IR Triplet Emission"

Full bibliographic information:
A. M. T. Muthig, M. Krumrein, J. Wieland, M. Gernertm F. Kerner, J. Pflaum, A. Steffen, "Trigonal Copper(I) Complexes with Cyclic (Alkyl)(amino)carbene Ligands for Single-Photon Near-IR Triplet Emission", *Inorg. Chem.* **2022**, *61*, 14833–14884.
Full-text: https://doi.org/10.1021/acs.inorgchem.2c02376
All syntheses and photophysical measurements were performed by Dr. André Muthig as part of his masters thesis *Synthese und photophysikalische Studien von trigonalen Kupfer(I)-cAAC-Komplexen* at the Julius-Maximilians-Universität Würzburg in 2017 and his PhD thesis *Nahinfrarote und Zirkular Polarisierte Lumineszenz von Donor-Kupfer(I)-Akzeptorkomplexen* at the TU Dortmund University in 2022 under the supervision of Prof. Dr. Andreas Steffen. Single-molecule photon correlation experiments were performed by Dr. Florian Kerner from the group of Prof. Dr. Jens Pflaum at Julius-Maximilians-Universität Würzburg. Written work was done mainly by Prof. Dr. Andreas Steffen. All authors contributed in proof-reading.
The own contribution consisted of performing and analysing quantum chemical calculations. As part of this, both time-dependent and independent density functional theory was applied to understand structural changes during excitation processes as well as elucidating the excited state nature.
Experimental contribution: ca. 15%
Written contribution: ca. 10%

Summary

A series of trigonal copper(I) complexes with a CAAC chromophore ligand and bidentate acetylacetonate or related ligands were synthesised and characterised. All complexes show broad and featureless phosphorescence in the visible to NIR range. The emission maxima are between 540 and 770 nm, but the broad emission bands extend far into the NIR range (approx. 1100 nm). All complexes have a trigonal structure, which changes to a T-shaped geometry in the excited state due to significant Jahn-Teller distortion. For the ground state, the trigonality changes to a pseudo-linearity

with increasing donor strength of the bidentate ligand. Thus, the C-Cu-D angles increase from 134.8/134.2° (L^L = acac), via 135.9/133.4° (Ph_2acac) and 140.6/123.8° (Nacac) to 152.4/110.2° (NacNac). The bathochromic shift in emission compared to linear [Cu(CAAC)Cl] can be attributed to the strong reorganisation in the excited state, which significantly destabilises the ground state in this geometry. However, this structural flexibility has two major disadvantages. In the T-shaped geometry of the excited state, there is strong coupling with the ground state and efficient non-radiative decay. At the same time, the radiative rate constant is reduced due to the unfavourable orbital geometry. Neither SOC can work effectively, nor can efficient TADF occur. Although these complexes suffer from the aforementioned limitations, the emission in the NIR is promising and should be more efficient with appropriate modification.

Intentionally left blank.

Intentionally left blank.

Intentionally left blank.

Intentionally left blank.

Intentionally left blank.

Intentionally left blank.

Intentionally left blank.

Intentionally left blank.

Intentionally left blank.

Intentionally left blank.

2.3 "Synthesis and Photophysical Studies of Copper(I) CAAC Half- Sandwich Complexes as a Highly Modifiable Class of Emitters"

Full bibliographic information:
A. M. T. Muthig, J. Wieland, S. Koop, C. Lenczyk, F. Kerner, B. Hupp, A. Steffen, "Synthesis and Photophysical Studies of Copper(I) CAAC Half- Sandwich Complexes as a Highly Modifiable Class of Emitters", *Inorg. Chem.* **2022**, *61*, 17427–17437.
Full-text: https://doi.org/10.1021/acs.inorgchem.2c02073
All syntheses and photophysical measurements were performed by Dr. André Muthig as part of his PhD thesis *Nahinfrarote und Zirkular Polarisierte Lumineszenz von Donor-Kupfer(I)-Akzeptorkomplexen* at the TU Dortmund University in 2022 under the supervision of Prof. Dr. Andreas Steffen. Single-Crystal diffraction measurements were performed and resolved by Dr. Stefan Koop and Carsten Lenczyk at TU Dortmund University. Written work was done mainly by Prof. Dr. Andreas Steffen. All authors contributed in proof-reading.
The own contribution consisted of performing and analysing quantum chemical calculations. As part of this, both time-dependent and independent density functional theory was applied to investigate structural flexibility by means of AIM calculations as well as elucidating the excited state nature.
Experimental contribution: ca. 15%
Written contribution: ca. 10%

Summary

The combination of the already known CAAC chromophore ligands with cylopentadienyl ligands enabled the investigation of various half-sandwich complexes of copper(I). In most cases, this rare class of compounds shows the expected η^5 coordination of the cp^R ligands. However, depending on the substitution, slight distortions in the direction of η^3 coordination can also be found. Particularly in electron-deficient or sterically demanding cp^R ligands (R = CO_2Me, 1,2,4–(^{t}Bu)$_3$), this reduced hapticity is clearly evident from the increased Cu-C_{cp} distance. The angle between the ligand planes and the coordination mode largely determine the symmetry and overlap of the donor and acceptor orbitals. These are therefore of significant importance for elec-

tronic excitation. In addition to the steric properties, the electronic mode also plays an important role. For example, the cp^{CO_2Me} complex shows a reduced carbene-Cu-cp(centroid) angle of just under 158°, although the ester functionality does not make any major steric demands. It can be assumed that the donor strength is reduced by the pronounced –M effect of the CO_2Me substituent to such an extent that efficient s-d orbital mixing at the copper atom cannot be maintained in order to stabilise the linear geometry. In contrast to the few known NHC, CAArC and phosphine analogues, all compounds show phosphorescence between 521 and 626 nm, whereby the emission wavelength is hypsochromically shifted with increasing Hammett parameter – i.e. decreasing electron richness – and quantum yields of up to 59% are achieved. Even in solutions of ^{ment}CAAC derivatives, detectable luminescence occurs, although significant non-radiative deactivation is usually found in structurally related complexes. Despite weak circular dichroism of these complexes, the emission dissymmetry is below the detection limit. Sterically demanding cp derivatives lead to higher radiative rate constants, as the structural reorganisation in the excited state is restricted. This is shown in small apparent Stokes shifts and could also be reproduced in DFT calculations.

Intentionally left blank.

Intentionally left blank.

Intentionally left blank.

Intentionally left blank.

Intentionally left blank.

Intentionally left blank.

Intentionally left blank.

Intentionally left blank.

Intentionally left blank.

Intentionally left blank.

2.4 New Insights into the Design of NIR Emitters

In the practical and theoretical work presented so far, various systems showing deep red to NIR emission have been presented and investigated. We were able to utilise several mechanisms to control the triplet energy. Firstly, the use of strong π-acceptor carbenes (NHArCs) leads to the expected bathohromic shift in emission due to the stabilisation of the acceptor orbital (LUMO) localised at the carbene ligand. For linear Cu(I) carbene complexes with halide donor, the emission energy can be reliably estimated from the LUMO energy.

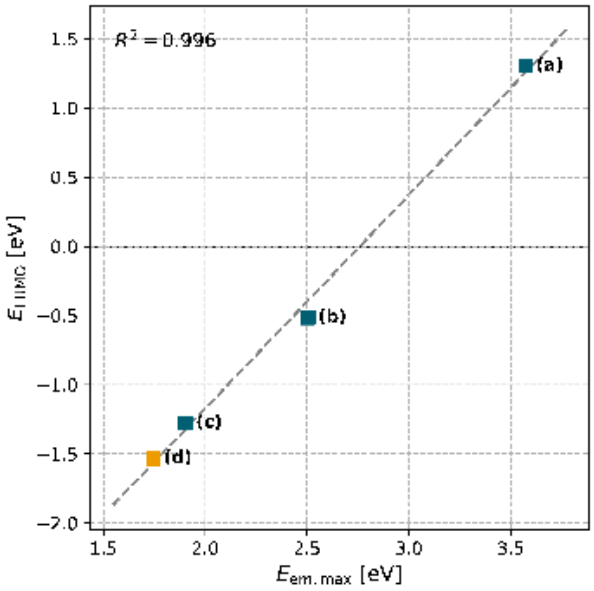

Figure 2.11: Plot of the calculated LUMO energy of isolated carbenes (PBE0/def2-TZVP) as a function of emission energy in linear carbene-Cu-halide complexes. Novel complex **33a** is shown in orange, known carbene complexes (a)–(c),**10**, **11** and **12** respectively, in blue and are taken from references [52, 60, 61].

If this LUMO energy is plotted as a function of the emission energy of the linear complexes, this not only highlights the linear correlation between the copper complexes known from the literature[52,60,61], but also extrapolates the novel complex **33a** particularly well. The coefficient of determination of the linear regression is $R^2 = 0.996$. Even if the amount of data is only small, a clear trend can be seen here. A comprehensive theoretical study, which investigates the influence of the donor ligand in addition to various acceptor carbenes, is currently part of other doctoral projects in the Steffen Group. With this computer-assisted approach, new highly π-acidic carbenes can be identified *in silico*, vastly reducing the active space of compounds of interest. Although destabilisation of the electronic ground state by deformation in trigonal complexes leads to strong bathochromic shift, linear geometries a favoured going forward. Y–T-deformation, necessary for the afore mentioned red-shift, effectively couples vibrational modes with the emissive excited state, thus limiting quantum yields. It remains to be investigated whether the trigonal-planar geometry can be stabilised by using more sterically demanding and rigid bidentate ligands, and to what extent these modifications affect the emission efficiency and wavelength. Furthermore, decreasing vibrational coupling between excited and ground state leads to the suppression of non-radiative decay paths. This can be achieved either by (partial) deuteration or by rigidification. By

introducing strong cyclopentadienyl ligands, a bathochromic shift can be achieved, but unfavourable orbital symmetry, especially between the cp ligands and the metal centre, leads to inefficient phosphorescence with increasing donor strength. Even though steric demand is an important parameter to suppress structural distortion in the excited state, sterically overloaded cp ligands lead to rapid decomposition. Overall, a generally valid structure-property relationship could be used for the design of red–NIR emitting copper(I) carbene complexes and new systems could be established whose luminescence can be made more efficient and low-energy by further fine-tuning.

3 Merging CPL with Mechanoluminochromism

3.1 Mechanically Induced CPL by Chiral Anion Interaction

Introduction

Given the multitude of mechanisms giving rise to mechanoluminochromic behaviours, in this chapter focus was placed on two literature known copper-complexes as the basis for further investigations. In the monocrystalline phase, the biscarbene-copper complexes of Hupp *et al.* show a very weak (QY 4%) emission in the UV-blue range (λ_{max} = 393 nm). Mechnichal stimulus brings the PF_6 anions closer to the cationic Cu(I). In the excited state, this results in the formation of excimers by Cu-F interactions, which then show a very bright (QY 51%) yellow-orange luminescence (λ_{max} = 550 nm).[130] This corresponds to a change of over 7,000 cm^{-1}. In contrast to these

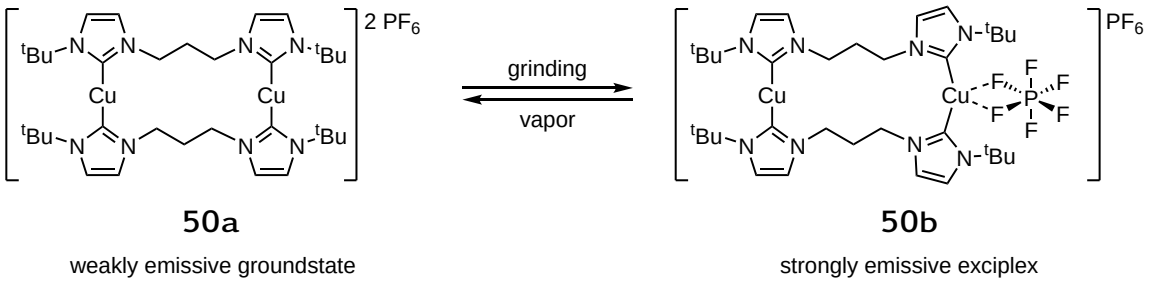

Scheme 3.1: Proposed formation of Cu-F-exciplex upon applying mechanical stimulus, according to reference [130].

excimers, Liske *et al.* found that in [Cu(IDipp)(^{R}py)](BF_4) complexes the practically non-emissive linear complex (extremely weak CT emission, λ_{max} = 460 nm) distorts towards a tetrahedral geometry upon stimulus due to the BF_4 anion stabily binding to the copper atom. In this new ground-state geometry intense blue-green emission is observed (QY 87%, λ_{max} = 455 nm).[131] Although there is no significant change in the emission wavelength (ΔE = 239 cm^{-1}), this system shows an enormous increase in quantum yield. The electronic environment at the copper centre can be used as an explanation for the drastically different causes of mechanoluminochromism. In the complexes of Hupp *et al.* , the copper atom has a very high electron density due to

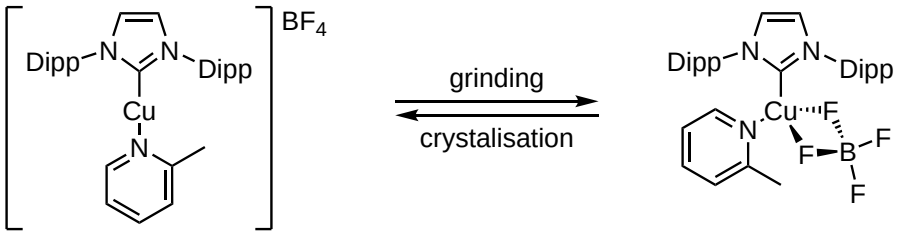

Scheme 3.2: Proposed formation of tetrahedral ground state upon applying mechanical stimulus, according to reference [131].

the two strongly σ-donating NHC ligands, and the s-d orbital mixing is also very pronounced (*vide supra*). In the excited state, the electron density is slightly reduced. This enables temporary coordination of the anion to the metal centre. The complexes of Liske *et al.* only have a σ-donating NHC and a significantly weaker pyridine donor. As a result, the electron density on the copper atom is considerably lower and s-d mixing (*vide supra*) is less pronounced, so that coordination can already occur even in the ground state. Based on these preliminary results, this chapter will investigate whether mechanoluminochromic complexes are formed by the introduction of chiral anions and whether these induce dissymmetry in the luminescence properties.

Results and Discussion

In the following, the [Cu(IDipp)(^{Me}py)] system from Liske *et al.*[131] is chosen as the test system and was prepared according to literature.[131]

In initial experiments, the double displacement reaction of **51a** with alkali metal salts of chiral anions was investigated (Scheme 3.3). However, the solubility of these salts is too low, making decomposition a dominating process, as solutions of **51a** appear to not tolerate moisture (waters of crystallization). Another concievable decomposition pathway might proceed by displacement of the pyridine ligand by the carboxylate/sulfonate anions, due chelating effects. Further research using salts with higher solubility, such as quartenary ammoinium salts, is needed and was not carried out due to time constraints.

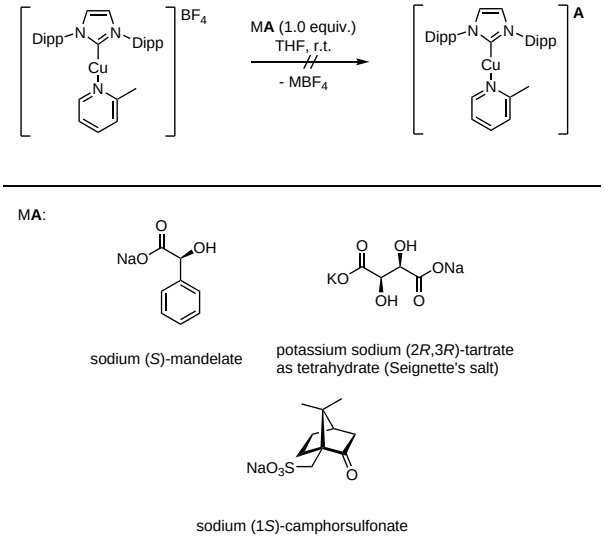

Scheme 3.3: First attempts of double displacement reaction using selcted chiral salts.

The positive experiences with anion exchange resins (*vide supra*) was investigated

as promising alternative to circumvent the lack of solubility instead. A setup was devised that can be used under both aqueous-aerobic and anhydrous-anaerobic conditions (Scheme 3.4). It consists of the barrel of a glass syringe with a Luer lock connection (A). A piece of PTFE tubing containing the anion exchange resin is connected via a Luer-Lock tube adapter (B) and a piece of glass wool (C) on both end to compress the resin. Another Luer-Lock tube adapter is used to attach a cannula to the lower end, which ends in a collection vessel (D). The aim is to carry out the loading

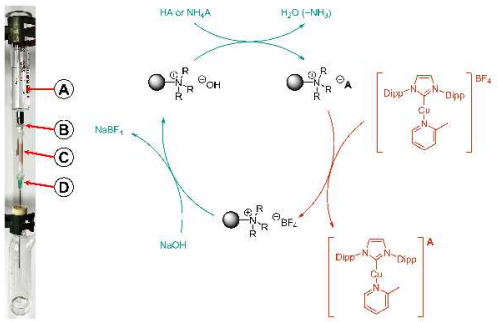

Scheme 3.4: Picture of the salt metathesis setup (left) and simplified scheme of the exchange cycle (right).

and recovery processes in aqueous solution (Scheme 3.4, turquoise) and, after suitable preparation, to perform the double displacement reaction under inert conditions in a glovebox (Scheme 3.4, orange), to minimize interference from waters of crystallization. For this a preliminary BF_4 ⟶ PF_6 exchange was executed to test the compatibility of linear copper complexes with the exchange resin, as the ^{19}F-NMR resonance can be used as a sensitive probe for the efficiency of the exchange. The ^{1}H-NMR spectra in

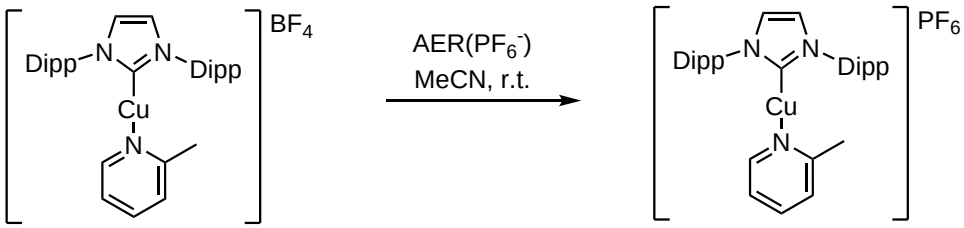

51a **52**

Scheme 3.5: Anion exchange of **51a** under anhydrous anaerobic conditions.

acetonitrile before and after passing through the exchange column show no differences apart from minor differences in the chemical shift (Fig. 3.1, a)). It can be assumed that these differences result from the slightly altered polarity, as residual traces of THF are detectable. Furthermore, there are no signs of decomposition.

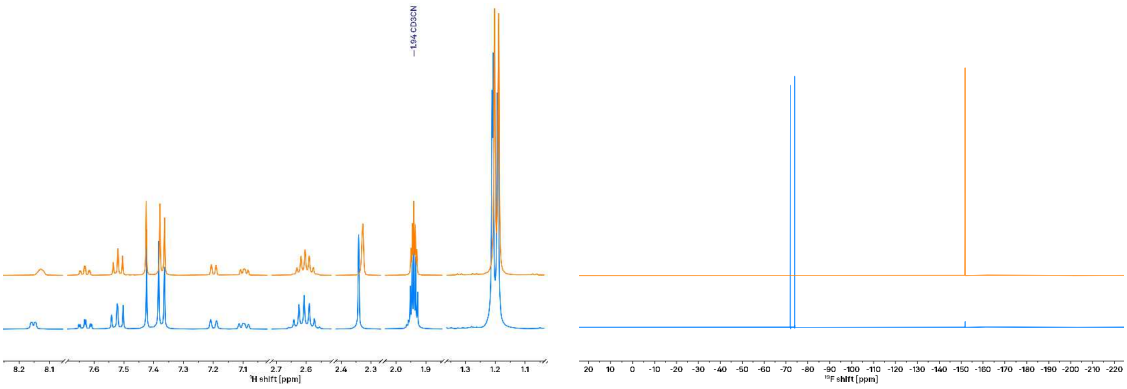

(a) (b)

Figure 3.1: ^{1}H- and ^{19}F-NMR-spectra of **51a** recorded in MeCN–d_3 before (orange) and after (blue) passing through an PF_6-loaded column.

The fluorine NMR spectrum shows a ratio of PF_6 : BF_4 = 20 : 1, deduced from integrals, corrisponding to a conversion of around 95%. Possible reasons for the incomplete conversion can be found in a too high flow rate or channel formation in the resin packing. Nevertheless, this experiment shows that the investigated copper complex is indeed stable on the AER under inert conditions and that the desired double displacement reaction takes place with high conversion. While this protocol can be used for strong mineral acids without further difficulties (*vide supra*), various difficulties arose when analysing organic acids, which will be discussed here. Both mandelic acid and tartaric acid are readily soluble in water, making the loading process (neutralization) sufficiently fast.

To limit the risk of incompatibility of **51a** and protic functionalities found in mandelic and tartaric acid, a benzoylated derivitive of the later (**54** is also included in the scope. Interestingly, all attempts of anion exchange with **51a** in different $MeCN/CH_2Cl_2$ mixtures[124] failed and the substrate was recovered unchanged. While the sizes of BF_4^- and PF_6^- anions are relatively similar and their polarity neglegible, the investigated organic acids are significantly bigger and much more polar. This leads to hindered mobility and stronger ionic interactions with the quatenary ammonium groups of the resin and might explain the insuficient reactivity. This theory aligns quite well with literatur, as Alcalde *et al.* report the anion exchange of polar ions to work best in polar-protic solvent slike methanol, while apolar anions tolerate less polar acetonitrile media.[124] Therefore attention was turned to the less polar water-insoluble chiral phosphoric acid ester (Fig. 3.2, **53**). Here, the

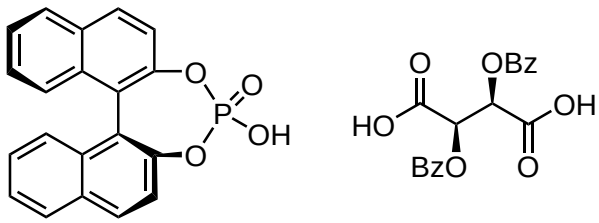

53 **54**

Figure 3.2: Chiral acids showing no satisfactory reactivity on basic anion exchange resin.

neutralisation reaction was investigated in different organic media of variing polarity, namely methanol, dmso, acetonitrile and mixtures thereof. However, like also previously reported[124], obmission of water leads to incomplete loading, due to the reduced acid strength and limited OH^--ion mobility in non-aqueous solution, no complete conversion can be achieved. It must also be taken into account that the released reaction water can lead to precipitation of the acid in the pores of the resin. At this stage, no successful synthesis strategy could be devised to introduce chiral anions into the investigated copper complex. However, as this is integral to the exploration of potential CPL mechanoluminochromism, new strategies are being developed.

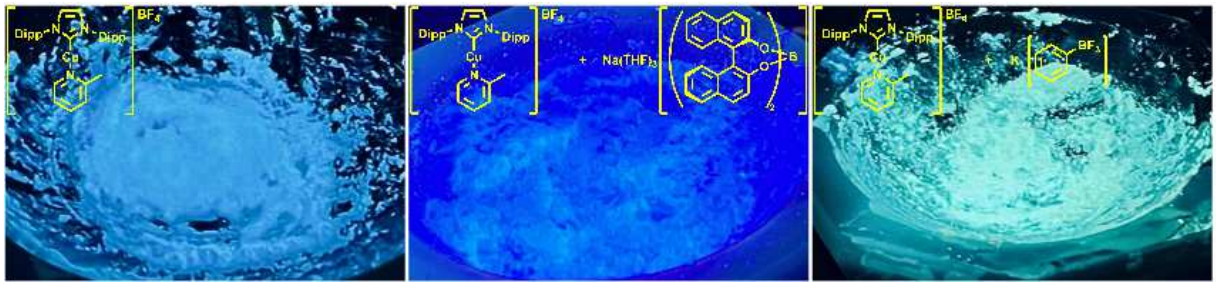

Figure 3.3: Pictures (from left to right) of **51b** (left), ground with **55** (middle) and $K[F_3BPh]$ under UV irradiation.

Hupp *et al.*were able to show that even grinding the native biscarbene copper complex with various alkali metal salts, e.g. $NaBPh_4$ and $Li[Al(OC(CF_3)_3)_4$, leads to a visible change in emission.[130] Since anions without obvious donor functionality, i.e. BPh_4, lead to a visible shift in emission, it can be assumed that in these cases exciplexes are induced via $\pi - \pi$ interactions and not by the involvement of the copper centre.

In a qualitative experiment, a sample of **51a** was first ground with the chiral borate $Na[B(BINOL)_2] \cdot 3\,THF$ (**55**) in the presence of a few drops of acetonitrile. The bright light blue emission of the **51b** (Fig. 3.3, left) changed to a dim blue-violet emission (Fig. 3.3, middle). Whether this is a new emission band or merely the fluorescence of **55** has currently not been investigated further. However, it can be assumed that the plausible donor atoms, the four oxygen atoms of the borate, are sterically shielded. A space-filling model of the anion clearly shows that Cu–O coordination would lead to increased steric pressure (Fig. 3.4). However, in a control experiment in which **51a** was ground with $K[F_3BPh]$, there was a visible bathochromic shift in the emission from light blue to green-blue (Fig. 3.3, right). It can therefore be concluded that BF_4^- anions

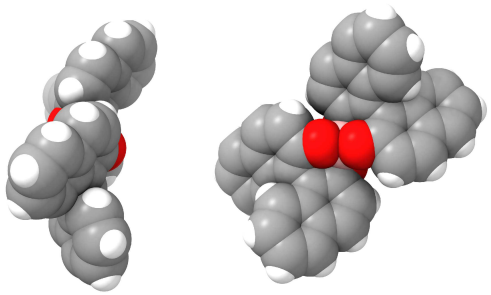

(a) (b)

Figure 3.4: Space-filling model of the $[B(BINOL)_2]^-$ anion **55**, viewed from the side (a) and the front (b).

are again partially displaced from the molecular bond by the formation of new Cu–F bonds and replaced by $PhBF_3^-$ anions.

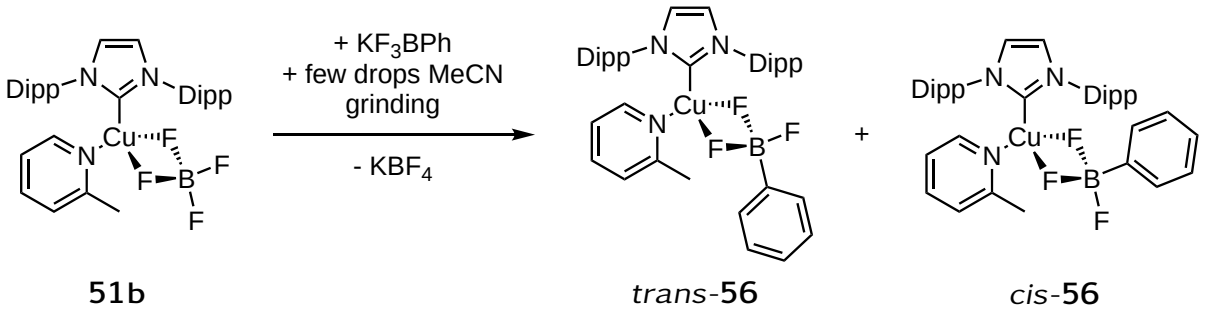

51b *trans*-**56** *cis*-**56**

Scheme 3.6: Proposed mechanism of anion displacement during grinding.

The different mechanism of mechanoluminochromism in the Liske system implies the need for (semi-)stable Cu-anion interactions to be accessible. In addition to the previously considered anions of chiral phosphoric acid **53** and benzoylated tartaric acid **54**, the following anions also represent promising candidates, as donor atoms are sterically accessible here and the necessary interactions are therefore plausible.

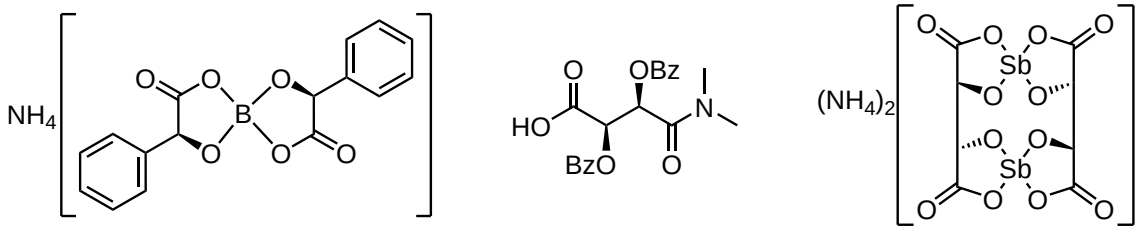

57 **58** **59**

Figure 3.5: Potential chiral compounds featuring multiple sterically accessible donation sites.

Antimonyl (L)-tartrate **59** in particular, which can be used for the efficient chiral resolution of optically active metal complexes by enantioselective crystallisation or ion chromatography[132–135], is a promising candidate by providing several sterically accessible donor atoms necessary for ion-interactions similar to the BF_4-analogues. It is chemically inert, can be freed of water of crystallization and has several sterically accessible donor atoms. The nearly isoenergetic orbitals HOMO–HOMO-3 form the non-bonding electron pairs of the four carbonyl functionalities. HOMO-4, which is only 0.01 E_h lower, is dominated by the free electron pairs of the oxygen and antimony atoms, whereby the latter are strongly orientated and therefore of particular interest for possible coordination. In a geometry optimisation (PBEh-3c) of a hypothetical $[Cu(IPh)(py)(Sb_2tart_2)]^-$ monoanion with κSb coordination and Cu–Sb bond length frozen at 3.80 Å, mean of covalence and vdW distances[125], however, a change

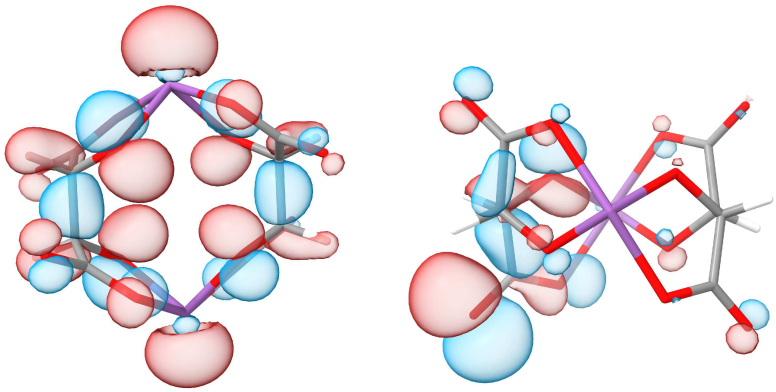

(a) (b)

Figure 3.6: Surfaceplots of **59**'s HOMO-4 (a) and HOMO (b).

in the coordination mode to a $\kappa^2 O$ coordination occurred, the coordination now takes place via a carbonyl oxygen atom and a hydroxyl function which is about 117 kcal/mol lower than the original Cu–Sb coordination.

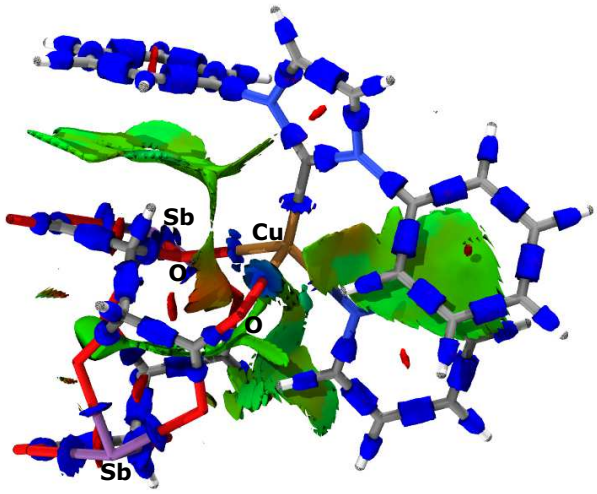

Figure 3.7: IRI-analysis of optimized $[Cu(IPh)(py)(Sb_2tart_2)]^-$ monoanion (PBEh-3c). For detail on IRI colour coding see Fig. 2.7.

In order to gain an insight into whether this change in coordination is also accompanied by the formation of non-covalent interactions, an IRI analysis was carried out on the final structure (Fig. 3.7). In fact, there are attractive interactions along the Cu–O path of similar strength as the Cu–NHC and Cu–py interactions. This implies a similar mode of coordination to known examples of chromium complexes.[132–135] In addition to $M[Cu(NHC)(py)(Sb_2tart_2)]$ ($M = Na, K, NR_4$), the electrically neutral $[(NHC)(py)Cu\{\mu\text{-}(Sb_2tart_2)\}Cu(NHC)(py)]$ is also possible, depending on the stoichiometry. Given the molecular orbitals of antimonyl tartrate, this bridged compound is conceivable as a stimulus responsive species and opens up access to exciton coupling, which can significantly increase the CPL intensity.[136]

Conclusion

It was not possible to synthesise pure copper complexes of the type [Cu(NHC)(py)]A*. Therefore mechanoluminochromic behaviours in relation to CPL could not be determinded. However we were able to demonstrate the unprecedented and unexpected stability of **51a** on non-aqueously conditioned anion exchange resins. This finding, albeit

only successfully demonstrated for a $BF_4 \rightarrow PF_6$ exchange, lays a important foundation for further investigations. Either by means of more carefully screening of possible loading and metathesis conditions, or by exploring different exchange resins. These anion exchange resins are available with different basic functionalities of varying base strength. In addition cation exchange resins like strongly acidic Amberlyst®-15 might be practical. The copper(I)-complex would be loaded onto the resin and be washed down with a solution of suitable chiral anion. If further practical and theoretical stud-

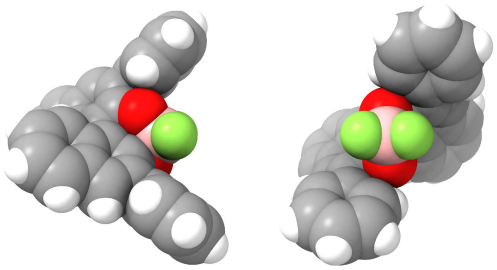

(a) **(b)**

Figure 3.8: Space-filling model of $[BF_2(BINOL)]^-$ anion, viewed from the site (a) and the front (b).

ies show that the formation of a Cu–F bond is of integral relevance for mechanoluminochromism, the BINOL-based borate $[BF_2(BINOL)]^-$ (Fig. 3.8) of the Arndtsen group, for example, will also be of increased interest.[137] Particularly in the space-filling model of the corresponding anion, the ligand atoms are much more accessible than in the $[B(BINOL)_2]^-$ anion, for example. In addition, π interactions of the phenyl groups with the copper complex are possible. This however was not further explored in this work due to time constraints.

3.2 "Towards Fast Circularly Polarized Luminescence in 2-Coordinate Chiral Mechanochromic Copper(I) Carbene Complexes"

The article *Towards Fast Circularly Polarized Luminescence in 2-Coordinate Chiral Mechanochromic Copper(I) Carbene Complexes* by Muthig *et al.* is reprinted in full from https://doi.org/10.1002/chem.202300946, used under CC BY-NC 4.0.
All syntheses and photophysical meausurements were performed by Dr. André Muthig as part of his PhD thesis *Nahinfrarote und Zirkular Polarisierte Lumineszenz von Donor-Kupfer(I)-Akzeptorkomplexen* at the TU Dortmund University in 2022 under the supervision of Prof. Dr. Andreas Steffen in corporation with Dr. Jacopo Tessarolo from the group of Prof. Dr. Guido Clever at TU Dortmund University. Single-Crystal diffraction measurements were performed and resolved by Dr. Stefan Koop and Carsten Lenczyk at TU Dortmund University. Written work was done mainly by Prof. Dr. Andreas Steffen. All authors contributed in proof-reading.
The own contribution consisted of performing and analysing quantum chemical calculations. As part of this, both time-dependent and independent density functional theory was applied to understand structural flexibility by means of conformer search as well as elucidating the excited state nature with special attention to the changes in electric and magnetic transition dipole moments.
Experimental contribution: ca. 15%
Written contribution: ca. 15%

Summary

Structure-property relationships for the design of efficient triplet emitters exhibiting circularly polarised luminescence are scarce despite their relevance for electroluminecent devices. A series of enantiopure copper(I) CAAC complexes with a variety of amide ligands as representatives of a class of highly efficient TADF emitters are studied. Influenced by the environment TADF from $^{1/3}$LLCT states and phosphorescence from ^{3}LLCT/ LC states can be observed with radiative rate constants in the range of $10^5\ s^{-1}$. Mechanochromic photoluminescence is observed in all compounds leading to a bathochromic shift and increased k_r in ground samples compared to the crystalline solid. This property is attributed to changes in intermolecular dipole-dipole interactions and large surface-to-volume ratio after stimulus application. Most studied compounds are not CPL active. Only the phenoxazine-bearing compound exhibits orange to deep red TADF with luminescence dissymmetry of $g_{lum} = -3.5 \cdot 10^{-3}$ by means of structural distortion in the excited state. Combined with limited rotation and inter-

molecular hydrogen-bonding between the ligand's oxygen atom and the PMMA matrix, the rotatory strength for the vertical transition is produced and is not available in carbazole analogues. This design motif gives rise to the first linear, non-aggregated CPL-active copper(I) complex with a high radiative rate constant of $6.7 \cdot 10^5\ s^{-1}$.

Towards Fast Circularly Polarized Luminescence in 2-Coordinate Chiral Mechanochromic Copper(I) Carbene Complexes

André M. T. Muthig,[a] Justin Wieland,[a] Carsten Lenczyk,[a] Stefan Koop,[a] Jacopo Tessarolo,[a] Guido H. Clever,[a] Benjamin Hupp,[a] and Andreas Steffen*[a]

[a] A. M. T. Muthig, J. Wieland, C. Lenczyk, S. Koop, Dr. J. Tessarolo, Prof. Dr. G. H. Clever, Dr. B. Hupp, Prof. Dr. A. Steffen
Department of Chemistry and Chemical Biology
TU Dortmund University
Otto-Hahn-Str. 6, 44227 Dortmund, Germany
E-mail: andreas.steffen@tu-dortmund.de

Supporting information for this article is given via a link at the end of the document.

Abstract: A series of chiral mechanochromic copper(I) cAAC (cAAC = cyclic (alkyl)(amino)carbene) complexes with a variety of amide ligands have been studied with regard to their photophysical and chiroptical properties to elucidate structure-property relationships for the design of efficient triplet exciton emitters exhibiting circularly polarized luminescence. Depending on the environment, which determines the excited state energies, either thermally activated delayed fluorescence (TADF) from $^{1/3}$LLCT states or phosphorescence from ^{3}LLCT/LC states occurs. However, neither chiral moieties at the carbene nor at the carbazolate ligands provide detectable luminescence dissymmetries g_{lum}. An exception is [Cu(phenoxazinyl)(cAAC)], showing orange to deep red TADF with λ_{max} = 601-715 nm in solution, powders and in PMMA. In this case, the amide ligand can undergo distortions in the excited state. This design motif leads to the first linear, non-aggregated CPL-active copper(I) complex with g_{lum} of -3.4·10^{-3} combined with a high radiative rate constant of 6.7·10^{5} s^{-1}.

Introduction

Circularly polarized luminescence (CPL) is a favorable tool for a variety of applications, including quantum computing,[1] cryptography,[2] spintronics,[3] chemical sensors,[4] biological probes[5] and display technologies.[6] The efficiency of a chiral molecular emitter for generating CPL with a defined handedness, i.e. the emission excess of photons with a spin-angular momentum of J_z = ±1, is typically quantified by the anisotropy factor g_{lum} and can reach maximum values of ±2, corresponding to purely left- or righthanded light, respectively. It is important to note that the dissymmetry of the radiative transition depends on the relative magnitudes of the electronic ($\vec{\mu}$) and magnetic ($\vec{m}$) transition dipole moment vectors, and the angle θ between them (Eq. 1).[7]

$$g = \frac{4 \cdot |\vec{\mu}||\vec{m}| \cos(\theta)}{|\vec{\mu}|^2 + |\vec{m}|^2} \quad (1)$$

Bearing in mind that $\vec{m}$ is often several orders of magnitude smaller than $\vec{\mu}$, and that the latter determines the radiative rate constant k_r, it becomes obvious that only electronic dipole forbidden transitions in chiral molecules can provide access to CPL. For example, high g_{lum} values > 1 have been reported for Laporte-forbidden f-f* transitions in lanthanide complexes,[8] while d-d* transitions in chiral octahedral Cr^{III} compounds can exhibit g_{lum} of up to 0.2.[9] However, implementation of these classes of CPL emitters in electrically driven luminescence applications that require triplet exciton emission, e.g. OLEDs, would lead to serious efficiency roll-offs and small external quantum efficiencies (EQE) due to their very low k_P < 50 s^{-1} for phosphorescence.[10] Archetypical molecular OLED emitters of the 4d and 5d elements have been found to display high k_P of 10^4-10^6 s^{-1},[11] but the dissymmetry factors g_{lum} of the majority of their chiral examples usually do not reach beyond g_{lum} = 10^{-4}-10^{-3}.[12] The only exception that we are aware of, showing remarkable g_{lum} of up to 1·10^{-2} combined with moderate k_p of 10^3-10^4 s^{-1}, is a family of chiral Pt^{II}-based complexes bearing helicene-type ligands.[13]

An interesting approach to bypass the dilemma of sacrificing a high k_r of triplet state emission for sufficiently high luminescence dissymmetries g_{lum} suitable for device applications would be the investigation of chiral thermally activated delayed fluorescence (TADF) emitters.[14] In contrast to spin-forbidden $T_1 \rightarrow S_0$ phosphorescence, this mechanism involves endothermic reverse intersystem crossing (rISC) $T_1 \rightarrow S_1$ with subsequent spin-allowed $S_1 \rightarrow S_0$ fluorescence. Although chiral luminophores with a high g_{lum} would exhibit low $\vec{\mu}$ for fluorescence, CP-TADF emission would still be faster than CP phosphorescence directly from T_1.

Various organic TADF emitters with chiral moieties or axial chirality have been studied and a few examples show g_{lum} of up to 1.8·10^{-2}.[15] Interestingly, the chiroptical properties of the fastest molecular TADF emitters to date with k_{TADF} reaching 10^5-10^6 s^{-1}, namely carbene coinage metal amides (CMA),[16–19,20] have not yet been reported. These linearly coordinated donor-M-acceptor (D-M-A, M = Cu, Ag, Au) type compounds exhibit ligand-to-ligand charge-transfer (LLCT) states with some metal-to-ligand (ML)CT admixture, which is most pronounced in copper(I) complexes. Consequently, they can benefit from rotation of the ligands and spin-orbit coupling (SOC) of the d^{10} metal centre, both factors greatly influencing ΔE(S$_1$-T$_1$) and k_{rISC} to provide high k_{TADF}.[18,21,22] Importantly, the torsion angle between the ligands also has an impact on $\vec{\mu}(S_1 \rightarrow S_0)$, and high-level quantum chemical (QC) calculations showed that k_F in CMAs varies between 10^4 s^{-1} for perpendicular orientation of the ligand planes to 10^7 s^{-1} for a coplanar arrangement.[23] Therefore, the specific structural features of CMA materials should allow control of their chiroptical properties as well. Very recently, Gong et al. discovered for some NHC-based chiral CMAs that their aggregation can give rise to luminescence dissymmetries with g_{lum} of 2.7·10^{-2} for one very specific single crystalline phase, while as monomers no CPL is observed.[24] However, this aggregation strategy is difficult to transfer into potential device applications.

The potential of molecular transition metal CP-TADF emitters has recently been demonstrated by our study on trigonally coordinated copper(I) carbazolate complexes bearing chiral (S/R)-BINAP ligands, which show efficient TADF with k_r of 3·10^5 s^{-1} combined with high g_{lum} of ±7·10^{-3} in solution and up to ±2.1·10^{-2} in the solid state.[25] The efficiency of the TADF process depends on the environment, but careful choice of the matrix materials allowed for successful implementation in CP-OLEDs. Given our long-

standing interest in d^{10} coinage metal emitters,[26,27] in particular copper(I) carbene TADF complexes,[17,28] we decided to investigate the chiroptical properties of a series of linearly coordinated [Cu(amide)(cAAC)] complexes (cAAC = cyclic (alkyl)(amino)carbene) featuring a D-M-A structure with chiral moieties either at the electrophilic carbene ligand or at the amide donor. Although CPL is not detectable for most CMA compounds, we find that [Cu(PZN)(cAAC^{Ment})] (PZN = phenoxazinyl) is an efficient orange-red triplet exciton emitter with high k_{TADF} = 6.7·10^5 s^{-1} and g_{lum} = 3.4·10^{-3} in PMMA films. The hindered ligand rotation in the rigid matrix in combination with a butterfly distortion of the PZN ligand, that is not available to the carbazolate donor ligands, appears to be responsible for the CP-TADF properties of the copper(I) carbene complex.

Results and Discussion

Synthesis and Structural Characterization.
The air- and moisture-sensitive chiral copper(I) cAAC amides **1-8** were prepared according to an established route by reaction of the corresponding potassium salt of the respective *N*-ligand with [CuCl(cAAC^R)] in THF at RT (Scheme 1).[16,18] While the precursor [CuCl(cAAC^{Me})] is available via the free carbene route,[26] its menthone derivative was obtained by treatment of cAAC^{Ment}·HCl with mesityl copper (see ESI). We isolated **1**-**8** as orange to green powders, which were characterized by multinuclear NMR spectroscopy, elemental analysis and mass spectrometry. However, the 11*H*-benzo[*a*]carbazolate compound **5** turned out to be unstable for further analysis even in the single-crystalline solid state, but its connectivity could be confirmed (Figure S2).

Comparison of the structural information obtained from single crystals of **3** and **6-8** suitable for X-ray diffraction analysis shows that a nearly ideal linear coordination geometry is favored (Figure 1 and Table S1). Substitution in the 2-position of the Cbz leads to deviations of the dihedral angle γ between the N-donor and carbene acceptor ligand planes, reaching a maximum of ca. 24° for **7**. As reported for some other d^{10} coinage metal carbazolates, we observe a tilting of the Cbz towards the cAAC that is most pronounced for [Cu(Cbz^{OMe})(cAAC^{Ment})] (**3**) with β = 153.17(9)° (Figure 1). The rationale behind these structural peculiarities is not clear and certainly involves electronic and steric effects, such as C(carbene)–M–N π conjugation and rehybridization of the ipso-*N*, but also packing effects in the solid state.[25] However, as demonstrated by the group of Marian,[14,23] the dihedral angle γ is the most important structural feature determining the efficiency of TADF in such D–M–A compounds.

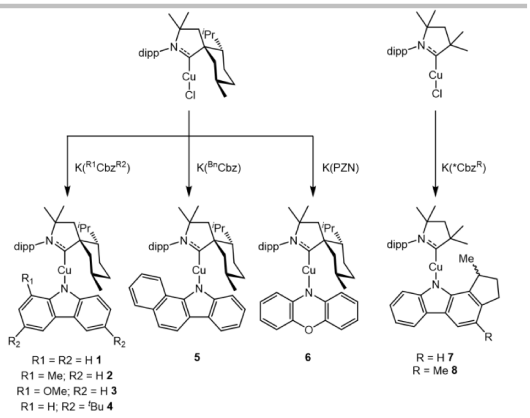

Scheme 1. Synthetic routes towards chiral [Cu(amide)(cAAC^R)] **1**-**8**.

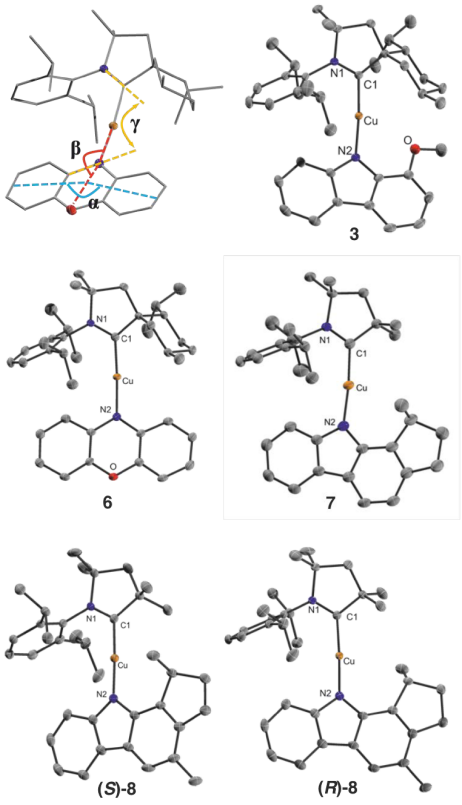

Figure 1. Molecular structures obtained by single crystal X-ray diffraction and depiction of important angles α, β and γ with values [in deg] for **3**: 173.82(5), 153.17(9), 12.58(19); for **6**: 173.43(9), 165.43(11), 0.4(3); for **7**: 178.75(7), 174.6(1), 24.3(2); for **8**: 176.84(9), 167.01(10), 21.4(2).

We note that **6** is less distorted, with γ = 0.4(3)° and a butterfly angle between the two aromatic planes of the amide ligand of only α = 173.43(9)°, than found for [Au(PZN)(cAAC^{Ad})] with 160.5(3)° and 21.1(4)° for α and γ, respectively (vide infra).[18] It is important to note that our NMR studies suggest that free rotation occurs in solution at room temperature, as only half as many signals as expected are found in the ^{1}H and ^{13}C NMR spectra for the symmetrical *N*-donor ligands of **2**, **4** and **6**. An alternative explanation is that the chiral cAAC^{Ment} does not influence the *trans* ligand, however, dynamical rotation processes occurring with low activation barriers at room temperature have previously been reported for structurally related carbene complexes. Thus, the degree of flexibility facilitated by the environment should greatly influence the electronic communication between the donor and acceptor ligand and, consequently, the excited state behavior of the CT states.

Photophysical Studies.

The UV/vis absorption spectra of the chiral copper(I) carbazolate complexes **1-4** and **6-8** in THF are very similar to those of previously reported structurally related CMAs and show intense high energy MLCT and ππ* transitions of the *N*-Dipp substituent between λ = 250-320 nm (Figure 2, Figures S15 and S16).[16,19] The vibrationally resolved band at λ = 320-375 nm (ε = 5-8·10^{3} M^{-1}cm^{-1}) is typical for LC(ππ*) states of the Cbz-type ligands (Figure 3). A very broad and moderately intense (ε = 4-6·10^{3} M^{-1}cm^{-1}) low energy absorption, with λ_{max} varying between 370-400 nm in dependence of the Cbz substitution and overlapping with the LC(Cbz) band, can be assigned to the $S_0 \rightarrow S_1$ transition of dominantly LL(Cbz→cAAC)CT character with some ML(Cu→cAAC)CT admixture according to our TD-DFT calculations (Figures 3 and S16). The $S_0 \rightarrow S_1$ transition of [Cu(PZN)(cAAC^{Ment})] (**6**), which we conclude to be LL(PZN→cAAC)/MLCT in nature, is also very broad but significantly bathochromically shifted to λ_{max} = 475 nm. In contrast to the Cbz localized ππ* bands, the LC(PZN) band at λ_{max} = 350 nm is broad and apparently contains an intraligand (IL)CT contribution.

The carbazolate compounds **1-4, 7** and **8** exhibit bright green luminescence in THF at room temperature with a broad spectral appearance indicative of LLCT states (Table 1 and ESI). The combination of moderate to high quantum yields ϕ = 0.36-0.88 and high radiative rate constants k_r of ca. 3-4·10^{5} s^{-1} are the result of an efficient TADF process as described by Thompson et al. for structurally related copper(I) complexes, and is highly environment sensitive.[16] In general, the emission wavelengths found in flexible polar media undergo a hypsochromic shift in rigid polar matrices, e.g. microcrystalline solid state or PMMA, as depicted in Figure 4 for [Cu(*Cbz^{Me})(CAAC^{Me})] (**8**) (see also Table 1 and ESI). Interestingly, upon grinding the crystalline material, the emission again shifts bathochromically.

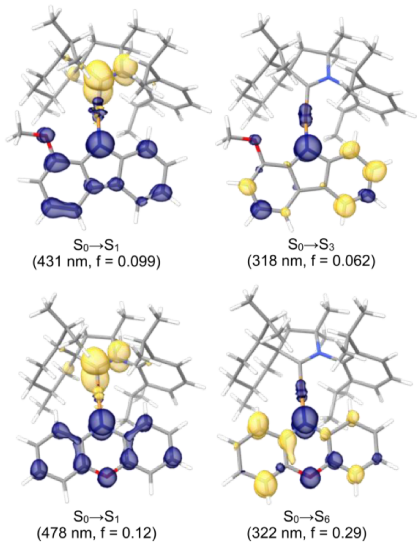

D3(BJ)-PBE0/ZORA/def2-SVP level of theory. Loss of electron density is indicated in blue and gain in yellow.

Figure 3. Selected electron density differences (isovalue ±0.005) relevant for the experimental absorption spectra of **3** (top) and **6** (bottom) in THF calculated at the

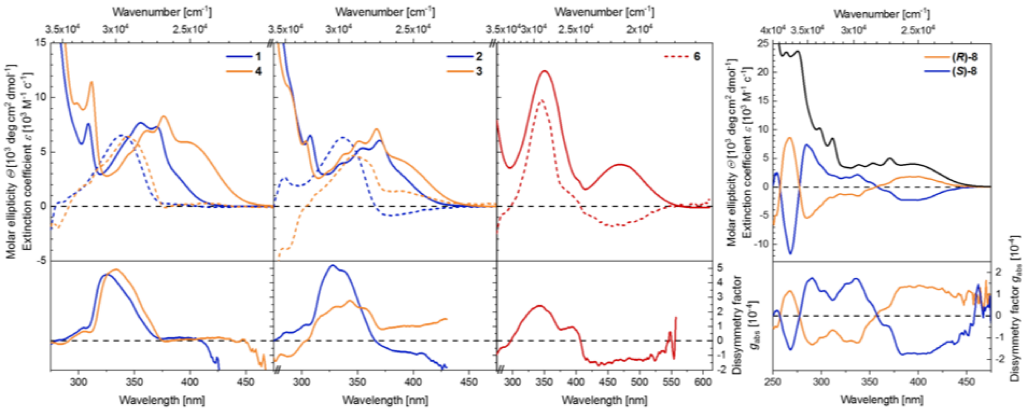

Figure 2. Absorption(solid) and ECD (dashed) spectra of **1**-**4**, **6** and **(*S*/*R*)-8** recorded in THF (c = 10^{-5} – 10^{-4} mol L^{-1}) at room temperature.

Table 1. Selected photophysical data of the chiral copper(I) complexes **1-4** and **6-8** recorded in the solid state at room temperature. For biexponential lifetime decays, the relative pre-exponential factors are given in parentheses.

	Medium	λ_{em} [nm]	τ [µs]	$^a\phi$	k_r [10^4 s^{-1}]	k_{nr} [10^4 s^{-1}]		Medium	λ_{em} [nm]	τ [µs]	$^a\phi$	k_r [10^4 s^{-1}]	k_{nr} [10^4 s^{-1}]
1	THF	509	2.7	0.88	32	4.4	**6**	THF	715	0.032	0.01	31	3069
	Crystal	466	25.6 (72)/ 86.4 (28)	0.12	0.28	2.1		Toluene	698	0.048	0.01	21	2079
	Ground	492	4.8 (90)/ 34.2 (10)	0.44	5.6	7.1		Crystal	553	0.26 (13)/ 1.0 (88)	0.72	79	31
	PMMA	472	6.8 (90)/ 31.5 (10)	0.53	5.8	5.1		Ground	635	0.09 (46)/ 0.25 (54)	0.12	70	513
2	THF	537	1.5	0.47	31	35		PMMA	601	0.16 (20)/ 0.53 (60)/ 1.0 (20)	0.29	67	164
	Crystal	476	2.3 (76)/ 5.6 (24)	0.15	4.9	28	**7**	THF	530	1.6	0.52	33	30
	Ground	503	1.5 (95)/ 4.1 (5)	0.37	23	39		Crystal	440	1.1 (76)/ 2.3 (24)	0.27	20	54
	PMMA	485	1.0 (93)/ 7.1 (7)	0.39	26	41		Ground	490	1.8	0.45	25	31
3	THF	540	0.86	0.38	44	72	**8**	THF	550	1.3	0.36	28	50
	Crystal	490	2.1 (88)/ 4.8 (12)	0.01	0.41	41		Crystal	470	2.1 (76)/ 4.1 (24)	0.33	11	22
	Ground	513	1.9 (91)/ 5.5 (9)	0.21	9.3	35		Ground	505	1.9	0.63	33	19
	PMMA	484	2.2 (90)/ 7.2 (11)	0.65	24	13		PMMA	498	1.8 (84)/ 4.8 (16)	0.13	5.7	38
4	THF	537	1.8	0.65	36	19							
	Ground	519	1.8	0.91	51	5.0							
	PMMA	485	3.2 (90)/ 15.7 (10)	0.13	2.9	19							

[a]Error margin ±0.02.

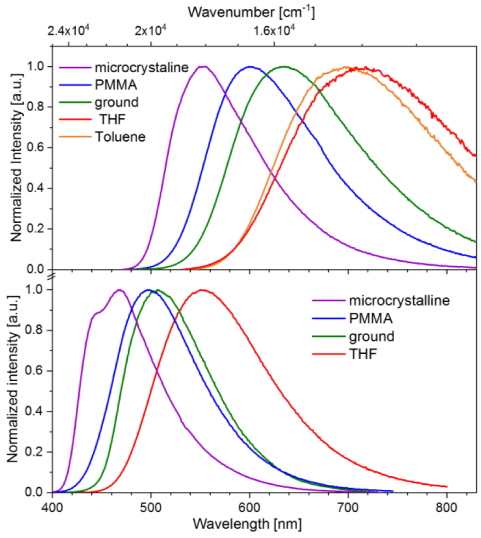

Figure 4. Normalized emission spectra of **6** (top) and **8** (bottom) in various media under argon at room temperature.

Theoretical work by Marian suggests that the ground state S_0 of CMAs is more polar than the LLCT excited state and the respective static electric dipole moments point in opposite directions.[16,17,23] Since a rigid polar environment cannot reorganize to acknowledge the new dipole moment of the excited species, the $^{1/3}$LLCT states are then more destabilized than in fluxional media and thus higher emission energies are observed. The emission in polar THF solution, which can readjust its dipole orientation on the timescale of the excited state lifetime, is further shifted bathochromically due to destabilization of the ground state at the reorganized LLCT geometry and its environment within the Franck-Condon principle. In contrast, the $^{1/3}$LLCT states of the Cu^I complexes in the ground samples experience a smaller destabilization by the environment, i.e. the surrounding complex molecules that remain in their S_0 state. We attribute this finding to partial disruption of the crystalline order and a larger surface-to-volume ratio upon grinding, increasing the number of surface molecules that influence the photophysical properties of the macroscopic sample. Both effects decrease the destabilizing influence of the dipole-dipole interactions mentioned above, and thus give rise to a bathochromic shift compared to the single crystalline solid state.

In other media than THF, the chiral copper(I) complexes **2-4**, **8** and racemic **7** show higher k_r in comparison to [Cu(Cbz)(cAAC^{Ment})] (**1**), which can vary by two orders of magnitude between 10^3–10^5 s^{-1} at room temperature in dependence of the environment, with a record within this series of k_r = $5.1 \cdot 10^5$ s^{-1} resulting in ϕ = 0.91 for [Cu(Cbz^{tBu})(cAAC^{Ment})] (**4**) in the ground solid. The substitution patterns at the *N*-donor ligand also lead to significantly higher rate constants for non-radiative decay k_{nr} on the order of 10^5 s^{-1}, giving quite diverse ϕ between 0.01-0.91 (Table 1).

The changes in k_r and k_{nr}, and thus in ϕ, do not follow any obvious trend but rather seem to be the result of a combination of various effects. While free rotation and other reorganisation processes of the

Cbz ligand allow for facile ISC and rISC that are paramount for efficient TADF, rigidification can hamper this mechanism.[22] Furthermore, the polarity of the environment has a large influence on the energy gap between the LLCT and LC states, which determines on the one hand the nature of the emitting states, but on the other hand the operative SOC and thus the efficiency of spin-forbidden processes.[29] We also note that the copper(I) carbazolate complexes experience diverse specific environments in the single crystalline solid state because of their different space groups, which also influence the respective dipole interactions between the complex molecules. As a result, these combined parameters can even switch the emission from TADF to dominantly phosphorescence from the ^{3}LLCT state with weak SOC as is evident from the broad spectral appearance and low k_r of **2** ($4.9\cdot10^4$ s^{-1}) and **3** ($4.1\cdot10^3$ s^{-1}) in crystalline samples, or **4** ($2.9\cdot10^4$ s^{-1}) and **8** ($5.7\cdot10^4$ s^{-1}) in PMMA.

Shifting the $^{1/3}$LLCT states to lower energy by introduction of a stronger *N*-donor in [Cu(PZN)(cAAC^{Ment})] (**6**) gives rise to efficient TADF in rigid environments, with very high k_r of up to $7.9\cdot10^5$ s^{-1} and concomitant ϕ = 0.79 in crystalline material (Table 1). We note that previously reported [Cu(PZN)(cAAC^{Ad})] is too weak an emitter for determination of k_r, while its heavier congener [Au(PZN)(cAAC^{Ad})] exhibits k_r of only 0.4-$2.2\cdot10^5$ s^{-1}.[18] As such, **6** is in general amongst the most efficient copper(I)-based triplet exciton emitters and even rivals the k_r of structurally related gold(I) cAAC amides, underlining the potential of earth abundant 3d elements for photoactive materials. Increasing λ_{max} from 553 nm in the single crystals to 601 and 635 nm in PMMA and the ground material, respectively, leads to more pronounced non-radiative decay and ϕ = 0.12 as a result of Siebrand´s rule, which states that vibrational overlap and k_{nr} increase with decreasing energy gap between the excited state and the ground state.[30] The bathochromic shift even in rigid environments is much more severe for **6** than observed for the other investigated CMA compounds.

In solution, the emission shifts even further to lower energies with emission maxima at 698 and 735 nm in toluene and THF, respectively. High k_r of 2–$3\cdot10^5$ s^{-1} typical for TADF are maintained, but the energy-gap law and increased structural flexibility leads to enhanced radiationless deactivation of the excited states.

Chiroptical Analysis.

The chiral copper(I) complexes described above feature efficient TADF in THF solution from the lowest energy ^{1}LLCT state. In this scenario, we expect the measured dissymmetry of the lowest energy absorption band g_{abs} (Eq. 2) to be of the same order of magnitude as the g_{lum} of the triplet exciton emission.[31] Therefore, we first analyzed the circular dichroism of the $S_0\rightarrow S_1$ transition to relate the chiroptical properties to the structural peculiarities of the ground state (Figure 2 and ESI). Important data obtained from Eqs. 1 and 2 that connect the measured dissymmetry with the electronic ($\vec{\mu}$) and magnetic ($\vec{m}$) transition dipole moments, and the angle θ between their vectors, are given in Table 2.

$$g_{\mathrm{abs}} = \frac{\Delta\varepsilon}{\varepsilon} = \frac{\varepsilon_L - \varepsilon_R}{\frac{1}{2}(\varepsilon_L + \varepsilon_R)} \qquad (2)$$

Table 2. Chiroptical properties of the $S_0\rightarrow S_1$ transition of **1-4**, **6** and **(*S*/*R*)-8** in THF solution.

	λ_{max} [nm]	ε [M^{-1} cm^{-1}]	FWHM [cm^{-1}]	f	$\lvert\vec{\mu}\rvert$ [D]	g_{abs} [10^{-4}]	$\lvert\vec{m}\rvert\cos(\theta)$ [10^{-3} μ_B]
1	370[a]	4500[a]	3200[a]	0.061	2.2	0.2	1
2	375[a]	4000[a]	3200[a]	0.055	2.1	0.9	5
3	385[a]	4600[a]	3500[a]	0.070	2.4	-1.0	6.4
4	395	5900	3600[a]	0.091	2.8	0.1	0.7
6	470	3850	3600	0.059	2.4	-1.0	6.6
(*S*)-8	395	4000	3600	0.061	2.3	-1.7	10
(*R*)-8	395	4000	3600	0.061	2.3	1.4	8.6

[a]Data approximated due to partial overlap of the $S_0\rightarrow S_1$ transition with the absorption band of the LC($\pi\pi^*$) state of the Cbz ligand.

The g_{abs} values increase by ca. one order of magnitude from $2\cdot10^{-5}$ and $1\cdot10^{-5}$ for **1** and **4** with symmetric carbazolate ligands, respectively, to $9\cdot10^{-5}$ and $1.0\cdot10^{-4}$ for compounds **2** and **3** bearing asymmetric carbazolates. For the **(*R*/*S*)**-enantiomers of **8** we find g_{abs} of $1.4\cdot10^{-4}$ and $-1.7\cdot10^{-4}$, respectively, while the LLCT band of the PZN compound **6** at 475 nm exhibits g_{abs} = $1.0\cdot10^{-4}$. Surprisingly, there seems to be no direct correlation between ε_{max} of the LLCT band and its g_{abs} value, implying that either $\lvert\vec{m}\rvert$ or $\cos(\theta)$ also varies. Since the oscillator strength f can be obtained from the experimental data and is directly related to the electronic transition dipole moment $\lvert\vec{\mu}\rvert$ via

$$f_{1,0} = \frac{4\varepsilon_0 \cdot m_e \cdot c^2 \cdot \ln(10)}{N_A \cdot e^2} \cdot \int \varepsilon(\tilde{\nu}) d\tilde{\nu} = \frac{8\pi^2 \cdot m_e \cdot c}{3h \cdot e^2} \cdot \tilde{\nu}_{max} \cdot \mu^2_{1\leftarrow 0} \qquad (3)$$

with the integrated transition intensity being approximated by $\pi/2\cdot\varepsilon_{max}\cdot\Gamma$ (Γ = full width at half maximum),[32] we could estimate the product of $\lvert\vec{m}\rvert\cos(\theta)$ using Eq. 1.

While f and $\lvert\vec{\mu}\rvert$ for our complexes are in line with earlier published data (f ≈ 0.1 and $\lvert\vec{\mu}\rvert$ ≈ 3 D) obtained from QC calculations,[16] the values of $\lvert\vec{m}\rvert\cos(\theta)$ vary greatly from only $0.7\cdot10^{-3}$ μ_B for **4** to $10\cdot10^{-3}$ μ_B for **8**. It is reasonable to assume that the decreased "kink" angle β or the increased torsion angle γ between the amide and carbene ligands are generally responsible for enhancing $\lvert\vec{m}\rvert\cos(\theta)$ as the PZN ligand and substitution in the 1-position of the Cbz are obviously advantageous for the dissymmetry. Since $\cos(\theta) < 1$, the minimum value we deduce for $\lvert\vec{m}\rvert$ of the ^{1}LLCT is $6.6\cdot10^{-3}$ μ_B, which is relatively small compared to, e.g., f-f* transitions in lanthanide complexes ($\lvert\vec{m}\rvert$ ≈ 0.2 μ_B) or the absorption in chiral knot copper(I) complexes reported by Meskers and co-workers ($\lvert\vec{m}\rvert$ ≈ 0.5 μ_B).[33,34] However, we note that on the one hand the structural flexibility in solution can have a drastic effect on the relative orientation of $\vec{\mu}$ and $\vec{m}$, but on the other hand it also allows for beneficial high k_r (vide supra).[17,23]

Studies on the circularly polarized triplet emission of copper(I) complexes are scarce and recently, linearly coordinated C_1-symmetric [CuCl(cAAC^{Ment})] has been reported by Ung et al. to show g_{lum} = $1.3\cdot10^{-3}$ for yellow luminescence with λ_{max} = 555 nm and ϕ = 0.018 in THF solution.[35] In order to ensure comparability of data, we

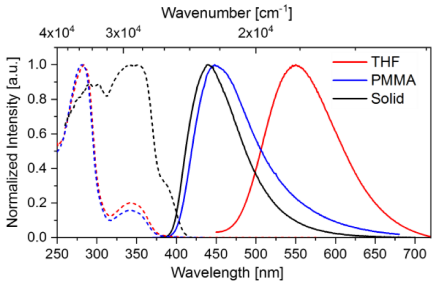

reinvestigated that compound with our instrumental set-up and obtained dissymmetry values for the absorption of g_{abs} = 2.6·10^{-3} (Figure S13), similar to the data we extract from the $\Delta\varepsilon$ and ε plots given in the ESI of Ung et al. of 3.4x10^{-3}. Also, the dissymmetry values for the emission at concentrations of 1-4·10^{-4} M could be confirmed. However, a significant hypsochromic shift of the emission to λ_{max} = 450 nm is observed in PMMA and in the solid state that is more in line with our own studies on structurally related [CuX(cAAC^{Me})] complexes, arguing for excimer formation in solution (Figure 5).[26]

Figure 5. Normalized excitation (dashed) and emission (solid) spectra of [CuCl(cAAC^{Ment})] in THF, PMMA and in the solid state at room temperature, indicating excimer formation in solution.

Indeed, the quantum yields are enhanced to 0.12 upon increasing the concentration to 4·10^{-4} M, which suggests reduced non-radiative decay due to higher rigidity of the excited state. Furthermore, Thompson et al. have previously demonstrated that copper(I) cAAC halide complexes are prone to excimer and exciplex formation in non-coordinating and coordinating solvents, respectively, leading to severe bathochromic shifts from blueish-green to orange, which is hindered in rigid matrices.[36] Since [CuCl(cAAC^{Ment})] shows identical emission spectra and g_{lum} in concentrated benzene and in THF solutions (5·10^{-3} M),[37] we thus conclude that the CPL detected for [CuCl(cAAC^{Ment})] most likely originates from a dimeric species with a {Cu(μ-Cl)$_2$Cu} core, i.e. trigonally coordinated Cu^{I} ions, and not linearly coordinated monomers.

We were therefore curious to study the CPL properties of our linearly coordinated copper(I) amide compounds, but unfortunately the g_{lum} of the Cbz complexes in THF solution as well as in PMMA matrices is below the detection limit of our instrument (<1·10^{-3}). Actually, this finding coincides with the obtained low values for g_{abs} of the ^{1}LLCT states, which are responsible for the TADF process (Table 2). In contrast, and counterintuitively, [Cu(PZN)(cAAC^{Ment})] (**6**) exhibits g_{lum} = -3.4·10^{-3} for triplet exciton emission in PMMA (1-2.5 wt%) (Figure 6), but not in other media. Optical artefacts, which might derive from linear dichroism and birefringence, were further excluded by measurement of several angles and positions of the films. It is important to note that the CPL of [Cu(PZN)(cAAC^{Ment})] (**6**) is similar to other chiral organic TADF emitters,[38] but combines the relatively high dissymmetry with higher k_r of nearly 7·10^5 s^{-1} in the red region of the electromagnetic spectrum (Table 1). Furthermore, the circular polarisation brightness $B_{CPL} = \varepsilon \cdot \phi \cdot g_{lum}/2$ of 1.9 M^{-1}cm^{-1} is similar to other CPL emitting materials, and even better than obtained for most Ir^{III}- and Pt^{II}-based triplet emitters featuring comparable k_r,[39] highlighting the potential of linearly coordinated copper(I) TADF emitters for this purpose.

Figure 6. Normalized emission spectrum (dotted red), CPL spectrum (solid red) and corresponding g_{lum} values (grey) of [Cu(PZN)(cAAC^{Ment})] (**6**) in PMMA at room temperature.

The origin of the CPL performance of **6** in comparison to the other CMA compounds must be related to the specific excited state structure and coupling with energetically higher lying states, which should depend on the limited geometrical reorganisation in PMMA as a rigid polar environment (*vide supra*). This can be concluded from the fact that CD measurements of **6** in PMMA films provide g_{abs} similar to those in THF (1.0·10^{-4}), and one order of magnitude smaller

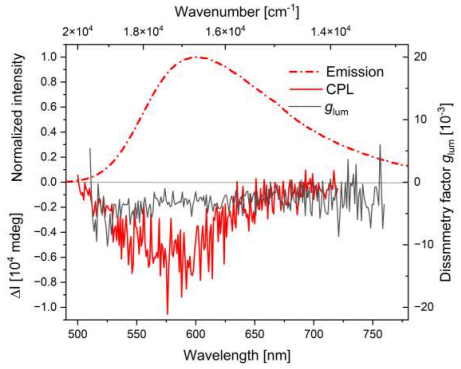

than the g_{lum}, which suggests negligible rotatory strength *R* of the ^{1}LL(PZN→cAAC^{Ment})CT transition at the ground state geometry. In addition, a "chaotic" reorganisation process is indicated by the three lifetime components necessary to fit the time-resolved luminescence decay. The increasing g_{lum} observed at higher emission energies (5·10^{-3} at 520 nm) indicates that more destabilized and less reorganised conformations exhibit enhanced *R*.

If indeed the reduced reorganisation in PMMA is responsible for the high g_{lum}, it does not at the same time decrease k_r significantly in comparison to other media (see Table 1). This beneficial result might be due to one of the following two extreme scenarios within the TADF scheme or, more likely, a combination of both: 1) as g_{lum}^2 scales with k_F^{-1}, a higher k_{RISC} might compensate a decreased oscillator strength $f(S_1 \rightarrow S_0)$, or 2) the product $|\vec{m}| \cdot \cos\theta$ is increased. Assuming for the first case $k_{RISC} >> k_F$, and therefore $k_r \approx k_F$, a maximum possible value of $|\vec{m}| \cdot \cos\theta$ = 0.046 μ_B for $S_1 \rightarrow S_0$ is obtained using Eqs. 1 and 3, with k_F = 6.7·10^5 s^{-1} and $\tilde{\nu}_{max}$ = 19,000 cm^{-1} providing f = 0.0022 and $|\vec{\mu}|$ = 0.50 D for the ^{1}LLCT emission. Regarding the second possibility, we use $|\vec{\mu}|$ = 2.4 D of the $S_0 \rightarrow S_1$ absorption band, which then yields f = 0.05, and Eq. 1 with $|g_{lum}|$ = 0.0034 provides a magnetic transition dipole moment of $|\vec{m}| \cdot \cos\theta$ = 0.22 μ_B. In both extreme cases, i.e. either minimized $k_r(S_1 \rightarrow S_0)$ or maximized $|\vec{m}| \cdot \cos\theta$, the latter is greatly increased in comparison to the estimated value of the absorption process of 0.0066 μ_B (vide supra). This result appears indeed realistic, in particular if $\cos(\theta) \approx 1$, considering that for a similarly sized [Cu(phen)$_2$]$^+$ complex a value of 0.5 μ_B was found for $|\vec{m}|$.[34]

Large differences between the dissymmetry values *g* in solution and rigid media are often explained with aggregation or excimer formation of emitter molecules.[40] These effects have been described in detail to be of importance for planar Pt^{II} complexes and extended (organic) π-systems, and can lead to greatly enhanced g_{lum}.[12] An interesting behavior was also reported by Wang et al. for highly ordered assemblies of a non-planar phosphorescent Cu^{I} complex, showing negligible CPL in DMSO suspension, but increasing g_{lum} values of 5·10^{-3} for films and 1·10^{-2} for microcrystalline solid state.[41] A similar behavior was also found for aggregated chiral NHC copper(I) amide complexes.[24] However, for [Cu(PZN)(cAAC^{Ment})] (**6**) we exclude excimer formation or aggregation being responsible for the remarkable g_{lum} in PMMA due to the low concentration of the dopant of 1 to 2.5 wt%, and the emission and excitation parameters do not show typical signs for such processes.

Besides restricted reorganisation in PMMA, either a butterfly or a "kink" angle distortion of the PZN ligand in the excited state can also provide a mechanism to enhance the rotatory strength of the transition. A butterfly distortion of the more rigid Cbz ligands in **1-4**,

7 and **8** would be hindered, while the excited state structure in CMAs is typically coplanar,[17,23] which could thus further explain the inefficiency of CPL in such compounds. Also, the polar matrix PMMA could support distortions by hydrogen bonding to the oxygen of the PZN ligand, an interaction mechanism that would also not be available for the Cbz ligands.

An indication of a possible environment dependent distortion is provided by our DFT/TD-DFT calculations on **6** in the gas phase, showing that the rotatory strength *R* of the vertical transitions between the ground state S_0 and the S_1 state are very structure sensitive (Figure 7).

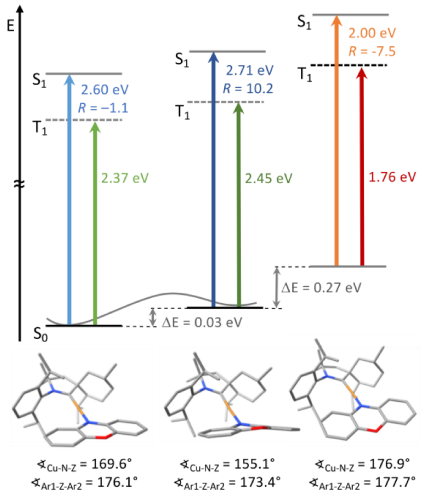

Figure 7. TD-DFT (D3BJ-PBE0/ZORA/def2-SVP) calculated vertical transitions of [Cu(PZN)(cAAC^{Ment})] (**6**) from the DFT (D3BJ-PBE0/ZORA/def2-TZVP) optimized geometries of the ground state S_0 (left and middle), and from S_0 at the optimized T_1 geometry (right). *Z* denotes the centroid of the amide ligand, while Ar1 and Ar2 denote their two arene rings. Rotatory strengths *R* given in 10^{-40} cgs.

The lowest energy conformation of the S_0 state adopts a nearly coplanar arrangement of the phenoxazine and cAAC^{Ment} ligands and bears very little rotatory strength *R* in the vertical transition $S_0 \rightarrow S_1$ (Figure 7), which is in line with the measured CD spectra in solution (Figure 2 and Table 2). Interestingly, we found a "kink" angle β distortion of **6** as a local minimum on the energy potential surface of the ground state only 0.03 eV above the planar geometry, which is thus thermally accesible at room temperature. The vertical transition to the S_1 state then exhibits a ten-fold increased *R* value of $10.2 \cdot 10^{-40}$ cgs. Furthermore, the mathematical sign of the luminescence dissymmetry is also very sensitive to the structural pecularities, since the $S_0 \rightleftarrows S_1$ transition at the optimized T_1 geometry, which ist most likely very relevant for the TADF process, shows $R = -7.5 \cdot 10^{-40}$ cgs.

Conclusion

Structure-property relationships for the design of chiroptical properties of transition metal CP-TADF emitters are very scarce despite their relevance for electroluminescent devices. We have thus studied a series of chiral copper(I) carbene amide complexes as representatives of a class of highly efficient TADF emitters, which emit from $^{1/3}$LLCT/MLCT states with high k_r in the range of 10^5 s^{-1} at room temperature as reported previously for non-chiral or racemic analogues. For all compounds, pronounced mechanochromic photoluminescence behavior upon grinding the single crystalline materials leading to bathochromic emission shifts and increased k_r is observed. We trace this phenomenon back to changes in the intermolecular dipol-dipol interactions and larger surface-to-volume ratio after application of the stimulus. However, the chiral moieties at the cAAC acceptor or amide donor ligand do not lead to detectable CPL of the carbazolate complexes irrespective of the medium.

In contrast, [Cu(PZN)(cAAC^{Ment})] (**6**) is a very efficient orange-red TADF emitter in PMMA (k_r = $6.7 \cdot 10^5$ s^{-1}) with a notable dissymmetry factor of $g_{lum} = -3.4 \cdot 10^{-3}$. Either restricted ligand rotation or a "kink" angle distortion of the PZN ligand supported by hydrogen bonding of the ligand´s oxygen atom with the PMMA matrix might be responsbile for producing the rotatory strength of the electron density change of the vertical transition. Such an interaction with the matrix is not available to the carbazolate ligands and is thus most likely responsible for the effective chiroptical properties of the excited states, which are inherently introduced by the chiral carbene ligand. Further exploitation of this design motif for efficient CP-TADF is a currently ongoing work in our group and will be reported in due course.

Experimental Section

Essential Experimental Procedures/Data.All experimental details provided in the Supporting Information in a separate file (pdf), including synthetic procedures, details of characterization, X-ray crystallographic data, photophysical spectra, as well as computational details.

Deposition Number(s) <url href="https://www.ccdc.cam.ac.uk/services/structures?id=doi:10.1002/chem.202300946"> 2175343 (for **3**), 2195861 (for **6**), 2195860 (for **7**), 2175342 (for ***R*-8**), 2175341 (for ***S*-8**)</url> contain(s) the supplementary crystallographic data for this paper. These data are provided free of charge by the joint Cambridge Crystallographic Data Centre and Fachinformationszentrum Karlsruhe <url href="http://www.ccdc.cam.ac.uk/structures">Access Structures service</url>.

Acknowledgements

Financial support by the Deutsche Forschungsgemeinschaft (DFG STE1834/4-2, STE1834/9-1) is gratefully acknowledged. This work was funded by the Deutsche Forschungsgemeinschaft (DFG, German Research Foundation) under Germany's Excellence Strategy EXC2033, project number 390677874, RESOLV. The authors gratefully acknowledge the computing time provided on the Linux HPC cluster at Technical University Dortmund (LiDO3), partially funded in the course of the Large-Scale Equipment Initiative by the German Research Foundation (DFG) as project 271512359.

Keywords: copper • TADF • chirality • circularly polarized luminescence • excited states

[1] C. Wagenknecht, C.-M. Li, A. Reingruber, X.-H. Bao, A. Goebel, Y.-A. Chen, Q. Zhang, K. Chen, J.-W. Pan, *Nat. Photon.* **2010**, *4*, 549–552.
[2] C. H. Bennett, G. Brassard, *Theor. Comput. Sci.* **2014**, *560*, 7–11.
[3] R. Farshchi, M. Ramsteiner, J. Herfort, A. Tahraoui, H. T. Grahn, *Appl. Phys. Lett.* **2011**, *98*, 162508.

[4] S. J. Bradberry, A. J. Savyasachi, M. Martinez-Calvo, T. Gunnlaugsson, *Coord. Chem. Rev.* **2014**, *273-274*, 226–241.
[5] G. Muller, *Dalton Trans.* **2009**, 9692–9707.
[6] M. Schadt, *Annu. Rev. Mater. Sci.* **1997**, *27*, 305–379.
[7] a) L. Rosenfeld, *Z. Physik* **1929**, *52*, 161–174; b) J. A. Schellman, *Chem. Rev.* **1975**, *75*, 323–331.
[8] a) F. Zinna, L. Di Bari, *Chirality* **2015**, *27*, 1–13; b) T. Harada, H. Tsumatori, K. Nishiyama, J. Yuasa, Y. Hasegawa, T. Kawai, *Inorg. Chem.* **2012**, *51*, 6476–6485.
[9] J.-R. Jiménez, B. Doistau, C. M. Cruz, C. Besnard, J. M. Cuerva, A. G. Campaña, C. Piguet, *J. Am. Chem. Soc.* **2019**, *141*, 13244–13252.
[10] C. Murawski, K. Leo, M. C. Gather, *Adv. Mater.* **2013**, *25*, 6801–6827.
[11] a) E. Zysman-Colman (Hrsg.) *Iridium (III). In optoelectronic and photonics applications*, John Wiley & Sons Inc, Chichester, West Sussex, **2017**; b) G. Hong, X. Gan, C. Leonhardt, Z. Zhang, J. Seibert, J. M. Busch, S. Bräse, *Adv. Mater.* **2021**, *33*, e2005630.
[12] B. Doistau, J.-R. Jiménez, C. Piguet, *Front. Chem.* **2020**, *8*, 555.
[13] C. Shen, E. Anger, M. Srebro, N. Vanthuyne, K. K. Deol, T. D. Jefferson, G. Muller, J. A. Gareth Williams, L. Toupet, C. Roussel, J. Autschbach, R. Réau, J. Crassous, *Chem. Sci.* **2014**, *5*, 1915–1927.
[14] L. Frédéric, A. Desmarchelier, L. Favereau, G. Pieters, *Adv. Funct. Mater.* **2021**, *31*, 2010281.
[15] Z.-L. Tu, Z.-P. Yan, X. Liang, L. Chen, Z.-G. Wu, Y. Wang, Y.-X. Zheng, J.-L. Zuo, Y. Pan, *Adv. Sci.* **2020**, *7*, 2000804.
[16] R. Hamze, J. L. Peltier, D. Sylvinson, M. Jung, J. Cardenas, R. Haiges, M. Soleilhavoup, R. Jazzar, P. I. Djurovich, G. Bertrand, M. E. Thompson, *Science* **2019**, *363*, 601–606.
[17] M. Gernert, L. Balles-Wolf, F. Kerner, U. Müller, A. Schmiedel, M. Holzapfel, C. M. Marian, J. Pflaum, C. Lambert, A. Steffen, *J. Am. Chem. Soc.* **2020**, *142*, 8897-8909.
[18] A. S. Romanov, S. T. E. Jones, Q. Gu, P. J. Conaghan, B. H. Drummond, J. Feng, F. Chotard, L. Buizza, M. Foley, M. Linnolahti, D. Credgington, M. Bochmann, *Chem. Sci.* **2020**, *11*, 435–446.
[19] D. Di, A. S. Romanov, Le Yang, J. M. Richter, J. P. H. Rivett, S. Jones, T. H. Thomas, M. Abdi Jalebi, R. H. Friend, M. Linnolahti, M. Bochmann, D. Credgington, *Science* **2017**, *356*, 159–163.
[20] a) S. Shi, M. C. Jung, C. Coburn, A. Tadle, D. Sylvinson M R, P. I. Djurovich, S. R. Forrest, M. E. Thompson, *J. Am. Chem. Soc.* **2019**, *141*, 3576–3588; b) R. Tang, S. Xu, T.-L. Lam, G. Cheng, L. Du, Q. Wan, J. Yang, F.-F. Hung, K.-H. Low, D. L. Phillips, C.-M. Che, *Angew. Chem. Int. Ed.* **2022**, *61*, e202203982; c) A. Ruduss, B. Turovska, S. Belyakov, K. A. Stucere, A. Vembris, G. Baryshnikov, H. Ågren, J.-C. Lu, W.-H. Lin, C.-H. Chang, K. Traskovskis, *ACS Appl. Mater. Interfaces* **2022**, *14*, 15478–15493; d) A. Ying, Y.-H. Huang, C.-H. Lu, Z. Chen, W.-K. Lee, X. Zeng, T. Chen, X. Cao, C.-C. Wu, S. Gong, C. Yang, *ACS Appl. Mater. Interfaces* **2021**, *13*, 13478–13486; e) A. Ruduss, B. Turovska, S. Belyakov, K. A. Stucere, A. Vembris, K. Traskovskis, *Inorg. Chem.* **2022**, *61*, 2174–2185.
[21] M. J. Leitl, V. A. Krylova, P. I. Djurovich, M. E. Thompson, H. Yersin, *J. Am. Chem. Soc.* **2014**, *136*, 16032–16038.
[22] E. J. Taffet, Y. Olivier, F. Lam, D. Beljonne, G. D. Scholes, *J. Phys. Chem. Lett.* **2018**, *9*, 1620–1626.
[23] J. Föller, C. M. Marian, *J. Phys. Chem. Lett.* **2017**, *8*, 5643–5647.
[24] A. Ying, Y. Ai, C. Yang, S. Gong, *Angew. Chem. Int. Ed.* **2022**, *61*, e202210490.
[25] A. M. T. Muthig, O. Mrozek, T. Ferschke, M. Rödel, J. Kuhnt, C. Lenczyk, J. Pflaum, A. Steffen, *J. Am. Chem. Soc.* **2023**, https://doi.org/10.1021/jacs.2c09458.
[26] M. Gernert, U. Müller, M. Haehnel, J. Pflaum, A. Steffen, *Chem. Eur. J.* **2017**, *23*, 2206–2216.
[27] a) P. Roesch, J. Nitsch, M. Lutz, J. Wiecko, A. Steffen, C. Müller, *Inorg. Chem.* **2014**, *53*, 9855–9859; b) J. Nitsch, C. Kleeberg, R. Fröhlich, A. Steffen, *Dalton Trans.* **2015**, *44*, 6944–6960; c) P. Bissinger, A. Steffen, A. Vargas, R. D. Dewhurst, A. Damme, H. Braunschweig, *Angew. Chem. Int. Ed.* **2015**, *54*, 4362–4366; d) J. Nitsch, F. Lacemon, A. Lorbach, A. Eichhorn, F. Cisnetti, A. Steffen, *Chem. Commun.* **2016**, *52*, 2932–2935; e) B. Hupp, C. Schiller, C. Lenczyk, M. Stanoppi, K. Edkins, A. Lorbach, A. Steffen, *Inorg. Chem.* **2017**, *56*, 8996–9008; f) E. Hobbollahi, M. List, B. Hupp, F. Mohr, R. J. F. Berger, A. Steffen, U. Monkowius, *Dalton Trans.* **2017**, *46*, 3438–3442; g) H. Braunschweig, T. Dellermann, R. D. Dewhurst, B. Hupp, T. Kramer, J. D. Mattock, J. Mies, A. K. Phukan, A. Steffen, A. Vargas, *J. Am. Chem. Soc.* **2017**, *139*, 4887–4893; h) B. Hupp, J. Nitsch, T. Schmitt, R. Bertermann, K. Edkins, F. Hirsch, I. Fischer, M. Auth, A. Sperlich, A. Steffen, *Angew. Chem. Int. Ed.* **2018**, *57*, 13671–13675; i) N. V. Tzouras, E. A. Martynova, X. Ma, T. Scattolin, B. Hupp, H. Busen, M. Saab, Z. Zhang, L. Falivene, G. Pisanò, K. van Hecke, L. Cavallo, C. S. J. Cazin, A. Steffen, S. P. Nolan, *Chem. Eur. J.* **2021**, *27*, 11904–11911; j) A. Steffen, B. Hupp in *Comprehensive Coordination Chemistry III* (Hrsg.: E. Constable), Elsevier, San Diego, **2021**, S. 466–502; k) T. Hölzel, A. Belyaev, M. Terzi, L. Stenzel, M. Gernert, C. M. Marian, A. Steffen, C. Ganter, *Inorg. Chem.* **2021**, *60*, 18529–18543; l) A. M. T. Muthig, M. Krumrein, J. Wieland, M. Gernert, F. Kerner, J. Pflaum, A. Steffen, *Inorg. Chem.* **2022**, *61*, 14833–14844; m) A. M. T. Muthig, J. Wieland, S. Koop, C. Lenczyk, F. Kerner, B. Hupp, A. Steffen, *Inorg. Chem.* **2022**, *61*, 17427-17437.
[28] a) A. Liske, L. Wallbaum, T. Hölzel, J. Föller, M. Gernert, B. Hupp, C. Ganter, C. M. Marian, A. Steffen, *Inorg. Chem.* **2019**, *58*, 5433–5445; b) J. Föller, C. Ganter, A. Steffen, C. M. Marian, *Inorg. Chem.* **2019**, *58*, 5446–5456.
[29] J. Feng, E. J. Taffet, A.-P. M. Reponen, A. S. Romanov, Y. Olivier, V. Lemaur, L. Yang, M. Linnolahti, M. Bochmann, D. Beljonne, D. Credgington, *Chem. Mater.* **2020**, *32*, 4743–4753.
[30] a) W. Siebrand, *Chem. Phys.* **1967**, *46*, 440–447; b) W. Siebrand, *Chem. Phys.* **1967**, *47*, 2411–2422.
[31] Y. Nagata, T. Mori, *Front. Chem.* **2020**, *8*, 448.
[32] P. Klán, J. Wirz, *Photochemistry of organic compounds. From concepts to practice*, Wiley, Chichester, **2009**.
[33] S. C. J. Meskers, *ChemPhotoChem* **2022**, *6*, e202100154.
[34] Stefan C. J. Meskers, Harry P. J. M. Dekkers, Gwénaël Rapenne, Jean-Pierre Sauvage, *Chem. Eur. J.* **2000**, *6*, 2129–2134.
[35] M. Deng, N. F. M. Mukthar, N. D. Schley, G. Ung, *Angew. Chem. Int. Ed.* **2020**, *59*, 1228–1231.
[36] a) A. S. Romanov, D. Di, Le Yang, J. Fernandez-Cestau, C. R. Becker, C. E. James, B. Zhu, M. Linnolahti, D. Credgington, M. Bochmann, *Chem. Commun.* **2016**, *52*, 6379–6382; b) R. Hamze, R. Jazzar, M. Soleilhavoup, P. I. Djurovich, G. Bertrand, M. E. Thompson, *Chem. Commun.* **2017**, *53*, 9008–9011.
[37] E. E. Braker, N. F. M. Mukthar, N. D. Schley, G. Ung, *ChemPhotoChem* **2021**, *5*, 902–905.
[38] a) M. Li, Y.-F. Wang, D. Zhang, L. Duan, C.-F. Chen, *Angew. Chem. Int. Ed.* **2020**, *59*, 3500–3504; b) S.-Y. Yang, Y.-K. Wang, C.-C. Peng, Z.-G. Wu, S. Yuan, Y.-J. Yu, H. Li, T.-T. Wang, H.-C. Li, Y.-X. Zheng, Z.-Q. Jiang, L.-S. Liao, *J. Am. Chem. Soc.* **2020**, *142*, 17756–17765.
[39] L. Arrico, L. Di Bari, F. Zinna, *Chem. Eur. J.* **2021**, *27*, 2920–2934.
[40] a) Y. Kitayama, T. Amako, N. Suzuki, M. Fujiki, Y. Imai, *Org. Biomol. Chem.* **2014**, *12*, 4342–4346; b) H. Tanaka, Y. Inoue, T. Mori, *ChemPhotoChem* **2018**, *2*, 386–402.
[41] J.-J. Wang, H.-T. Zhou, J.-N. Yang, L.-Z. Feng, J.-S. Yao, K.-H. Song, M.-M. Zhou, S. Jin, G. Zhang, H.-B. Yao, *J. Am. Chem. Soc.* **2021**, *143*, 10860–10864.

3.3 New Insights into CPL-active Emitters

Reliable structure-property-relationships for both CPL and mechanoluminochromism remain elusive. Even though the synthesis of the desired linear copper complexes with chiral anions was not successful, some important findings for further research steps were obtained. It remains to be examined whether resins with different functionalisation are more suitable and allow access to the desired chiral compounds. Furthermore, trifluorophenyl borate was identified as an achiral anion that leads to mechanoluminochromic behaviour. Here, too, Cu – F interactions can be assumed as the mechanism. Since $B(BINOL)_2^-$ was not found to be responsive and potential ligand atoms are sterically shielded, it is reasonable to assume that only those anions lead to mechanoluminochromism that have sufficient accessible donor atoms to enable reversible association. A key observation of our theoretical studies on the phenoxazine complexes described above relates to the often overlooked inclusion of energetically accessible conformers. The fact that molecules adopt a variety of different conformers at room temperature is well known and has long since become a triviality. In theoretical studies and also synthetic protocols, a small energy difference is rarely taken into account. It is simply implied that the reactive conformer is always thermally accessible. However, as soon as complex organic and metal-organised compounds are investigated, one usually relies on the single crystal XRay structure and/or the optimised minimum structure. But of course, in addition to this minimum, there are often many other structures that fulfil the convergence criteria. Applied to the CMA investigated in this work, the comparatively high CPL activity of [Cu(^{Ment}CAAC)(pnz)] could only be mapped density functionally by such a conformer. The minimum structure derived from the crystal structure dominates the absorption properties, but not the emission. Especially for phenomena based on high flexibility or steric-electronic effects, here explicitly CPL and mechanoluminochromism, other local minimum structures should always be included in the analysis by a conformer search.

4 Appendix

4.1 General Remarks

General considerations

Copper(I)-tert-butoxide was synthesised according to literature procedure.[122] All other starting materials were purchased from commercial sources and used without further purifications, unless stated otherwise. Synthetic work was performed in standard glassware and under an inert argon atmosphere (argon 4.6, 99.996%) using standard Schlenk-technique or in a *Glovebox Systemtechnik* glovebox if necessary. All organic solvents were of HPLC grade and either used directly or by prior purification using an *Inert Systems PureSolv MD7 Solvent Purification System* followed by standard degassing procedures. Solvents prepared this way where stored in a borosillicate bottle with J Young PTFE screw cap over molecular sieves and under an argon atmosphere.

Nuclear magnetic resonance spectroscopy

All NMR-spectra were measured either on a *Bruker Avance III HD 400* (^{1}H, 400 MHz; ^{13}C{^{1}H}, 101 MHz; ^{19}F, 376 MHz), *Bruker Avance III HD 500* (^{1}H, 500 MHz; ^{13}C{^{1}H}, 126 MHz), *Bruker Avance III HD 600* (^{1}H, 600 MHz; ^{13}C{^{1}H}, 150 MHz; ^{19}F, 564 MHz) or *Bruker Avance Neo 500* (^{1}H, 500 MHz; ^{13}C{^{1}H}, 126 MHz) NMR spectrometer. Chemical shifts are reported as *parts per million* (ppm, δ scale) relative to the residual solvent resonance (chloroform-d: 7.26 ppm (^{1}H), 77.2 ppm (^{13}C); THF-d_8: 1.72 ppm (^{1}H), 25.3 ppm (^{13}C); dichloromethane-d_2: 5.32 ppm (^{1}H), 53.8 ppm (^{13}C); acetonitrile-d_3: 1.94 ppm (^{1}H), 1.3 ppm (^{13}C)).

Elemental analysis

Elemental analysis (C, H, N) was performed on an *Elementar Vario MICRO Cube* by *Elementar Analysensystem GmbH* with tin sample capsules.

Single-crystal X-ray diffraction

Data collection was carried out on a *Bruker D8 Venture* four-circle diffractometer from *Bruker AXS GmbH* with a *Photon II* detector and microfocus source *IμS* Mo (Mo$_{K_\alpha}$ radiation, $\lambda = 71.073$ pm) from *Incoatec GmbH* with HELIOS mirror optics and single-hole

collimator from *Bruker AXS GmbH*. Single crystals were kept under NVH oil, mounted on a MiTiGen sample holder and cooled to 100 K during the measurement using a *Cryostream open-flow N_2 gas cryostat*. Solving the molecular structure in the solid state was carried out using intrinsic phase methods (SHELXT).[138] These were refined with the aid of SHELXL[139] and subsequently extended using Fourier techniques. Hydrogen atoms were assigned to idealized positions or found directly and all non-hydrogen atoms were refined anisotropically.

Photophysical measurements

The sample preparation was carried out in a *Glovebox Systemtechnik* glove box. The amorphous samples were ground for ten minutes. UV-Vis absorption spectra were recorded using an *Agilent* Cary 5000 spectrophotometer (UV-Vis-NIR spectrophotometer series). Standard quartz cuvettes with a path length of 1 cm and a screw cap were used. Emission and excitation spectra were recorded using a FLS1000 photoluminescence spectrometer from *Edinburgh Instruments*, which is equipped with double monochromators for the emission and excitation beam paths, a 450 W xenon gas discharge lamp and photomultipliers (PMT-980 or PMT-1400-LN2) as detectors. The excitation wavelength was set by a double grating monochromator and the emission was detected at right angles to the excitation source by the photomultiplier. The measured excitation and emission spectra were corrected using the manufacturer's standard corrections for the sensitivity of the detector and the intensity distribution of the light source. The luminescence lifetimes were measured using either a μF2-60 W xenon microsecond flash lamp and a multi-channel scaling (MCS) module, a variable pulsed LED (VPLED) and MCS or a pulsed laser diode (EPLED) with a pulse width of 200 ps and a time-correlated single photon counting (TCSPC) module. Low temperatur measurements were performed using an EPR Dewar (77 K) module with quartz sample tubes from *Edinburgh Instruments*. Room temperature quantum yields were recorded using an Uhlbricht-integration sphere.

Computational Details

Calculations for all complexes were performed with the ORCA 5.0.3 program suite[140,141] with tight SCF convergence criteria. Gas-phase geometry optimizations were carried out using the PBE0 hybrid functional[142,143] as implemented in ORCA. The absence of negative frequencies ensured convergence to a true minimum structure. The def2-TZVP basis set[144,145] was used on all atoms together with the def2/J auxiliary basis set. All computations were accelerated using RIJCOSX approximation schemes with addition of empirical dispersion correction (D3BJ).[146] TD-DFT calculations for the first 20 singlet and triplet excited states were performed using the same functional but

with all-electron basis set ZORA-def2-TZVP[147] and segmented all-electron relativistically contracted auxiliary basis set SARC/J using a conductor-like polarizable continuum model (CPCM) for THF. Representations of electronic transition differences at isovalues of 0.005 a.u. were produced with the orca_plot module as provided by ORCA 5.0.3 and ChimeraX[148,149]. Single point calculations were performed using ωB97X-D3BJ range-separated hybrid functional[150] and def2-TZVP basis set. Wavefunction files (.wfn) for IRI analysis were generated using orca_2aim module on single point calulation geometry-basis-wavefunction (gbw) files. IRI analysis was performed using Multiwfn3.8 program suite[37,127] and visualized with VMD software[151].

4.2 Experimental Details to Section 2.1

4.2.1 Synthesis and Characterization

Synthesis of phthalazinium salts 37 and 39 via alkylation (method A)

A dry Schlenk-tube equipped with a magnetic stir bar, is charged with phthalazine (7.5 mmol, 1.0 equiv.) and haloalkane (1.5 equiv.) under a stream of argon. The flask is sealed with a greased glass stopper and placed into a preheated oil-bath (oil temperature 90 °C) with constant stirring. After a few minutes a dark-orange liquid forms, which solidifies shortly after. The solid mixture is then heated at 90 °C for 2h. Upon completion, the mixture is left to cool to room temperature. The solid, resembling cold wax, is broken up and suspended with diethyl ether (approx. 5 mL). The mixture was transferred onto a fritted glass filter. After removing the solvent, the solid is washed with diethyl ether (3× 20 mL) and pentanes (2× 20 mL). The product is then dried *in vacuo* yielding a yellow powder. Recrystalisation from hot ethanol is performed if needed.

2-Isopropylphthalazin-2-ium iodide (37)

Using 2-iodopropane (1.91 g, 1.13 mL) the product (1.71 g, 76%) was obtained as a yellow powder.

^{1}H-NMR (600 MHz, $CDCl_3$): δ = 12.05 (s, 1H), 9.84 (s, 1H), 9.11 (d, ^3J = 7.2 Hz, 1H), 8.50 (d, ^3J = 7.2 Hz, 1H), 8.41 (dd, ^3J = 7.7, 1.1 Hz, 1H), 8.31 (td, ^3J = 7.7, 1.1 Hz, 1H), 5.64 (sept, ^3J = 6.5 Hz, 1H), 1.81 (d, ^3J = 6.6 Hz, 6H) ppm.

^{13}C{^{1}H}-NMR (150 MHz, $CDCl_3$): δ = 154.3, 149.7, 149.6, 139.4, 136.4, 131.7, 128.3, 127.9, 67.6, 22.4 ppm.

2-Benzhydrylphthalazin-2-ium bromide (39)

Using bromodiphenylmethane (2.57 g) the product (2.42 g, 85%) was obtained as a pale-yellow powder after recrystalisation.

^{1}H-NMR (500 MHz, CD_2Cl_2): δ = 12.64 (s, 1H), 9.75 (s, 1H), 8.94 (d, ^3J = 8.1 Hz, 1H), 8.47 – 8.36 (m, 3H), 8.30 (ddd, ^3J = 8.2, 6.6, 1.7 Hz, 1H), 7.62 – 7.54 (m, 4H), 7.44 – 7.35 (m, 6H) ppm.

^{13}C{^{1}H}-NMR (125 MHz, CD_2Cl_2): δ = 154.5, 152.9, 152.7, 140.1, 136.8, 136.4, 132.1, 129.7, 129.2, 128.5, 128.22, 128.15 ppm.

Synthesis of phthalazinium salt 38 via condensation/ dehydratisation (method B)

By analogy to known procedure[Mariz2010], a dry Schlenk-flask equipped with a magnetic stir bar and water cooled reflux condencer, is charged with phthaldialdehyde (11.0 mmol, 1.0 equiv.), 1-substituted hydrazine (2.5 equiv.), glacial acetic acid (10 mol-%) and dry THF under argon. The mixture is refluxed for 24 h. After complete conversion (as indicated by GC-MS), the reaction mixture is filtered through a short plug of celite and concentrated *in vacuo*. The residue is taken up in dry diethyl ether, purged with argon and cooled to 0 °C in an ice-bath. Trifluoromethanesulfonic anhydride (1.1 equiv.) is slowly added with constant stirring at 0 °C. After complete addition an off-white solid forms and the suspension is stirred at that temperature for 30 min. and then at room temperatur for 1 h. The solid is filtered of and washed with diethyl ether (3× 20 mL) and *n*-pentane (2× 10 mL). After drying *in vacuo*, the product is obtained as an off-white solid.

2-(*tert*-Butyl)phthalazin-2-ium triflate (38)

Using *tert*-butyl hydrazine (2.42 g), the product (1.99 g, 55%) was obtained as an off-white solid.

^{1}H-NMR (600 MHz, $CDCl_3$): δ = 10.88 (s, 1H), 9.61 (s, 1H), 9.10 (d, ^3J = 8.4 Hz, 1H), 8.40 (ddd, ^3J = 8.2, 7.2, 1.2 Hz, 1H), 8.34 (dd, ^3J = 8.0, 1.1 Hz, 1H), 8.30 (ddd, ^3J = 8.3, 7.2, 1.2 Hz, 1H), 1.94 (s, 9H) ppm.

^{13}C{^{1}H}-NMR (150 MHz, $CDCl_3$): δ = 153.4, 149.0, 139.5, 136.6, 133.1, 128.6, 127.4, 127.0, 120.7 (q, $^1J_{C-F}$ = 318 Hz), 74.1 ppm.

^{19}F-NMR (376 MHz, $CDCl_3$): δ = –78.9 ppm.

Anion exchange using *Amberlyst-A26* anion exchange resin

Preparing the resin:
Amberlyst®-A26 (OH-Form) (0.5 g/mmol) is added to a thin glass- or PTFE-column (inner diameter 5 mm) and rinsed with water (10 mL), aq. NaOH (0.1 M, 5 mL) and again with water until pH of eluent reaches 7.
Loading of the resin:
A 2 wt-% aqueous solution of free acid or ammonium salt of desired anion is prepared and passed over the resin slowly using gravity. The loading is complete when the pH of the eluent is equal to the pH of the initial solution (eluent with incomplete loading is strongly basic).
Washing and conditioning of the resin:

The loaded resin is washed with copious amounts of water until the pH of eluent is 7. The resin is conditioned to organic solvents by passing through water:methanol mixtures of different ratios (20 mL each of 1:0, 3:1, 1:1, 1:3, 0:1).
Anion exchange:
A 1 wt-% solution of phthalazinium salt in methanol is passed through the resin column dropwise using gravity. The eluent is collected in a round bottom flask. When the solution is passed through, the column is washed with methanol (at least 3-times the volume of initial methanol solution). Volatiles of combined organic fractions are removed *in vacuo*. Phthalazinium chlorides tend to be highly hydroscopic and are therefore kept in a vacuum desicator over anhydrous calcium chloride for 10 days before storage in a glovebox.

2-Isopropylphthalazin-2-ium chloride (43)

From **37** (1.5 g) using NH_4Cl, the product was obtained as a yellow hydroscopic crisp foam (991 mg, 95%).

^{1}H-NMR (400 MHz, $CDCl_3$): δ = 12.69 (s, 1H), 9.77 (s, 1H), 9.20 (dd, ^3J = 8.1, 1.1 Hz, 1H), 8.47–8.40 (m, 1H), 8.38 (ddd, ^3J = 8.1, 7.0, 1.1 Hz, 1H), 8.28 (ddd, ^3J = 8.2, 7.1, 1.3 Hz, 1H), 5.74 (sept, ^3J = 6.6 Hz, 1H), 1.78 (d, ^3J = 6.6 Hz, 6H) ppm.

^{13}C{^{1}H}-NMR (101 MHz, $CDCl_3$): δ = 154.2, 151.7, 139.2, 136.3, 132.5, 128.7, 127.9, 127.6, 67.4, 22.6 ppm.
Product-purity was confirmed by absence of iodide mass peak at m/z = 127 and positive silver nitrate test.

2-Isopropylphthalazin-2-ium bromide (44)

From **37** (1.05 g) using HBr, the product was obtained as a dark-yellow solid (807 mg, 91%).

^{1}H-NMR (500 MHz, $CDCl_3$): δ = 12.45 (s, 1H), 9.74 (s, 1H), 9.20 (dd, ^3J = 8.2, 1.0 Hz, 1H), 8.45–8.35 (m, 2H), 8.30 (ddd, ^3J = 8.3, 6.7, 1.3 Hz, 1H), 5.71 (sept, ^3J = 6.6 Hz, 1H), 1.81 (d, ^3J = 6.6 Hz, 6H) ppm.

^{13}C{^{1}H}-NMR (126 MHz, $CDCl_3$): δ = 154.1, 151.0, 139.3, 136.4, 132.3, 128.5, 128.0, 127.6, 67.5, 22.6 ppm.
Product-purity was confirmed by absence of iodide mass peak at m/z = 127 and positive silver nitrate test.

2-(*tert*-Butyl)phthalazin-2-ium chloride (45)

From **38** (611 mg) using NH_4Cl, the product was obtained as a dark-yellow hydroscopic crisp foam (356 mg, 88%).

^{1}H-NMR (400 MHz, $CDCl_3$): δ = 12.47 (t, ^3J = 1.0 Hz, 1H), 9.79 (tq, ^3J = 7.9, 1.0 Hz, 1H), 9.65 (t, ^3J = 1.0 Hz, 1H), 8.40–8.24 (m, 3H), 2.00 (s, 9H) ppm.

^{13}C{^{1}H}-NMR (101 MHz, $CDCl_3$): δ = 153.1, 150.2, 139.2, 136.2, 134.1, 129.1, 127.2, 126.8, 74.0, 29.7 ppm.
Product-purity was confirmed by absence of ^{19}F-NMR resonance and positive silver nitrate test.

Complexation using CuOtBu

In an argon-filled glovebox, a screw-capped glass vial is charged with the respective phthalazinium salt (1.0 equiv.) and CuOtBu (1.0 equiv.) in dry THF (10 mL). The solution turns yellow-orange to deep orange and was stirred for 48 h at room temperature. Iodide-complexes tend to be insoluble in THF and are filtered off and washed with diethyl ether and pentane. Choride- and bromide-complexes are very soluble. Volatiles are removed *in vacuo* and the residual solids are washed with small amounts of very cold THF (< –30 °C), followed by diethyl ether and *n*-pentane.
Crystals suitable for X-Ray diffraction are grown by slowly diffusing diethyl ether into a sat. THF solution.

Chloro[2-isopropylphthalazin-1-ylidene] copper(I) (33a)

From **43** (250 mg), the product (146 mg, 45%) is obtained as a yellow solid.

^{1}H-NMR (500 MHz, THF-d_8): δ = 9.34 (s, 1H), 8.74 (dq, ^3J = 7.6, 1.2 Hz, 1H), 8.18–8.08 (m, 3H), 5.67 (sept, ^3J = 6.6 Hz, 1H), 1.70 (d, ^3J = 6.5 Hz, 6H) ppm.

^{13}C{^{1}H}-NMR (126 MHz, THF-d_8): δ = 151.3, 140.1, 138.0, 136.6, 134.5, 128.2, 124.4, 72.0, 22.8 ppm. *Signal of carbene-carbon is missing.*

CHN-analysis
Calculated for $C_{11}H_{12}ClCuN_2$: %C 48.71, %H 4.46, %N 10.33.
Found: %C 48.63, %H 4.43 %N 10.38

Bromo[2-isopropylphthalazin-1-ylidene] copper(I) (47)

From **45** (250 mg), the product (175 mg, 56%) is obtained as a dark-yellow solid.

^{1}H-NMR (400 MHz, THF-d_8): δ = 9.35 (s, 1H), 8.79–8.76 (m, 1H), 8.15–8.09 (m, 3H), 5.69 (sept, ^3J = 6.6 Hz, 1H), 1.70 (d, ^3J = 6.6 Hz, 6H) ppm.

^{13}C{^{1}H}-NMR (101 MHz, THF-d_8): δ = 200.7, 151.1, 139.7, 137.6, 136.3, 134.2, 127.9, 124.2, 71.4, 22.6 ppm.

CHN-analysis

Calculated for $C_{22}H_{24}Br_2Cu_2N_4$: %C 41.85, %H 3.83, %N 8.87.
Found: %C 41.85, %H 3.97, %N 8.63

Iodo[2-isopropylphthalazin-1-ylidene] copper(I) (42)

From **37** (250 mg), the product (163 mg, 54%) is obtained as a red-orange solid.

^{1}H-NMR (600 MHz, THF-d_8): δ = 9.33 (s, 1H), 8.93–8.80 (m, 1H), 8.14–8.08 (m, 3H), 5.75 (sept, ^3J = 6.6 Hz, 1H), 1.71 (d, ^3J = 6.6 Hz, 6H) ppm.

^{13}C{^{1}H}-NMR (125 MHz, THF-d_8): δ = 204.1, 151.2, 139.7, 137.5, 136.2, 134.2, 128.1, 124.5, 70.8, 22.8 ppm.

CHN-analysis
Calculated for $C_{22}H_{24}I_2Cu_2N_4$: %C 36.43, %H 3.34, %N 7.72.
Found: %C 35.95, %H 3.35, %N 7.77

Chloro[2-(*tert*-butyl)phthalazin-1-ylidene] copper(I) (44)

From **45** (250 mg), the product (165 mg) is obtained as a yellow solid. Minor impurity of starting material **45** could not be removed.

Bromo[2-benzhydrylphthalazin-1-ylidene] copper(I) (48)

From **39** (250 mg), the product (142mg) is obtained as a yellow solid. Minor impurity of starting material **39** could not be removed.

4.2.2 NMR Spectra

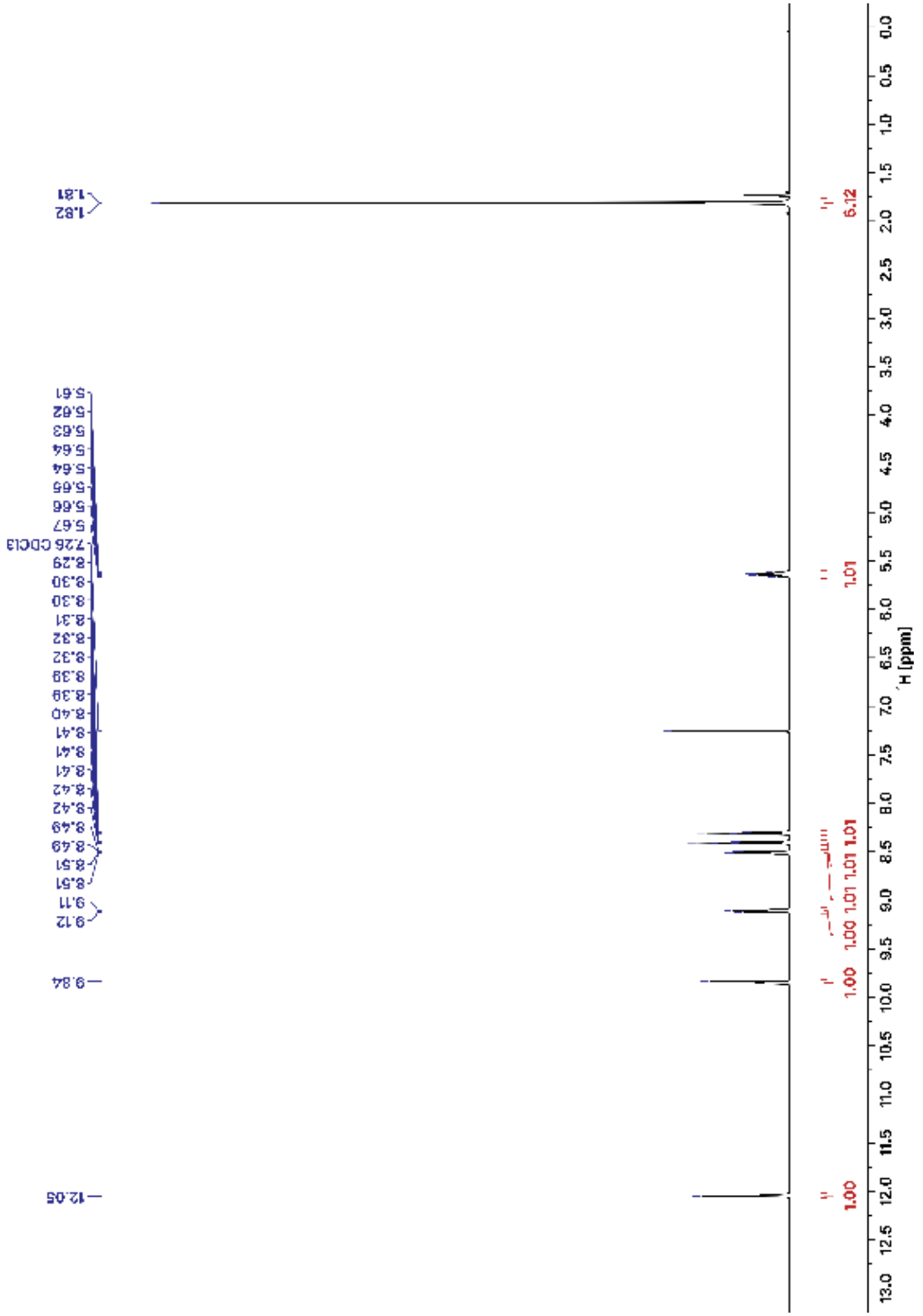

Figure 4.1: ^{1}H-NMR spectrum of **37** in $CDCl_3$.

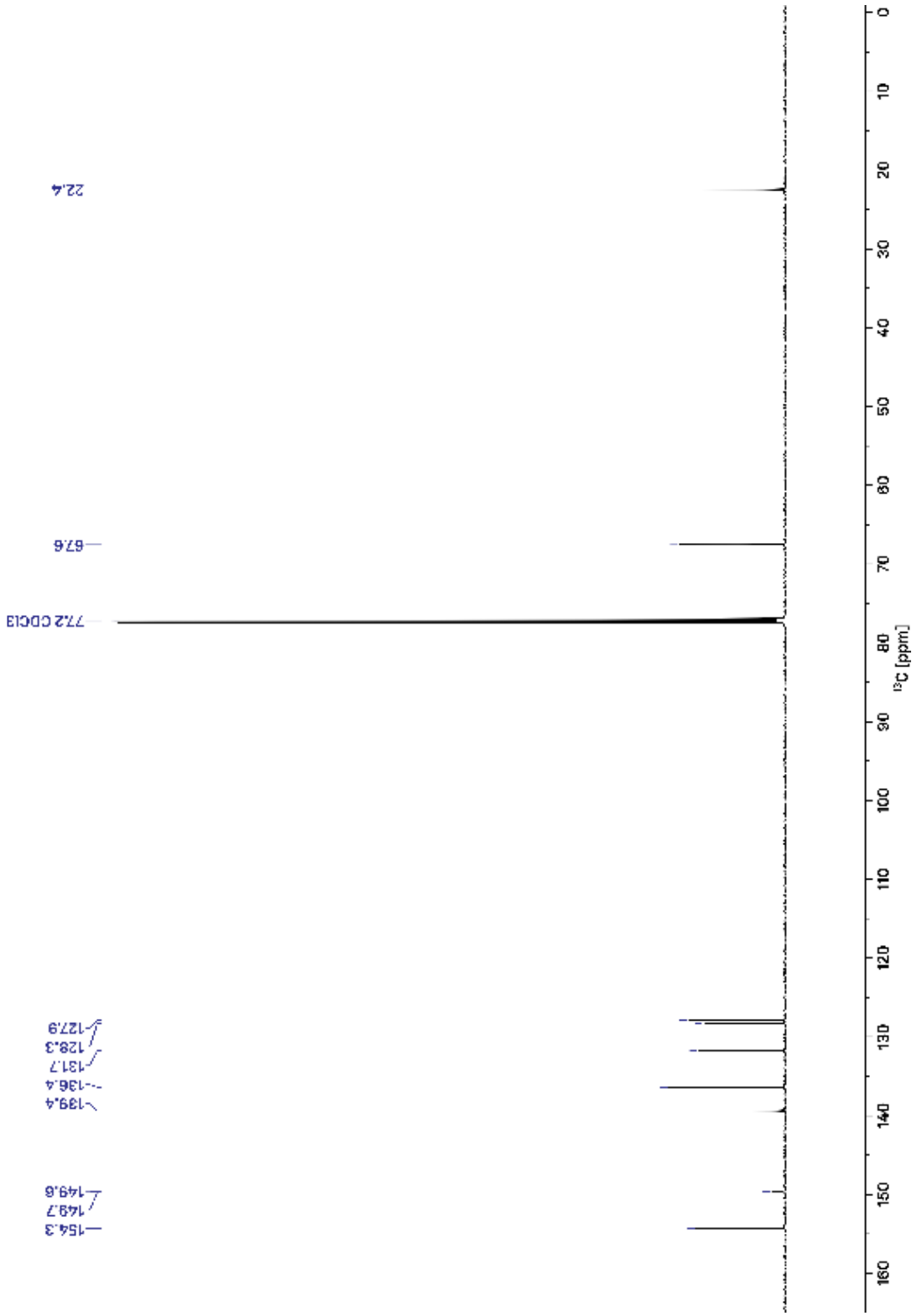

Figure 4.2: ^{13}C-NMR spectrum of **37** in $CDCl_3$.

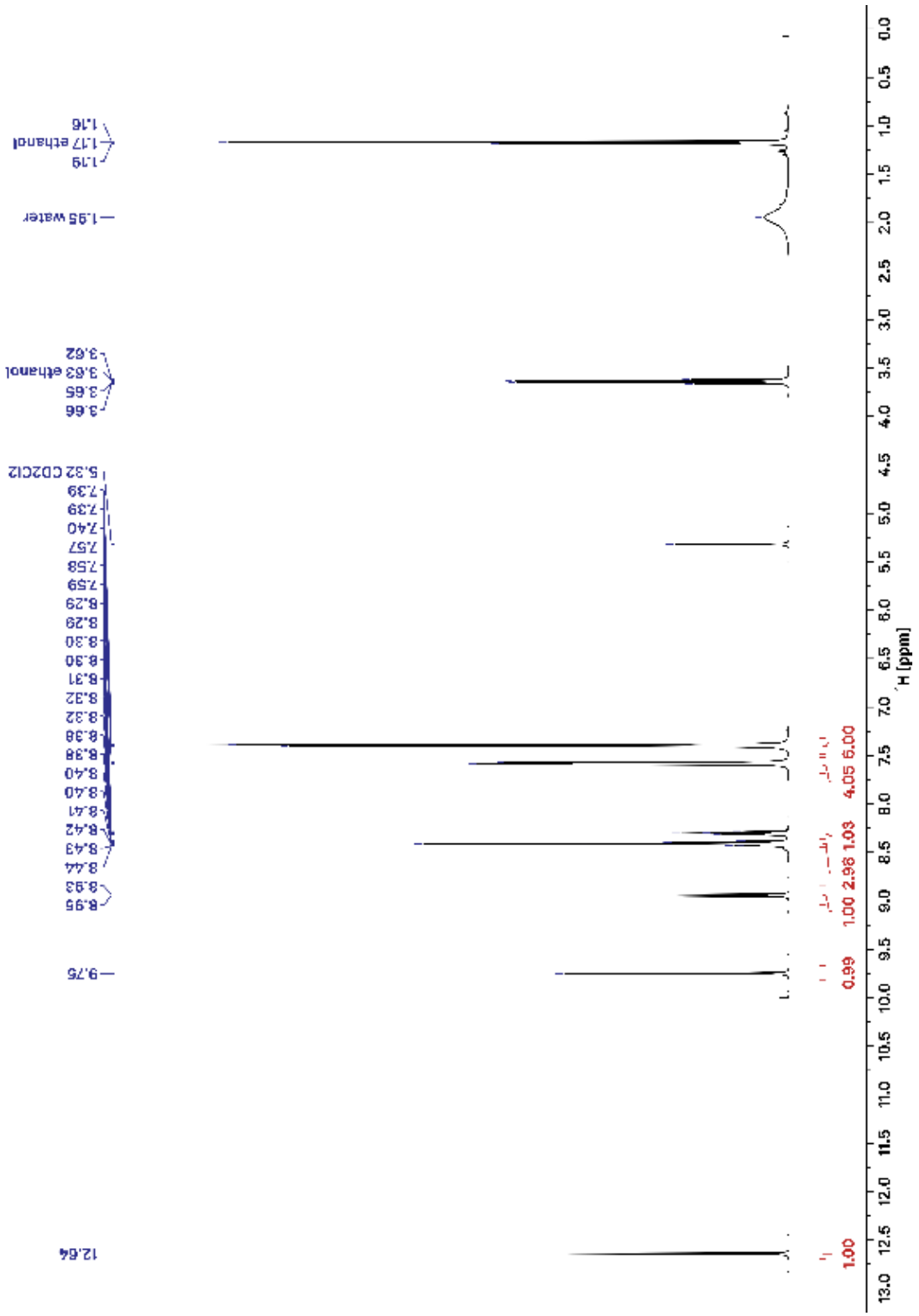

Figure 4.3: ^{1}H-NMR spectrum of **44** in CD_2Cl_2.

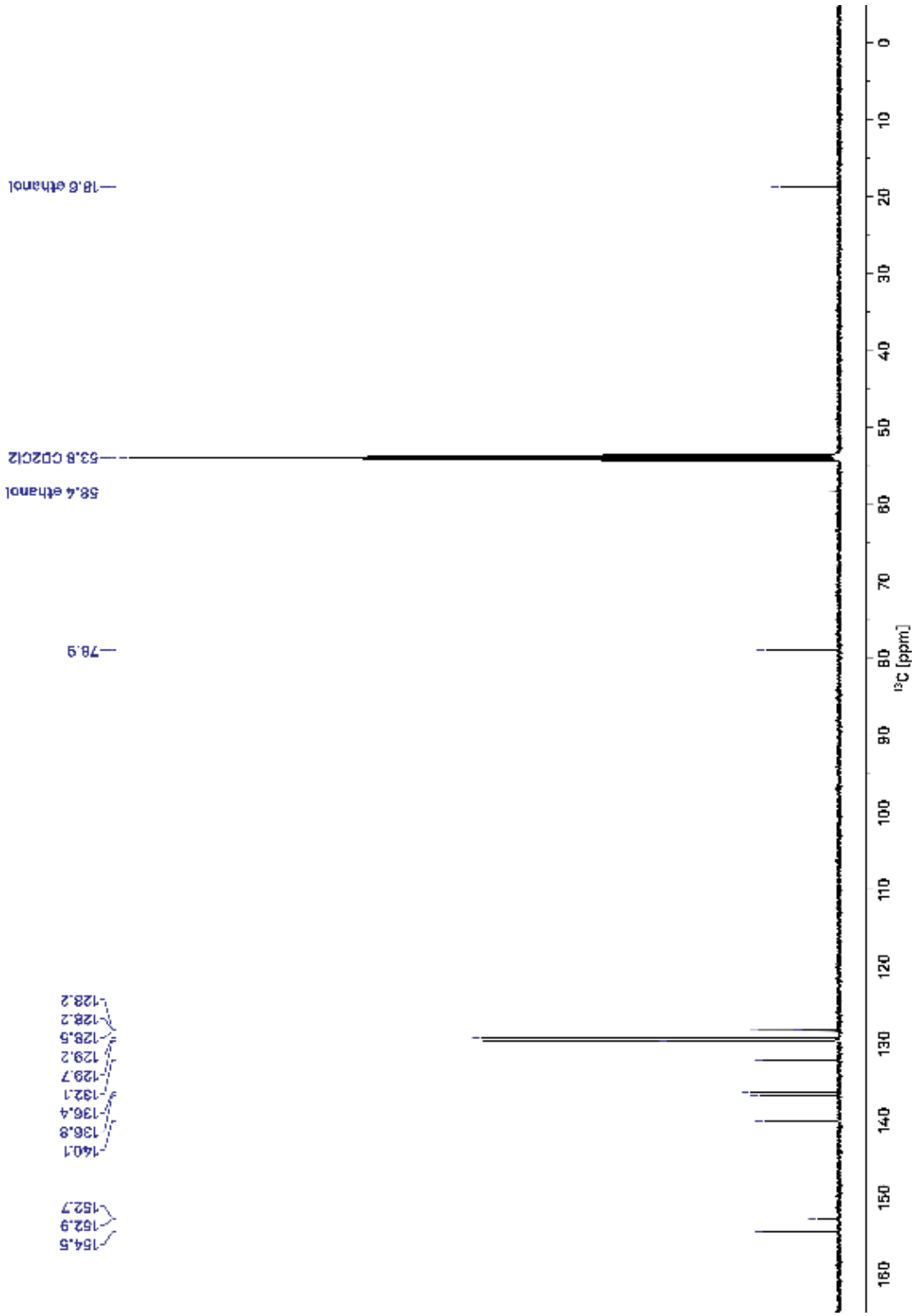

Figure 4.4: ^{13}C-NMR spectrum of **44** in CD_2Cl_2.

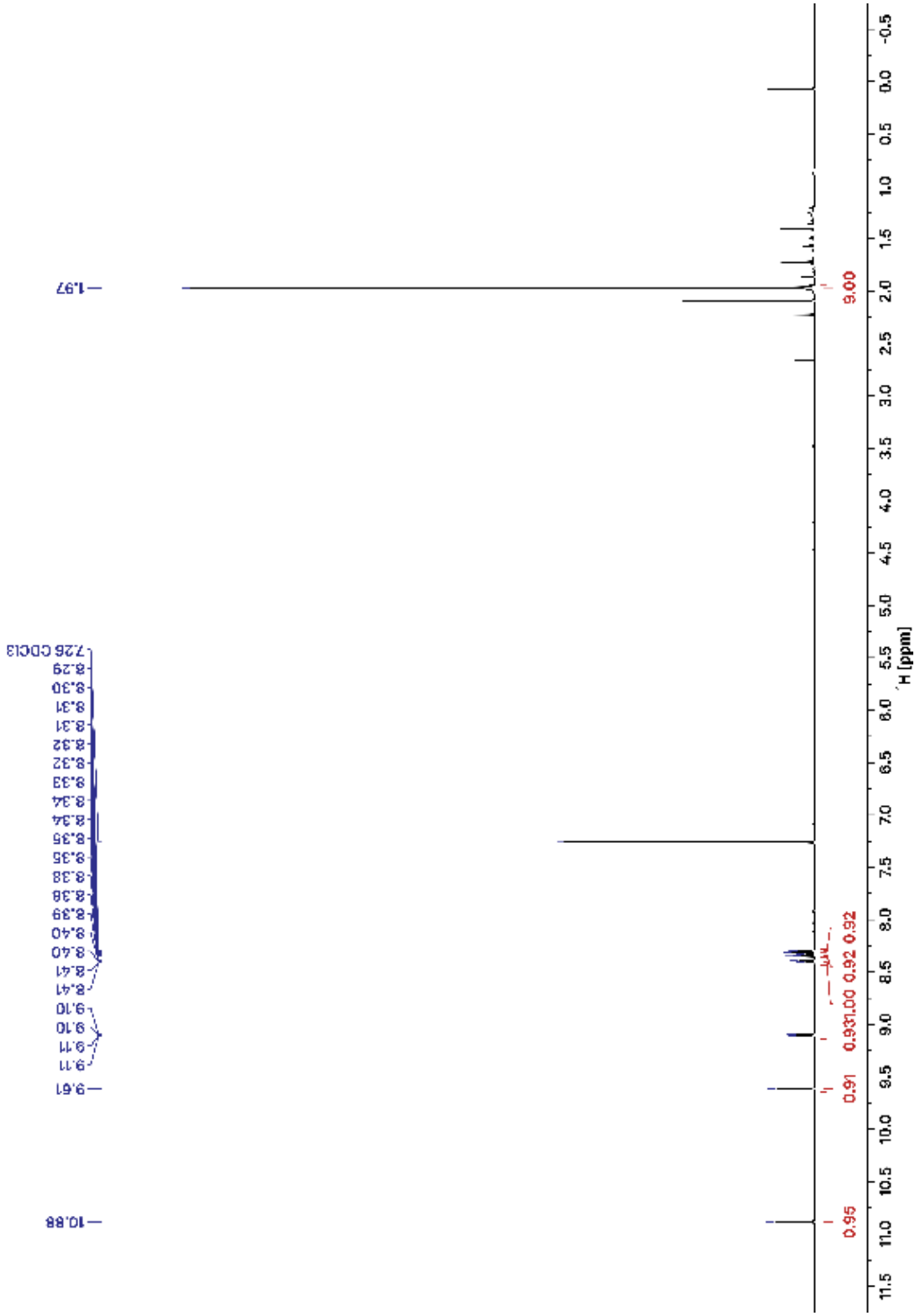

Figure 4.5: ^{1}H-NMR spectrum of **38** in $CDCl_3$.

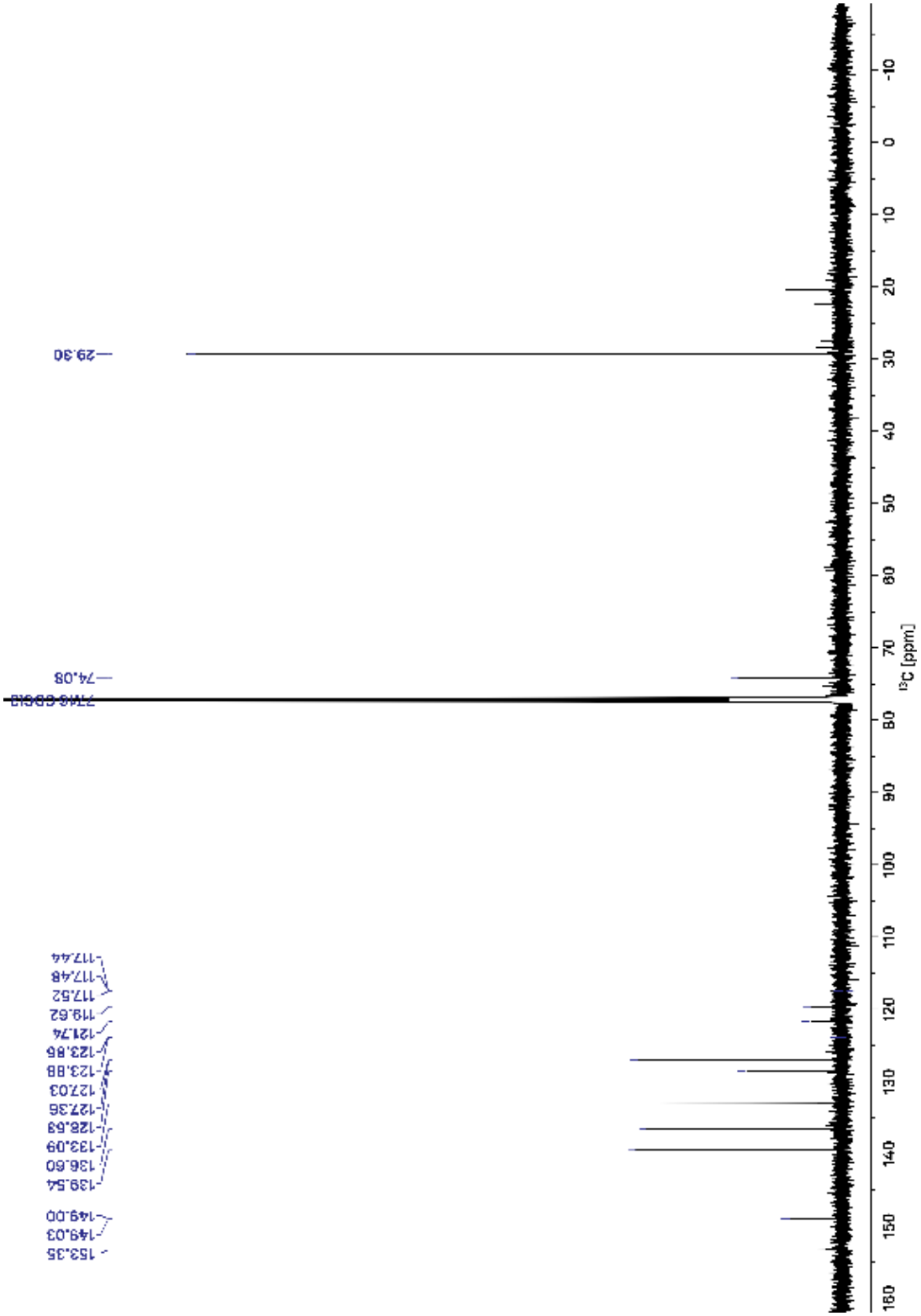

Figure 4.6: ^{13}C-NMR spectrum of **38** in $CDCl_3$.

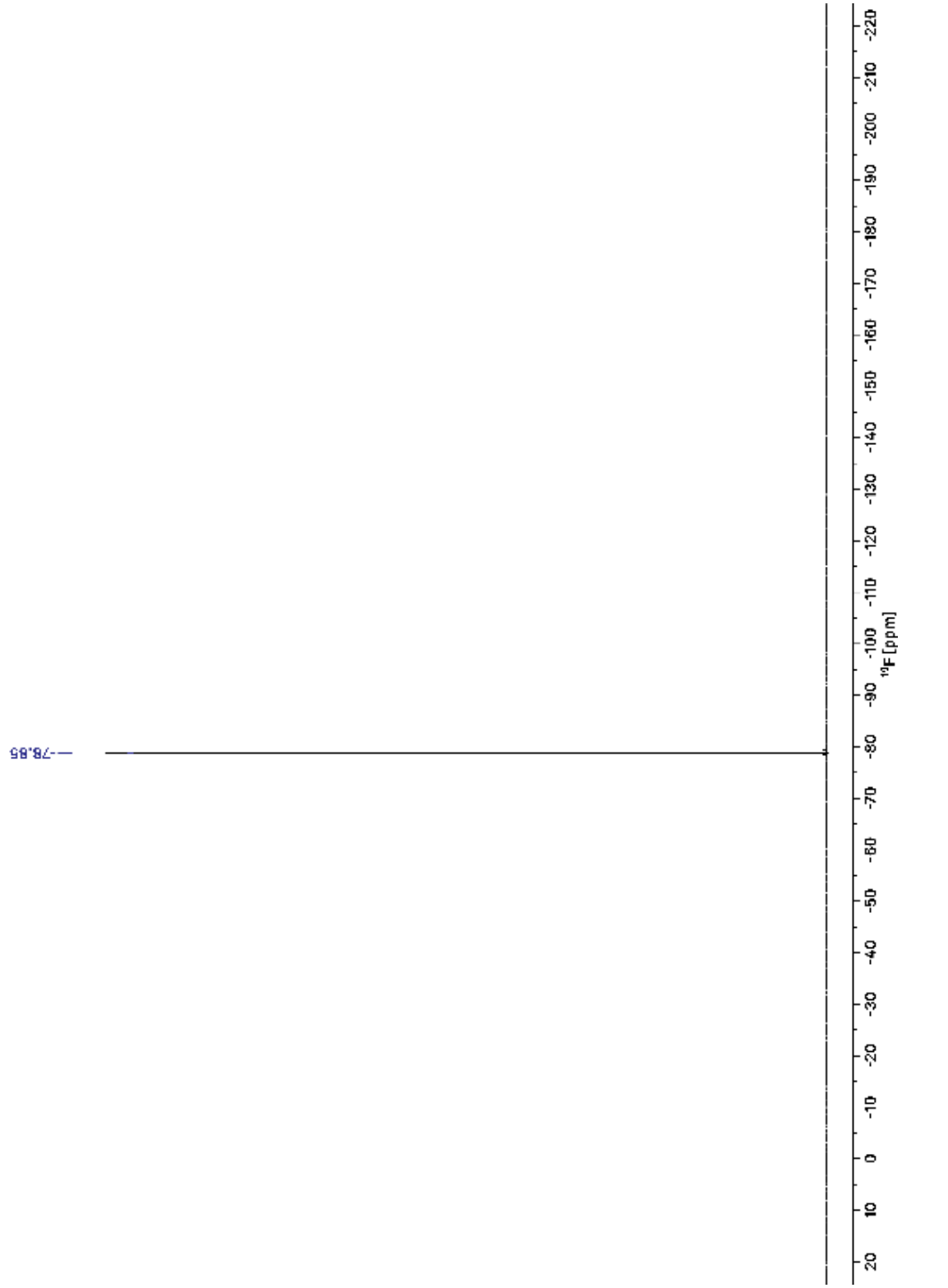

Figure 4.7: ^{19}F-NMR spectrum of **38** in $CDCl_3$.

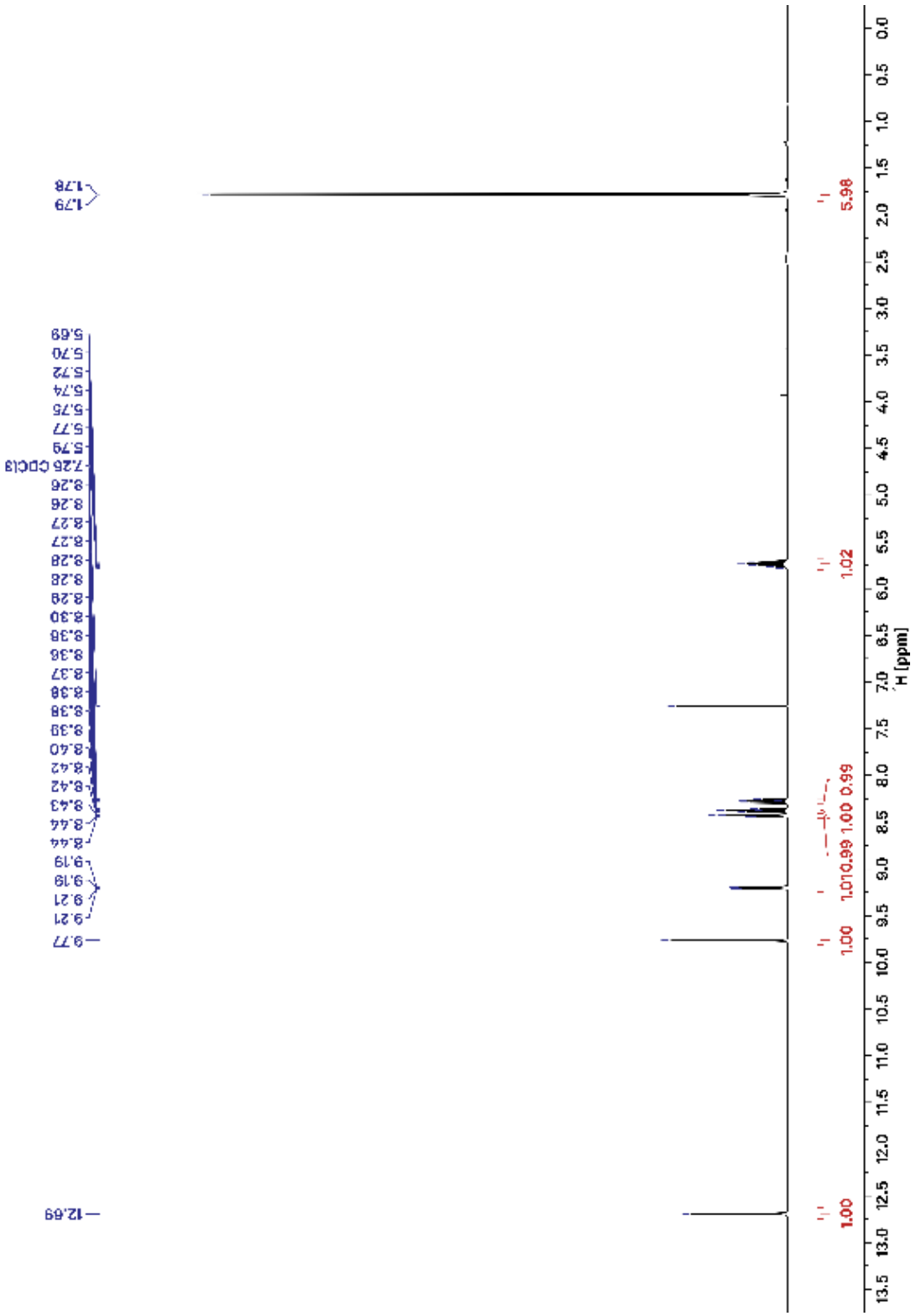

Figure 4.8: ^{1}H-NMR spectrum of **43** in $CDCl_3$.

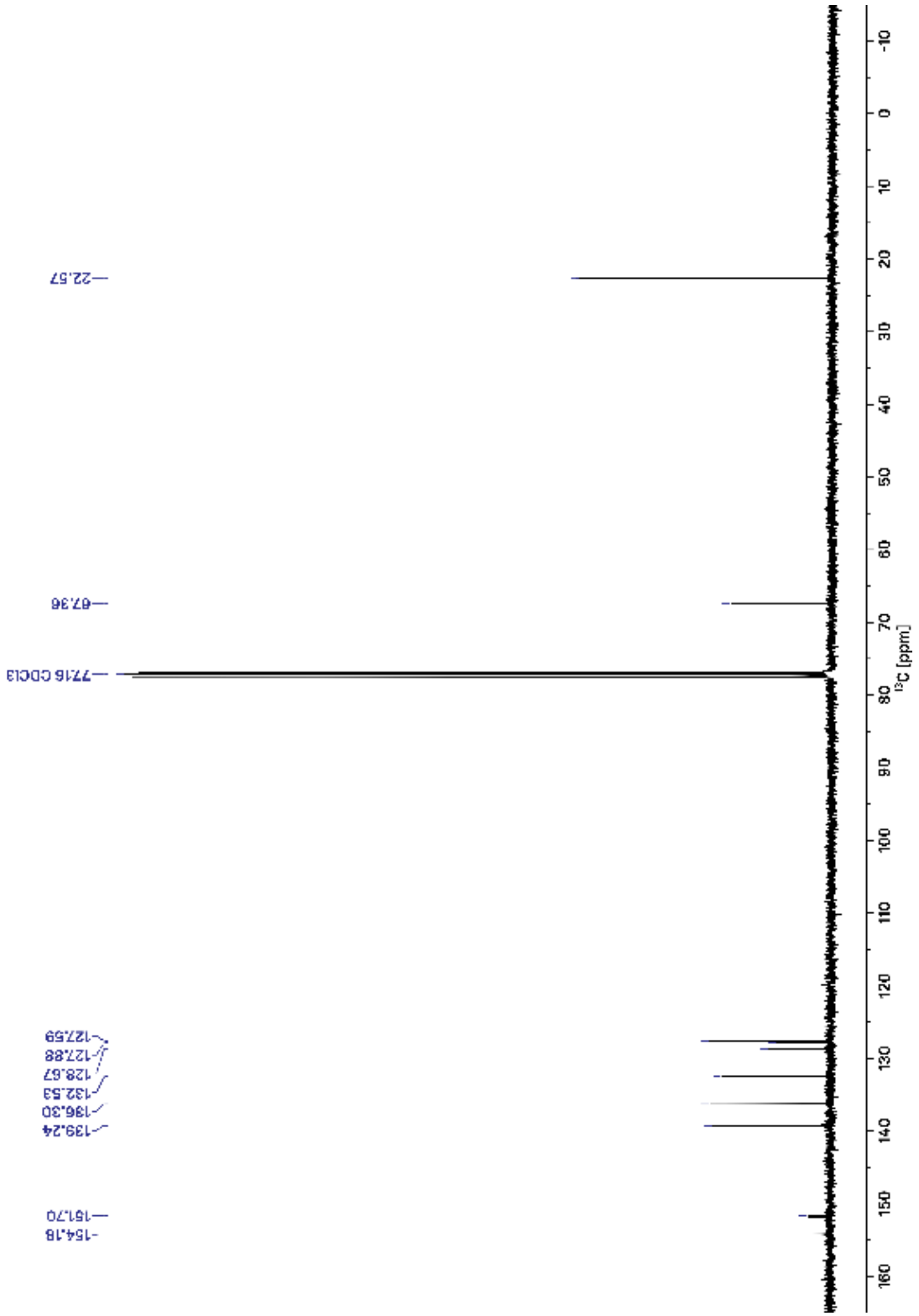

Figure 4.9: ^{13}C-NMR spectrum of **43** in $CDCl_3$.

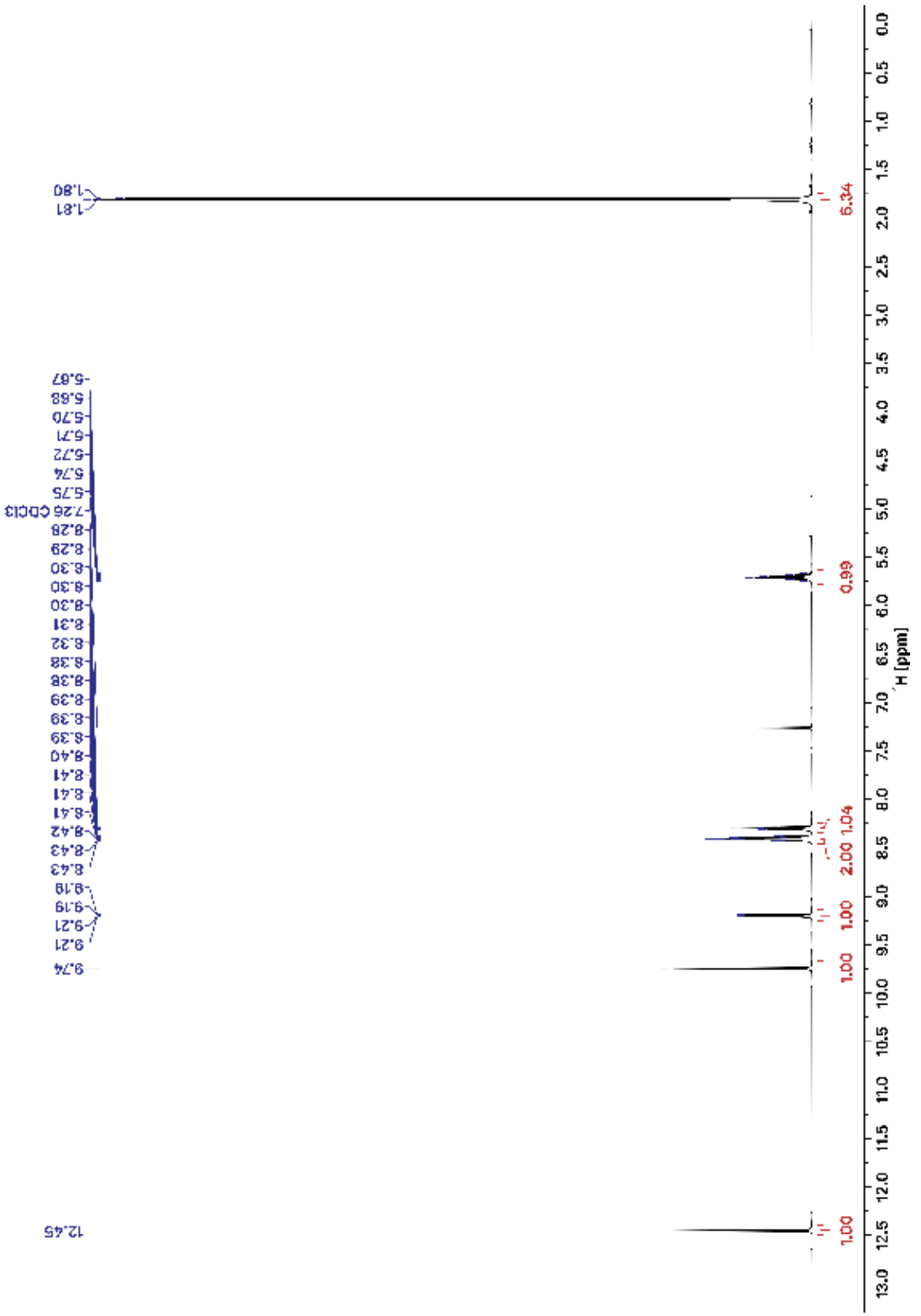

Figure 4.10: ^{1}H-NMR spectrum of **44** in $CDCl_3$.

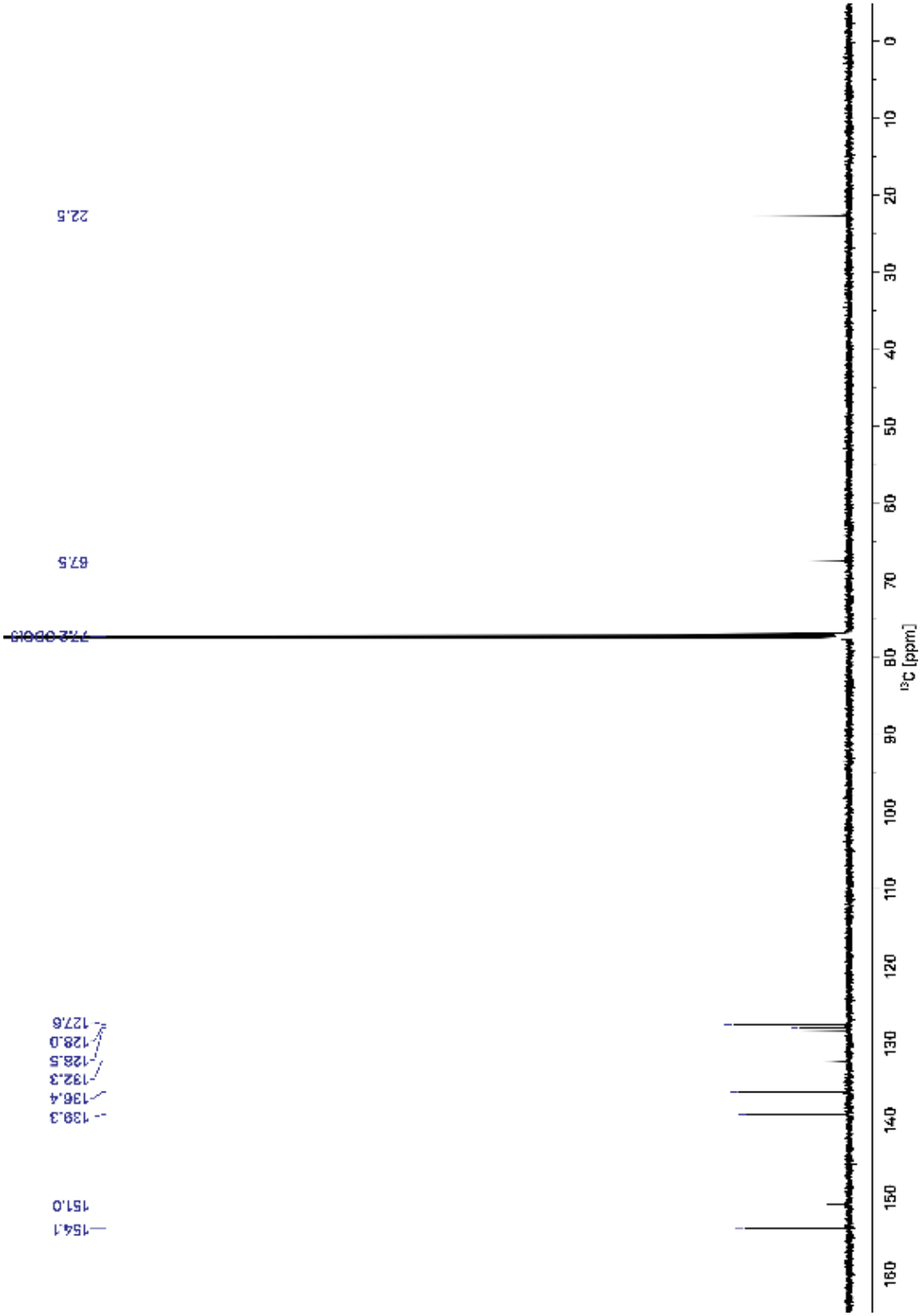

Figure 4.11: ^{13}C-NMR spectrum of **44** in $CDCl_3$.

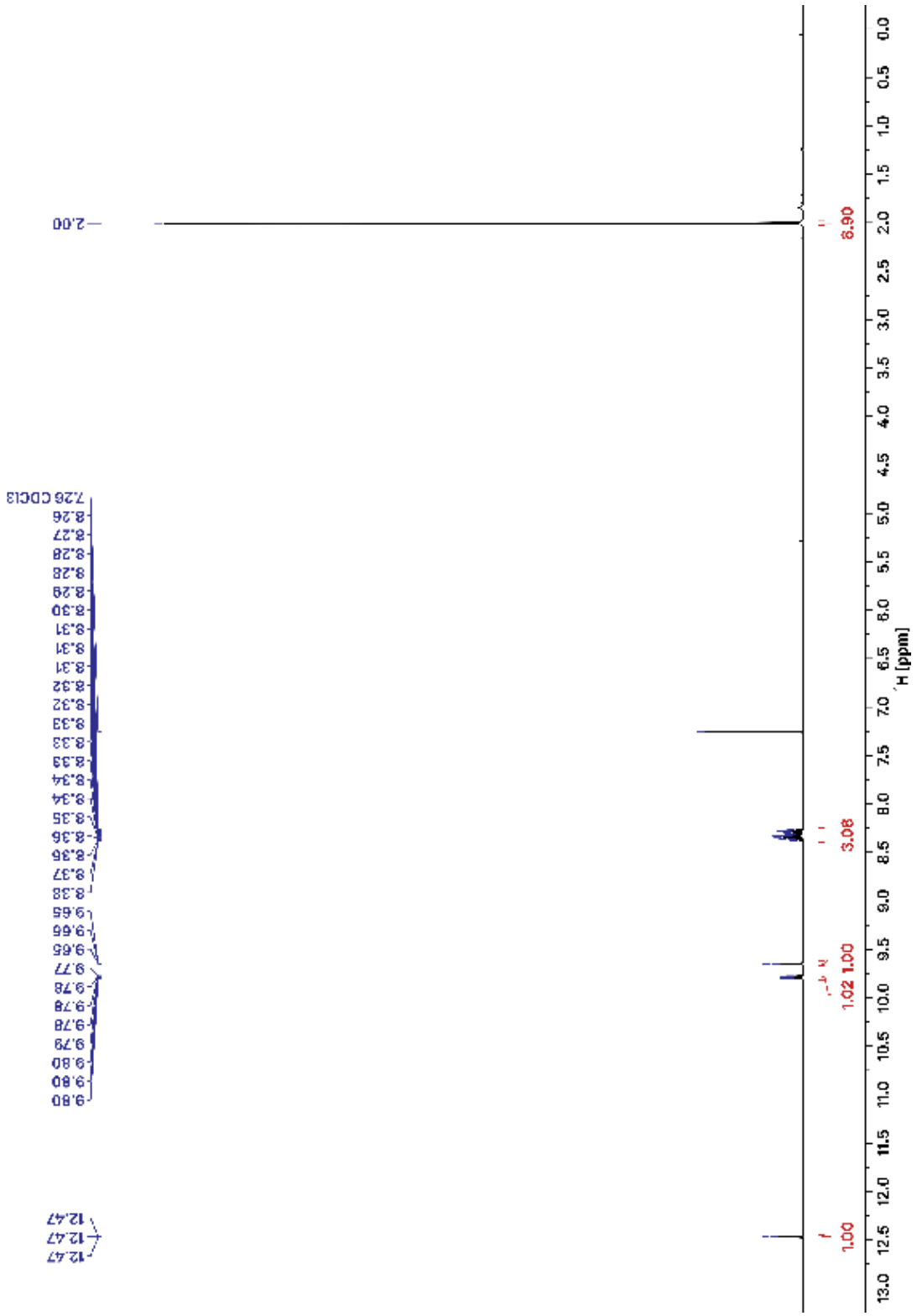

Figure 4.12: ^{1}H-NMR spectrum of **45** in $CDCl_3$.

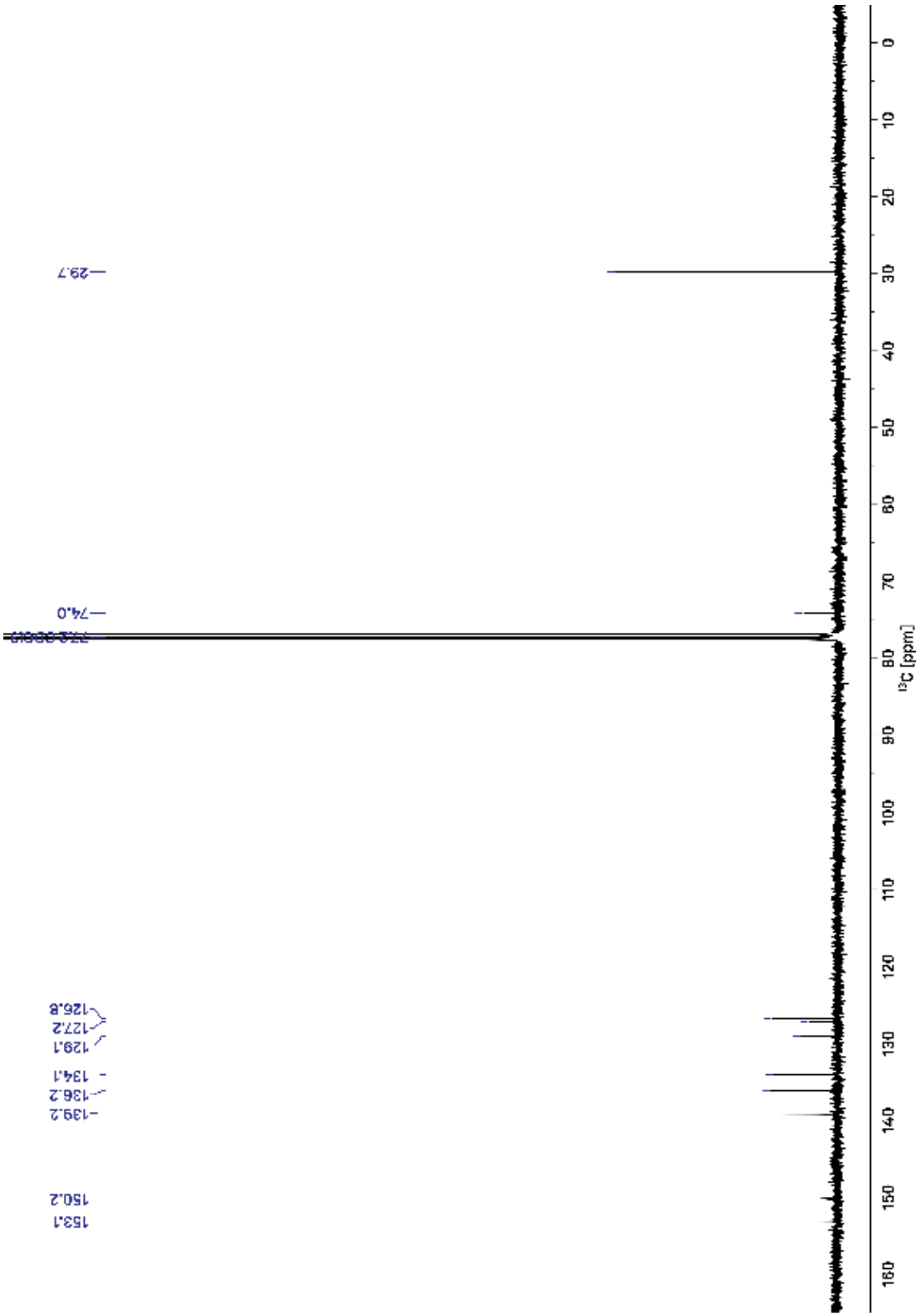

Figure 4.13: ^{13}C-NMR spectrum of **45** in $CDCl_3$.

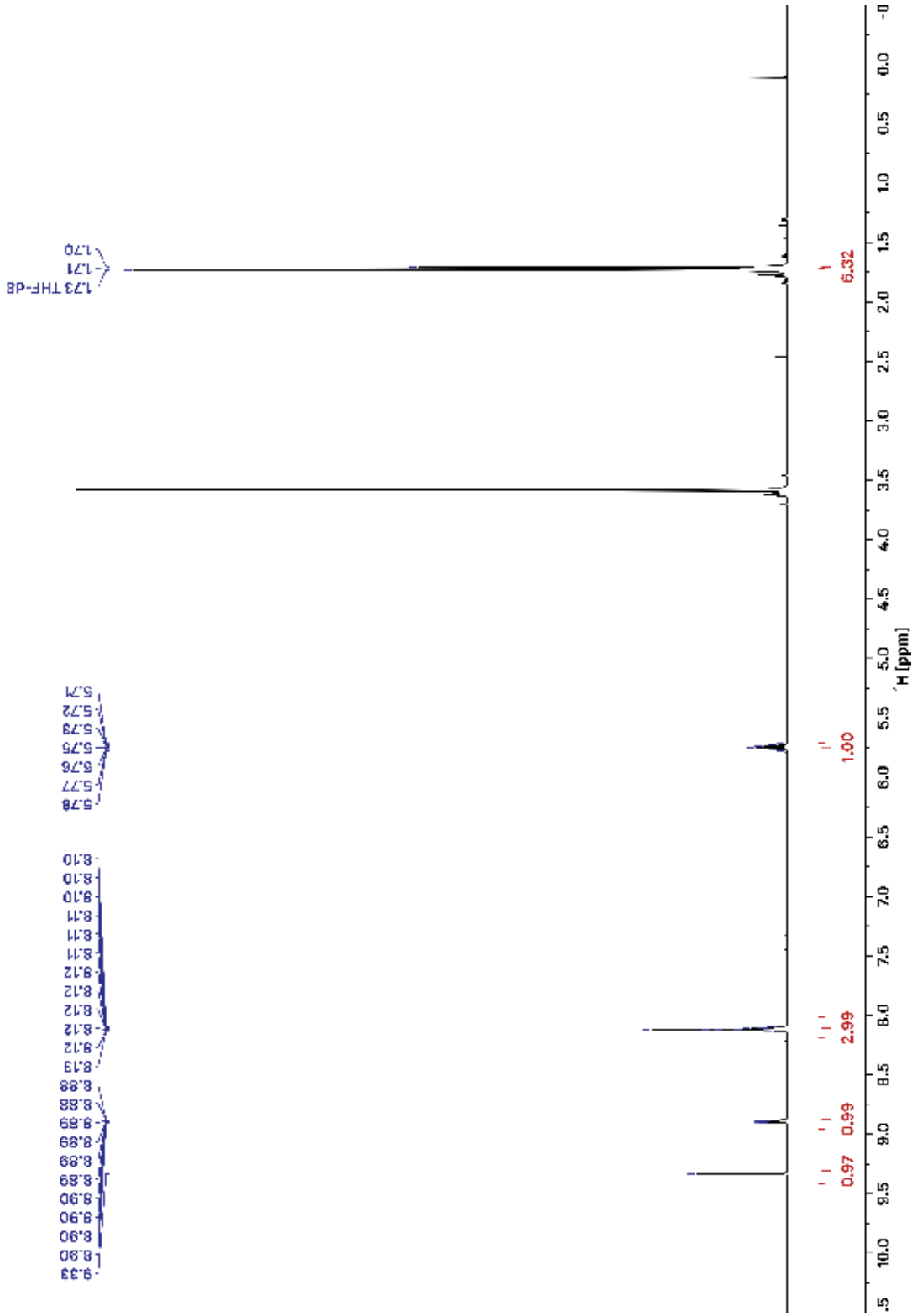

Figure 4.14: ^{1}H-NMR spectrum of **42** in THF-d_8.

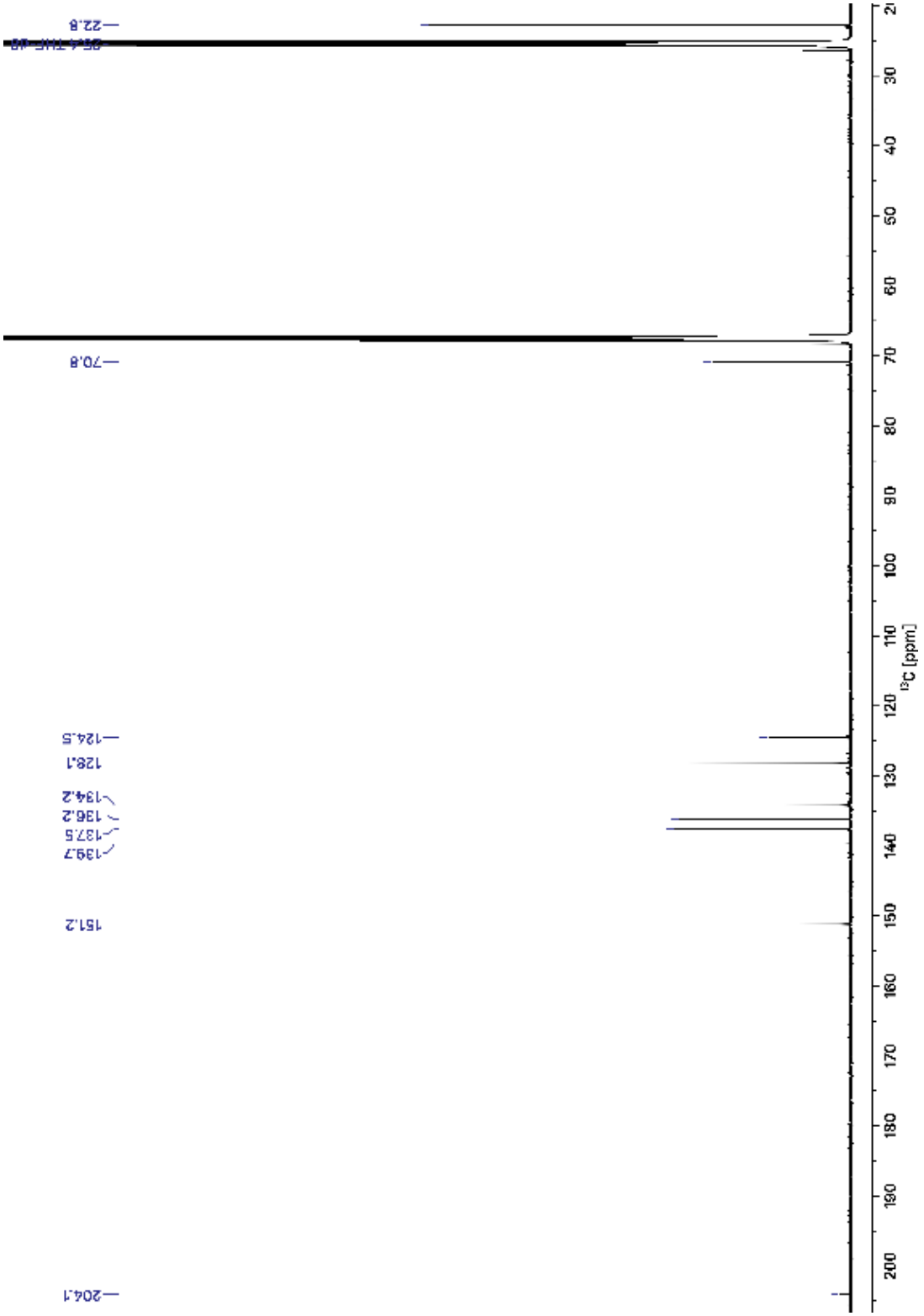

Figure 4.15: ^{13}C-NMR spectrum of **42** in THF-d_8.

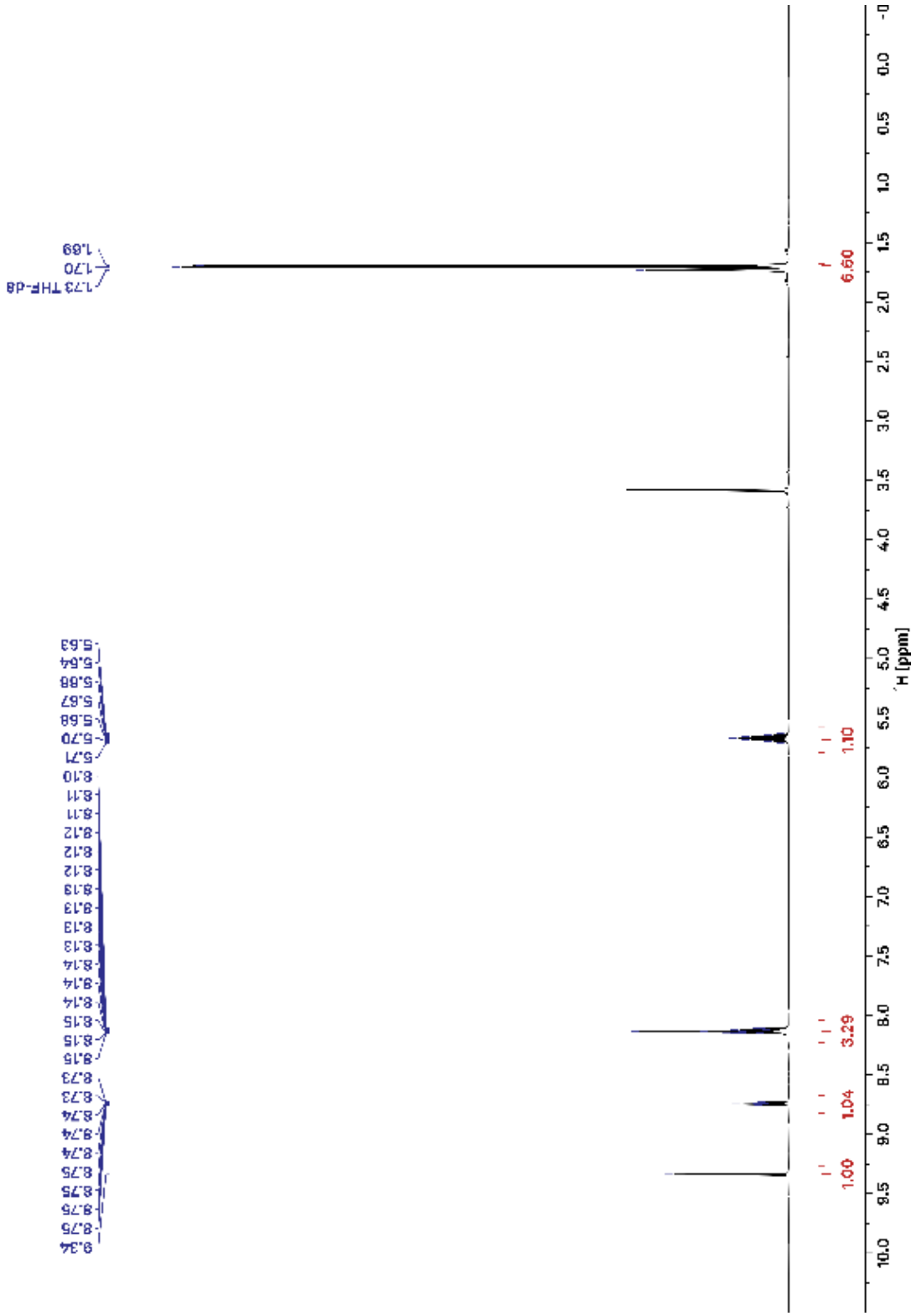

Figure 4.16: ^{1}H-NMR spectrum of **33a** in THF-d_8.

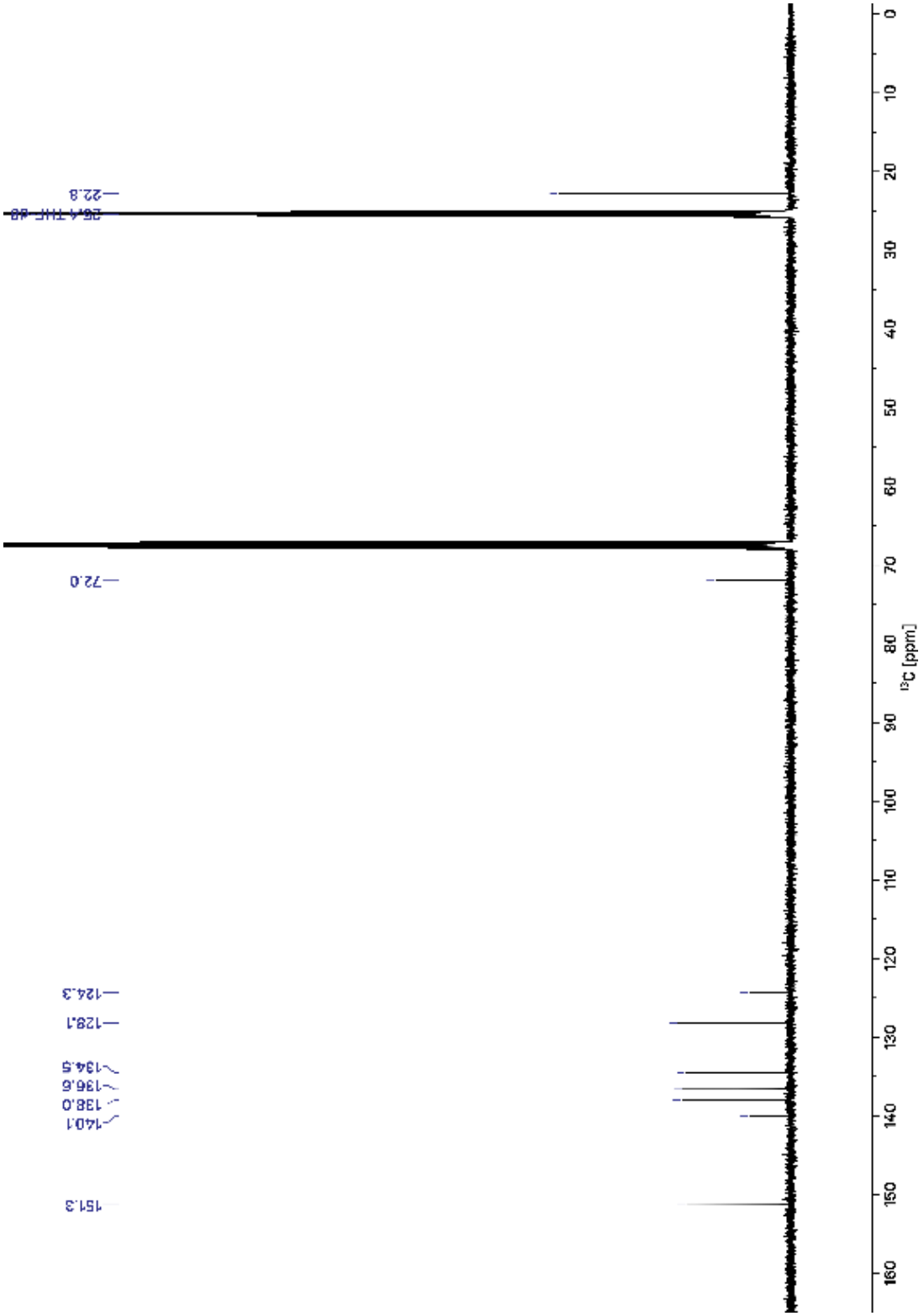

Figure 4.17: ^{13}C-NMR spectrum of **33a** in THF-d_8.

4.2.3 Single-crystal X-ray diffraction studies

Table 4.1: Selected bond lengths (in Å) and angels (in deg).

	33a	**46**	**47**	**42**	**48**
C1-Cu1	1.8911(36)	1.9020(2)	1.9363(34)	1.9152(17)	1.9105(24)
Cu1-X1	2.0952(18)	2.173(0)	2.5296(4)	2.3449(0)	2.4385(0)
Cu1-X1’			2.6798(4)	2.6087(0)	2.4428(6)
Cu1-Cu1’	3.2403(12)	3.4433(4)	2.7495(5)	2.8703(1)	3.1514(7)
C1-Cu1-X1	173.126(120)	162.987(59)	138.571(97)	146.647(48)	133.698(67)
C1-Cu1-X1’	-	-	116.656(105)	115.556(53)	126.967(73)
X1-Cu1-X1’	-	-	104.721(3)	97.790(0)	99.157(19)
N1-C1-C1’-N1’	-	-	30.337(294)	30.199(144)	168.895(264)
C1-Cu1-Cu1’-C1’	56.964(159)	56.836(83)	-	-	-

Table 4.2: Crystal data and X-ray experimental details.

Data	**33a**	**47**	**42**	**46**	**48**
empirical formula	$C_{11}H_{12}ClCuN_2$	$C_{22}H_{24}Br_2Cu_2N_4$	$C_{22}H_{24}I_2Cu_2N_4$	$C_{12}H_{14}ClCuN_2$	$C_{42}H_{32}Br_2Cu_2N_4$
formula weight [g·mol^{-1}]	271.22	631.36	725.36	285.25	879.64
colour/ crystal habit	yellow/ tabular	yellow/ tabular	orange/ tabular	yellow/ tabular	yellow/ tabular
temperature [K]	100(2)	100(2)	100(2)	100(2)	100(2)
λ [Å]	0.71073	0.71073	0.71073	0.71073	0.71073
crystal system	monoclinic	monoclinic	monoclinic	monoclinic	triclinic
space group	$P\,1\,2_1/c\,1$	$C\,1\,2/c\,1$	$C\,1\,2/c\,1$	$P\,1\,2_1/c\,1$	$P\,\overline{1}$
a [Å]	6.8576(15)	18.3346(5)	18.202(3)	9.822(2)	10.805(3)
b [Å]	18.382(4)	8.1827(2)	8.2559(15)	18.150(5)	11.942(4)
c [Å]	18.133(3)	15.1171(4)	15.912(3)	6.8831(9)	20.689(6)
α [deg]	90	90	90	90	73.934(8)
β [deg]	93.829(13)	97.1410(10)	96.987(11)	104.715(8)	88.167(11)
γ [deg]	90	90	90	90	68.954(9)
volume [Å^3]	2280.7(8)	2250.37(10)	2373.4(7)	1186.8(5)	2387.4(12)
Z	8	4	8	4	2
calc. density [Mg·m^{-3}]	1.580	1.863	2.030	2.596	1.524
absorption coefficient [mm^{-1}]	2.116	5.458	4.410	2.037	2.613
F(0 0 0)	1104	1248	1392	584	1120
recorded 2θ [deg]	2.98–26.02	2.73–36.35	2.58–26.73	3.10–26.82	1.89–25.68

Table 4.2: Continued: Crystal data and X-ray experimental details.

Data	**33a**	**47**	**42**	**46**	**48**
independent reflexions	4493	5453	2524	2535	9061
goodness-of-fit on F^2	1.240	1.006	1.161	1.092	1.090
R_1 [I>2σ(I)]	0.0446	0.0287	0.0263	0.0313	0.0310
ωR^2 (all data)	0.1038	0.0736	0.0676	0.0801	0.0667
min/max transmission	1.197/–0.708	0.842/–0.920	1.588/–0.691	1.327/–0.346	0.596/–0.766

4.2.4 Photophysical measurements

Table 4.3: Photophysical Date

	T [K]	λ_{max} [nm]	τ [μs]	$\langle\tau\rangle_{amp}$ [μs]	Φ_{em}	k_r [10^3 s^{-1}]
33a	295	710	0.31 (87.7), 38.41 (12.3)	0.36	<0.01	<27.8
	77	760	5.78 (52.4), 17.97 (36.1), 154.72 (11.5)	8.96	-	-
47	295	600	2.07 (9.8), 6.07 (54.2), 11.41 (36.0)	7.60	0.12	15.8
42	295	595	1.79 (9.1), 6.62 (46.3), 14.73 (44.6)	6.60	0.06	9.1

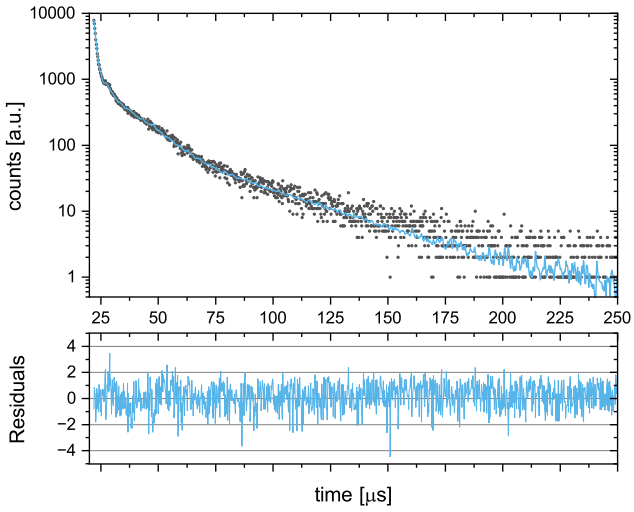

(a)

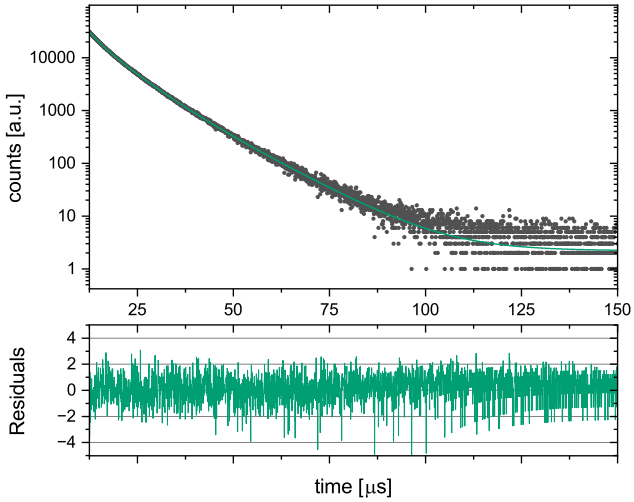

(b)

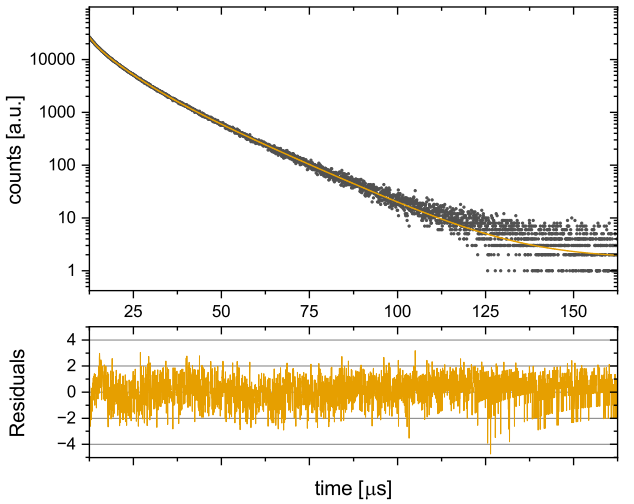

(c)

Figure 4.18: Decays, fits and residuals of **33a** (a), **47** (b) and **42** (c).

4.2.5 Computational Studies

Molecular Coordinates

Table 4.4: Cartesian coordinates of **33a** at optimized ground-state geometry.

atom	x	y	z
H	3.749509	6.904816	1.863538
H	4.374594	7.352420	0.290573
H	4.525616	8.501459	1.629355
C	4.556927	7.443169	1.362403
Cl	5.421182	2.198375	2.527334
H	5.863833	5.770863	1.496819
C	5.890796	6.847270	1.683768
Cu	5.929301	4.133348	3.214378
N	6.177323	6.952312	3.149402
C	6.237484	5.865085	3.918603
N	6.310237	8.268608	3.530580
C	6.533541	6.122316	5.307098
H	6.549934	4.057036	5.859594
C	6.554418	8.475219	4.793247
H	6.654957	9.518538	5.077103
C	6.664958	5.070859	6.226785
C	6.685827	7.445440	5.767768
H	6.859501	7.306039	-0.166634
C	6.951541	5.319019	7.537991
C	6.953912	7.699268	7.117616
C	7.032008	7.472727	0.897484
H	7.057452	8.723348	7.458757
H	7.059465	4.498038	8.236105
C	7.081371	6.650002	7.996451
H	7.085725	8.546706	1.078334
H	7.293832	6.839184	9.041977
H	7.989025	7.019111	1.162767

Table 4.5: Cartesian coordinates of **33a** at optimized T_1-geometry.

atom	x	y	z
H	3.958720	6.495357	1.852990
H	4.484320	6.937252	0.225601
H	4.409160	8.172323	1.497926
C	4.649283	7.128284	1.287141
Cl	4.975111	2.595324	2.640422
H	6.305624	5.776990	1.472977
C	6.094417	6.834829	1.658434
Cu	5.041006	4.511149	3.483644
N	6.299031	6.998468	3.097332
C	6.188984	5.910154	3.944390
N	6.326789	8.260015	3.540023
C	6.522268	6.085396	5.310401
H	6.556546	4.008858	5.889868
C	6.514218	8.458326	4.801277
H	6.564681	9.499738	5.103197
C	6.673786	5.032599	6.229371
C	6.695663	7.415697	5.776207
H	6.956192	7.476478	-0.195081
C	6.982213	5.300179	7.546981
C	7.005336	7.661224	7.107459
C	7.075875	7.679551	0.870546
H	7.121757	8.686512	7.443216
H	7.098703	4.476083	8.241570
C	7.150974	6.609619	7.998360
H	6.898859	8.740892	1.045512
H	7.390482	6.801147	9.036619
H	8.104272	7.448132	1.152813

Table 4.6: Cartesian coordinates of **47** at optimized ground-state geometry.

atom	x	y	z
H	-7.534281	11.595485	0.579436
H	-7.202425	9.197061	0.067307
C	-6.688531	11.063501	0.999286
C	-6.508016	9.726731	0.709789

Table 4.6: Continued: Cartesian coordinates of **47** at optimized ground-state geometry.

atom	x	y	z
H	-5.970946	12.784736	2.080779
C	-5.800127	11.740220	1.849868
H	-5.770776	7.097512	0.332877
C	-5.393739	9.054490	1.238842
C	-5.109958	7.684368	0.964020
C	-4.716548	11.083961	2.391744
C	-4.477966	9.728710	2.067454
N	-4.076248	7.049615	1.421668
H	-4.016191	11.589329	3.048028
C	-3.294419	9.055467	2.561716
H	-3.237140	5.612626	3.880661
N	-3.211520	7.767784	2.220076
H	-2.862023	4.984335	2.267073
C	-2.472013	5.562734	3.103291
C	-2.041879	6.948360	2.654850
Cu	-1.877772	9.965856	3.474585
H	-1.639667	7.510214	3.501193
H	-1.604737	5.041237	3.511173
H	-1.449275	6.386304	0.664790
Br	-1.049239	10.741623	5.526351
C	-1.022183	6.887795	1.536084
H	-0.754919	6.251111	5.668305
H	-0.690320	7.889098	1.253984
H	-0.310154	7.880580	6.191337
H	-0.149783	6.318806	1.862922
C	0.081870	6.887373	5.963406
Br	0.109724	10.741975	1.974132
H	0.534654	6.453139	6.857859
H	0.668667	5.046657	3.971256
H	0.700090	7.509779	3.998063
Cu	0.938142	9.965682	4.025684
C	1.101608	6.947848	4.844646
C	1.531436	5.562445	4.395850
H	1.908197	4.977796	5.233905
N	2.271453	7.766745	5.279615

Table 4.6: Continued: Cartesian coordinates of **47** at optimized ground-state geometry.

atom	x	y	z
H	2.308575	5.614734	3.630980
C	2.354608	9.054641	4.938314
H	3.079811	11.584011	4.445617
N	3.135957	7.048193	6.077854
C	3.538219	9.727508	5.432783
C	3.776982	11.082807	5.108880
C	4.169714	7.683120	6.535710
C	4.453768	9.052888	6.261248
H	4.829832	7.097654	7.168344
C	4.860621	11.738698	5.650968
H	5.031382	12.783809	5.421639
C	5.568109	9.724767	6.790518
C	5.748810	11.061587	6.501402
H	6.269959	9.207332	7.435637
H	6.594620	11.582851	6.931607

Table 4.7: Cartesian coordinates of **42** at optimized ground-state geometry.

atom	x	y	z
H	1.665748	0.628143	0.643685
H	1.994969	3.009553	0.089932
C	2.502955	1.169511	1.069240
C	2.680522	2.498701	0.756983
H	3.192238	-0.520175	2.200635
C	3.364573	0.519079	1.947782
H	3.407836	5.128590	0.346176
C	3.780065	3.189604	1.289224
C	4.061433	4.559708	1.001425
C	4.447147	1.187804	2.491608
C	4.681302	2.534639	2.143675
N	5.069944	5.219852	1.478735
H	5.136757	0.698053	3.170415
C	5.844665	3.223008	2.653743
H	5.851443	6.563794	4.084292

Table 4.7: Continued: Cartesian coordinates of **42** at optimized ground-state geometry.

atom	x	y	z
N	5.927600	4.507442	2.308128
H	6.150436	7.280384	2.489376
C	6.590578	6.688067	3.290397
C	7.074229	5.342523	2.765523
Cu	7.300405	2.315094	3.552547
H	7.443041	7.233925	3.698266
H	7.508829	4.755699	3.578287
H	7.606684	6.032919	0.804223
I	7.887558	1.512768	5.878729
C	8.063701	5.499104	1.640187
H	8.326692	6.110662	5.926531
H	8.422767	4.527014	1.296410
H	8.777968	4.529577	6.568115
H	8.925034	6.075763	1.983344
C	9.169616	5.499817	6.255960
I	9.346932	1.512143	2.018885
H	9.638851	5.999282	7.106552
H	9.723939	4.757382	4.318285
H	9.790677	7.234319	4.196750
Cu	9.933416	2.315198	4.345103
C	10.159980	5.342888	5.131275
C	10.642716	6.688254	4.605360
H	11.084833	7.280649	5.405306
N	11.306517	4.507959	5.588574
H	11.381804	6.561742	3.812019
C	11.389357	3.223423	5.243010
H	12.099237	0.701187	4.723620
N	12.164266	5.220659	6.418103
C	12.552827	2.535222	5.753673
C	12.787096	1.188287	5.406552
C	13.171884	4.560673	6.895030
C	13.454167	3.190487	6.608270
H	13.824676	5.125803	7.553949
C	13.868787	0.519752	5.949987
H	14.041514	-0.519923	5.698054

Table 4.7: Continued: Cartesian coordinates of **42** at optimized ground-state geometry.

atom	x	y	z
C	14.552827	2.499770	7.140147
C	14.730509	1.170470	6.828686
H	15.242520	2.999451	7.812309
H	15.568481	0.637562	7.261976

Table 4.8: Cartesian coordinates of **42** at optimized T_1-geometry.

atom	x	y	z
H	2.375324	0.251965	-0.203493
H	2.042498	2.709975	0.045926
C	3.078418	0.845912	0.366274
C	2.892963	2.219976	0.510173
H	4.340732	-0.820277	0.856795
C	4.186593	0.247819	0.966842
H	2.851827	4.940241	0.927386
C	3.787838	2.979702	1.239529
C	3.669373	4.405926	1.402852
C	5.093494	0.983269	1.699772
C	4.923206	2.379210	1.866376
N	4.480611	5.136466	2.082834
H	5.949075	0.496244	2.156690
C	5.790725	3.192039	2.595126
H	5.191896	5.909187	5.016043
N	5.502268	4.540527	2.717768
H	5.073471	7.078003	3.691212
C	5.759445	6.441202	4.250497
C	6.454563	5.462044	3.324791
Cu	7.385012	2.527869	3.431938
H	6.499801	7.073507	4.745712
H	7.106741	4.830037	3.936749
H	6.653358	6.753657	1.612361
I	7.452629	2.461453	5.980990
C	7.293274	6.150898	2.260058
H	9.359661	7.022534	5.094564

Table 4.8: Continued: Cartesian coordinates of **42** at optimized T_1-geometry.

atom	x	y	z
H	7.818324	5.415602	1.646186
H	9.515110	5.821782	6.382709
H	8.033061	6.810212	2.721411
C	10.064815	6.375725	5.619240
I	9.510255	2.101245	2.111996
H	10.816163	7.003317	6.101567
H	9.947957	4.776436	4.199866
H	10.713291	6.732569	2.933980
Cu	9.678489	2.544399	4.666030
C	10.711336	5.431615	4.626857
C	11.432758	6.137389	3.498282
H	12.209407	6.799391	3.882658
N	11.630212	4.508525	5.331973
H	11.884517	5.416988	2.813861
C	11.341110	3.216321	5.432400
H	11.237914	0.586713	5.883841
N	12.709932	5.147810	5.829612
C	12.311050	2.428903	6.129926
C	12.131232	1.046788	6.291984
C	13.581738	4.437410	6.462034
C	13.464644	3.036060	6.658290
H	14.437718	4.982680	6.848251
C	13.077384	0.304527	6.954767
H	12.939727	-0.762947	7.077421
C	14.423264	2.270249	7.334526
C	14.226271	0.918207	7.476877
H	15.309225	2.749236	7.736362
H	14.962847	0.316723	7.996379

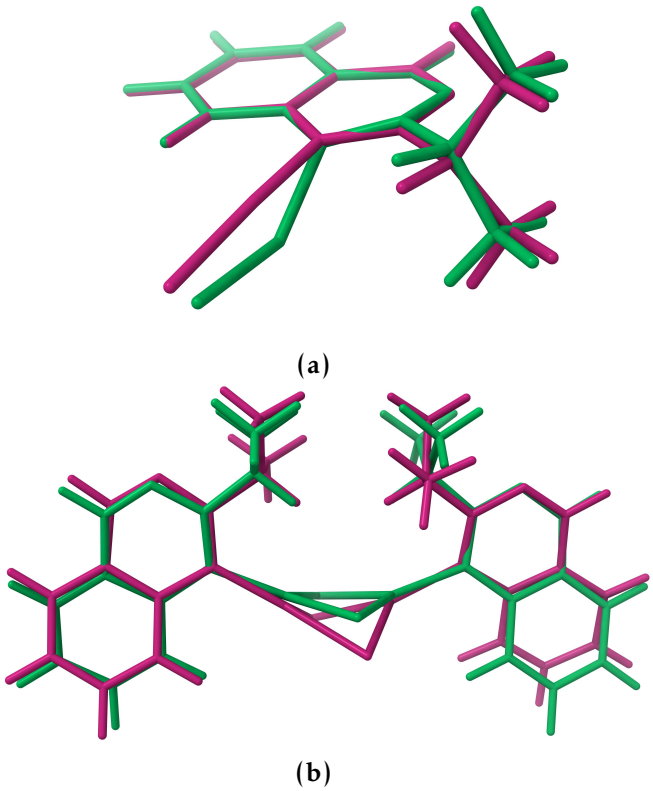

(a)

(b)

Figure 4.19: Superimposed ground-state (purple) and T_1-optimized (green) structures of **33a** (a) and **42** (b).

IRI plots

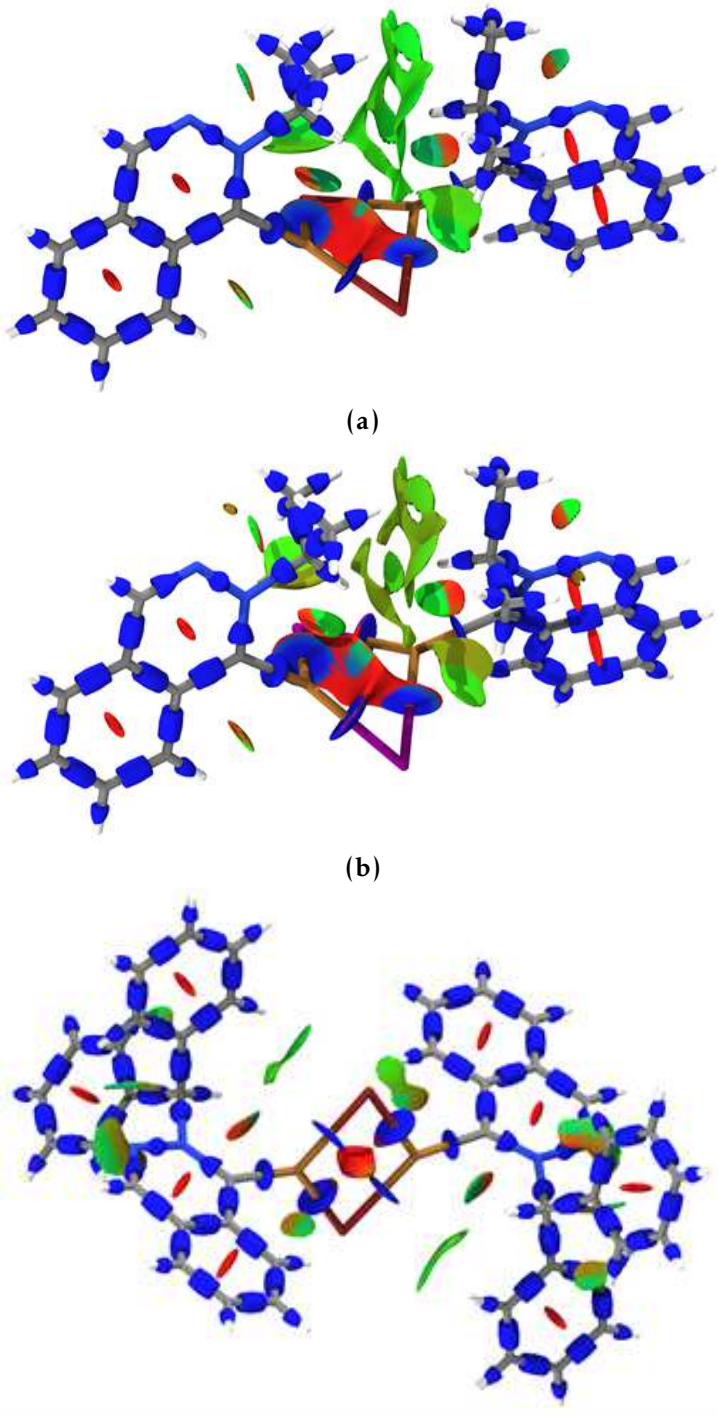

(a)

(b)

(c)

Figure 4.20: 3D IRI surface plots of **47** (a), **42** (b) and **48** (c).

TD-DFT Data

Table 4.9: Transition electron density differences of selected absoptions with their respective calculated wavelength and oscilator strength. Blue is a loss of electron density, gold is a gain thereof.

33a	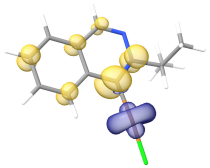	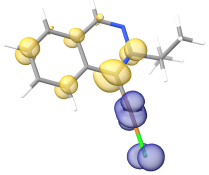	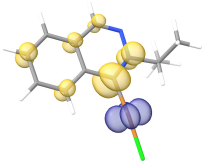	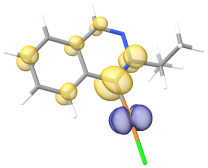	
	$S_0 \rightarrow S_1$	$S_0 \rightarrow S_4$	$S_0 \rightarrow S_5$	$S_0 \rightarrow S_6$	
	382.5 nm	314.9 nm	306.9 nm	305.9 nm	
	$f_{osc} = 0.008$	$f_{osc} = 0.133$	$f_{osc} = 0.007$	$f_{osc} = 0.016$	
47	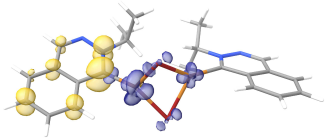	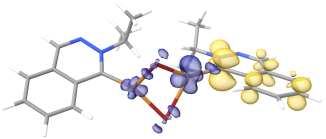	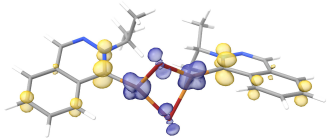	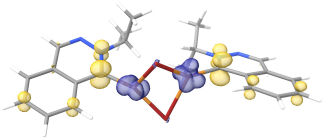	
	$S_0 \rightarrow S_1$	$S_0 \rightarrow S_2$	$S_0 \rightarrow S_5$	$S_0 \rightarrow S_{17}$	
	462.3 nm	462.1 nm	365.7 nm	315.5 nm	
	$f_{osc} = 0.015$	$f_{osc} = 0.024$	$f_{osc} = 0.145$	$f_{osc} = 0.151$	
42	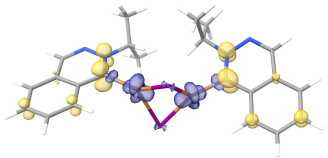	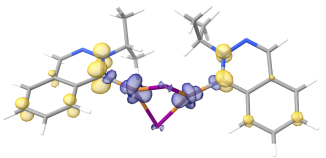	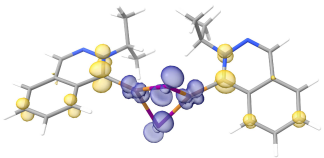	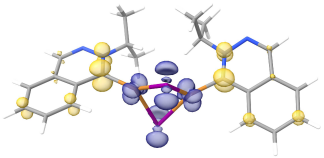	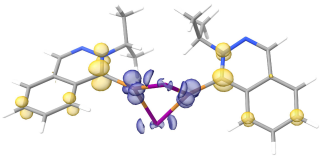
	$S_0 \rightarrow S_1$	$S_0 \rightarrow S_2$	$S_0 \rightarrow S_5$	$S_0 \rightarrow S_{13}$	$S_0 \rightarrow S_{17}$
	466.0 nm	465.5 nm	381.4 nm	328.7 nm	311.1 nm
	$f_{osc} = 0.035$	$f_{osc} = 0.003$	$f_{osc} = 0.178$	$f_{osc} = 0.017$	$f_{osc} = 0.173$

Table 4.10: TD-DFT absorption data of **33a** at optimized ground-state geometry.

State	Energy (cm-1)	Wavelength (nm)	fosc	T2 (au**2)	TX (au)	TY (au)	TZ (au)
1	25478.3	392.5	0.00808324	0.10445	0.31602	-0.02062	-0.06443
2	29817.0	335.4	0.00037738	0.00417	-0.06059	0.01965	0.01046
3	29937.6	334.0	0.00004347	0.00048	0.01524	-0.01398	-0.00708
4	31758.3	314.9	0.13279827	1.37661	0.21581	1.05453	0.46691
5	32581.8	306.9	0.00652945	0.06597	-0.06541	0.24755	0.02034
6	32689.6	305.9	0.01554313	0.15653	0.02465	0.28321	0.27516
7	33947.8	294.6	0.02849694	0.27635	0.11413	0.18380	0.47911
8	34522.0	289.7	0.00045173	0.00431	0.00545	-0.04847	-0.04392
9	37300.1	268.1	0.05612680	0.49538	-0.12518	0.11795	-0.68249
10	37792.4	264.6	0.00063097	0.00550	0.01617	-0.06226	-0.03686
11	38073.9	262.6	0.01759462	0.15213	0.00654	-0.37557	0.10508
12	38828.5	257.5	0.00187270	0.01588	-0.03413	-0.00034	-0.1213
13	39088.8	255.8	0.01459368	0.12291	-0.04521	-0.32043	-0.13488
14	41007.7	243.9	0.00349998	0.02810	-0.14437	-0.03721	0.07663
15	42138.6	237.3	0.02103127	0.16431	-0.39378	0.03462	0.08900
16	44323.8	225.6	0.07840724	0.58236	0.14337	0.29616	0.68855
17	44443.2	225.0	0.03015108	0.22334	0.05178	0.19777	0.42609
18	45838.1	218.2	0.00683229	0.04907	0.00530	0.11198	0.19106
19	46131.6	216.8	0.04730605	0.33759	0.19271	0.28635	0.46740
20	46594.0	214.6	0.00110439	0.00780	-0.06438	0.00907	-0.0598
21	23689.5	422.1	spin forbidden (mult=3)				
22	26783.6	373.4	spin forbidden (mult=3)				
23	28119.7	355.6	spin forbidden (mult=3)				
24	29341.2	340.8	spin forbidden (mult=3)				
25	29498.6	339.0	spin forbidden (mult=3)				
26	30056.5	332.7	spin forbidden (mult=3)				
27	31656.7	315.9	spin forbidden (mult=3)				
28	31887.3	313.6	spin forbidden (mult=3)				
29	33809.3	295.8	spin forbidden (mult=3)				
30	34281.4	291.7	spin forbidden (mult=3)				
31	34709.4	288.1	spin forbidden (mult=3)				
37	36301.1	275.5	spin forbidden (mult=3)				
33	36561.7	273.5	spin forbidden (mult=3)				
34	36991.4	270.3	spin forbidden (mult=3)				

Table 4.10: Continued: TD-DFT absorption data of **33a** at optimized ground-state geometry.

State	Energy (cm-1)	Wavelength (nm)	fosc	T2 (au**2)	TX (au)	TY (au)	TZ (au)
35	37811.2	264.5	spin forbidden (mult=3)				
36	38014.2	263.1	spin forbidden (mult=3)				
37	39659.9	252.1	spin forbidden (mult=3)				
38	40359.8	247.8	spin forbidden (mult=3)				
39	40999.0	243.9	spin forbidden (mult=3)				
40	42742.3	234.0	spin forbidden (mult=3)				

Table 4.11: TD-DFT absorption data of **47** at optimized ground-state geometry.

State	Energy (cm-1)	Wavelength (nm)	fosc	T2 (au**2)	TX (au)	TY (au)	TZ (au)
1	21630.4	462.3	0.01532	0.23317	0.44119	0.19309	-0.03514
2	21642.1	462.1	0.02873	0.43700	0.64579	-0.13163	-0.05133
3	24771.1	403.7	0.00219	0.02915	0.16947	0.02024	-0.00421
4	24797.5	403.3	0.00058	0.00764	-0.07476	0.04528	0.00108
5	27345.1	365.7	0.14492	1.74475	-1.10245	-0.00152	-0.72756
6	27722.5	360.7	0.00336	0.03989	0.01349	-0.19908	0.00869
7	28311.6	353.2	0.04264	0.49577	0.63600	0.00709	0.30202
8	28456.5	351.4	0.01415	0.16370	0.01009	-0.40443	0.00521
9	29494.1	339.1	0.01527	0.17043	-0.37041	-0.03284	-0.17930
10	29538.1	338.5	0.00280	0.03121	-0.08019	0.15269	-0.03835
11	30472.0	328.2	0.00204	0.02201	0.12838	0.06851	0.02891
12	30484.1	328.0	0.00171	0.01847	0.10497	-0.08300	0.02369
13	30763.7	325.1	0.00212	0.02273	0.09805	0.11130	0.02699
14	30787.9	324.8	0.00236	0.02521	-0.13174	0.08317	-0.03061
15	30879.0	323.8	0.00077	0.00819	0.03298	0.05672	0.06233
16	30890.7	323.7	0.00100	0.01067	0.03677	-0.04715	0.08421
17	31700.6	315.5	0.15071	1.56512	-1.10984	-0.00822	-0.57733
18	31857.4	313.9	0.01751	0.18099	0.02216	-0.42469	0.01178
19	32924.2	303.7	0.02415	0.24143	-0.42695	-0.01872	-0.24247
20	32963.2	303.4	0.00351	0.03510	0.04178	-0.18106	0.02398
21	19625.8	509.5	spin forbidden (mult=3)				
22	19638.7	509.2	spin forbidden (mult=3)				

Table 4.11: Continued: TD-DFT absorption data of **47** at optimized ground-state geometry.

State	Energy (cm-1)	Wavelength (nm)	fosc	T2 (au**2)	TX (au)	TY (au)	TZ (au)
23	23776.7	420.6	spin forbidden (mult=3)				
24	23823.7	419.7	spin forbidden (mult=3)				
25	24453.3	408.9	spin forbidden (mult=3)				
26	24477.8	408.5	spin forbidden (mult=3)				
27	27049.4	369.7	spin forbidden (mult=3)				
28	27060.4	369.5	spin forbidden (mult=3)				
29	27549.0	363.0	spin forbidden (mult=3)				
30	27554.0	362.9	spin forbidden (mult=3)				
31	28816.0	347.0	spin forbidden (mult=3)				
32	28821.1	347.0	spin forbidden (mult=3)				
33	29658.6	337.2	spin forbidden (mult=3)				
34	29684.7	336.9	spin forbidden (mult=3)				
35	29970.5	333.7	spin forbidden (mult=3)				
36	29980.2	333.6	spin forbidden (mult=3)				
37	30278.2	330.3	spin forbidden (mult=3)				
38	30291.2	330.1	spin forbidden (mult=3)				
39	30469.6	328.2	spin forbidden (mult=3)				
40	30494.9	327.9	spin forbidden (mult=3)				

Table 4.12: TD-DFT absorption data of **42** at optimized ground-state geometry.

State	Energy (cm-1)	Wavelength (nm)	fosc	T2 (au**2)	TX (au)	TY (au)	TZ (au)
1	21457.3	466.0	0.03481502	0.53416	-0.72001	-0.01185	0.1249
2	21483.6	465.5	0.00329151	0.05044	-0.03956	0.22096	0.00698
3	24223.7	412.8	0.00134567	0.01829	0.13278	0.00597	-0.02494
4	24252.7	412.3	0.00014354	0.00195	-0.03853	0.01987	0.00832
5	26218.3	381.4	0.17791188	2.23396	-1.2882	-0.00295	-0.75795
6	26814.9	372.9	0.01713441	0.21036	0.00846	-0.45855	0.0045
7	27856.0	359.0	0.00152993	0.01808	-0.0017	0.13445	-0.00114
8	27976.2	357.4	0.00530682	0.06245	-0.2491	-0.00628	-0.01897
9	28050.5	356.5	0.00750093	0.08803	0.24235	0.0264	0.16912
10	28078.6	356.1	0.00156269	0.01832	-0.06214	0.11433	-0.03727

Table 4.12: Continued: TD-DFT absorption data of **42** at optimized ground-state geometry.

State	Energy (cm-1)	Wavelength (nm)	fosc	T2 (au**2)	TX (au)	TY (au)	TZ (au)
11	30324.9	329.8	0.00011953	0.0013	0.03057	0.01799	0.0063
12	30345.6	329.5	0.00054087	0.00587	0.0763	-0.00602	0.00325
13	30418.5	328.7	0.01689786	0.18288	-0.35812	-0.00003	-0.23374
14	30584.8	327.0	0.00025827	0.00278	-0.00181	0.05268	-0.00098
15	31748.8	315.0	0.00308510	0.03199	-0.17722	0.00047	-0.02413
16	31766.8	314.8	0.00003488	0.00036	0.00491	0.01836	0.0005
17	32148.0	311.1	0.17295647	1.77116	-1.18314	-0.0067	-0.60935
18	32231.4	310.3	0.02928064	0.29907	0.01276	-0.54669	0.00651
19	33262.4	300.6	0.00144596	0.01431	0.06122	-0.04127	0.09413
20	33274.8	300.5	0.00125449	0.01241	-0.01374	-0.1066	-0.0293
21	19550.4	511.5	spin forbidden (mult=3)				
22	19648.8	508.9	spin forbidden (mult=3)				
23	23674.1	422.4	spin forbidden (mult=3)				
24	23725.9	421.5	spin forbidden (mult=3)				
25	23965.1	417.3	spin forbidden (mult=3)				
26	23991.8	416.8	spin forbidden (mult=3)				
27	26594.2	376.0	spin forbidden (mult=3)				
28	26627.2	375.6	spin forbidden (mult=3)				
29	27311.7	366.1	spin forbidden (mult=3)				
30	27390.2	365.1	spin forbidden (mult=3)				
31	28347.8	352.8	spin forbidden (mult=3)				
32	28390.0	352.2	spin forbidden (mult=3)				
33	29918.6	334.2	spin forbidden (mult=3)				
34	30012.1	333.2	spin forbidden (mult=3)				
35	30122.9	332.0	spin forbidden (mult=3)				
36	30142.9	331.8	spin forbidden (mult=3)				
37	30454.2	328.4	spin forbidden (mult=3)				
38	30501.0	327.9	spin forbidden (mult=3)				
39	30932.0	323.3	spin forbidden (mult=3)				
40	30939.3	323.2	spin forbidden (mult=3)				

4.3 Experimental Details to Section 3.1

4.3.1 Synthesis and Characterization

Anion exchange using *Amberlyst-A26* anion exchange resin

Preparing the resin:
Under ambient conditions *Amberlyst®-A26* (OH-Form) (0.5 g/mmol) is added to a PTFE tube with glass-wool on either end (see Scheme 3.4) and rinsed with water (10 mL), aq. NaOH (0.1 M, 5 mL) and again with water until pH of eluent reaches 7.
Loading of the resin:
A 2 wt-% solution of free acid or ammonium salt of desired anion is prepared and passed over the resin slowly using gravity. The loading is complete when the pH of the eluent is equal to the pH of the initial solution (eluent with incomplete loading is strongly basic).
Washing and conditioning of the resin:
The loaded resin is washed with copious amounts of water until the pH of eluent is 7. The resin is conditioned to organic solvents by passing through water:methanol mixtures of different ratios (20 mL each of 1:0, 3:1, 1:1, 1:3, 0:1). The column is then rinsed with HPLC-grade dichloromethane (10 mL) and dried thouroghly by passing dry air through the setup for several minutes.
Anion exchange:
Inside the glovebox a 1 wt-% solution of **51a** in MeCN or THF is passed through the resin collumn dropwise using gravity. The eluent is collected in a scintillationn vial. When the solution is passed through, the column is washed with MeCN (at least 3-times the volume of initial solution). Volatiles of combined organic fractions are removed *in vacuo*.

1,3-Bis(2,6-diisopropylphenyl)-2,3-dihydro-1H-imidazol-2-ilyden-(2-methyl)-pyridine-copper(I) hexafluorophosphate
(52)

From **51a** (200 mg) using NH_4PF_6, the product was obtained from MeCN as a white powder (yiel not determined).

^{1}H-NMR (400MHz, MeCN-d_3): δ = 8.15 (ddd, ^3J = 8.1, 1.1 Hz, 1H), 9.77 (s, 1H), 9.20 (dd, ^3J = 5.1, 1.9, 1.0 Hz, 1H), 7.63 (td, ^3J = 7.7, 1.9 Hz, 1H), 7.52 (^3J = 8.3, 7.3 Hz, 1H), 7.43 (s, 2H), 7.38–7.38 (m, 4H), 7.2 (d, ^3J = 7.9 Hz, 1H), 7.12–7.08 (m, 1H), 2.61 (sept, ^3J = 6.9 Hz, 4H), 2.34 (s, 3H), 1.2 (dd, ^3J = 6.9, 1.6 Hz, 24H) ppm.

^{19}F-NMR (376 MHz, MeCN-d_3): δ = –73.0 (d, ^{2} = 706.6 Hz) ppm.

^{31}P{^{1}H}-NMR (162 MHz, MeCN-d$_3$): δ = –144.6 (hept, ^{2}J = 706.3 Hz) ppm.

Synthesis of Chiral Anions

Sodium 4,4'-spirobi[dinaphtho[2,1-d:1',2'-f][1,3,2]dioxaborepin]-4-uide tris tetrahydrofuran adduct (55)

Synthesis was performed according to modified literature-known procedure.[152] In an argon-flushed Schlenk-flask, sodium borohydride (681 mg, 18.0 mmol, 1.0 equiv.) was suspended in dry THF (300 mL) and cooled in an ice-bath. Dry methanol (2.91 mL, 72.0 mmol, 4.0 equiv.) was added drop-wise under constant stirring and pressure equalisation. The solution was stirred at that temperature for 1 h and at room temperature for 30 min. (*R*)-BINOL (10.3 g, 36.0 mmol, 2.0 equiv.) was added and the solution was refluxed under argon for 7 h. Upon cooling to around 40°C, trimethylborate (2.5 mL, 22.5 mmol, 1.25 equiv.) was added and a white precipitate formed spontaneously. The suspension was stirred at 40°C for additional 5 h. Subsequently, the solution was cooled to around 5°C for 12 h. The precipitate was filtered and washed with ice-cold THF (20 mL), Et_2O (2× 20 mL) and pentanes (2× 10 mL). Drying *in vacuo* yielded the product as a white microcrystaline powder (13.1 g, 89%) Spectroscopic data are consistent with the literature.[152]

Ammonium 2,7-dioxo-3,8-diphenyl-1,4,6,9-tetraoxa-5-boraspiro[4.4]nonan-5-ide (57)

(*S*)-Hydroxy(phenyl)acetic acid (3.04 g, 20.0 mmol, 2.0 equiv.) and boric acid (618 mg, 10.0 mmol, 1.0 equiv.) were dissoleved in methanol (15 mL). Aqueous ammonia (25%, 0.75 mL, 10.0 mmol, 1.0 equiv.) was added under constant stirring. The clear solution was kept at r.t. for 5 h. The volume was reduced *in vacuo* to about 5 mL. Copious amounts of Et_2O (approx. 100 mL) were added. The white precipitate was filtered using a glass-fritted funnel and washed with more Et_2O (3 × 50 mL) and dried *in vacuo*. Product **57** (3.03 g, 92%) was obtained as a white powder.

^{1}H-NMR (400 MHz, acetone-d$_6$): δ = 7.65–7.57 (m, 4H), 7.35–7.31 (m, 4H), 7.27–7.25 (m, 2H), 5.21 (d, ^{3}J = 22.1 Hz, 2H) ppm.

^{11}B{^{1}H}-NMR (128 MHz, acetone-d$_6$): δ = 11.2 ppm.

CHN-analysis
Calculated for $C_{16}H_{16}BNO_6$: %C 58.39, %H 4.90, %N 4.36.
Found: %C 58.46, %H 5.01, %N 4.21

Ammonium antimonyl tartrate (59)

Ammonium (2*R*,3*R*)-hydrogentartrate (11.14 g, 66.67 mmol, 2.0 equiv.) was dissolved in boiling deionised water (100 mL) under constant stirring. Over the course of 1 h, antimony(III) oxide (9.72 g, 33.33 mmol, 1.0 equiv.) was added in small portions to the hot solution. After complete addition the suspension was diluted with more hot deionised water (100 mL) and left to stirr at 90°C for 3 h. The now only slightly cloudy solution was filtered hot using a preheated glass-fritted funnel. The clear and colourless filtrate was left to cool to room temperature. The product was precipitated as a white solid by slowly pouring the cool solution into ice-cold ethanol (1 L). After filtration and drying, **59** · 3 H_2O was obtained as a white free-flowing powder (16.33 g, 78%).

CHN-analysis
Calculated for $C_8H_{18}N_2O_{15}Sb_2$: %C 15.36, %H 2.90, %N 4.48.
Found: %C 15.59, %H 2.87, %N 4.45

4.3.2 NMR Spectra

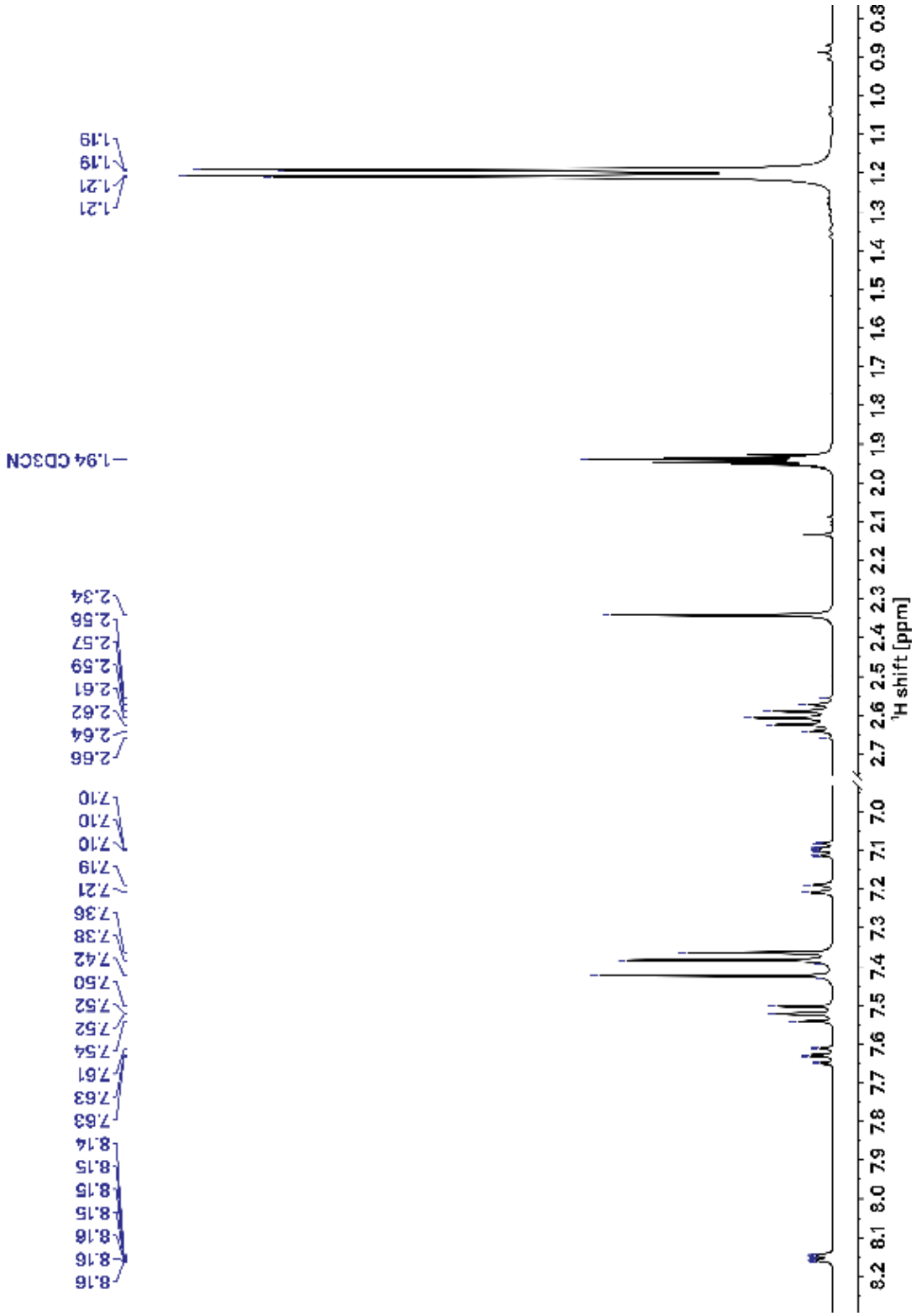

Figure 4.21: ^{1}H-NMR spectrum of **52** in MeCN-d_3.

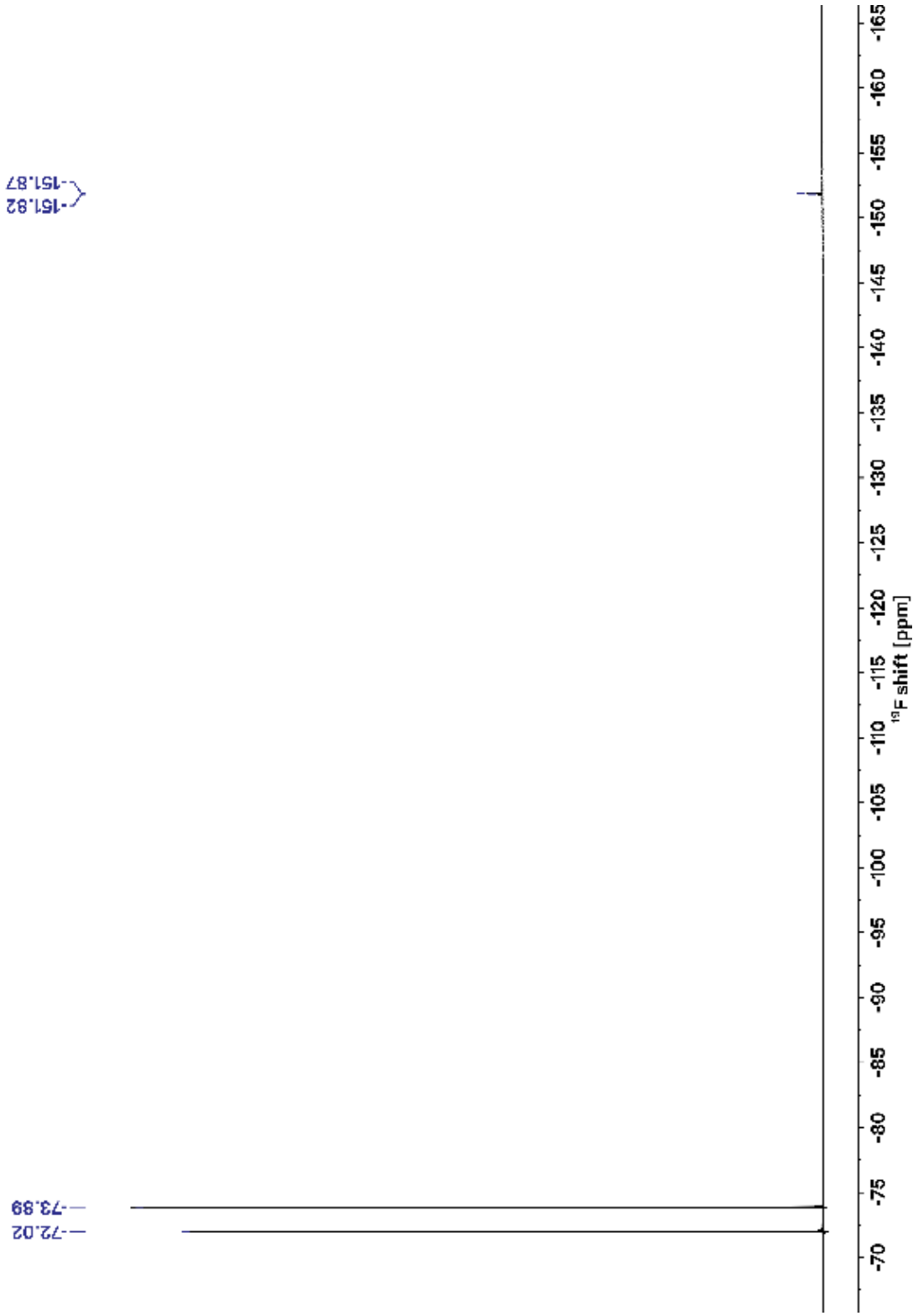

Figure 4.22: ^{19}F-NMR spectrum of **52** in MeCN-d_3.

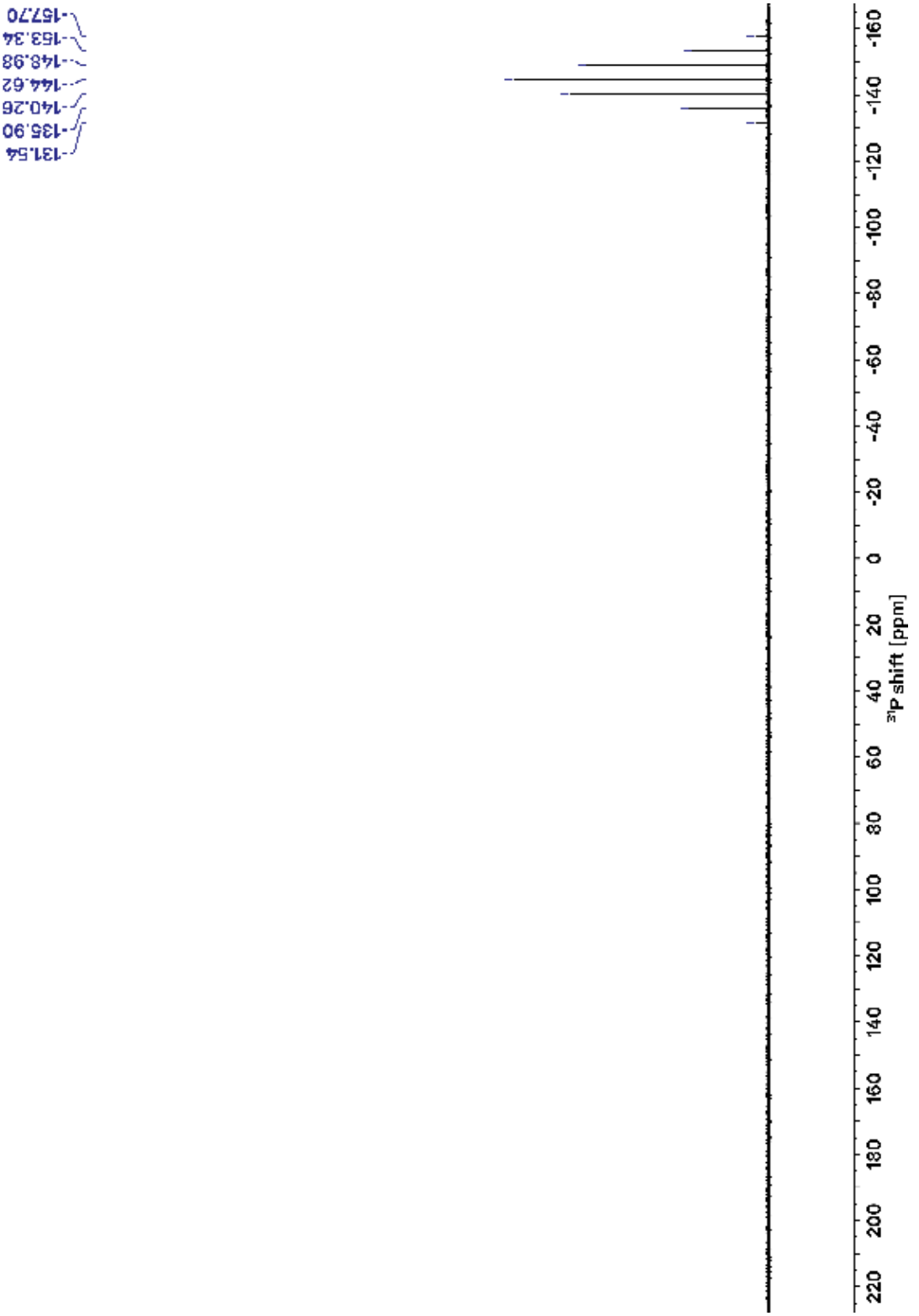

Figure 4.23: ^{3}1P-NMR spectrum of **52** in MeCN-d_3.

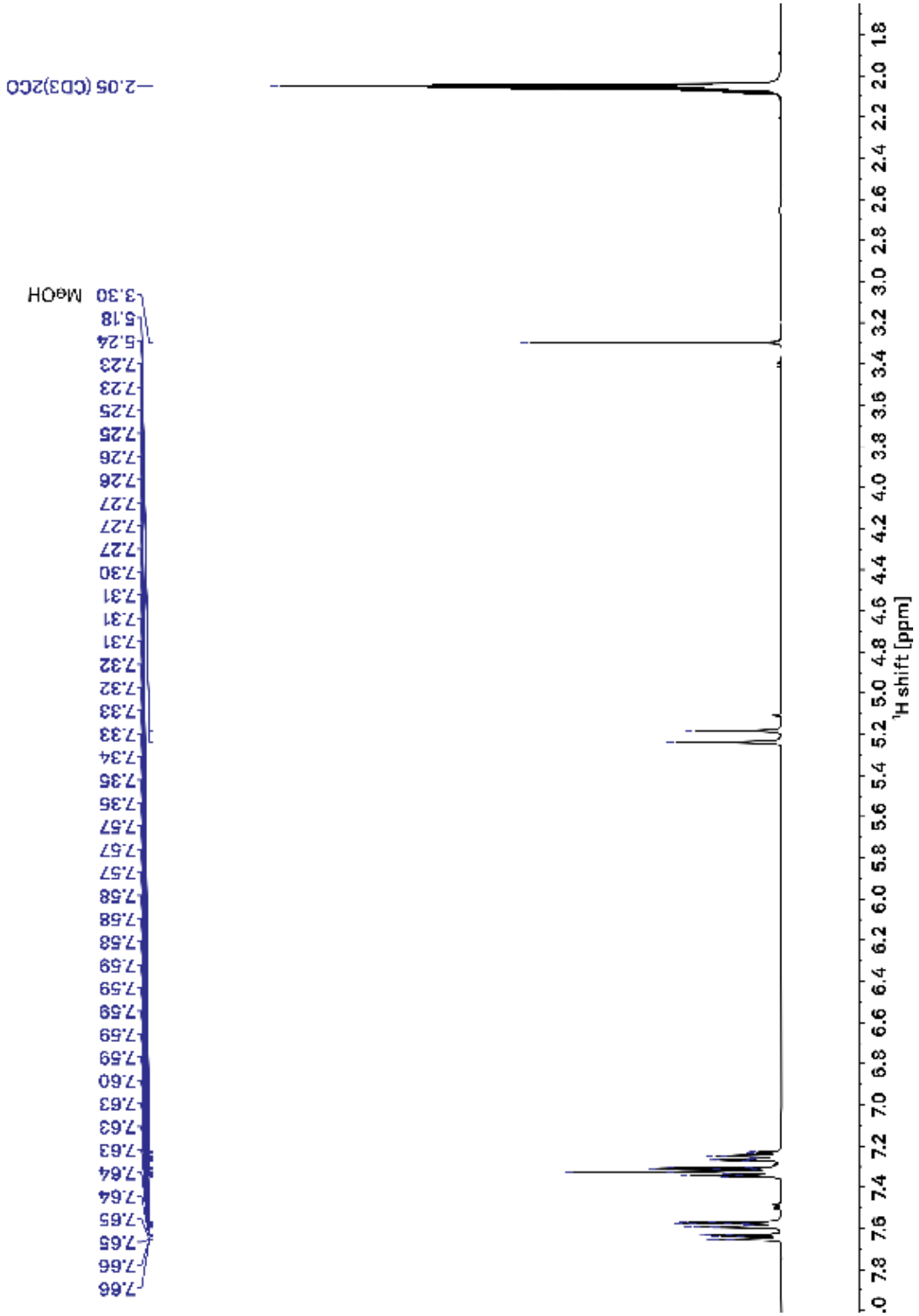

Figure 4.24: ^{1}H-NMR spectrum of **57** in acetone-d_6.

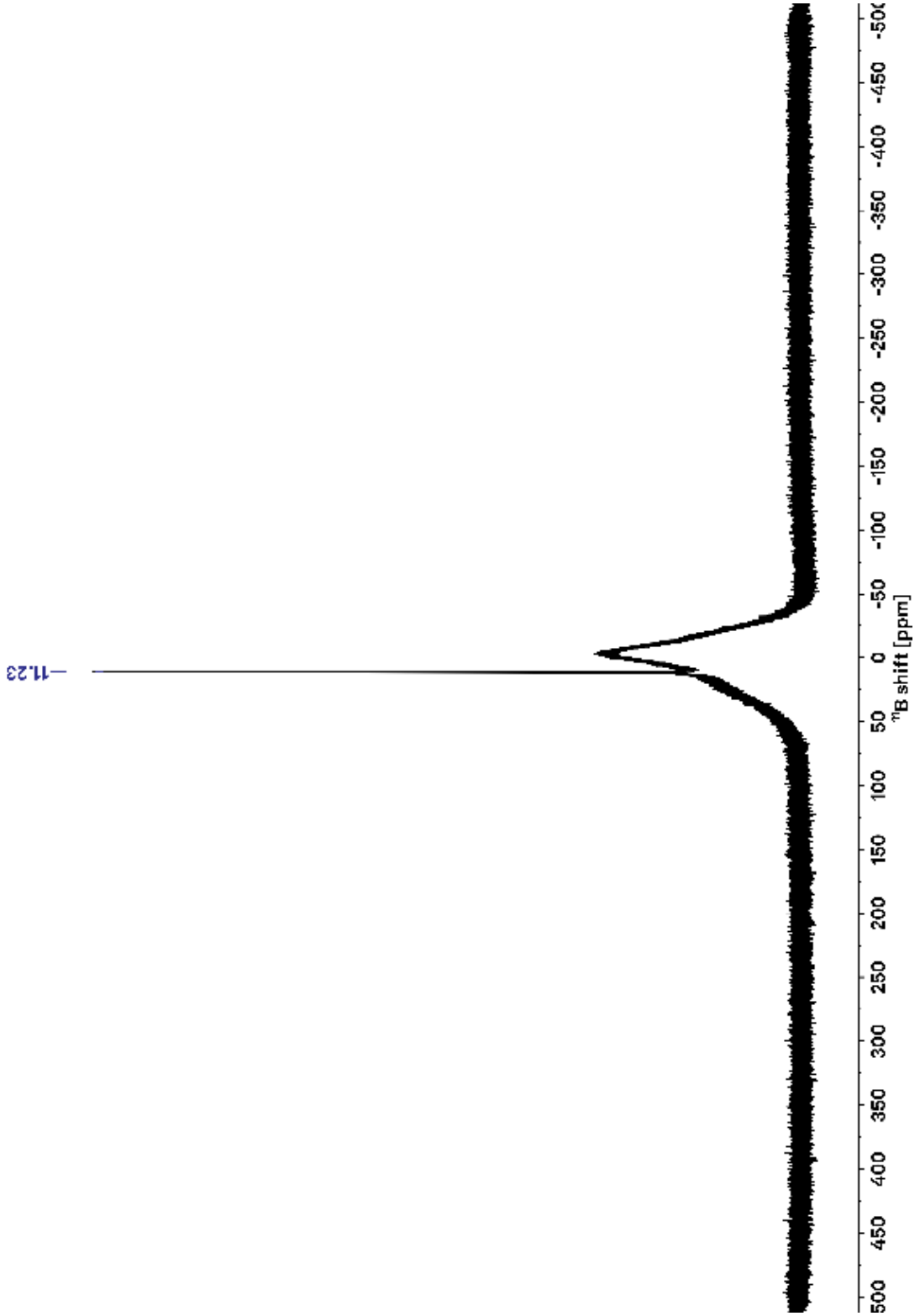

Figure 4.25: ^{11}B-NMR spectrum of **57** in acetone-d_6.

4.4 Supporting Information of Paper Contributions

In this section the relevant pages of the electronic supporting informations of the publications presented in this work are printed.

"Trigonal Copper(I) Complexes with Cyclic (Alkyl)(amino)carbene Ligands for Single-Photon Near-IR Triplet Emission"

The complete ESI is available free of charge at
https://pubs.acs.org/doi/10.1021/acs.inorgchem.2c02376.

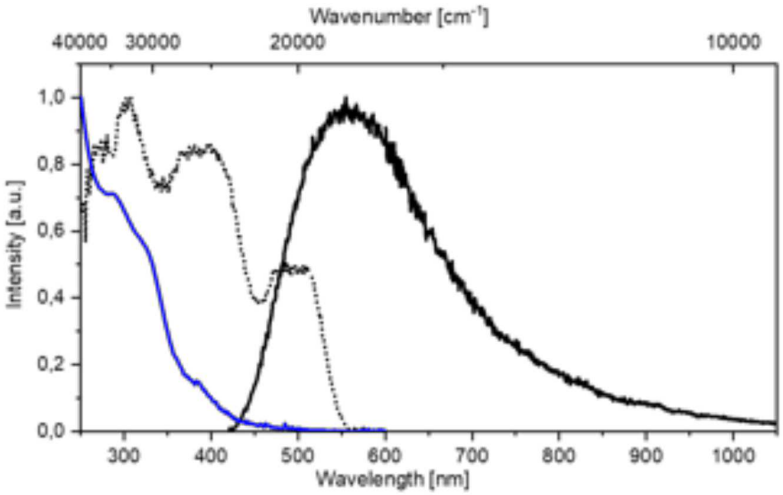

Figure S12. Excitation (dotted) and emission (solid) spectra in the solid state and absorption spectra in THF (blue) of **7** at room temperature

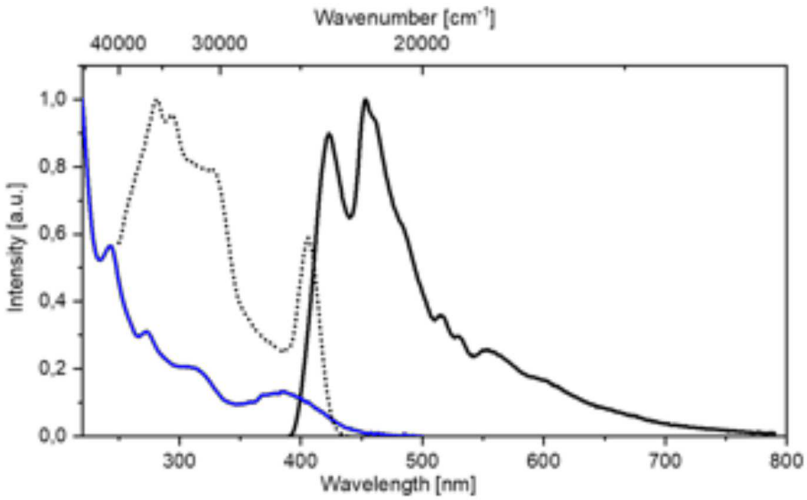

Figure S13. Excitation (dotted) and emission (solid) spectra in the solid state and absorption spectra in THF (blue) of **8** at room temperature

Computational studies. Calculations were performed with the ORCA 4.2.1 program suite[9,10] and the PBE0[11] hybrid functional, using density functional theory (DFT) by KOHN und SHAM[12] on the Linux-HPC-Cluster of TU Dortmund University. For geometry optimisations and calculations of molecular orbitals the split-valence basis set def2-TZVP with zero-order regular approximation of relativistic effects (ZORA) and BECKE-JOHNSON damping (D3BJ) were used.[13–16] Frequency analysis was used to confirm convergence into a global minimum structure. For time-dependent DFT calculations the single-valence base set ZORA-def2-SVP was used as implemented in ORCA 4.2.1. All calculations were performed with tight SCF convergence ($\Delta E = 1 \cdot 10^{-8}$ au).

2

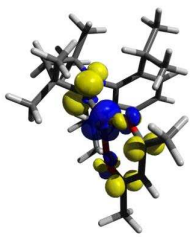

$S_0 \rightarrow S_1$
(368 nm, f = 0.003)

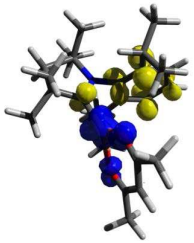

$S_0 \rightarrow S_6$
(310 nm, f = 0.070)

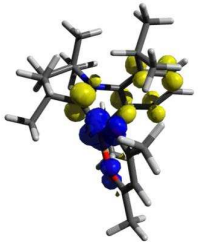

$S_0 \rightarrow S_{11}$
(286 nm, f = 0.124)

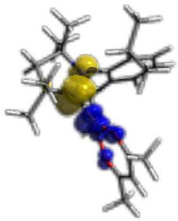

$S_0 \rightarrow T_1$
(492 nm)

3

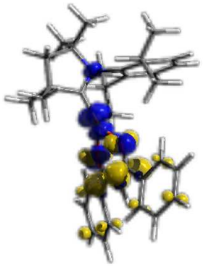

$S_0 \rightarrow S_1$
(486 nm, f = 0.0003)

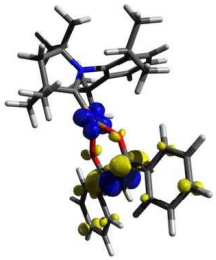

$S_0 \rightarrow S_5$
(333 nm, f = 0.228)

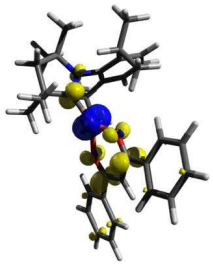

$S_0 \rightarrow S_7$
(317 nm, f = 0.094)

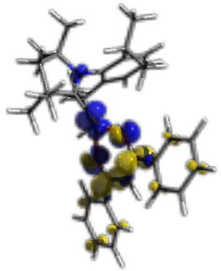

$S_0 \rightarrow T_1$
(540 nm)

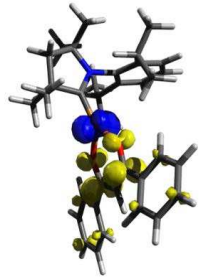

$S_0 \rightarrow T_8$
(368 nm)

4

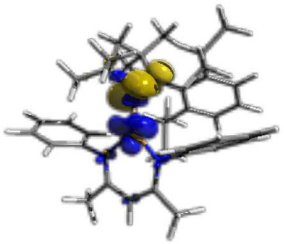

$S_0 \rightarrow S_1$
(381 nm, f = 0.007)

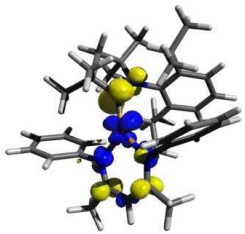

$S_0 \rightarrow S_2$
(359 nm, f = 0.031)

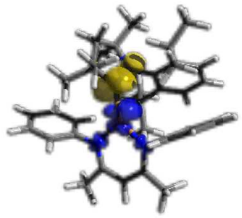

$S_0 \rightarrow T_1$
(534 nm)

Figure S14. Electron density differences of selected transitions of [Cu(acac/dbm/nacnac)(CAAC^{Me})] (**2**/**3**/**4**) (gold: gain of electron density; blue: loss of electron density).

6

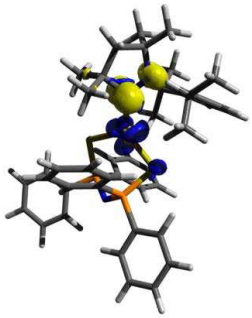

$S_0 \rightarrow S_1$
(397 nm, f = 0.011)

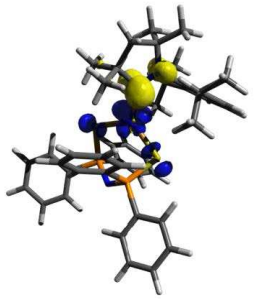

$S_0 \rightarrow S_5$
(333 nm, f = 0.041)

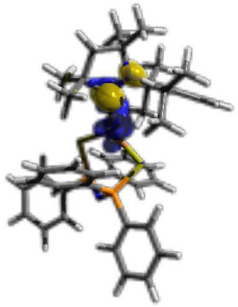

$S_0 \rightarrow T_1$
(475 nm)

7

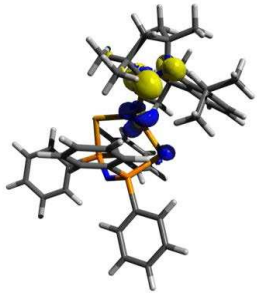

$S_0 \rightarrow S_1$
(404 nm, f = 0.014)

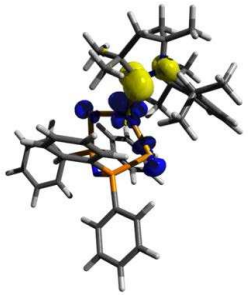

$S_0 \rightarrow S_5$
(343 nm, f = 0.035)

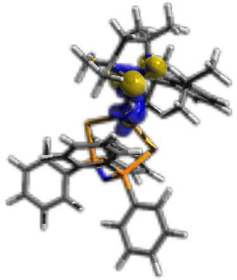

$S_0 \rightarrow T_1$
(483 nm)

Figure S15. Electron density differences of selected transitions of [Cu((N(SPPh$_2$)$_2$)/(N(SePPh$_2$)$_2$))(CAAC^{Me})] (**6**/**7**) (gold: gain of electron density; blue: loss of electron density).

References.

(1) Gernert, M.; Mueller, U.; Haehnel, M.; Pflaum, J.; Steffen, A. A Cyclic Alkyl(amino)carbene as Two-Atom π-Chromophore Leading to the First Phosphorescent Linear Cu̲ Complexes. *Chem. Eur. J.* **2017**, *23* (9), 2206–2216.

(2) Wang, F. T.; Najdzionek, J.; Leneker, K. L.; Wasserman, H.; Braitsch, D. M. A Facile Synthesis of Imidotetraphenyldiphosphinic Acids. *Syn. React. Inorg. Met.* **1978**, *8* (2), 119–125.

(3) Lee, D.-H.; Jin, M.-J. An extremely active and general catalyst for Suzuki coupling reaction of unreactive aryl chlorides. *Org. Lett.* **2011**, *13* (2), 252–255.

(4) Lee, D. H.; Park, S.-E.; Cho, K.; Kim, Y.; Athar, T.; Lee, I.-M. Highly efficient microwave-accelerated preparation of β-ketoimines. *Tetrahedron Lett.* **2007**, *48* (47), 8281–8284.

(5) Sheldrick, G. M. SHELXT – Integrated space-group and crystal-structure determination. *Acta Crystallogr. A* **2015**, *71* (1), 3–8.

(6) Sheldrick, G. M. A short history of SHELX. *Acta Crystallogr. A* **2008**, *64* (Pt 1), 112–122.

(7) Hübschle, C. B.; Sheldrick, G. M.; Dittrich, B. ShelXle: a Qt graphical user interface forSHELXL. *J. Appl. Crystallogr.* **2011**, *44* (6), 1281–1284.

(8) 4.6.0; Crystal Impact-Dr. H. Putz & Dr. K. Brandenburg GbR: Bonn, 2020. *Diamond - Crystal and Molecular Structure Visualization*.

(9) Neese, F. The ORCA program system. *WIREs Comput. Mol. Sci.* **2012**, *2* (1), 73–78.

(10) Neese, F. Software update: the ORCA program system, version 4.0. *WIREs Comput. Mol. Sci.* **2018**, *8* (1), e1327.

(11) Perdew, J. P.; Ernzerhof, M.; Burke, K. Rationale for mixing exact exchange with density functional approximations. *J. Chem. Phys.* **1996**, *105* (22), 9982–9985.

(12) Kohn, W.; Sham, L. J. Self-Consistent Equations Including Exchange and Correlation Effects. *Phys. Rev.* **1965**, *140* (4A), A1133-A1138.

(13) Weigend, F.; Ahlrichs, R. Balanced basis sets of split valence, triple zeta valence and quadruple zeta valence quality for H to Rn: Design and assessment of accuracy. *Phys. Chem. Chem. Phys.* **2005**, *7* (18), 3297–3305.

(14) Stefan Grimme; Jens Antony; Stephan Ehrlich; Helge Krieg. A consistent and accurate ab initio parametrization of density functional dispersion correction (DFT-D) for the 94 elements H-Pu. *J. Chem. Phys.* **2010**, *132* (15), 154104.

(15) Grimme, S.; Ehrlich, S.; Goerigk, L. Effect of the damping function in dispersion corrected density functional theory. *J. Comput. Chem.* **2011**, *32* (7), 1456–1465.

(16) van Lenthe, E.; Baerends, E. J.; Snijders, J. G. Relativistic total energy using regular approximations. *J. Chem. Phys.* **1998**, *101* (11), 9783.

SI of "Synthesis and Photophysical Studies of Copper(I) CAAC Half-Sandwich Complexes as a Highly Modifiable Class of Emitters"

The complete ESI is available free of charge at https://pubs.acs.org/doi/10.1021/acs.inorgchem.2c02073.

Table S3. Concentration dependent PLQY and lifetime measurements of [Cu(CAAC^{Ment})Cl] **2-Cl** in THF

c (10^{-4} M^{-1})	PLQY Φ_{PL}	τ ($\propto$s)	k_r (10^4 s^{-1})
3	9.2	4.4	2.1
4	12.5	5.4	2.3

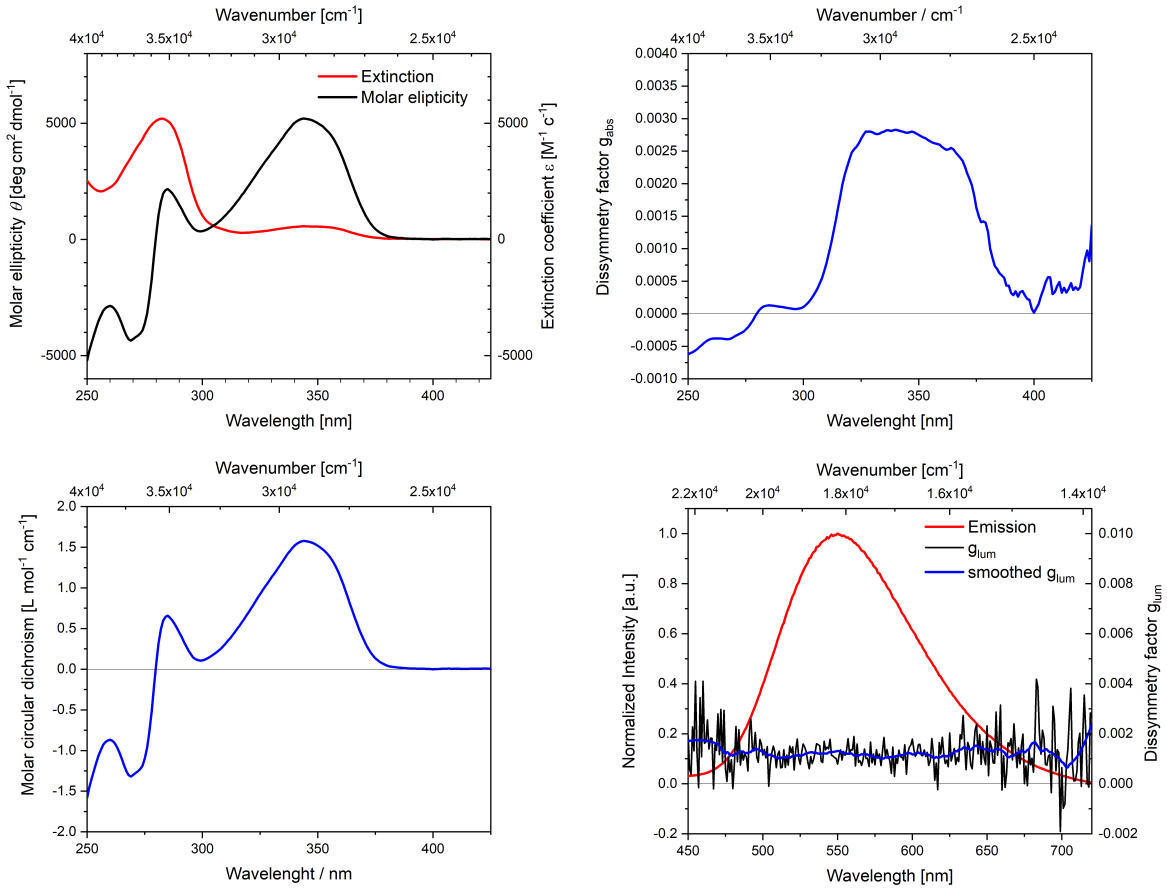

Figure S15. Molar ellipticity, extinction coefficient, dissymmetry factor g_{abs} and molar circular dichroism of **2-Cl** as functions of wavelength.

Computational studies. Calculations were performed with the ORCA 4.2.1 program suite[12,13] and the PBE0[14] hybrid functional, using density functional theory (DFT) by KOHN und SHAM[15] on the Linux-HPC-Cluster of TU Dortmund University. For geometry optimisations and calculations of molecular orbitals the split-valence basis set def2-TZVP with zero-order regular approximation of relativistic effects (ZORA) and BECKE-JOHNSON damping (D**3-Cp***J) were used.[16–19] Frequency analysis was used to confirm convergence into a global minimum structure. For time-dependent DFT calculations the single-valence base set ZORA-def2-SVP was used as implemented in ORCA 5.0.1. All calculations were performed with tight SCF convergence(ΔE = $1 \cdot 10^{-8}$ au).

1-Cp

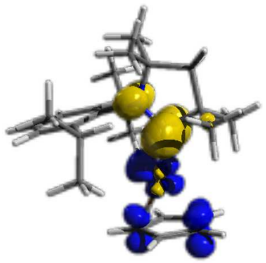

$S_0 \rightarrow S_1$
(413 nm, f = 0.002)

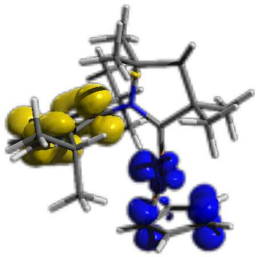

$S_0 \rightarrow S_2$
(346 nm, f = 0.022)

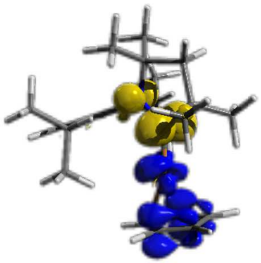

$S_0 \rightarrow S_5$
(333 nm, f = 0.14)

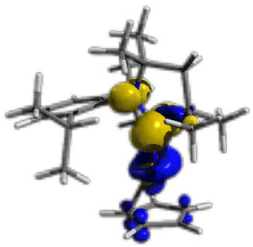

$S_0 \rightarrow S_6$
(329 nm, f = 0.043)

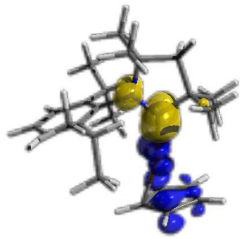

$S_0 \rightarrow T_1$
(469 nm)

1-Cp*

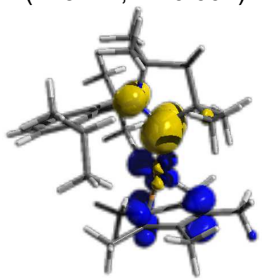

$S_0 \rightarrow S_1$
(483 nm, f = 0.00005)

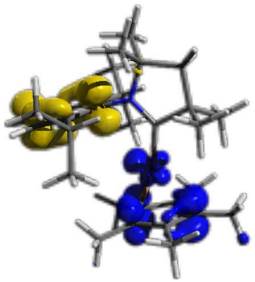

$S_0 \rightarrow S_2$
(405 nm, f = 0.024)

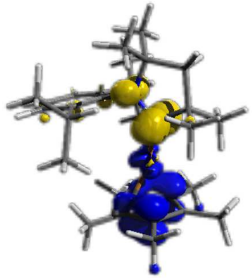

$S_0 \rightarrow S_5$
(383 nm, f = 0.19)

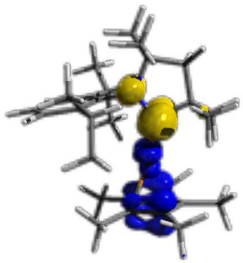

$S_0 \rightarrow T_1$
(545 nm)

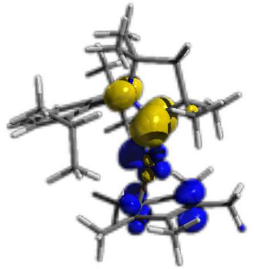

$S_0 \rightarrow T_2$
(535 nm)

1-Ind

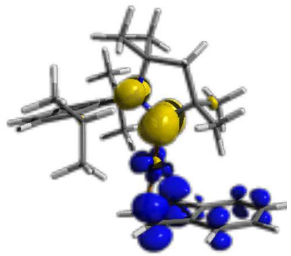

$S_0 \rightarrow S_1$
(397 nm, f = 0.18)

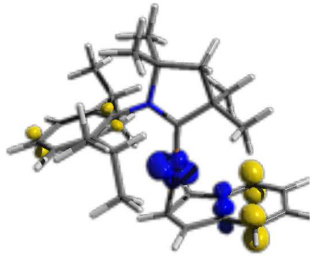

$S_0 \rightarrow S_8$
(274 nm, f = 0.15)

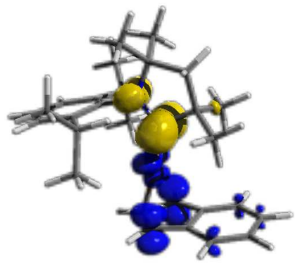

$S_0 \rightarrow T_1$
(526 nm)

Figure S16. Electron density differences of selected transitions of [Cu(Cp/Cp*/Ind)($CAAC^{Me}$)] (**1-Cp**/**1-Cp***/**1-Ind**) (gold: gain of electron density; blue: loss of electron density).

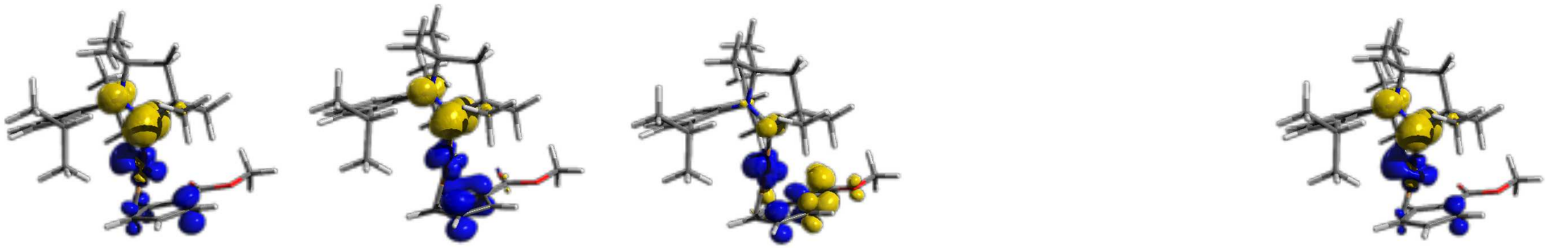

Figure S17. Electron density differences of selected transitions of [Cu(Cp^{CO2Me}/Cp^{tBu})($CAAC^{Me}$)] (**1-Cp^{CO2Me}**/**1-Cp^{tBu}**) and [CuCl($CAAC^{Ment}$)] **2-Cl** (gold: gain of electron density; blue: loss of electron density).

2-Cp

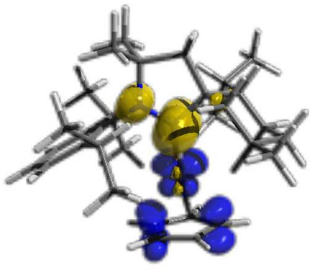

$S_0 \rightarrow S_1$ (417 nm, f = 0.0001)

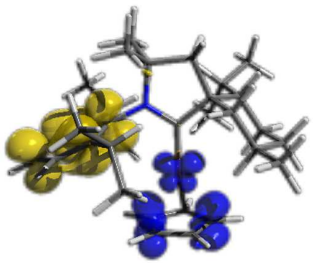

$S_0 \rightarrow S_2$ (347 nm, f = 0.006)

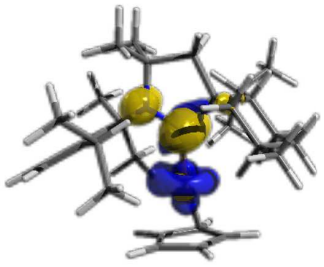

$S_0 \rightarrow S_3$ (343 nm, f = 0.004)

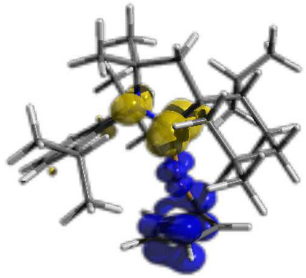

$S_0 \rightarrow S_6$ (338 nm, f = 0.17)

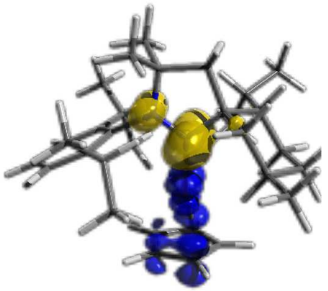

$S_0 \rightarrow T_1$ (470 nm)

2-Cp*

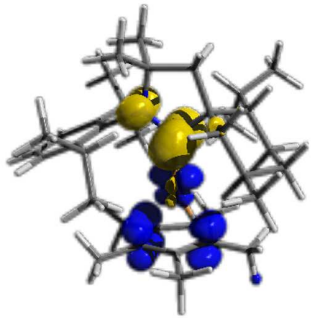

$S_0 \rightarrow S_1$ (491 nm, f = 0.00005)

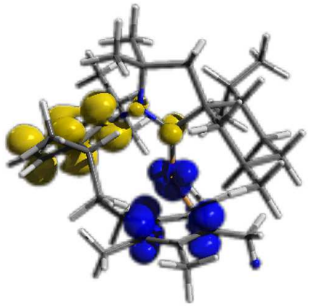

$S_0 \rightarrow S_4$ (391 nm, f = 0.017)

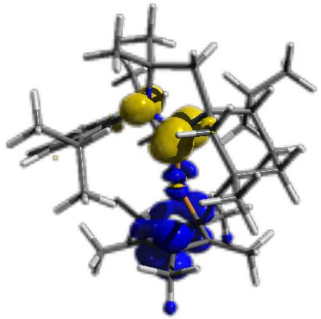

$S_0 \rightarrow S_5$ (389 nm, f = 0.18)

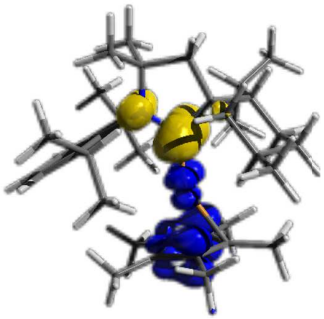

$S_0 \rightarrow T_1$ (549 nm)

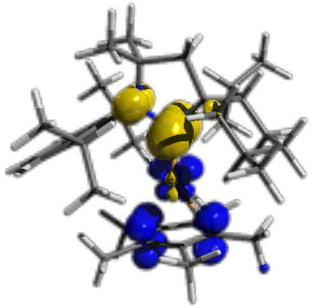

$S_0 \rightarrow T_2$ (544 nm)

3-Cp

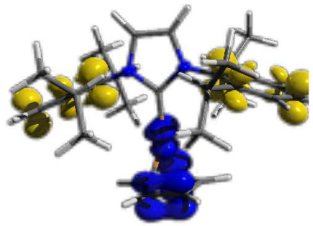

$S_0 \rightarrow S_1$ (340 nm, f = 0.0008)

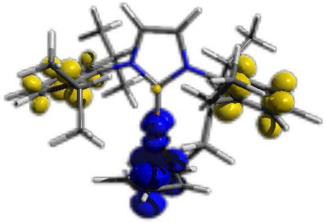

$S_0 \rightarrow S_6$ (330 nm, f = 0.03)

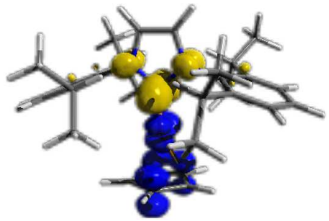

$S_0 \rightarrow S_{10}$ (282 nm, f = 0.16)

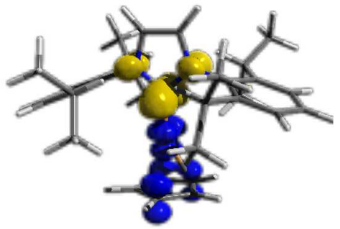

$S_0 \rightarrow T_1$ (368 nm)

Figure S18. Electron density differences of selected transitions of [Cu(Cp/Cp*)(CAAC^{Ment})] (**2-Cp**/**2-Cp***) and [Cu(Cp)(IDipp)] (**3-Cp**) (gold: gain of electron density; blue: loss of electron density).

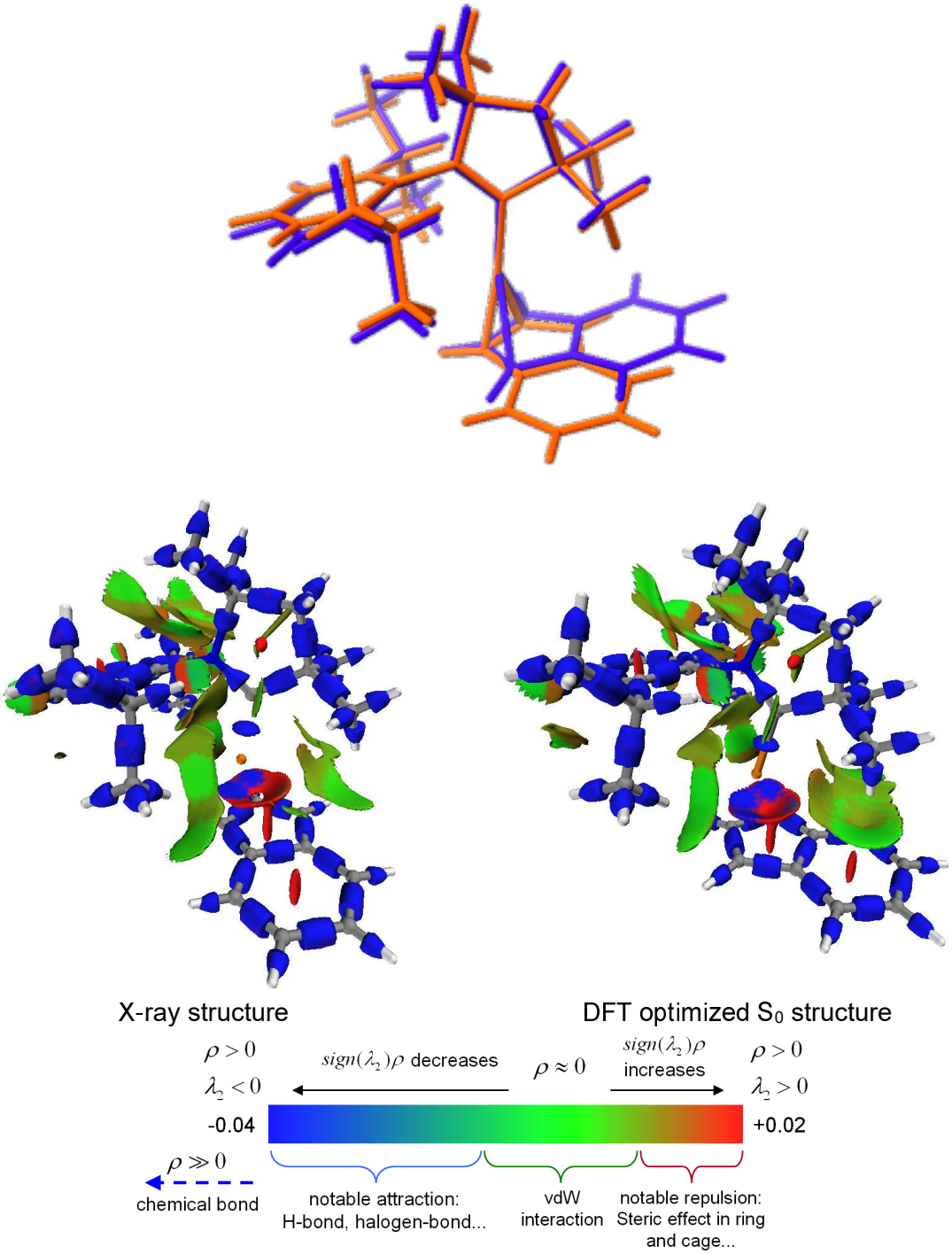

Figure S19. Comparison of structures of **1-Ind** derived in X-ray (top, red) and DFT optimized S_0 (top, blue), and the interaction region indicator (IRI) analysis (bottom). The two blue spots for the Cu-C29 and Cu-C21 bonds depicted in the IRI analysis of the X-ray structure (left) supports an $\eta^2(\sigma,\pi)$ bonding mode, while upon DFT optimization (right) a third blue mark is found in addition for the Cu-C22 bond suggesting a η^3-bonding mode being energetically accessible in solution.

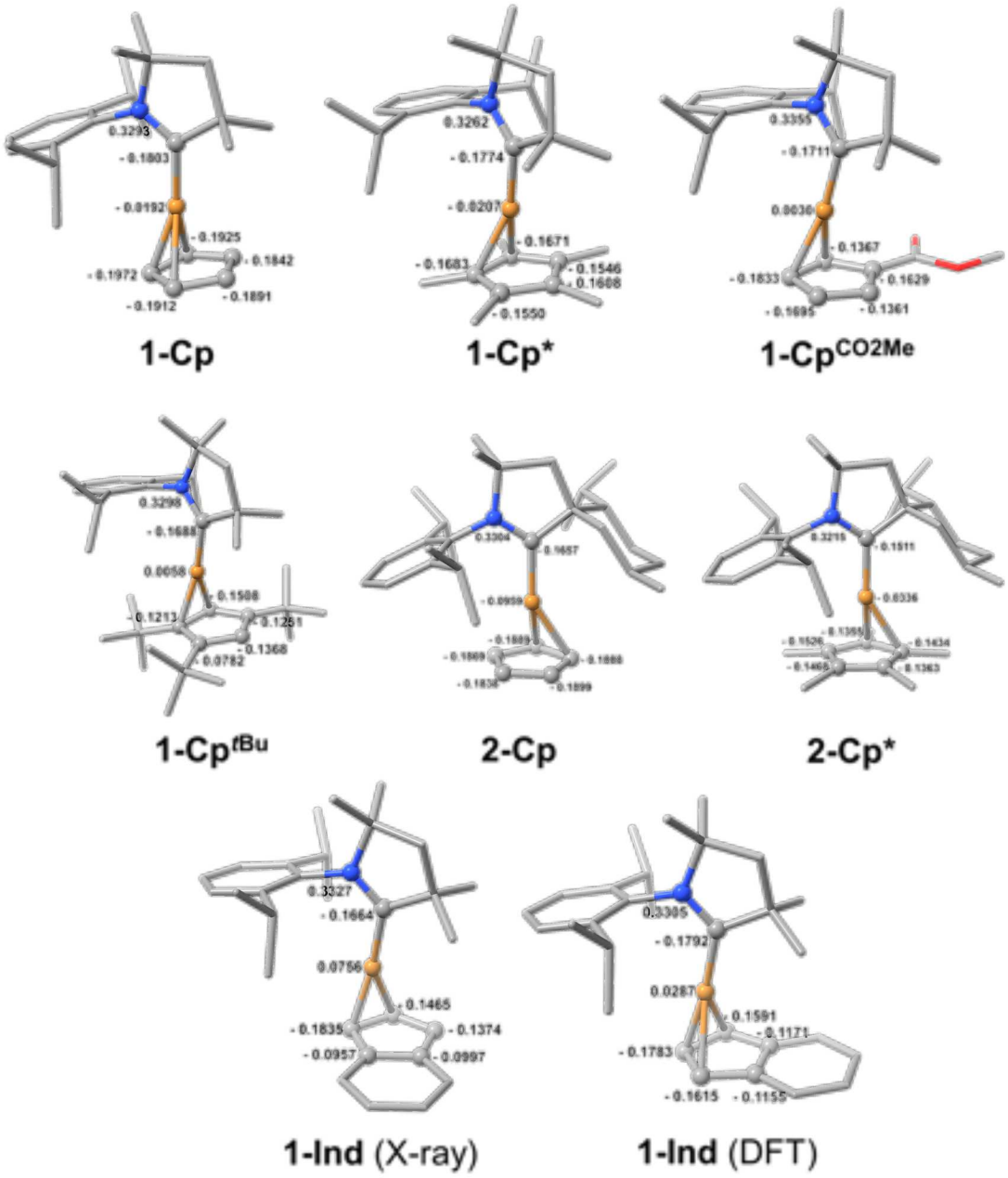

Figure S20. Löwdin population analysis of [Cu(CAAC)(Cp^{R})] compounds in their DFT optimized structures, as well as [Cu(CAAC^{Me})(Ind)] in its X-ray and DFT optimized structure.

References.

(1) Gernert, M.; Müller, U.; Haehnel, M.; Pflaum, J.; Steffen, A. A Cyclic Alkyl(amino)carbene as Two-Atom π-Chromophore Leading to the First Phosphorescent Linear Cu^{I} Complexes. *Chemistry* **2017**, *23* (9), 2206–2216.

(2) Hamze, R.; Peltier, J. L.; Sylvinson, D.; Jung, M.; Cardenas, J.; Haiges, R.; Soleilhavoup, M.; Jazzar, R.; Djurovich, P. I.; Bertrand, G.; Thompson, M. E. Eliminating nonradiative decay in Cu(I) emitters: 99% quantum efficiency and microsecond lifetime. *Science* **2019**, *363* (6427), 601–606.

(3) Santoro, O.; Collado, A.; Slawin, A. M. Z.; Nolan, S. P.; Cazin, C. S. J. A general synthetic route to Cu(X)(NHC) (NHC = N-heterocyclic carbene, X = Cl, Br, I) complexes. *Chem. Commun.* **2013**, *49* (89), 10483–10485.

(4) Wang, F. T.; Najdzionek, J.; Leneker, K . L.; Wasserman, H.; Braitsch, D. M. A Facile Synthesis of Imidotetraphenyldiphosphinic Acids. *Syn. React. Inorg. Met.* **1978**, *8* (2), 119–125.

(5) Lee, D.-H.; Jin, M.-J. An extremely active and general catalyst for Suzuki coupling reaction of unreactive aryl chlorides. *Org. Lett.* **2011**, *13* (2), 252–255.

(6) Lee, D. H.; Park, S.-E.; Cho, K.; Kim, Y.; Athar, T.; Lee, I. -M. Highly efficient microwave-accelerated preparation of β-ketoimines. *Tetrahedron Lett.* **2007**, *48* (47), 8281–8284.

(7) Power, P. P., Ed. *Inorganic syntheses*:*Volume 37*; Inorganic Syntheses; John Wiley and Sons Inc, 2018.

(8) Sheldrick, G. M. SHELXT– Integrated space-group and crystal-structure determination. *Acta Crystallogr. A* **2015**, *71* (1), 3–8.

(9) Sheldrick, G. M. A short history of SHELX. *Acta Crystallogr. A* **2008**, *64* (Pt 1), 112–122.

(10) Hübschle, C. B.; Sheldrick, G. M.; Dittrich, B. ShelXle: a Qt graphical user interface forSHELXL. *J. Appl. Crystallogr.* **2011**, *44* (6), 1281–1284.

(11) Dolomanov, O. V.; Bourhis, L. J.; Gildea, R. J.; Howard, J. A. K.; Puschmann, H. OLEX2 : a complete structure solution, refinement and analysis program. *J. Appl. Crystallogr.* **2009**, *42* (2), 339–341.

(12) Neese, F. The ORCA program system. *WIREs Comput. Mol. Sci.* **2012**, *2* (1), 73–78.

(13) Neese, F. Software update: th e ORCA program system, version 4.0. *WIREs Comput. Mol. Sci.* **2018**, *8* (1), e1327.

(14) Perdew, J. P.; Ernzerhof, M.; Burke, K. Rationale for mixing exact exchange with density functional approximations. *J. Chem. Phys.* **1996**, *105* (22), 9982–9985.

(15) Kohn, W.; Sham, L. J. Self-Consistent Equations Including Exchange and Correlation Effects. *Phys. Rev.* **1965**, *140* (4A), A1133-A1138.

(16) Weigend, F.; Ahlrichs, R. Balanced basis sets of split valence, triple zeta valence and quadruple zeta valence quality for H to Rn: Design and assessment of accuracy. *Phys. Chem. Chem. Phys.* **2005**, *7* (18), 3297–3305.

(17) Stefan Grimme; Jens Antony; Stephan Ehrlich; Helge Krieg. A consistent and accurate ab initio parametrization of density functional dispersion correction (DFT-D) for the 94 elements H-Pu. *J. Chem. Phys.* **2010**, *132* (15), 154104.

(18) Grimme, S.; Ehrlich, S.; Goerigk, L. Effect of the damping function in dispersion corrected density functional theory. *J. Comput. Chem.* **2011**, *32* (7), 1456–1465.

(19) E. van Lenthe; E. J. Baerends; J. G. Snijders. Relativistic total energy using regular approximations. *J. Chem. Phys.* **1998**, *101* (11), 9783.

(20) Noviandri, I.; Brown, K. N.; Fleming, D. S.; Gulyas, P. T.; Lay, P. A.; Masters, A. F.; Phillips, L. The Decamethylferrocenium/Decamethylferrocene Redox Couple: A Superior Redox Standard to the Ferrocenium/Ferrocene Redox Couple for Studying Solvent Effects on the Thermodynamics of Electron Transfer. *J. Phys. Chem. B* **1999**, *103* (32), 6713–6722.

SI of "Towards Fast Circularly Polarized Luminescence in 2-Coordinate Chiral Mechanochromic Copper(I) Carbene Complexes"

The complete ESI is available free of charge at https://chemistry-europe.onlinelibrary.wiley.com/doi/10.1002/chem.202300946.

Computational studies. Calculations were performed with the ORCA 5.0.1 program suite[7] and the PBE0[8] hybrid functional, using density functional theory (DFT) by KOHN und SHAM[9] on the Linux-HPC-Cluster of TU Dortmund University. For geometry optimisations and calculations of molecular orbitals the split-valence basis set def2-TZVP with zero-order regular approximation of relativistic effects (ZORA) and BECKE-JOHNSON damping (D3BJ) were used.[10] Frequency analysis was used to confirm convergence into a global minimum structure. For time-dependent DFT calculations the single-valence base set ZORA-def2-SVP was used as implemented in ORCA 5.0.1. All calculations were performed with tight SCF convergence ($\Delta E = 1 \cdot 10^{-8}$ au).

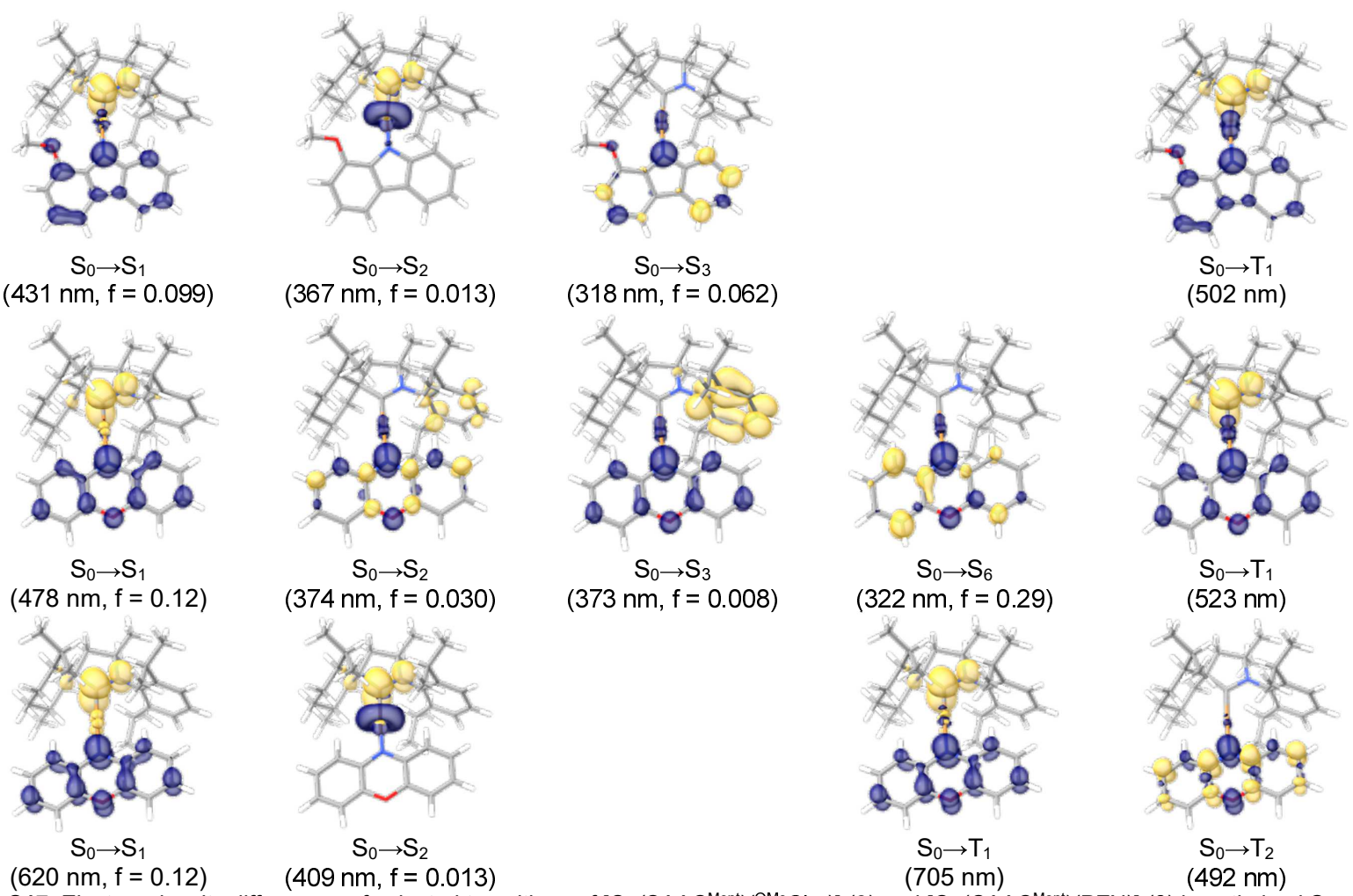

Figure S17. Electron density differences of selected transitions of [Cu(CAAC^{Ment})(^{OMe}Cbz)] (**3**) and [Cu(CAAC^{Ment})(PZN)] (**6**) in optimized S_0-geometry (middle) or T_1-geometry (bottom) (gold: gain of electron density; blue: loss of electron density).

Table S2. Calculated energies for the first 20 electronic singlet and triplet excitations of [Cu(^{OMe}Cbz)(cAAC^{Ment})] (**3**) in its geometry optimized ground state S_0.

State	Energy (cm^{-1})	Wavelength (nm)	f (au^2)	T2 (au)	TX (au)	TY (au)	TZ (au)
1	23183.5	431.3	0.09855	1.3995	-0.68116	-0.88022	0.40092
2	27228.6	367.3	0.01287	0.15564	0.38308	-0.08452	-0.04173
3	31458.2	317.9	0.06183	0.64704	-0.61214	-0.49125	0.17606
4	26856.5	372.3	0.00101	0.01238	-0.06612	-0.08072	-0.03864
5	28644.9	349.1	0.00064	0.00736	-0.05548	-0.05064	-0.04144
6	28537.8	350.4	0.00108	0.01245	0.00762	0.0395	0.1041
7	34453.7	290.2	0.00032	0.00305	-0.04674	0.00986	-0.02773
8	34798.4	287.4	0.00324	0.03065	0.14488	-0.08842	0.04286
9	34842.9	287	0.00136	0.01284	0.03547	-0.008	-0.10732
10	36742.1	272.2	0.00245	0.02199	0.05181	0.04075	-0.13285
11	35307.9	283.2	0.01359	0.12676	0.18633	0.29464	-0.07229
12	35826.4	279.1	0.00893	0.08205	0.08025	0.11771	0.24851
13	32905	303.9	0.00067	0.00671	-0.06736	-0.04017	-0.02363
14	37556.9	266.3	0.00100	0.00878	-0.00788	0.09338	-0.00043
15	39216.4	255	0.01645	0.13807	-0.23235	-0.17203	0.23343
16	37009.5	270.2	0.00065	0.0058	0.04546	0.05591	0.02471
17	40193.6	248.8	0.03348	0.2742	0.19862	0.34023	-0.34496
18	40569.3	246.5	0.03260	0.26454	-0.33791	-0.3874	0.01668
19	40625.6	246.1	0.00263	0.02132	-0.02149	-0.13505	-0.05115
20	42716.1	234.1	0.20571	1.58541	-0.14574	0.01278	-1.2506
21	19916.4	502.1	spin forbidden	(mult=3)			
22	23847.9	419.3	spin forbidden	(mult=3)			
23	25035.3	399.4	spin forbidden	(mult=3)			
24	28649.9	349	spin forbidden	(mult=3)			
25	31681.6	315.6	spin forbidden	(mult=3)			
26	31860.3	313.9	spin forbidden	(mult=3)			
27	24656	405.6	spin forbidden	(mult=3)			
28	26813.2	373	spin forbidden	(mult=3)			
29	27147.1	368.4	spin forbidden	(mult=3)			
30	32694.1	305.9	spin forbidden	(mult=3)			
31	32755.7	305.3	spin forbidden	(mult=3)			
32	32742.3	305.4	spin forbidden	(mult=3)			
33	33081.9	302.3	spin forbidden	(mult=3)			
34	34914.5	286.4	spin forbidden	(mult=3)			
35	35930.3	278.3	spin forbidden	(mult=3)			
36	36058.7	277.3	spin forbidden	(mult=3)			
37	36535.3	273.7	spin forbidden	(mult=3)			
38	37695.4	265.3	spin forbidden	(mult=3)			
39	34320	291.4	spin forbidden	(mult=3)			
40	34881.6	286.7	spin forbidden	(mult=3)			

Table S3. Calculated rotatory strengths and magnetic transition dipole moments for the first 20 electronic singlet excitations of [Cu(^{OMe}Cbz)(cAAC^{Ment})] (**3**) in its geometry optimized ground state S_0.

State	Energy (cm^{-1})	Wavelength (nm)	R (1e40*cgs)	MX (au)	MY (au)	MZ (au)
1	23183.5	431.3	-1.54394	0.07288	-0.05809	-0.01188
2	27228.6	367.3	2.18864	0.04195	0.01686	0.23965
3	31458.2	317.9	-4.45164	0.00574	0.01852	0.01801
4	26856.5	372.3	1.0604	0.01728	-0.03354	-0.01772
5	28644.9	349.1	0.4539	0.04969	-0.05605	-0.02127
6	28537.8	350.4	-2.16522	0.10974	0.09186	0.0173
7	34453.7	290.2	-0.73654	-0.08651	-0.12827	0.15654
8	34798.4	287.4	1.2347	0.02191	-0.01768	-0.04943
9	34842.9	287	-0.12259	-0.06111	0.09582	-0.02492
10	36742.1	272.2	0.11989	0.07117	-0.08424	-0.00001
11	35307.9	283.2	-3.98734	-0.0362	0.0012	0.02856

12	35826.4	279.1	-5.43099	0.07319	-0.08899	-0.02784
13	32905	303.9	-0.99187	0.00251	0.03511	0.0222
14	37556.9	266.3	2.16041	0.00807	0.04993	0.03874
15	39216.4	255	-7.48877 -	0.00813	0.04224	-0.04501
16	37009.5	270.2	-1.18665	0.21259	0.19399	0.05409
17	40193.6	248.8	-11.76128	0.03109	0.05882	-0.03221
18	40569.3	246.5	4.34072	0.22432	-0.22059	-0.02696
19	40625.6	246.1	1.10797	0.08007	0.00454	-0.09157
20	42716.1	234.1	2.07518	0.54094	-0.53671	-0.07205

Table S4. Cartesian coordinates of the geometry optimized ground state S_0 of [Cu(^{OMe}Cbz)(cAAC^{Ment})] (**3**).

Cu	4.152375	11.86736	5.764427
N	3.036367	10.414505	6.085839
C	2.285276	9.865753	5.065408
C	2.463765	9.999149	3.68931
H	3.277337	10.591471	3.291781
C	1.583855	9.355846	2.840908
H	1.719296	9.452569	1.76925
C	0.528944	8.579202	3.334979
H	-0.142822	8.084239	2.643176
C	0.346443	8.436594	4.697685
H	-0.467081	7.830739	5.082586
C	1.224434	9.07523	5.569449
C	1.341302	9.131555	6.997382
C	0.612163	8.55398	8.036336
H	-0.254718	7.937697	7.826955
C	1.021819	8.778354	9.330933
H	0.475978	8.345484	10.16104
C	2.159856	9.551449	9.599163
H	2.464152	9.689807	10.627914
C	2.893073	10.128064	8.576956
C	2.471548	9.944898	7.251865
O	4.031785	10.852279	8.776576
C	4.603411	10.778839	10.057425
H	4.741619	9.738381	10.368975
H	3.991733	11.293802	10.807204
H	5.573696	11.267822	9.99536
C	5.106372	13.377714	5.203042
N	5.209933	13.705434	3.94303
C	5.9812	14.95483	3.617946
C	6.413869	15.407685	5.011714
H	6.114208	16.44143	5.18935
H	7.499884	15.371255	5.099995
C	5.747807	14.463678	6.032271
C	5.106509	15.983075	2.918933
H	5.71966	16.854648	2.682416
H	4.280399	16.31554	3.546438
H	4.704843	15.591235	1.983497
C	7.161115	14.634021	2.716081
H	6.82915	14.224952	1.760454
H	7.847184	13.926497	3.181294
H	7.710389	15.555956	2.516115
C	4.600552	12.95655	2.877708
C	5.327656	11.930037	2.260188
C	4.764764	11.318802	1.144923
H	5.305003	10.520639	0.650299
C	3.51759	11.687495	0.678783
H	3.098243	11.19947	-0.193211
C	2.781123	12.635795	1.362005
H	1.77311	12.863349	1.038074
C	3.296428	13.283039	2.478847

C	6.613051	11.373134	2.828806
H	6.950429	12.034917	3.627097
C	6.337577	10.008986	3.460618
H	5.985087	9.297016	2.710641
H	5.573734	10.07229	4.239178
H	7.249204	9.608055	3.909601
C	7.731045	11.264388	1.799061
H	7.486052	10.538712	1.02036
H	8.6504	10.923828	2.281373
H	7.936065	12.219173	1.312331
C	2.396365	14.210692	3.265345
H	3.006784	14.736539	3.999148
C	1.364096	13.399173	4.045906
H	0.737775	12.807639	3.374721
H	0.716462	14.067758	4.618787
H	1.841342	12.704833	4.740329
C	1.707116	15.254263	2.394087
H	2.417843	15.830196	1.79904
H	1.145091	15.950223	3.021081
H	0.994291	14.793241	1.707102
C	6.772627	13.967453	7.076251
H	7.221232	14.895998	7.458532
C	6.115352	13.273679	8.258685
H	5.664104	12.33517	7.927292
H	6.887932	13.010652	8.988681
C	5.034646	14.113294	8.911958
H	4.589372	13.570125	9.749389
H	5.465683	15.03562	9.325556
C	3.958157	14.474708	7.904293
H	3.529307	13.534855	7.53041
C	4.599941	15.213968	6.744082
H	5.02114	16.15439	7.123072
H	3.841226	15.494597	6.004432
C	7.92319	13.132295	6.474533
H	8.059538	13.452262	5.434759
C	7.656303	11.633541	6.44803
H	6.690904	11.392387	5.997312
H	7.660285	11.208977	7.454262
H	8.43186	11.123503	5.87147
C	9.231025	13.418697	7.198966
H	10.047919	12.821832	6.786007
H	9.151483	13.173773	8.262207
H	9.508798	14.472968	7.119795
C	2.839325	15.293299	8.519624
H	2.066785	15.526427	7.782247
H	3.218375	16.240025	8.918566
H	2.364328	14.750967	9.340213

Table S5. Calculated energies for the first 20 electronic singlet and triplet excitations of [Cu(PZN)(cAAC^{Ment})] (**6**) in its geometry optimized ground state S_0.

State	Energy (cm^{-1})	Wavele (nm)	ngth f	T2 (au^2)	TX (au)	TY (au)	TZ (au)
1	20937.8	477.6	0.12043612	1.89366	-0.86221	-0.98186	0.43151
2	26731.9	374.1	0.03019008	0.3718	0.13723	0.18652	0.56407
3	26766.5	373.6	0.00836776	0.10292	-0.02583	-0.05615	-0.3148
4	27674.6	361.3	0.01649291	0.1962	0.37702	-0.22995	0.03429
5	28571.9	350	0.02215907	0.25532	-0.16531	-0.15455	0.45178
6	31053.4	322	0.29493221	3.12672	-0.2031	-0.28506	-1.73327
7	31775.3	314.7	0.01501911	0.15561	-0.10642	-0.01482	0.37956
8	35906.2	278.5	0.00332599	0.03049	0.17105	-0.03488	0.00441
9	36073.9	277.2	0.0017693	0.01615	-0.0373	0.06874	0.10015
10	36127.6	276.8	0.00300556	0.02739	0.04847	-0.0626	0.14533
11	36619.2	273.1	0.00608238	0.05468	-0.01721	-0.22021	0.07677
12	38477	259.9	0.03279686	0.28061	-0.14899	-0.2072	-0.4642
13	39330.4	254.3	0.0012915	0.01081	0.00914	-0.10336	0.00661
14	39448.5	253.5	0.0045799	0.03822	0.08278	-0.08058	-0.15772
15	40106.9	249.3	0.05553625	0.45586	0.27898	0.37426	-0.48781
16	40630.3	246.1	0.13031842	1.05592	0.66747	0.69836	-0.35028
17	40898.9	244.5	0.00083923	0.00676	-0.07276	0.03571	-0.01364
18	41149.8	243	0.00167275	0.01338	-0.01263	0.02984	-0.11105
19	41698.3	239.8	0.01341004	0.10587	-0.18142	-0.20587	-0.17486
20	41797.9	239.2	0.02275879	0.17925	-0.41256	-0.08383	0.04491
21	19107.3	523.4	spin forbidden	(mult=3)			
22	21649.9	461.9	spin forbidden	(mult=3)			
23	24682.3	405.1	spin forbidden	(mult=3)			
24	25304.6	395.2	spin forbidden	(mult=3)			
25	25594.4	390.7	spin forbidden	(mult=3)			
26	26778.3	373.4	spin forbidden	(mult=3)			
27	28166.6	355	spin forbidden	(mult=3)			
28	31321.1	319.3	spin forbidden	(mult=3)			
29	31452.3	317.9	spin forbidden	(mult=3)			
30	33329.6	300	spin forbidden	(mult=3)			
31	34464.8	290.2	spin forbidden	(mult=3)			
32	34587.2	289.1	spin forbidden	(mult=3)			
33	34862.4	286.8	spin forbidden	(mult=3)			
34	35060.9	285.2	spin forbidden	(mult=3)			
35	35247.9	283.7	spin forbidden	(mult=3)			
36	35918	278.4	spin forbidden	(mult=3)			
37	36042	277.5	spin forbidden	(mult=3)			
38	37815.3	264.4	spin forbidden	(mult=3)			
39	37908.2	263.8	spin forbidden	(mult=3)			
40	38326.6	260.9	spin forbidden	(mult=3)			

Table S6. Calculated rotatory strengths and magnetic transition dipole moments for the first 20 electronic singlet excitations of [Cu(PZN)(cAAC^{Ment})] (**6**) in its globally geometry optimized ground state S_0.

State	Energy (cm^{-1})	Wavelength (nm)	R (1e40*cgs)	MX (au)	MY (au)	MZ (au)
1	20937.8	477.6	-1.12972	0.06172	-0.06401	-0.02787
2	26731.9	374.1	-14.05864	0.40688	-0.62228	0.05391
3	26766.5	373.6	0.37191	-0.15439	0.23354	-0.03149
4	27674.6	361.3	7.53147	0.02362	-0.00005	0.20581
5	28571.9	350	14.50022	0.17275	-0.28359	0.03427
6	31053.4	322	-4.05052	0.51287	-0.43606	0.01658
7	31775.3	314.7	6.49064	-0.12205	0.10953	0.00633
8	35906.2	278.5	1.35203	0.01406	-0.01876	-0.04332
9	36073.9	277.2	-0.48245	0.00708	-0.15046	0.09569
10	36127.6	276.8	-7.68609	0.11598	0.07854	-0.11704
11	36619.2	273.1	2.93792	-0.01981	-0.03449	-0.02219

12	38477	259.9	-4.21825	-0.04054	0.08203	-0.00432
13	39330.4	254.3	0.00537	-0.01521	0.00472	0.09652
14	39448.5	253.5	0.63034	-0.00255	-0.06541	0.0236
15	40106.9	249.3	2.49298	-0.02801	0.06879	0.02592
16	40630.3	246.1	-22.29204	-0.22645	0.185	0.07232
17	40898.9	244.5	-2.91162	0.00946	-0.12691	0.07004
18	41149.8	243	-1.24389	0.06138	0.14413	0.05551
19	41698.3	239.8	9.61599	-0.08255	-0.00676	-0.02304
20	41797.9	239.2	9.35467	-0.06467	0.11188	0.05659

Table S7. Cartesian coordinates of the globally geometry optimized ground state S_0 of [Cu(PZN)(cAAC^{Ment})] (**6**).

H	-0.727989	7.689347	4.447346
H	-0.326362	8.385967	8.903136
C	0.150122	8.279902	4.191731
H	0.05803	7.908271	2.065643
O	0.314985	8.76473	6.484092
C	0.574844	8.989525	8.809288
C	0.591539	8.409065	2.871256
H	0.579849	13.910141	4.599438
H	0.598661	12.708333	3.289908
H	0.879445	9.262281	10.930791
C	0.821893	8.915683	5.224345
C	1.034444	9.266048	7.53061
H	0.949523	14.756785	1.696278
C	1.250037	9.480643	9.931242
H	1.070926	15.861537	3.066526
C	1.227732	13.256758	4.001585
H	1.67961	12.518626	4.675713
C	1.647275	15.179635	2.429448
C	1.717402	9.183061	2.612803
H	1.703664	12.805299	0.992639
C	1.971551	9.703589	4.990648
H	2.08545	9.3035	1.595703
H	1.799648	15.268376	7.83609
H	2.015948	14.371978	9.348028
C	2.190891	10.046588	7.309453
C	2.400862	10.238441	9.743266
C	2.294241	14.08702	3.279855
H	2.388251	15.770925	1.8797
C	2.392304	9.815198	3.658001
N	2.63214	10.344998	6.029031
C	2.539118	14.963639	8.587335
C	2.709189	12.561663	1.330298
H	2.956718	10.620389	10.598718
C	2.859098	10.504869	8.452585
H	2.893609	14.574455	4.055878
H	2.923898	15.872582	9.070847
H	3.050305	11.163529	-0.269279
H	3.268804	10.425002	3.444011
C	3.209445	13.177285	2.480617
H	3.214051	13.264061	7.492437
C	3.457248	11.624106	0.62957
H	3.769725	11.080022	8.306457
C	3.665163	14.158486	7.956182
H	3.651092	15.294215	6.11224
Cu	3.856831	11.702716	5.695046
H	4.200024	16.155659	3.647928
H	4.192514	13.078334	9.75201
C	4.374961	14.953059	6.867719
C	4.513495	12.833409	2.896196

C	4.688471	13.687613	8.9842
C	4.700091	11.232651	1.111246
H	4.707758	15.486674	2.077536
H	4.800917	15.864174	7.319027
C	4.91847	13.174047	5.252761
C	5.062461	15.846052	3.049878
N	5.099884	13.538825	4.00404
H	5.104575	14.566663	9.50405
H	5.248176	10.442429	0.600771
C	5.247665	11.811673	2.260395
H	5.406414	11.961546	7.923507
H	5.685722	16.730645	2.876747
C	5.538304	14.217327	6.157203
H	5.418228	9.90346	4.205296
C	5.812943	12.895066	8.33435
C	5.898775	14.788537	3.763337
H	5.934571	16.230076	5.394399
H	5.869606	9.146138	2.673416
C	6.253452	15.20025	5.19955
C	6.208487	9.846884	3.446499
H	6.55023	12.595931	9.091835
C	6.52157	13.654739	7.217613
C	6.516309	11.223356	2.847514
H	6.477632	11.150119	5.983323
H	6.857361	14.102557	1.931991
H	6.839077	11.866618	3.673129
H	6.954262	14.562112	7.673969
C	7.133251	14.48523	2.921
H	7.103609	9.425281	3.919583
H	7.338178	15.174845	5.347378
H	7.433727	10.429434	1.032042
H	7.416991	10.857463	7.452548
C	7.435675	11.356237	6.475947
H	7.703004	15.410538	2.778641
H	7.788077	13.757102	3.409783
C	7.663777	11.131164	1.843183
C	7.702821	12.853097	6.617103
H	7.892702	12.101219	1.388203
H	7.881754	13.242832	5.603497
H	8.227042	10.882805	5.88189
H	8.571327	10.765309	2.338955
H	8.862519	12.771861	8.458755
C	8.982616	13.091402	7.414748
H	9.261158	14.152899	7.421388
H	9.823031	12.52501	6.994459

Table S8. Calculated energies for the first 20 electronic singlet and triplet excitations of [Cu(PZN)(cAAC^{Ment})] (**6**) in its locally geometry optimized (distorted) ground state S_0.

State	Energy (cm^{-1})	Wavelength (nm)	*f* (au^2)	T2 (au)	TX (au)	TY (au)	TZ (au)
1	21838.3	457.9	0.131537063	1.98292	0.83381	1.04058	-0.45262
2	27201.1	367.6	0.033550474	0.40606	-0.16985	-0.15575	-0.5941
3	27633.4	361.9	0.015425037	0.18377	0.40913	-0.12679	-0.01749
4	27732.2	360.6	0.004158888	0.04937	-0.21406	-0.05481	-0.02333
5	29278.9	341.5	0.019980612	0.22466	-0.16736	-0.20051	0.39554
6	31242.9	320.1	0.294105338	3.09904	0.38512	0.14177	1.71191
7	31926.9	313.2	0.009993493	0.10305	0.10637	-0.04813	-0.29902
8	36054.9	277.4	0.003700954	0.03379	-0.17772	0.02257	0.0412
9	36194.3	276.3	0.000762234	0.00693	0.01563	0.03452	0.07414
10	36346	275.1	0.003314393	0.03002	-0.06532	0.04656	-0.15358

11	37243	268.5	0.019301727	0.17062	0.08581	0.37361	-0.15385
12	38553	259.4	0.0363834	0.31068	0.1096	0.14572	0.52672
13	39248.3	254.8	0.006664081	0.0559	0.06142	-0.07176	-0.21674
14	39750.6	251.6	0.016082678	0.1332	-0.23178	-0.27001	0.08106
15	40162.6	249	0.048727421	0.39942	-0.28657	-0.30431	0.47401
16	40757.4	245.4	0.099366627	0.80262	-0.7093	-0.51016	0.19811
17	41001.3	243.9	0.008732671	0.07012	-0.02577	-0.11668	0.2363
18	41367.9	241.7	0.018388331	0.14634	0.06862	0.04603	0.37351
19	41639.7	240.2	0.013117982	0.10371	0.17488	-0.23897	0.12659
20	42024.5	238	0.001921942	0.01506	-0.0373	-0.03586	0.11126
21	19746	506.4	spin forbidden	(mult=3)			
22	22260.9	449.2	spin forbidden	(mult=3)			
23	24612.3	406.3	spin forbidden	(mult=3)			
24	25555.6	391.3	spin forbidden	(mult=3)			
25	25840.4	387	spin forbidden	(mult=3)			
26	27688.5	361.2	spin forbidden	(mult=3)			
27	28848.7	346.6	spin forbidden	(mult=3)			
28	31254.6	320	spin forbidden	(mult=3)			
29	31323.1	319.3	spin forbidden	(mult=3)			
30	33557.8	298	spin forbidden	(mult=3)			
31	34566.1	289.3	spin forbidden	(mult=3)			
32	34698.5	288.2	spin forbidden	(mult=3)			
33	34959.4	286	spin forbidden	(mult=3)			
34	35108.5	284.8	spin forbidden	(mult=3)			
35	35572.5	281.1	spin forbidden	(mult=3)			
36	35954.4	278.1	spin forbidden	(mult=3)			
37	36065	277.3	spin forbidden	(mult=3)			
38	37999.1	263.2	spin forbidden	(mult=3)			
39	38113.9	262.4	spin forbidden	(mult=3)			
40	38378.6	260.6	spin forbidden	(mult=3)			

Table S9. Calculated rotatory strengths and magnetic transition dipole moments for the first 20 electronic singlet excitations of [Cu(PZN)(cAAC^{Ment})] (**6**) in its locally geometry optimized (distorted) ground state S_0.

State	Energy (cm^{-1})	Wavelength (nm)	R (1e40*cgs)	MX (au)	MY (au)	MZ (au)
1	21838.3	457.9	10.15308	-0.06938	0.10586	0.06799
2	27201.1	367.6	-31.91678	-0.18575	0.74243	-0.02759
3	27633.4	361.9	0.68917	0.01465	0.00841	0.19815
4	27732.2	360.6	3.81506	-0.08748	0.22235	-0.06658
5	29278.9	341.5	28.87574	0.04315	-0.27097	0.03574
6	31242.9	320.1	-6.33616	-0.49772	0.39491	0.07141
7	31926.9	313.2	9.63438	0.09927	-0.09767	-0.0173
8	36054.9	277.4	2.42135	-0.01306	-0.01241	0.07512
9	36194.3	276.3	-0.42785	0.02298	-0.16574	0.06007
10	36346	275.1	-7.86623	-0.0902	-0.11053	0.1135
11	37243	268.5	-1.99597	0.00415	0.01424	0.06442
12	38553	259.4	-4.59796	0.03884	-0.08799	-0.00225
13	39248.3	254.8	5.16822	0.04529	-0.13201	0.00596
14	39750.6	251.6	-2.93047	0.04771	0.02343	0.13781
15	40162.6	249	-5.17223	0.02392	-0.0714	-0.05452
16	40757.4	245.4	-18.06986	0.14602	-0.16012	-0.083
17	41001.3	243.9	-14.71735	-0.0432	0.11997	-0.07758
18	41367.9	241.7	7.77659	-0.10502	0.01533	0.06157
19	41639.7	240.2	27.37435	0.1474	-0.17099	-0.06773
20	42024.5	238	3.22596	-0.18499	0.00305	0.00046

Table S10. Cartesian coordinates of the locally geometry optimized (distorted) ground state S_0 of [Cu(PZN)(cAAC^{Ment})] (**6**).

H	-1.0935031787	8.3036519338	4.7717175247
H	-0.4022498136	8.2246718023	2.3532791812
C	-0.0946168573	8.6015437084	4.4575190849
C	0.2962786002	8.5664409525	3.1147355844
H	-0.1780834024	8.7602362487	9.1916536855
O	0.3345596054	9.1086920140	6.7193004403
H	0.5498498246	13.3423174558	4.8442048834
H	0.6465300753	12.1148242276	3.5605024434
C	0.7886402943	9.0423264657	5.4305673674
H	0.7126470001	14.2084279652	1.9576427459
H	0.8247378592	15.3296377869	3.3155296955
C	1.2395018745	12.7434499986	4.2360574784
C	1.5845003812	8.9665650252	2.7740681406
C	0.8552778329	9.0567763734	9.0197522062
H	1.9122237652	8.9447172072	1.7361759078
C	1.2613193583	9.2683337348	7.7113445715
C	1.4154661666	14.6905302397	2.6479670249
H	1.7874149545	12.0718494011	4.9073715433
H	1.5866302696	12.3183336858	1.2172545137
C	2.0999485470	9.4548552859	5.1095878043
H	1.7839157428	14.4603710954	8.0667302140
C	2.4728168345	9.3981590320	3.7601143994
H	2.1723118637	13.5286382746	9.5216262588
H	1.4255277183	9.0798407213	11.1027237992
C	2.1940594487	13.6567440202	3.4618749942
C	1.7532976862	9.2384533594	10.0771850807
H	2.0757133390	15.3339053119	2.0555676534
C	2.5858472242	14.2171265274	8.7750399165
C	2.6307981318	12.1732453730	1.4872524859
N	2.9521606106	9.9389936875	6.0924289056
H	3.4788723228	9.7177377750	3.4892405957
C	2.5782210033	9.6710295959	7.4011925872
H	2.7910978852	14.1936148182	4.2061233189
H	2.8733787994	15.1441086055	9.2910166930
H	3.0016455747	10.8187564420	-0.1430922466
C	3.1406186945	12.8303088471	2.6099472384
H	3.4179495739	12.6684461695	7.5713589736
C	3.4188091191	11.3142334589	0.7321971655
H	3.5587172414	14.8116893402	6.2922972177
C	3.0658483671	9.6047622382	9.7957684590
C	3.7757781509	13.5884189691	8.0661432032
Cu	4.1139645092	11.3254609623	5.7068212469
C	3.4701180959	9.8022046932	8.4738846894
H	4.4881081878	12.4810826917	9.7750054386
H	3.9031615775	15.8796782969	3.8594981275
C	4.3473899605	14.5164804503	7.0006771696
H	3.7888022662	9.7242592102	10.6018523115
C	4.4941702941	12.6096724039	2.9440061581
C	4.8833248504	13.1860588828	9.0316167630
C	4.7224150618	11.0465045137	1.1296030483
H	4.3833220515	15.3183110723	2.2393063716
H	4.6858472543	15.4459695181	7.4870832710
C	5.0108472267	12.8969726826	5.2777837391
H	4.5046266673	10.0526281173	8.2441854079
C	4.7559877577	15.6747214760	3.2060099826
N	5.0713852850	13.3391203818	4.0428753322
H	5.2224184879	14.0766891936	9.5867414331
C	5.2825493046	11.6707057107	2.2485961512
H	5.3144823756	10.3204666232	0.5744860283
H	5.7117466524	11.6213786389	7.8308941825

H	5.8010035779	9.7334720466	4.0981184556
C	5.5572052646	13.9568521133	6.2061793777
H	5.2837448833	16.6201409318	3.0367974316
C	6.0530265887	12.5583277908	8.2907494032
H	6.2434053703	9.0812038178	2.5124086577
C	5.7252189862	14.6748468881	3.8291295930
H	5.6976128658	16.0341140562	5.5318908757
C	6.5427550881	9.7933418798	3.2916398291
C	6.1116725995	15.0546838254	5.2679582234
H	6.8183230460	11.0481737162	5.8197795056
C	6.6460360116	11.2159192301	2.7326874076
C	6.6367646620	13.4560640555	7.2022670882
H	6.8473006728	12.2819007878	8.9977719766
H	6.9452220612	11.8634586585	3.5638217240
H	6.6486761589	14.1698174452	1.9243189395
H	6.9782451244	14.3803004806	7.6997810026
H	7.5083884431	9.4665365556	3.6961631583
C	6.9382399362	14.5350892416	2.9160954415
H	7.1994935747	15.1395726945	5.3607664200
H	7.8337033949	10.7635268318	7.2391585895
H	7.5272437771	10.6094326530	0.8283864381
C	7.7668786034	11.3216233222	6.2973346550
C	7.7273962065	11.3003192781	1.6567261507
C	7.8800944645	12.8265705472	6.5285953561
H	7.4068475064	15.5177860456	2.7905738143
H	7.6867966056	13.8551380523	3.3350765283
H	7.9949921858	13.2928795510	5.5377850650
H	7.8090929291	12.3081337908	1.2353056434
H	8.5819257847	10.9717455298	5.6517478555
H	8.7029102315	11.0276235166	2.0779352358
H	9.0869174476	12.7552368310	8.3399060023
C	9.1470580621	13.1502661789	7.3168528476
H	9.3114126687	14.2329425137	7.3870682201
H	10.0320461925	12.7044226069	6.8458811112

Table S11. Calculated energies for the first 20 electronic singlet and triplet excitations of [Cu(PZN)(cAAC^{Ment})] (**6**) in its geometry optimized triplet state T_1.

State	Energy (cm^{-1})	Wavelength (nm)	f (au^2)	T2 (au)	TX (au)	TY (au)	TZ (au)
1	16124	620.2	0.11545424	2.35729	-0.9157	-1.14073	0.4664
2	24463.7	408.8	0.01264103	0.17011	0.33066	-0.24614	0.01385
3	25293.5	395.4	0.01743273	0.2269	-0.0404	-0.15101	-0.44996
4	25961.9	385.2	0.02172638	0.2755	-0.02635	-0.14094	-0.50492
5	27369.9	365.4	0.01191391	0.1433	-0.11556	-0.0751	0.35257
6	30050.4	332.8	0.25256337	2.76691	0.00742	0.38871	1.61733
7	30674.1	326	0.0716496	0.76898	-0.01102	0.12375	0.86807
8	32559.3	307.1	0.00047622	0.00482	-0.0288	-0.0502	0.03829
9	32787.4	305	0.00474394	0.04763	-0.18815	0.09943	0.04845
10	32864.7	304.3	0.00402655	0.04033	0.08616	0.00019	0.18142
11	32971.1	303.3	0.00047947	0.00479	-0.04155	-0.03773	0.04047
12	35878.7	278.7	0.00541025	0.04964	0.0097	-0.0785	0.20829
13	36754.3	272.1	0.00469142	0.04202	-0.10454	0.1046	0.14196
14	37913.3	263.8	0.03970159	0.34474	-0.2412	-0.39599	0.36021
15	37988.4	263.2	0.0948997	0.82241	-0.51436	-0.60662	0.43572
16	38123.5	262.3	0.04142768	0.35774	-0.31601	-0.5041	0.06137
17	39466.3	253.4	0.0018274	0.01524	0.03611	0.11733	0.01317
18	39849.6	250.9	0.00439576	0.03631	0.03234	0.01468	-0.18723
19	39877.4	250.8	0.03856559	0.31838	0.09514	0.21832	-0.51153
20	39974.7	250.2	0.01667998	0.13737	-0.09246	-0.12931	0.33481
21	14185.6	704.9	spin forbidden	(mult=3)			
22	20309.6	492.4	spin forbidden	(mult=3)			

23	21563.1	463.8	spin forbidden	(mult=3)
24	24134.5	414.3	spin forbidden	(mult=3)
25	24498.8	408.2	spin forbidden	(mult=3)
26	25711	388.9	spin forbidden	(mult=3)
27	27111.3	368.8	spin forbidden	(mult=3)
28	28928.2	345.7	spin forbidden	(mult=3)
29	31005.2	322.5	spin forbidden	(mult=3)
30	31144.5	321.1	spin forbidden	(mult=3)
31	31237.5	320.1	spin forbidden	(mult=3)
32	31309.3	319.4	spin forbidden	(mult=3)
33	31502.7	317.4	spin forbidden	(mult=3)
34	32450	308.2	spin forbidden	(mult=3)
35	34686.4	288.3	spin forbidden	(mult=3)
36	35262.3	283.6	spin forbidden	(mult=3)
37	35491	281.8	spin forbidden	(mult=3)
38	35528	281.5	spin forbidden	(mult=3)
39	35761.7	279.6	spin forbidden	(mult=3)
40	36575.3	273.4	spin forbidden	(mult=3)

Table S12. Calculated rotatory strengths and magnetic transition dipole moments for the first 20 electronic singlet excitations of [Cu(PZN)(cAAC^{Ment})] (**6**) in its geometry optimized triplet state T_1.

State	Energy (cm^{-1})	Wavelength (nm)	R (1e40*cgs)	MX (au)	MY (au)	MZ (au)
1	16124	620.2	-7.44673	0.06587	-0.04357	-0.01111
2	24463.7	408.8	1.8142	0.00179	-0.00353	0.17249
3	25293.5	395.4	0.44651	-0.52671	0.35115	-0.07266
4	25961.9	385.2	3.70117	-0.46377	0.29751	-0.07439
5	27369.9	365.4	-3.03775	0.24689	-0.17382	0.02562
6	30050.4	332.8	7.79619	-0.48176	0.37173	-0.07691
7	30674.1	326	-0.75799	-0.31613	0.21589	-0.03664
8	32559.3	307.1	-3.07134	0.05859	0.05073	-0.05957
9	32787.4	305	-1.62361	0.0099	-0.06694	0.10474
10	32864.7	304.3	1.05925	0.10633	-0.04619	-0.03807
11	32971.1	303.3	6.2245	-0.09721	-0.15087	0.08579
12	35878.7	278.7	-1.04946	-0.08158	0.02899	0.00404
13	36754.3	272.1	-7.91013	0.03876	-0.07576	-0.03382
14	37913.3	263.8	13.90367	0.0199	-0.05765	0.03183
15	37988.4	263.2	-19.8244	0.10935	-0.06258	-0.05454
16	38123.5	262.3	10.61479	0.11855	-0.11723	0.01432
17	39466.3	253.4	-7.15093	-0.07992	-0.10274	-0.01724
18	39849.6	250.9	10.6442	0.06825	-0.05879	-0.11341
19	39877.4	250.8	43.95606	-0.21705	0.15084	-0.15826
20	39974.7	250.2	-52.24183	-0.03415	-0.08469	-0.37311

Table S13. Cartesian coordinates of the geometry optimized triplet state T_1 of [Cu(PZN)(cAAC^{Ment})] (**6**).

H	0.267346	6.686578	4.50425
H	0.279289	7.680013	8.973315
C	0.869187	7.555773	4.248399
H	0.873493	7.209812	2.128582
O	0.94671	8.067554	6.53975
C	0.887305	8.571201	8.834213
C	1.211883	7.857844	2.934796
H	0.54919	14.181536	4.637411
H	0.449934	13.040412	3.279133
H	0.910423	9.14972	10.903199
C	1.303667	8.387836	5.274325
C	1.314079	8.888489	7.548591
H	0.996038	15.082905	1.749941

C	1.243661	9.394993	9.896728
H	1.192675	16.127073	3.162351
C	1.132897	13.498572	4.006694
H	1.529951	12.704142	4.651346
C	1.71757	15.42312	2.50409
C	1.983643	8.993287	2.649247
H	1.541259	12.993237	1.041264
C	2.098157	9.532238	5.013986
H	2.246085	9.240811	1.623527
H	2.096229	15.906832	7.655981
H	2.086726	15.009092	9.186009
C	2.112288	10.03065	7.295089
C	2.025241	10.537645	9.671407
C	2.271821	14.252329	3.314478
H	2.508119	15.973422	1.983284
C	2.419931	9.81882	3.669996
N	2.539115	10.337982	6.030992
C	2.737173	15.489735	8.443332
C	2.542211	12.698852	1.355761
H	2.298617	11.185667	10.501731
C	2.451995	10.848981	8.39303
H	2.920095	14.639401	4.107918
H	3.24525	16.329014	8.93914
H	2.782417	11.297142	-0.26322
H	3.014465	10.706041	3.45353
C	3.109192	13.295692	2.487118
H	3.182473	13.70028	7.357016
C	3.230224	11.732081	0.630002
H	3.051305	11.735267	8.198293
C	3.742837	14.504071	7.868231
H	4.004908	15.603761	6.034723
Cu	3.727008	11.778076	5.682192
H	4.326115	16.255328	4.005275
H	3.995631	13.364121	9.697338
C	4.63078	15.142513	6.810987
C	4.422306	12.92612	2.867386
C	4.618908	13.873099	8.945199
C	4.47659	11.299712	1.070321
H	4.62996	15.794926	2.315188
H	5.202058	15.962254	7.2821
C	4.888172	13.17108	5.257382
C	5.104862	15.991109	3.283402
N	5.071613	13.583744	3.938061
H	5.149283	14.674912	9.485784
H	4.988587	10.500748	0.534208
C	5.079775	11.864353	2.199965
H	5.098159	12.040737	7.917912
H	5.763902	16.860165	3.164091
C	5.626541	14.16486	6.13704
H	5.332582	9.940688	4.121646
C	5.629382	12.901717	8.351223
C	5.917669	14.774696	3.739507
H	6.54352	16.031493	5.418901
H	5.711353	9.183445	2.560974
C	6.502071	14.968895	5.149191
C	6.084201	9.877458	3.326143
H	6.268517	12.492803	9.14685
C	6.49564	13.526942	7.258422
C	6.36448	11.261553	2.734077
H	6.259795	10.977623	6.116372
H	6.593098	14.293641	1.724547
H	6.697686	11.899328	3.560797

H	7.018372	14.381969	7.724225
C	7.018531	14.536123	2.706433
H	6.997686	9.449627	3.75786
H	7.534716	14.603339	5.163496
H	7.215109	10.478451	0.881703
H	7.016721	10.660493	7.695905
C	7.182151	11.088622	6.698652
H	7.62709	15.441952	2.595094
H	7.680767	13.71974	3.010817
C	7.473112	11.180279	1.685463
C	7.599997	12.55552	6.769853
H	7.672724	12.153602	1.224266
H	7.864145	12.846583	5.743138
H	7.967932	10.494381	6.214182
H	8.404423	10.822183	2.142251
H	8.656493	12.472899	8.673669
C	8.860592	12.707028	7.619316
H	9.253164	13.731298	7.577769
H	9.653824	12.02749	7.281513

References.

[1] M. Gernert, U. Müller, M. Haehnel, J. Pflaum, A. Steffen, *Chem. Eur. J.* **2017**. *23*, 2206.

[2] R. Jazzar. J.-B. Bourg, R. D. Dewhurst, B. Donnadieu, G. Bertrand, *J. Org. Chem.* **2007**, *72*, 3492.

[3] G. M. Sheldrick, *Acta Crystallogr. A* **2015**, *71*, 3.

[4] G. M. Sheldrick, *Acta Crystallogr. A* **2008**, *64*, 112.

[5] C. B. Hübschle, G. M. Sheldrick, B. Dittrich, *J. Appl. Crystallogr.* **2011**, *44*, 1281.

[6] 4.6.0. Crystal Impact-Dr. H. Putz & Dr. K. Brandenburg GbR: Bonn, 2020, *Diamond - Crystal and Molecular Structure Visualization*.

[7] a) F. Neese, *WIREs Comput. Mol. Sci.* **2012**, *2*, 73; b) F. Neese, *WIREs Comput. Mol. Sci.* **2018**, *8*, e1327.

[8] J. P. Perdew , M. Ernzerhof, K. Burke, *J. Chem. Phys.* **1996**, *105*, 9982.

[9] W. Kohn, L. J. Sham, *Phys. Rev.* **1965**, *140*, A1133-A1138.

[10] a) F. Weigend , R. Ahlrichs, *Phys. Chem. Chem. Phys.* **2005**, *7*, 3297; b) S. Grimme, J. Antony, S. Ehrlich, H. Krieg, *J. Chem. Phys.* **2010**, *132*, 154104; c) S. Grimme, S. Ehrlich, L. Goerigk, *J. Comput. Chem.* **2011**, *32*, 1456; d) E. van Lenthe, E. J. Baerends, J. G. Snijders, *J. Chem. Phys.* **1998**, *101*, 9783.

5 Bibliography

[1] S-kei, Schematic Diagrams of Light Emitting Diodes (LED), **2011**.

[2] W. Dong in 2021 Int. Conf. Electron. Circuits Inf. Eng. ECIE, IEEE, Zhengzhou, China, **2021**, pp. 60–64.

[3] H. J. Jang, J. Y. Lee, G. W. Baek, J. Kwak, J. H. Park, *J. Inf. Disp.* **2022**, *23*, 1–17.

[4] J. Kang, G. W. Baek, J. Y. Lee, J. Kwak, J. H. Park, *J. Inf. Disp.* **2024**, *25*, 219–234.

[5] K. Yoshida, P. P. Manousiadis, R. Bian, Z. Chen, C. Murawski, M. C. Gather, H. Haas, G. A. Turnbull, I. D. W. Samuel, *Nat. Commun.* **2020**, *11*, 1171.

[6] L. Yao, B. Yang, Y. Ma, *Sci. China Chem.* **2014**, *57*, 335–345.

[7] B. Geffroy, P. le Roy, C. Prat, *Polym. Int.* **2006**, *55*, 572–582.

[8] X. Y. Zeng, Y. Q. Tang, X. Y. Cai, J. X. Tang, Y. Q. Li, *Mater. Chem. Front.* **2023**, *7*, 1166–1196.

[9] J. Zhao, X. Du, C. Zheng, Z. He, J. Guo, N. Zhang, H. Lin, S. Tao, *Org. Electron.* **2020**, *87*, 105985.

[10] C. Adachi, M. A. Baldo, M. E. Thompson, S. R. Forrest, *J. Appl. Phys.* **2001**, *90*, 5048–5051.

[11] Q. Zhang, D. Tsang, H. Kuwabara, Y. Hatae, B. Li, T. Takahashi, S. Y. Lee, T. Yasuda, C. Adachi, *Adv. Mater.* **2015**, *27*, 2096–2100.

[12] C. Han, R. Du, H. Xu, S. Han, P. Ma, J. Bian, C. Duan, Y. Wei, M. Sun, X. Liu, W. Huang, *Nat. Commun.* **2021**, *12*, 3640.

[13] S. Lee, H. Kim, Y. Kim, *InfoMat* **2021**, *3*, 61–81.

[14] Z. Li, L. Zhang, H. Xue, H. Yang, Y. Yu, L. Xu, Y. Li, J. Peng, *Org. Electron.* **2022**, *103*, 106468.

[15] X. Liang, K. Wang, R. Zhang, K. Li, X. Lu, K. Guo, H. Wang, Y. Miao, H. Xu, Z. Wang, *Dyes Pigment.* **2017**, *139*, 764–771.

[16] A. Steffen, B. Hupp in *Comprehensive Coordination Chemistry III*, Elsevier, **2021**, pp. 466–502.

[17] M. Klessinger, J. Michl, *Excited States and Photochemistry of Organic Molecules*, VCH, New York, Weihnheim, **1995**.

[18] T. J. Penfold, E. Gindensperger, C. Daniel, C. M. Marian, *Chem. Rev.* **2018**, *118*, 6975–7025.

[19] N. J. Turro, V. Ramamurthy, J. C. Scaiano, *Modern Molecular Photochemistry*, University Science Books, Sausalitos, California, **2010**.

[20] M. A. El-Sayed, *J. Chem. Phys.* **1963**, *38*, 2834–2838.

[21] G. Baryshnikov, B. Minaev, H. Ågren, *Chem. Rev.* **2017**, *117*, 6500–6537.

[22] H. Uoyama, K. Goushi, K. Shizu, H. Nomura, C. Adachi, *Nature* **2012**, *492*, 234–238.

[23] A. Endo, K. Sato, K. Yoshimura, T. Kai, A. Kawada, H. Miyazaki, C. Adachi, *Appl. Phys. Lett.* **2011**, *98*, 083302.

[24] Y. Tao, K. Yuan, T. Chen, P. Xu, H. Li, R. Chen, C. Zheng, L. Zhang, W. Huang, *Adv. Mater.* **2014**, *26*, 7931–7958.

[25] K. Mori, T. P. M. Goumans, E. Van Lenthe, F. Wang, *Phys. Chem. Chem. Phys.* **2014**, *16*, 14523–14530.

[26] M. Cocchi, J. Kalinowski, D. Virgili, J. A. G. Williams, *Appl. Phys. Lett.* **2008**, *92*, 113302.

[27] P.-K. Chow, G. Cheng, G. S. M. Tong, W.-P. To, W.-L. Kwong, K.-H. Low, C.-C. Kwok, C. Ma, C.-M. Che, *Angew. Chem. Int. Ed.* **2015**, *54*, 2084–2089.

[28] K. Tuong Ly, R.-W. Chen-Cheng, H.-W. Lin, Y.-J. Shiau, S.-H. Liu, P.-T. Chou, C.-S. Tsao, Y.-C. Huang, Y. Chi, *Nat. Photonics* **2017**, *11*, 63–68.

[29] S. Lamansky, P. Djurovich, D. Murphy, F. Abdel-Razzaq, H.-E. Lee, C. Adachi, P. E. Burrows, S. R. Forrest, M. E. Thompson, *J. Am. Chem. Soc.* **2001**, *123*, 4304–4312.

[30] C. Adachi, R. C. Kwong, P. Djurovich, V. Adamovich, M. A. Baldo, M. E. Thompson, S. R. Forrest, *Appl. Phys. Lett.* **2001**, *79*, 2082–2084.

[31] N. A. Romero, D. A. Nicewicz, *Chem. Rev.* **2016**, *116*, 10075–10166.

[32] F. Strieth-Kalthoff, M. J. James, M. Teders, L. Pitzer, F. Glorius, *Chem. Soc. Rev.* **2018**, *47*, 7190–7202.

[33] F. Strieth-Kalthoff, F. Glorius, *Chem* **2020**, *6*, 1888–1903.

[34] J. Parthiban, D. Garg, S. Ahuja, S. Jockusch, A. Ugrinov, J. Sivaguru, *ACS Catalysis* **2024**, *14*, 8794–8802.

[35] N. Iwata, S. Kitanaka, *Chem. Pharm. Bull.* **2011**, *59*, 1409–1412.

[36] D. Zhao, X. Han, D. Wang, M. Liu, J. Gou, Y. Peng, J. Liu, Y. Li, F. Cao, C. Zhang, *Front. Microbiol.* **2019**, *10*, 1–10.

[37] T. Lu, F. Chen, *J. Comput. Chem.* **2012**, *33*, 580–592.

[38] J. Jin, T. Yu, J. Chen, R. Hu, G. Yang, Y. Zeng, Y. Li, *Curr. Opin. Green Sustain. Chem.* **2023**, *43*, 100841.

[39] J. H. Correia, J. A. Rodrigues, S. Pimenta, T. Dong, Z. Yang, *Pharmaceutics* **2021**, *13*, 1332.

[40] D. Van Straten, V. Mashayekhi, H. De Bruijn, S. Oliveira, D. Robinson, *Cancers* **2017**, *9*, 19.

[41] A. T. Byrne, A. E. O'Connor, M. Hall, J. Murtagh, K. O'Neill, K. M. Curran, K. Mongrain, J. A. Rousseau, R. Lecomte, S. McGee, J. J. Callanan, D. F. O'Shea, W. M. Gallagher, *Br. J. Cancer* **2009**, *101*, 1565–1573.

[42] W. M. Gallagher, L. T. Allen, C. O'Shea, T. Kenna, M. Hall, A. Gorman, J. Killoran, D. F. O'Shea, *Br. J. Cancer* **2005**, *92*, 1702–1710.

[43] K. J. Mellish, R. D. Cox, D. I. Vernon, J. Griffiths, S. B. Brown, *Photochem. Photobiol.* **2002**, *75*, 392.

[44] H. D. Cole, A. Vali, J. A. Roque, G. Shi, G. Kaur, R. O. Hodges, A. Francés-Monerris, M. E. Alberto, C. G. Cameron, S. A. McFarland, *Inorg. Chem.* **2023**, *62*, 21181–21200.

[45] M. Baroncini, M. Canton, L. Casimiro, S. Corra, J. Groppi, M. La Rosa, S. Silvi, A. Credi, *Eur. J. Inorg. Chem.* **2018**, *2018*, 4589–4603.

[46] R. Hamze, S. Shi, S. C. Kapper, D. S. Muthiah Ravinson, L. Estergreen, M.-C. Jung, A. C. Tadle, R. Haiges, P. I. Djurovich, J. L. Peltier, R. Jazzar, G. Bertrand, S. E. Bradforth, M. E. Thompson, *J. Am. Chem. Soc.* **2019**, *141*, 8616–8626.

[47] R. Hamze, J. L. Peltier, D. Sylvinson, M. Jung, J. Cardenas, R. Haiges, M. Soleilhavoup, R. Jazzar, P. I. Djurovich, G. Bertrand, M. E. Thompson, *Science* **2019**, *363*, 601.

[48] S. Meißner, *Resources* **2021**, *10*, 120.

[49] M. Tost, B. Bayer, M. Hitch, S. Lutter, P. Moser, S. Feiel, *Sustainability* **2018**, *10*, 2881.

[50] M. G. Crestani, G. F. Manbeck, W. W. Brennessel, T. M. McCormick, R. Eisenberg, *Inorg. Chem.* **2011**, *50*, 7172–7188.

[51] D. Kakizoe, M. Nishikawa, Y. Fujii, T. Tsubomura, *Dalton Trans.* **2017**, *46*, 14804–14811.

[52] M. Gernert, L. Balles-Wolf, F. Kerner, U. Müller, A. Schmiedel, M. Holzapfel, C. M. Marian, J. Pflaum, C. Lambert, A. Steffen, *J. Am. Chem. Soc.* **2020**, *142*, 8897–8909.

[53] M. A. Carvajal, J. J. Novoa, S. Alvarez, *J. Am. Chem. Soc.* **2004**, *126*, 1465–1477.

[54] M. Iwamura, S. Takeuchi, T. Tahara, *Acc. Chem. Res.* **2015**, *48*, 782–791.

[55] V. A. Krylova, P. I. Djurovich, J. W. Aronson, R. Haiges, M. T. Whited, M. E. Thompson, *Organometallics* **2012**, *31*, 7983–7993.

[56] S. Lin, Q. Peng, Q. Ou, Z. Shuai, *Inorg. Chem.* **2019**, *58*, 14403–14409.

[57] L. Gao, D. V. Partyka, J. B. Updegraff, N. Deligonul, T. G. Gray, *Eur. J. Inorg. Chem.* **2009**, *2009*, 2711–2719.

[58] T.-y. Li, D. S. Muthiah Ravinson, R. Haiges, P. I. Djurovich, M. E. Thompson, *J. Am. Chem. Soc.* **2020**, *142*, 6158–6172.

[59] B. Rao, H. Tang, X. Zeng, L. L. Liu, M. Melaimi, G. Bertrand, *Angew. Chem. Int. Ed.* **2015**, *54*, 14915–14919.

[60] A. Vogler, *Inorg. Chem. Commun.* **2017**, *84*, 81–83.

[61] M. E. Thompson, P. I. Djurovich, V. A. Krylova, *pat.*, 9853229, **2015**.

[62] Y. Xiao, H. Wang, Z. Xie, M. Shen, R. Huang, Y. Miao, G. Liu, T. Yu, W. Huang, *Chem. Sci.* **2022**, *13*, 8906–8923.

[63] J. T. Alander, I. Kaartinen, A. Laakso, T. Pätilä, T. Spillmann, V. V. Tuchin, M. Venermo, P. Välisuo, *Int. J. Biomed. Imaging* **2012**, *2012*, 1–26.

[64] D. Ndaleh, W. E. Meador, C. Smith, H. C. Friedman, M. McGuire, J. R. Caram, N. I. Hammer, J. H. Delcamp, *ChemPhotoChem* **2024**, *8*, e202300212.

[65] W. Feng, Y. Zhang, Z. Li, S. Zhai, W. Lv, Z. Liu, *Anal. Chem.* **2019**, *91*, 15757–15762.

[66] M. Casalboni, F. De Matteis, P. Prosposito, A. Quatela, F. Sarcinelli, *Chem. Phys. Lett.* **2003**, *373*, 372–378.

[67] J Frangioni, *Curr. Opin. Chem. Biol.* **2003**, *7*, 626–634.

[68] L. Van Manen, H. J. M. Handgraaf, M. Diana, J. Dijkstra, T. Ishizawa, A. L. Vahrmeijer, J. S. D. Mieog, *J. Surg. Oncol.* **2018**, *118*, 283–300.

[69] H. Zhao, H. Xiao, Y. Liu, H. Ju, *BMEMat* **2023**, *1*, e12032.

[70] *Mechanochromic Fluorescent Materials: Phenomena, Materials and Applications*, (Eds.: J. Xu, Z. Chi), Royal Society of Chemistry, Cambridge, **2014**.

[71] S. A. Oladepo, *Molecules* **2022**, *27*, 1453.

[72] L. D. C. De Castro, T. A. P. Engels, O. N. Oliveira, A. P. H. J. Schenning, *ACS Appl. Mater. Interfaces* **2024**, *16*, 14144–14151.

[73] K. Muthamma, D. Sunil, P. Shetty, S. D. Kulkarni, T. Ali, N. Dey, A. P.J., *Prog. Org. Coat.* **2023**, *184*, 107832.

[74] R. Janissen, G. A. Filonenko, *J. Am. Chem. Soc.* **2022**, *144*, 23198–23204.

[75] Y. Vidavsky, S. J. Yang, B. A. Abel, I. Agami, C. E. Diesendruck, G. W. Coates, M. N. Silberstein, *J. Am. Chem. Soc.* **2019**, *141*, 10060–10067.

[76] Y. Hirai, A. Wrona-Piotrowicz, J. Zakrzewski, A. Brosseau, R. Guillot, R. Métivier, C. Allain, *Photochem. Photobiol. Sci.* **2020**, *19*, 229–234.

[77] E. Contini, V. A. Dini, A. Rozzi, D. Genovese, N. Zaccheroni, A. Pedrini, E. Dalcanale, R. Pinalli, C. Gualandi, *ACS. Appl. Polym. Mater.* **2024**, *6*, 669–680.

[78] J. Han, K.-M. Tang, S.-C. Cheng, C.-O. Ng, Y.-K. Chun, S.-L. Chan, S.-M. Yiu, M.-K. Tse, V. A. L. Roy, C.-C. Ko, *Inorg. Chem. Front.* **2020**, *7*, 786–794.

[79] D. Li, G. Li, J. Xie, D. Zhu, Z. Su, M. R. Bryce, *J. Mater. Chem. C* **2019**, *7*, 10876–10880.

[80] S. Zhu, J. Hu, S. Zhai, Y. Wang, Z. Xu, R. Liu, H. Zhu, *Inorg. Chem. Front.* **2020**, *7*, 4677–4686.

[81] H. Ito, T. Saito, N. Oshima, N. Kitamura, S. Ishizaka, Y. Hinatsu, M. Wakeshima, M. Kato, K. Tsuge, M. Sawamura, *J. Am. Chem. Soc.* **2008**, *130*, 10044–10045.

[82] T. Seki, Y. Takamatsu, H. Ito, *J. Am. Chem. Soc.* **2016**, *138*, 6252–6260.

[83] G. A. Reider in *Photonik: Eine Einführung in die Grundlagen*, (Ed.: G. A. Reider), Springer, Berlin, Heidelberg, **2022**, pp. 1–39.

[84] S. Saito, *Front. Phys.* **2023**, *11*, 1225360.

[85] T. Kimoto, N. Tajima, M. Fujiki, Y. Imai, *Chem.: Asian J.* **2012**, *7*, 2836–2841.

[86] T. Mori in *Circularly Polarized Luminescence of Isolated Small Organic Molecules*, (Ed.: T. Mori), Springer, Singapore, **2020**, pp. 1–10.

[87] J. L. Lunkley, D. Shirotani, K. Yamanari, S. Kaizaki, G. Muller, *Inorg. Chem.* **2011**, *50*, 12724–12732.

[88] E. E. Braker, N. F. M. Mukthar, N. D. Schley, G. Ung, *ChemPhotoChem* **2021**, *5*, 902–905.

[89] A. M. T. Muthig, O. Mrózek, T. Ferschke, M. Rödel, B. Ewald, J. Kuhnt, C. Lenczyk, J. Pflaum, A. Steffen, *J. Am. Chem. Soc.* **2023**, *145*, 4438–4449.

[90] S. Ito, R. Sekine, M. Munakata, M. Asami, T. Tachikawa, D. Kaji, K. Mishima, Y. Imai, *ChemPhotoChem* **2021**, *5*, 920–925.

[91] M. Louis, R. Sethy, J. Kumar, S. Katao, R. Guillot, T. Nakashima, C. Allain, T. Kawai, R. Métivier, *Chem. Sci.* **2019**, *10*, 843–847.

[92] A. M. T. Muthig, J. Wieland, C. Lenczyk, S. Koop, J. Tessarolo, G. H. Clever, B. Hupp, A. Steffen, *Chem. Eur. J.* **2023**, *29*, 1–10.

[93] X.-H. Zhu, J. Peng, Y. Cao, J. Roncali, *Chem. Soc. Rev.* **2011**, *40*, 3509.

[94] X. Wu, S. Ni, C.-H. Wang, W. Zhu, P.-T. Chou, *Chem. Rev.* **2025**, *125*, 6685–6752.

[95] C. Wegeberg, O. S. Wenger, *JACS Au* **2021**, *1*, 1860–1876.

[96] O. S. Wenger, *J. Am. Chem. Soc.* **2018**, *140*, 13522–13533.

[97] J.-X. Liu, S.-L. Mei, X.-H. Chen, C.-J. Yao, *Crystals* **2021**, *11*, 155.

[98] F. Anelli, A. M. Loconsole, F. Prudenzano, *Optical Materials* **2025**, *167*, 117294.

[99] J. Markiewicz, M. Kochanowicz, T. Ragiń, P. Miluski, W. A. Pisarski, J. Pisarska, M. Kuwik, D. Dorosz, M. Leich, M. Jäger, *Sci Rep* **2025**, *15*, 4161.

[100] E. M. Kober, J. V. Caspar, R. S. Lumpkin, T. J. Meyer, *J. Phys. Chem. A* **1986**, *90*, 3722.

[101] R. Englman, J. Jortner, *J. Lumin.* **1970**, *1–2*, 134–142.

[102] C. Erker, T. Basché, *J. Am. Chem. Soc.* **2022**, *144*, 14053–14056.

[103] T. Micklitz, A. Morningstar, A. Altland, D. A. Huse, *Phys. Rev. Lett.* **2022**, *129*, 140402.

[104] C. Li, M. Wu, Z. Zhao, J. W. Lam, B. Xu, B. Z. Tang, *Chem* **2025**, *11*, 102654.

[105] S Lamansky, P Djurovich, D Murphy, F Abdel-Razzaq, R Kwong, I Tsyba, M Bortz, B Mui, R Bau, M. E. Thompson, *Inorg. Chem.* **2001**, *40*, 1704–1711.

[106] J. Qiao, L. Duan, L. Tang, L. He, L. Wang, Y. Qiu, *J. Mater. Chem.* **2009**, *19*, 6573.

[107] S. Diesing, L. Zhang, E. Zysman-Colman, I. D. W. Samuel, *Nature* **2024**, *627*, 747–753.

[108] B. Ayataka Endo, M. Ogasawara, A. Takahashi, D. Yokoyama, Y. Kato, C. Adachi, C Adachi, A Endo, D Yokoyama, M Ogasawara, Y Kato, A Takahashi, *Adv. Mater.* **2009**, *21*, 4802–4806.

[109] E.-B. Jang, G.-S. Choi, E.-J. Bae, B.-K. Ju, Y.-W. Park, *Nanomaterials* **2023**, *13*, 2366.

[110] A. M. T. Muthig, PhD thesis, Technische Universität Dortmund, **2022**.

[111] A. M. T. Muthig, M. Krumrein, J. Wieland, M. Gernert, F. Kerner, J. Pflaum, A. Steffen, *Inorg. Chem.* **2022**, *61*, 14833–14844.

[112] A. S. Romanov, D. Di, L. Yang, J. Fernandez-Cestau, C. R. Becker, C. E. James, B. Zhu, M. Linnolahti, D. Credgington, M. Bochmann, *Chem. Commun.* **2016**, *52*, 6379–6382.

[113] A. S. Romanov, S. T. E. Jones, Q. Gu, P. J. Conaghan, B. H. Drummond, J. Feng, F. Chotard, L. Buizza, M. Foley, M. Linnolahti, D. Credgington, M. Bochmann, *Chem. Sci.* **2020**, *11*, 435–446.

[114] O. Mrózek, M. Gernert, A. Belyaev, M. Mitra, L. Janiak, C. M. Marian, A. Steffen, *Chemistry* **2022**, *28*, e202201114.

[115] O. Mrózek, M. Mitra, B. Hupp, A. Belyaev, N. Lüdtke, D. Wagner, C. Wang, O. S. Wenger, C. M. Marian, A. Steffen, *Chem. Eur. J.* **2023**, *29*, 1–6.

[116] M. Gernert, U. Müller, M. Haehnel, J. Pflaum, A. Steffen, *Chem. - Eur. J.* **2017**, *23*, 2206–2216.

[117] R. Jazzar, J.-B. Bourg, R. D. Dewhurst, B. Donnadieu, G. Bertrand, *J. Org. Chem.* **2007**, *72*, 3492–3499.

[118] S. Gómez-Bujedo, M. Alcarazo, C. Pichon, E. Alvarez, R. Fernández, J. M. Lassaletta, *Chem. Commun.* **2007**, 1180–1182.

[119] A. Magriz, S. Gómez-Bujedo, E. Álvarez, R. Fernández, J. M. Lassaletta, *Organometallics* **2010**, *29*, 5941–5945.

[120] A. Collado, A. Gómez-Suárez, A. R. Martin, A. M. Z. Slawin, S. P. Nolan, *Chem. Commun.* **2013**, *49*, 5541–5543.

[121] R. Visbal, A. Laguna, M. C. Gimeno, *Chem. Commun.* **2013**, *49*, 5642–5644.

[122] T. Tsuda, T. Hashimoto, T. Saegusa, *J. Am. Chem. Soc.* **1972**, *94*, 658–659.

[123] T. Tsuda, T. Takeda, A. Tsubouchi in *Encyclopedia of Reagents for Organic Synthesis*, (Ed.: John Wiley & Sons, Ltd), John Wiley & Sons, Ltd, Chichester, UK, **2009**, rc212.pub2.

[124] E. Alcalde, I. Dinarès, A. Ibáñez, N. Mesquida, *Molecules* **2012**, *17*, 4007–4027.

[125] S. Alvarez, *Dalton Trans.* **2013**, *42*, 8617.

[126] B. Cordero, V. Gómez, A. E. Platero-Prats, M. Revés, J. Echeverría, E. Cremades, F. Barragán, S. Alvarez, *Dalton Trans.* **2008**, 2832–2838.

[127] T. Lu, Q. Chen, *Chem. Methods* **2021**, *1*, 231–239.

[128] J. Nitsch, F. Lacemon, A. Lorbach, A. Eichhorn, F. Cisnetti, A. Steffen, *Chem. Commun.* **2016**, *52*, 2932–2935.

[129] S. Ogawa, H. Katsuragi, T. Ikeda, K. Oshima, S. Satokawa, Y. Yamazaki, T. Tsubomura, *Dalton Trans.* **2021**, *50*, 8845–8850.

[130] B. Hupp, J. Nitsch, T. Schmitt, R. Bertermann, K. Edkins, F. Hirsch, I. Fischer, M. Auth, A. Sperlich, A. Steffen, *Angew. Chem.* **2018**, *130*, 13860–13864.

[131] A. Liske, L. Wallbaum, T. Hölzel, J. Föller, M. Gernert, B. Hupp, C. Ganter, C. M. Marian, A. Steffen, *Inorg. Chem.* **2019**, *58*, 5433–5445.

[132] F. P. Dwyer, F. L. Garvan, S. Kirschner in *Inorganic Syntheses*, *Vol. 6*, (Ed.: E. G. Rochow), Wiley, **1960**, pp. 195–197.

[133] H. Nakazawa, H. Yoneda, *J. Chromatogr. A* **1978**, *160*, 89–99.

[134] K. Miyoshi, S. Izumoto, K. Nakai, H. Yoneda, *Inorg. Chem.* **1986**, *25*, 4654–4657.

[135] T. Bark, A. von Zelewsky, D. Rappoport, M. Neuburger, S. Schaffner, J. Lacour, J. Jodry, *Chem. Eur. J.* **2004**, *10*, 4839–4845.

[136] K. Dhbaibi, L. Favereau, M. Srebro-Hooper, M. Jean, N. Vanthuyne, F. Zinna, B. Jamoussi, L. Di Bari, J. Autschbach, J. Crassous, *Chem. Sci.* **2018**, *9*, 735–742.

[137] A. Labelle, B. A. Arndtsen, *Chem. Commun.* **2023**, *59*, 728–731.

[138] G. M. Sheldrick, *Acta Crystallogr A Found Adv* **2015**, *71*, 3–8.

[139] G. M. Sheldrick, *Acta Crystallogr. C* **2015**, *71*, 3–8.

[140] F. Neese, *Wiley Interdiscip. Rev. Comput. Mol. Sci.* **2012**, *2*, 73–78.

[141] F. Neese, *Wiley Interdiscip. Rev. Comput. Mol. Sci.* **2022**, *12*, e1606.

[142] J. P. Perdew, M. Ernzerhof, K. Burke, *J. Chem. Phys.* **1996**, *105*, 9982–9985.

[143] C. Adamo, V. Barone, *J. Chem. Phys.* **1999**, *110*, 6158–6170.

[144] F. Weigend, R. Ahlrichs, *Phys. Chem. Chem. Phys.* **2005**, *7*, 3297.

[145] F. Weigend, *Phys. Chem. Chem. Phys.* **2006**, *8*, 1057.

[146] S. Grimme, S. Ehrlich, L. Goerigk, *J. Comput. Chem.* **2011**, *32*, 1456–1465.

[147] D. A. Pantazis, X.-Y. Chen, C. R. Landis, F. Neese, *J. Chem. Theory Comput.* **2008**, *4*, 908–919.

[148] T. D. Goddard, C. C. Huang, E. C. Meng, E. F. Pettersen, G. S. Couch, J. H. Morris, T. E. Ferrin, *Protein Sci.* **2018**, *27*, 14–25.

[149] E. F. Pettersen, T. D. Goddard, C. C. Huang, E. C. Meng, G. S. Couch, T. I. Croll, J. H. Morris, T. E. Ferrin, *Protein Sci.* **2021**, *30*, 70–82.

[150] A. Najibi, L. Goerigk, *J. Chem. Theory Comput.* **2018**, *14*, 5725–5738.

[151] W Humphrey, A Dalke, K Schulten, *J. Mol. Graph.* **1996**, *14*, 27–28, 33–38.

[152] J. A. Raskatov, J. M. Brown, A. L. Thompson, *CrystEngComm* **2011**, *13*, 2923.

Eidesstattliche Versicherung (Affidavit)

Krieger (geb. Wieland), Justin
Name, Vorname
(Surname, first name)

176623
Matrikel-Nr.
(Enrolment number)

Belehrung:

Wer vorsätzlich gegen eine die Täuschung über Prüfungsleistungen betreffende Regelung einer Hochschulprüfungsordnung verstößt, handelt ordnungswidrig. Die Ordnungswidrigkeit kann mit einer Geldbuße von bis zu 50.000,00 € geahndet werden. Zuständige Verwaltungsbehörde für die Verfolgung und Ahndung von Ordnungswidrigkeiten ist der Kanzler/die Kanzlerin der Technischen Universität Dortmund. Im Falle eines mehrfachen oder sonstigen schwerwiegenden Täuschungsversuches kann der Prüfling zudem exmatrikuliert werden, § 63 Abs. 5 Hochschulgesetz NRW.

Die Abgabe einer falschen Versicherung an Eides statt ist strafbar.

Wer vorsätzlich eine falsche Versicherung an Eides statt abgibt, kann mit einer Freiheitsstrafe bis zu drei Jahren oder mit Geldstrafe bestraft werden, § 156 StGB. Die fahrlässige Abgabe einer falschen Versicherung an Eides statt kann mit einer Freiheitsstrafe bis zu einem Jahr oder Geldstrafe bestraft werden, § 161 StGB.

Die oben stehende Belehrung habe ich zur Kenntnis genommen:

Official notification:

Any person who intentionally breaches any regulation of university examination regulations relating to deception in examination performance is acting improperly. This offence can be punished with a fine of up to EUR 50,000.00. The competent administrative authority for the pursuit and prosecution of offences of this type is the chancellor of the TU Dortmund University. In the case of multiple or other serious attempts at deception, the candidate can also be unenrolled, Section 63, paragraph 5 of the Universities Act of North Rhine-Westphalia.

The submission of a false affidavit is punishable.

Any person who intentionally submits a false affidavit can be punished with a prison sentence of up to three years or a fine, Section 156 of the Criminal Code. The negligent submission of a false affidavit can be punished with a prison sentence of up to one year or a fine, Section 161 of the Criminal Code.

I have taken note of the above official notification.

Ort, Datum
(Place, date)

Unterschrift
(Signature)

Titel der Dissertation:
(Title of the thesis):

Ich versichere hiermit an Eides statt, dass ich die vorliegende Dissertation mit dem Titel selbstständig und ohne unzulässige fremde Hilfe angefertigt habe. Ich habe keine anderen als die angegebenen Quellen und Hilfsmittel benutzt sowie wörtliche und sinngemäße Zitate kenntlich gemacht.
Die Arbeit hat in gegenwärtiger oder in einer anderen Fassung weder der TU Dortmund noch einer anderen Hochschule im Zusammenhang mit einer staatlichen oder akademischen Prüfung vorgelegen.

I hereby swear that I have completed the present dissertation independently and without inadmissible external support. I have not used any sources or tools other than those indicated and have identified literal and analogous quotations.

The thesis in its current version or another version has not been presented to the TU Dortmund University or another university in connection with a state or academic examination.*

*Please be aware that solely the German version of the affidavit ("Eidesstattliche Versicherung") for the PhD thesis is the official and legally binding version.

Ort, Datum
(Place, date)

Unterschrift
(Signature)

"The winds blew southward, through knotted forests, over shimmering plains and towards lands unexplored. This wind, it was not the ending. There are no endings, and never will be endings, to the turning of the Wheel of Time.
But it was an *ending."*

—Robert Jordan and Brandon Sanderson, *A Memory of Light*